STEAM CONDENSATION IN FLATTENED-TUBE AIR-COOLED CONDENSERS

BY

WILLIAM ALLEN DAVIES III

DISSERTATION

Submitted in partial fulfillment of the requirements
for the degree of Doctor of Philosophy in Mechanical Engineering
in the Graduate College of the
University of Illinois at Urbana-Champaign, 2019

Urbana, Illinois

Doctoral Committee:

Professor Predrag S. Hrnjak, Chair
Professor Anthony M. Jacobi
Professor J. Craig Dutton
Assistant Professor Nenad Miljkovic

ABSTRACT

Air-cooled condensers for power plants are an alternative to closed-cycle wet cooling with a condenser and cooling tower pair. Air-cooled condensers cool the process steam by forced-convection of air, replacing the water evaporation found in traditional power-plant designs. Air-cooled condensers are rising in prominence because they provide utility companies with additional freedoms – to build power plants away from large water sources and to avoid a lengthy environmental permitting process. In addition, the environmental benefits of reducing power-plant water consumption are significant. However, the lower thermal performance of air-cooling in comparison to water-cooling makes the cost of air-cooled condensers prohibitive in many cases. In order reduce this performance gap, the current designs of air-cooled condensers must be significantly improved. However, to improve the design, understanding of the condenser physics through experimental investigation is needed. As of yet, there are no experimental results in the open literature for steam-side performance of the most-common condenser design - the flattened-tube air-cooled condenser. This thesis provides the experimental results and analysis to address this deficiency.

The experiments contained herein provide visualization along with measurement of void fraction, pressure drop, capacity and heat transfer coefficient for flattened-tube air-cooled steam condensers with inner dimensions of 216 mm height x 16 mm width. Two lengths of tube are investigated: 10.7 m and 5.7 m. The tubes are steel with brazed wavy aluminum fins of 200 mm length x 19 mm height. Air is in cross-flow to the condensing steam. Typical condenser designs contain about 80% of the tubes in co-current configuration, with both steam vapor and liquid flowing downwards. The remaining 20% of tubes are in counter-flow configuration, with vapor flowing upwards and condensate flowing downwards. This thesis investigates only the co-current downward-flowing tubes. In addition, the effect of downward inclination angle of the tubes is investigated, with the condensers mounted on a hinged truss in the test facility to enable lifting to inclination angles from 0^{o} to 75^{o}.

Initial experiments are performed on the tube with 10.7 m length. The condenser tube is cut in half lengthwise and covered with a polycarbonate window to perform diabatic visualization simultaneously with the heat transfer and pressure drop measurements. The effect

of tube inclination on flow regimes, void fraction, pressure drop, capacity and heat transfer coefficient (HTC) is evaluated. The flow regime is found to be stratified for almost all conditions, with stratified-wavy flow observed near the inlet of the horizontal tube and near the outlet of tubes inclined 60^o or greater. Increasing downward inclination angle is found to increase the drainage of condensate from the tube, thereby increasing the average void fraction. The greatest increase in void fraction is seen near the tube outlet. Increasing inclination is also seen to decrease the pressure drop in the tube. This is the result of gravitational pressure recovery, as well as decreased vapor velocity from the increased void fraction. Increasing inclination also increases capacity, as the improved drainage of condensate reduces the condenser thermal resistance.

Following these initial results in the half-tube, a full (un-cut) tube is tested in the same experimental facility. This tube has a shorter length of 5.7 m and is able to be tested at lower condensing pressures. For this set of experiments, adiabatic visualization sections are designed and installed at the condenser inlet and outlet to provide identification of flow regimes and measurement of void fraction. The tube inclination is varied from 0^o to 49^o downwards, and the condensation pressure is varied from 60 kPa to 105 kPa. Similar results for flow regimes and void fraction are found as in the 10.7 m tube, with annular flow at the tube inlet and stratified flow at the tube outlet. Increasing tube inclination is found to decrease the depth of the condensate river. This decreasing depth is found to decrease frictional pressure drop and increase condenser heat transfer coefficient. The increase in heat transfer coefficient due to inclination is found only near the tube outlet, and is smaller than the increase measured in the 10.7 m tube. Overall, the results show that the reduced tube length leads to less condensate build-up and improved thermal performance.

From these experimental results, a thermo-hydraulic model for void fraction and capacity is developed. The model uses open-channel-flow theory to predict the depth and velocity of the condensate in the stratified layer at the tube bottom. The thermal model calculates local HTC on the air and steam sides and can provide a local description of heat flux in the condenser. The thermal model is validated by experiments in both the 10.7 m half tube and the 5.7 m full tube. The model predicts 86% of the experimental results for condensate river depth to within 20% accuracy and 98% of the experimental results for capacity within 5% accuracy.

Using the model, alternative airflow profiles that match non-uniformities on the air and steam sides of the condenser are proposed and tested experimentally. The first profile reverses airflow direction and yields an increase in condenser capacity of 3.5%. The second profile increases airflow near the steam inlet and reduces airflow near the steam outlet. This yields a 3.1% increase in capacity as well as a reduction in pressure drop (for a constant capacity).

Finally, to more accurately measure the steam-side heat transfer coefficient, a new condenser test section is designed. This test section replaces the air-cooled fins with a single pass of cooling water. The design maintains equivalent operating conditions with the air-cooled condenser while providing accurate local heat transfer coefficient determination. In particular, the test section maintains the non-uniform heat flux and wall temperature of the air-cooled section. The results show that two distinct heat transfer regions can be defined: the stratified condensate layer flowing axially at the tube bottom, and the condensing-film region along the tube side-walls and top. The heat transfer coefficient in the stratified layer depends mostly on the condensate depth, and the heat transfer coefficient in the condensing-film region depends mostly on the wall-steam temperature difference. The heat transfer coefficient in the stratified layer is much lower in magnitude (up to 30 times) than that in the condensing-film region. The heat transfer coefficient in the stratified region is under-predicted by the correlations of Rosson and Myers [1] and Dobson and Chato [2]. In the condensing-film region, the heat transfer coefficient can be accurately predicted by the theory of Nusselt [3] when considering the local wall-steam temperature difference. The experimental results are not accurately predicted by existing correlations for heat transfer coefficient during condensation, so a new correlation is developed that is a perimeter-weighted average of the heat transfer coefficient in the stratified condensate and condensing-film regions. The new correlation predicts 77% of the data within 20% accuracy, with a mean absolute percent error of 14%.

To my grandfather, William Allen Davies Sr.

ACKNOWLEDGEMENTS

This work is a culmination of a long journey, both academic, scientific and personal. Such a journey would not be possible without a strong leader, and for that I am forever indebted to my advisor, Professor Pega Hrnjak. In short, nothing in this work would have been completed without his guidance. He both led the way and pushed me throughout the entire process, with our weekend meetings providing the advice and criticism that kept me on the right path. His intellectual curiosity provided a blueprint for me to follow and provided new directions when my research hit a dead end. Perhaps, I appreciated him most as a mentor and role model - for his outlook on science, work, and life. Without exaggeration, I can say that it was an honor to work as his research assistant. I will be always grateful that he took me on as a naïve incoming graduate student five years ago.

I would also like to thank the members of my dissertation committee, Dr. Anthony Jacobi, Dr. J. Craig Dutton, and Dr. Nenad Miljkovic for their critical insight and advice. Dr. Jacobi, in particular, served as co-PI on my Master's project, and contributed to the design and calibration of my initial experimental facility.

Many additional people helped me along the way. Special thanks goes to Don Beeler at Creative Thermal Solutions (CTS), who taught me how to braze, how to weld, and dozens of other techniques around the shop. He also fixed all my poorly-brazed joints, consulted on my facility design, and helped me out whenever I had a problem with facility construction or repair. All of my experimental work was performed at Creative Thermal Solutions, where I received advice and helping hands for facility design, construction and operation from nearly all of the employees.

Contributions from my colleagues in the ACRC are too numerous to count, but special mention must go to several individuals. Yu Kang, who dove into building our ambitiously-large facility without complaint, and who navigated the early years of graduate school alongside me, has made a contribution to every piece of my graduate school work. His contribution and friendship were invaluable. Jun Li and Jiange Xiao, my co-researchers in condensation, helped me to puzzle out many of the trickier aspects of condensation physics. Many thanks also to Houpei Li, Jiu Xu, Cheng-Min Yang, Shenghan Jin, Huize Li, Abdel Farraj, and Rachel Hawken for their discussion and advice on my project, and to all my co-researchers in the ACRC for being such an outstanding group.

I am also grateful to Maria Piñeros, whose journey with me was as much a part of graduate school as any of the technical details in this dissertation. She set a high bar to follow and taught me countless ways to succeed in graduate school. I would never have started this doctoral program without her.

An enormous acknowledgement must go to my family! My grandparents, Allen and Eliza Davies, set an example for me to follow and were some of the biggest cheerleaders of my progress. I am especially grateful for my parents, Bill and Candy Davies. What they taught me is the basis for everything I know, including two important skills for this thesis – how to work in a shop and how to write! They also encouraged me to pursue more education. I would like to thank my sister, Kim Davies, for talking to me on the phone during my lonely first days as a graduate student and for showing me that you can spend way too many years in graduate school and still come out alright.

Finally, to the countless friends and family members who have shared fun times and companionship along the way, and who have eagerly asked about my progress – thank you! It is these interactions that gave me the energy to keep going on this project.

TABLE OF CONTENTS

LIST OF TABLES

LIST OF FIGURES

NOMENCLATURE

A	Area	m^2
ACC	Air-cooled condenser	
b^2	Capillary constant	m^2
C_d	Bulk drag coefficient	
$C_1; C_2$	Empirical constants	
c_p	Specific heat at constant pressure	J kg^{-1} K^{-1}
d_h	Hydraulic depth	m
D_h	Hydraulic diameter	m
Fr	Froude number; $Fr = v / \sqrt{g d_h}$	
f	Friction factor	
g	Gravitational acceleration	m s^{-2}
g_{eff}	Gravitational acceleration along tube curvature	m s^{-2}
G	Mass flux	kg m^{-2} s^{-1}
h	Heat transfer coefficient	W m^{-2} K^{-1}
H	Height	m
HTC	Heat transfer coefficient	
i	Specific enthalpy	J kg^{-1}
i_{fg}	Specific enthalpy of vaporization	J kg^{-1}
k	Thermal conductivity	W m^{-1} K^{-1}
L	Length	m
$LMTD$	Log mean temperature difference	^oC
$\dot{m}$	Mass flow rate	kg s^{-1}
M	Momentum	kg m s^{-1}
MAPE	Mean absolute percent error	
n	Manning's roughness coefficient	s $m^{-1/3}$
Nu	Nusselt number	
P	Pressure	kPa
p	Perimeter	m
Pe	Peclet number	
Pr	Prandtl number	
Q	Heat transferred	W
q''	Heat flux	W m^{-2}
$r(x)$	Local radius of curvature of condensate river surface	m
R	Radius of curvature of tube ends	m
R_h	Hydraulic radius	m
Re	Reynolds number	
Re_a	Reynolds number of air, based on hydraulic diameter of channel between fins	
$Re_{a,j}$	Reynolds number of air, based on distance X along the tube perimeter	
s	Length along condensate surface	m
t	Thickness	m
t_c	Thickness of the condensate river along the steel wall	m

$t_{c,PC}$	Height of the condensate river along the polycarbonate window	m
T	Temperature	^{o}C
u	Uncertainty	
U	Overall heat transfer coefficient, based on air-side area	W m^{-2} K^{-1}
v	Velocity	m s^{-1}
$\dot{V}$	Volumetric flow rate	m^3 s^{-1}
x	Quality	
W	Width	m
W_{top}	Width of the top of the condensate river	m
X	Position along wall height	m
Y	Position perpendicular to wall	m
Z	Axial position: Z = 0 at tube inlet	m

Greek Symbols

α	Void fraction	
β	Angle between river surface and Y-axis (tangent to tube bottom)	^{o}
Δ	Incremental step	
ΔP	Pressure drop	Pa
ε	Equivalent roughness	m
φ	Tube inclination angle	^{o}
η	Overall surface efficiency	
θ	Angle between velocity and temperature gradient	^{o}
μ	Dynamic viscosity	kg m^{-1} s^{-1}
ν	Kinematic viscosity	m^2 s^{-1}
ρ	Density	kg m^{-3}
σ	Surface tension	N m^{-1}
τ	Shear stress	N m^{-2}
ω	Weighting coefficient based on perimeter ratio	

Subscripts

1	Measurement section 1
a	Air
atm	Atmospheric
b	Bottom
	Back of tube (Ch. 9 only)
bulk	Bulk water temperature
c	Condensate
critical	Critical flow of condensate river; occurs when $Fr_c = 1$
cs	Cross section
c1	Primary condenser (consisting of air and water-cooled test sections)
c2	Secondary condenser
D	Diameter
Dhir	From [4]
diff	Pressure drop determined by difference between inlet and outlet gauge pressure
f	Fluid
	Front of the tube (location of thermocouple)

fin	Of the aluminum fins
fr	Frictional
g	Gas
gr	Gravitational
i	Inlet
int	Interfacial
j	Denotes measurement section in X-direction
	Channel number (Ch. 9 & 10 only)
k	Index of position along X-direction
l	Lower
loss	Lost to ambient
m	Middle (wall temperature measurement)
	Momentum (pressure drop)
n	Denotes measurement section in Z-direction
Nu	Nusselt
o	Outlet
PC	Polycarbonate
r	Water-cooling loop
river	Condensate river
s	Steam
sat	Saturation
st	Steel
strat	Stratified condensate layer (at bottom of tube)
sum	Pressure drop measured as sum of pressure drop in each measurement section
sur	Surface
t	Top
tot	Total pressure drop
u	Upper
w	Wall
wetted	Portion of tube covered by the condensate river

Chapter 1 Introduction

Air-cooled condensers are an emerging technology for power plants, where they serve to significantly reduce water use. In 2015, the World Economic Forum declared water scarcity to be the largest global risk to economies and the environment over the coming decade [5]. Energy, in particular, places a large strain on water resources, as water is used in all phases of electricity generation. In the United States, power generation accounts for the largest proportion of freshwater withdrawals, around 40% of the total [6]. The majority of this water is used for cooling thermoelectric plants. For example, a recirculating wet-cooling system, the current design recommended by the U.S. Department of Energy, consumes over 300,000 gallons of water per hour to cool a 520-MW coal-fired power plant [7]. This amounts to – at minimum – ½ gallon of water consumption for every kWh of electricity produced. Furthermore, the water intake kills enormous quantities of aquatic life. For example, twelve Southern California coastal power plants are estimated to account for up to 30% of the fish caught in the region every year [8].

Due to their high water consumption and high impact on plant efficiency, condensers represent the most crucial aspect of this energy-water nexus. At present, an alternative technology exists – dry cooling with air-cooled condensers (ACCs) – which consumes almost no water in cooling the plant. However, ACC installation costs are higher and plants with ACCs have reduced efficiency in comparison to plants with recirculating wet-cooling systems [9]. This is mainly due to the poorer heat transfer efficiency of air in comparison to water. On the hottest days, additional cooling can even be necessary to avoid de-rating of the air-cooled plants. As a result, currently only 0.9% of electricity is produced using ACCs [6]. However, as electricity consumption increases while water resources remain finite, ACCs are becoming more prevalent, with installed capacity tripling between the years 2000 and 2004 [10]. Today, ACCs are used for nearly 10% of new thermo-electric installations [11].

Improving ACC efficiency is accomplished in one of two ways: reducing condenser area for a given capacity and fan power, or decreasing steam-side pressure drop through the condenser tubes. However, a lack of fundamental understanding of the ACC performance has hindered improvements. A significant amount of research has been done on the cold (air) side of the condenser, but very little has been carried out on the hot (steam) side of the condenser. This is a crucial area, as studies in other condensers have shown that performance can be improved through

condensate management ([12],[13]). This work focuses on characterizing the fundamental steam-side physics in the ACC, in order to facilitate improvements in condenser design.

ACCs consist of finned tubes in an A-frame configuration, with axial fans blowing cooling air upwards. The tubes can be in bundles (round or elliptical-shaped) or single rows (flattened shape). The industry in the United States has trended towards the flattened steel tubes with aluminum fins [9]. Therefore, this thesis focuses on the flattened-tube design. In other countries, bundles of elliptical tubes are still prevalent due to their decreased manufacturing cost.

In the flattened-tube ACC design, steam enters in the upper manifold and flows downward in the tubes. Condensate forms along the tube walls, collects in a stratified layer along the tube length, and flows downward under the force of gravity. This co-current downwardly-inclined flow exits the tube at a quality near 20%. The condensate is drained, and the remaining vapor flows upward in counter-current reflux condenser tubes. This thesis examines the performance of the downward-flowing co-current condenser tubes, depicted in Figure 1.1. Figure 1.2 and Figure 1.3 show an installed ACC system at the PGE Gateway Station in Antioch, CA.

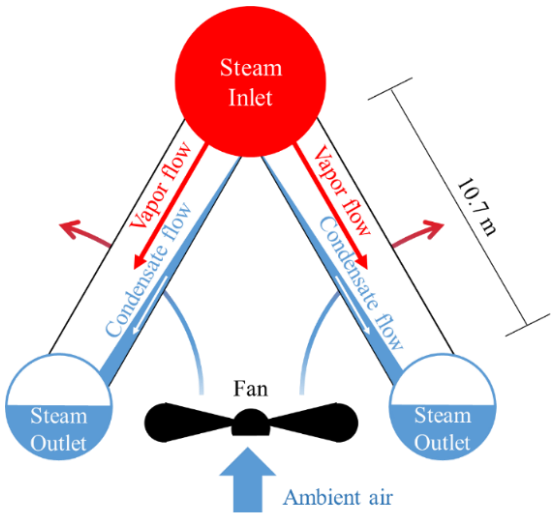

Figure 1.1: Diagram of co-current downward-flowing tubes in an ACC

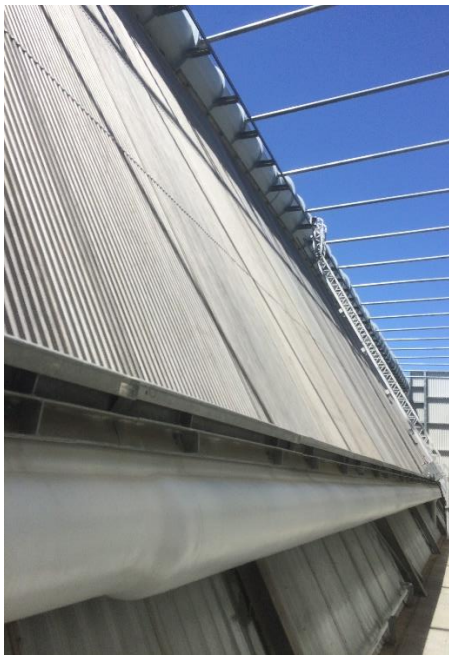

Figure 1.2: View along one leg of an array of condenser tubes, with steam distribution duct at the top and condensate collection line at the bottom

Figure 1.3: Air-cooled condenser installation at the PGE Gateway Station in Antioch, CA

This thesis experimentally investigates the basic characteristics of the steam condensation process in these flattened-tube steam condensers. The first part of the thesis discusses flow regimes and void fraction, followed by an analysis of heat transfer and pressure drop. From these results, models for void fraction and capacity are developed. The model provides additional insight into condenser design, and is used to propose two alternative airflow profiles. The experimental results for these alternative airflow profiles are then presented and analyzed. Finally, a correlation is developed from experimental results for steam-side heat transfer coefficient.

Chapter 2 Literature Review

This chapter presents a review of published studies on the steam-side performance of air-cooled condensers. These are limited in quantity, so an additional discussion of fundamental condensation studies in the areas of flow regimes, void fraction, pressure drop, and heat transfer coefficient is included. This chapter concludes with a discussion of component-level research, including the interaction between air- and steam-side non-uniformities and also relevant condenser models.

2.1 Air-Cooled Condensers

Examining first the component-level research, a large number of studies have been published investigating performance on the air side of these condensers (e.g. [14], [15], [16]), but much less research has been published investigating the steam-side performance. From a heat transfer perspective, the air side provides the larger resistance over the majority of the condenser. However, as the air-side performance has improved, there is an opportunity for additional performance gains to be made by reducing the steam-side heat transfer resistance. For the flattened-tube geometry at industrial lengths, there are no previously published experimental results, although some modeling studies have been published. Cheng *et al*. [17] analyzed the void fraction in the flattened ACC tube using a numerical model and conservation of mass arguments. They found an increase in void fraction as inclination angle increased.

In a study of round-tube ACCs, Kekaula *et al.* [18] performed a numerical analysis of at various inclination angles and air velocities. Their model couples air- and steam-side heat transfer to determine condensate flow configuration and overall heat transfer coefficient (HTC). Like the model of Cheng *et al.* [17], they assumed gravity-dominated film condensation, with negligible shear stress. They found condensate river depth to increase along the tube length, and to decrease as tube inclination angle increased. Overall HTC decreased along the tube length due to this accumulation of condensate.

In one of the only published experimental works for steam-side thermal performance of an ACC, Sukhanov *et al.* [19], [20] used a miniature version of an ACC with round tubes to examine in-tube condensation of an air-steam mixture. Their use of air on the cooling side creates large uncertainty in their determination of internal HTC, despite their best efforts to validate their assumptions in calculating external HTC. For example, their wall temperature was not measured

directly, but calculated by a numerical model. Even with this complicated method, they found that condensation HTC increased as inlet steam-air velocity increased. This is in contrast with the model of Kekaula *et al.* [18], which assumed condensation in the flow-rate independent regime. In addition, Sukhanov *et al.* [19] found that condensation HTC decreased as subcooling of the condensate increased. However, it is unclear if the results are generalizable to full-size or flattened tubes.

O'Donovan and Grimes [21] experimentally analyzed a flattened-tube ACC array in a power plant, with tubes of 2 m length. They experimentally determined overall condenser thermal resistance, and inferred steam-side thermal resistance by subtracting the theoretical air-side resistance from this overall resistance. They found that ACC steam-side resistance accounted for up to 33% of the total ACC thermal resistance. They found that this percentage decreased as steam-side flow rate increased, indicating a possible dependence of HTC on Reynolds number. In addition, steam-side resistance increased as fan speed increased, indicating a dependence of HTC on heat flux. However, they did not measure concentration of non-condensable air, and explained that changing non-condensable concentration could also explain the variation in steam-side resistance.

O'Donovan and Grimes [21] also looked at the effect of condensation pressure as a system-level parameter. They showed that decreasing condensation pressure improves power-plant performance by increasing the Carnot efficiency. They [22] also found that steam-side frictional pressure drop in a round-tube ACC bundle increases as inlet vapor velocity increases. However, they also found that momentum recovery also increases, so total pressure drop only increases slightly. They found the correlation of Lockhart and Martinelli [23] for frictional pressure drop most closely matched their experimental data. However, this correlation was developed for small round tubes with high mass flux.

Another pertinent experimental study is that of air-cooled round tubes by Kim *et al.* [24]. They measured heat flux while observing the flow regime of condensing steam in a tube with a slight downward inclination angle. They had low mass flux and stratified flow. They found that despite the air-side dominance of heat transfer resistance, heat flux decreased significantly as steam quality decreased.

At the steam-side component level, Owen and Kroger [25] numerically investigated the distribution of steam through the array of tubes. They found that significant maldistribution of

steam occurs, which causes significant influx of non-condensables – reducing condenser performance and placing additional demand on the vacuum pump.

In summary, steam-side investigations of ACCs have only begun in recent years. The models developed for heat transfer have defaulted to assumptions of Nusselt-like condensation, yet this assumption appears to be contradicted by the experimental results of Sukhanov *et al.* [19]. The importance of accurate steam-side HTC determination has been shown by Mahvi *et al.* [26]. They demonstrated that the required condenser length can vary by over 25% depending on the HTC correlation used. Therefore, a proper characterization of steam-side heat transfer is necessary to further the field of study.

For pressure drop, no studies have been published for the large-diameter, flattened-tube design. In addition, no studies have been published investigating the effect of tube inclination on condenser performance. In short, this study is the first to investigate the basic steam-side physics in this condenser geometry.

2.2 Flow Regimes during Internal Convective Condensation

For condensation, most flow regime maps have been developed with air-conditioning and refrigeration systems in mind, using small, round tubes and refrigerants. Although the conditions for a flattened-tube ACC are different, many of the principles explained by these studies are relevant. Being a well-developed field, this is a good place to start the discussion of condensation flow regimes. The existing flow regime maps have many similarities, such as annular flow for high mass flux and quality, and stratified flow for low mass flux and quality. However, they have been developed using different principles. El Hajal *et al.* [27] focused on mean void fraction, while Thome *et al.* [28] focused on flow regime transitions. Xiao and Hrnjak [29] analyzed the onset of condensation to better predict the flow regimes at the quality of one and earlier. They demonstrated that condensation must begin in the annular flow regime. In particular, for low-mass-flux condensation in macro-scale tubes, they demonstrated that the flow pattern will begin in the annular regime, transition to stratified-wavy and then end in stratified flow.

For large-diameter horizontal tubes, several studies have been performed for adiabatic flows with liquid and air. Dong *et al.* [30] found predominantly stratified flow for 15.2 cm ID pipe at low liquid loads. Chen *et al.* [31] observed only stratified and stratified-wavy flows for 7.8 cm ID pipe.

Several experimental studies have investigated the effect of inclination on flow regimes. For adiabatic air-water stratified flow in a 5 cm diameter round tube, Andreussi and Persen [32] showed that stratified flow extends over a larger range of superficial gas velocities for tubes downwardly-inclined at 0.65^{o} and 2.1^{o} than for horizontal tubes. Woods et al. [33] also found that the transition to slug flow from stratified flow was delayed for slight downward inclinations (0.2^{o}-0.8^{o}) in 7.6 cm diameter pipes for air-water flows. For upwardly-inclined 12.7 cm adiabatic flows, Hasan and Kabir [34] found that the transitions at high fluid velocities (slug-churn, churn-annular) were unaffected by inclination angle, while the transitions for lower fluid velocities were significantly affected. For inclined tubes, two maps are in general use. The first, by Crawford *et al.* [35], is modified from Weisman *et al.'s* [36] map for horizontal flow. It uses empirical correlations for flow regime transitions, and was developed using R113 in adiabatic, downwardly-inclined flow. The second inclined-condensation map by Barnea [37] is valid for the entire range of tube inclinations. It was verified using adiabatic air-water flow in 5 cm diameter pipes. It adapts the flow regime transitions from Taitel and Dukler [38] and Taitel *et al.* [39] to inclined flow using analytical arguments. Verification of these maps by Lips and Meyer [13] for inclined round tubes in refrigerant condensation showed that Crawford's map gives the best agreement to experimental results. Despite the extensive research on flow regimes in inclined tubes, all of the studies are for adiabatic conditions in round tubes.

For the effect of the flattened-tube shape, Coleman and Garimella [40] found that tube aspect ratio did not affect flow regime, although they only investigated tube hydraulic diameters less than 5 mm.

2.3 Void Fraction Models for Condensation in Large-Diameter Tubes

Significant research has been performed on the topic of void fraction models in large-diameter tubes, and several models have been developed for round tubes. Traditional void fraction correlations for condensation, such as that of Lockhart and Martinelli [23], assume pressure-driven flow, where pressure drop through each phase and slip ratio between the phases are the important parameters. However, these models can have errors for low-mass-flux gravity-driven flows, where the interfacial shear force between the vapor and liquid is negligible and does not affect the void fraction.

For determination of void fraction in large-diameter inclined tubes, several studies have been made. That of Beggs and Brill [41] is the most-widely cited. They developed a flow-pattern-based correlation from their experimental results in inclined tubes with 2.5 and 3.8 cm diameters. Their correlation is applicable for low mass flux. Andreussi and Persen [32] also studied large-diameter inclined tubes. They found the void fraction to be functions of liquid Reynolds number and liquid friction factor only. This contrasts with traditional models for smaller-diameter tubes, where void fraction is modeled as a function of quality and property ratios between liquid and vapor, e.g. in Turner and Wallis [42]. This indicates that the physics governing void fraction in large-diameter tubes is different than that in small-diameter tubes with high vapor shear force on the condensate. In adapting the previous pipe flow correlations to a range of flow patterns, Xiao *et al.* [43] developed a comprehensive mechanistic model for void fraction in two-phase flow. However, like most of the pipe flow correlations, it is for fully-developed flow with a long pipe length after the test section. These correlations are all independent of outlet flow condition. This causes inaccuracies during subcritical flow, when void fraction is a function of the tube outlet condition.

In the ACC, with gravity-driven flow, the situation is similar to a lateral spillway, where void fraction depends greatly on tube inclination and heat flux. Spatially-varied open-channel-flow models can be used for these tubes. Chow [44] described an early solution to this problem when developing his open-channel-flow framework. Kao [45] specifically analyzed the problem of spatially-varied flow, both experimentally and numerically. Kao's model accurately predicted the water surface profile when varying several parameters, including channel slope, discharge, and lateral inflow rate. Lateral inflow rate was found to have the largest effect on the water surface profile. Yen [46] derived the spatially-varied flow equations from first principles. He then analyzed the common assumptions used in these models under different flow conditions. He found the conventionally-used equations to be simplifications of special cases of the general spatially-varied flow equations. Chato [47] applied an open-channel-flow model to a round-tube condenser, and found that void fraction increased for low downward inclination angles ($<10^{o}$) in comparison to horizontal tubes.

2.4 Internal Condensation Heat Transfer Coefficient

In-tube convective condensation has been well studied ([48],[49],[50]), in varying tube geometries and conditions, and several correlations for HTC are in wide use. However, the majority

of the investigations of HTC have focused on small tubes and refrigerants. Several aspects of the ACC make it difficult to apply previous correlations with reasonable certainty. The ACC tubes are inclined, with large diameter and an elongated-slot cross-section, with HTC, heat flux, and temperatures varying circumferentially around the tube.

The correlations for condensation HTC have many different formulations. However, they have generally agreed on the existence of two regimes of condensation: the gravity-driven regime and the shear-driven regime [2]. The gravity-driven regime occurs during low mass flux, and includes stratified and stratified-wavy flow. In this regime, the predominant heat transfer mechanism is through the liquid film along the walls, and the HTC depends on ΔT between the vapor and wall, but not on Reynolds number of the flow. The correlations for this regime are all based on the theory of Nusselt [3] for condensation on a flat plate under natural convection.

The shear-driven regime occurs for high mass flux, and includes annular flow. In this case, the HTC depends on Reynolds number, but not ΔT. Correlations for this regime are based on two-phase multipliers (e.g. [51],[52]) or quantification of the interfacial shear (e.g. [53]). Intermittent flow regimes are generally described by a linear combination of the correlations for the two dominant regimes. Only the gravity-driven regime is expected to be encountered in this study, so only the correlations pertinent to this regime will be discussed in detail.

The correlations for gravity-driven flow either assume a continuous liquid film (Shah [51], Cavallini *et al.* [52], Jaster and Kosky [54]), or divide the tube into two sections – the thin film on the wall, and the stratified liquid layer at the tube bottom (Rosson and Meyers [1], Dobson and Chato [2]). All of them use a modification of Nusselt theory [3] to quantify the heat transfer through the thin film. These correlations were predated by the work of McAdams [55], who originally modified the constant in Nusselt's equation for in-tube condensation. Later, Dhir and Lienhard [4] made an analytical modification to Nusselt's equation, replacing the gravitational acceleration with a local effective gravitational acceleration to account for the curvature of a tube. The HTC predicted by this equation is useful in predicting a lower-bound for HTC in low mass flux.

Early analyses, such as by Chato [47], neglected the heat transfer through the stratified condensate at the bottom of the tube. Chato correctly determined that the heat transfer resistance of this layer is much greater than that of the film. It is valid to neglect this area for of heat transfer for low-mass-flux flow under uniform wall temperature. However, for higher-speed flow of this condensate, or non-uniform external conditions, this heat transfer area may become significant.

Several different methods have been used to quantify the convective HTC in the stratified condensate. For example – using an analogy between heat and mass transfer – Rosson and Meyers [1] developed a correlation based on Reynolds number, Prandtl number, and the Lockart-Martinelli [23] parameter. They used local experimental measurements of HTC to develop this correlation. Dobson and Chato [2] developed another correlation for heat transfer through the stratified condensate based on the Dittus-Boelter [56] single-phase convection correlation. They did not measure this local HTC, however.

For experimental validation of these correlations, several studies have been performed for steam condensation in horizontal tubes in annular flow (e.g. [57]), but there are few results available for stratified steam condensation. Jaster and Kosky [54] presented one such study. Their focus was on identifying the annular-stratified flow transition, but they also presented local heat transfer coefficients. For a round, horizontal tube, they experimentally found steam condensation HTC in the stratified flow regime in the range of 7 – 13 kW $m^{-2} K^{-1}$, however they did not publish their ΔT_w for these data. For laminar film condensation of steam on the outside of vertical tubes, Hebbard and Badger [58] experimentally found HTC averaged 33% higher than the prediction of Nusselt theory.

2.5 The Effect of Elongated Cross-Sections on Condensation Heat Transfer Coefficient

To expand the correlations to non-circular tubes, Fieg and Roetzel [59] analytically compared the condensation HTC in elliptical vs. round tubes. They found that elliptical tubes with a longer vertical axis would have a greater mean HTC than would circular tubes of equivalent heat transfer area. They found the maximum ratio of elliptical-tube HTC to circular-tube HTC to be 1.157 (an increase of 15.7%) for tubes of infinite length. The ratio is even larger for tubes of finite length. For tubes elongated in the horizontal direction, they found that HTC would decrease.

Wilson et al. [60] experimentally measured HTC for refrigerants in tubes that had been flattened, with the long axis in the horizontal direction. Contradicting the analytical prediction of Fieg and Roetzel [59], they found an increase in HTC vs. round tubes. However, the flow of Wilson *et al.* [60] was likely in the shear-dominated regime. Kim *et al.* [61] showed that increasing the tube width will increase HTC in the annular flow regime but decrease HTC in the stratified flow regime.

2.6 The Effect of Inclination on Condensation Heat Transfer Coefficient

Several studies have investigated condensation in inclined round tubes, although inclination was only studied sparingly until the last decade [62]. Nearly all of the studies show that inclination has an effect on condensation HTC. However, the magnitude of the effect varies widely. The majority of studies have found that for high mass flux or annular flow, the inclination effect is minimal [13], [63]. This reduced effect is generally found for smaller-diameter tubes and high vapor quality – the shear-dominated flows. Higher inclination dependence has been found for the gravity-driven flows with low mass flux [63], [64]. These studies with high inclination dependence can be further divided into those that show an increase in HTC with increasing inclination angle, and those that show a decrease in HTC with increasing inclination angle. Chato [47] showed an increase in HTC with a low increase in downward inclination angle. Lyulin [65] found a maximum in HTC for inclination angles between 15-35^{o} downward for low mass flux. Lips and Meyer [13] also looked at refrigerant flow in small, round tubes, and found a peak in HTC for small downward inclinations between 15^{o} and 30^{o} and low mass flux and quality. In a more recent study [64], they extended the analysis to mass flux as low as 50 kg m^{-2} s^{-1}. They concluded that the inclination effect increases as mass flux, quality, and wall-vapor temperature difference decrease. In a larger, 2 cm-diameter round tube with condensing n-heptane, Wurfel *et al*. [66] found that HTC increased for all downward inclination angles, with a maximum at vertical downward flow.

In a microfin tube, Akhavan-Behabadi *et al.* [67] found that HTC decreased for all downward inclination angles. For a square tube with 1.23 mm hydraulic diameter, Del Col *et al.* [68] found that HTC of R32 and R134a decreased for downwardly inclined tubes at low qualities.

As can be seen, this division between the direction (increase vs. decrease) of the inclination effect is less generalizable than the magnitude of the effect. As explained by Chato [47], the net inclination effect depends on the competing effects on the film and the condensate river. As inclination increases, film thickness increases, while river depth decreases. In addition, inclination can also change the flow regime. At some point, the angle becomes so steep that gravity no longer holds the stratified layer against the wall, and plug-slug or annular flows can result. Vertical flows have no stratified flow regime. The change from stratified to other regimes generally decreases HTC [13]. Therefore, the net effect of inclination depends on the relative importance of the condensate river and the film in each condenser, as well as the point of transition away from a stratified flow regime.

From these results, several correlations have been developed for inclined condensation. Chato [47] added a multiplier for the inclination effect to his stratified-flow correlation, and validated the result for 0-10^o downward inclination angle. In a purely analytical analysis, Kroger [69] modified Nusselt theory for an ACC geometry and stratified steam flow to arrive at a local correlation for HTC. Based on a large data bank from published inclined condensation studies, Shah [70] modified his horizontal, convective-condensation correlation [51] for inclined applications. For stratified flow in circular tubes, Lips and Meyer [71] developed a combined hydrodynamic and thermal model to predict HTC in inclined flow.

2.7 Effect of Non-Isothermal Walls on Condensation Heat Transfer Coefficient

Very little research has been published detailing the effect of non-isothermal walls on condensation. Chen and Yang [72] showed analytically that a sinusoidally-varying wall temperature in an elliptical tube with low mass flux will increase local and mean HTC. Brouwers [73] numerically showed that laminar film condensation on a vertical plate is dependent on the McAdam number when wall temperature is varying. The McAdam number is the ratio between HTC of the plate and HTC of the film. He determined that lower McAdam number yielded higher dependence on wall temperature. No experimental validation of these results has been found.

2.8 Experimental Determination of Heat Transfer Coefficient in Condensers with Varying U and Wall Temperature

When designing an air-cooled condenser, significant uncertainty is created by non-uniformity in the HTCs on both the air and steam sides. Conventional methods of evaluating condensers assume constant overall HTC, *U*, in the condenser [74]. However, Sparrow *et al.* [75] have shown that using a constant-U model can lead to errors as great as 50% for cases where both HTCs vary. This limitation has been recognized throughout the past century, and methods to compensate for non-constant U have been developed as early as Colburn and du Pont in 1933 [76]. Many of the methods, such as that of Roetzel and Spang [77] involve evaluating *U* at multiple points along the condenser in order to determine a modified constant *U*. Despite these efforts, Shah and Sekulic [78] showed that none of the approximation methods could accurately determine *U* for all cases of HTC and temperature non-uniformity. They determined that exact local determination of HTC and *U* was the only way to properly determine *U* in cases of HTC non-uniformity.

For stratified flow, condensation HTC is dependent on the temperature difference between the wall and the condensing vapor – ΔT_w [2, 52]. Therefore, when designing an experiment to determine HTC in stratified flow condensation, it is important to match the wall temperature and heat flux found in an operating condenser. For a flattened-tube air-cooled condenser, this thesis will show that heat flux and wall temperature vary around the tube circumference. In order to match these conditions, the laboratory determination of HTC becomes more complicated. Typical methods of determining condensation HTC involve maintaining a constant heat flux or wall temperature around the tube circumference, for example [13, 79]. Constant heat flux is easier to measure than variable heat flux. Constant heat flux can be determined by measuring total capacity in the cooling loop and total condensation area. Determining local heat flux requires more intrusive measurements. In addition, the constant heat flux assures uniform conditions around the tube circumference, which simplifies the analysis of the in-tube HTC. Unfortunately, for a large-diameter ACC, using constant heat flux will not produce an accurate determination of HTC. An alternative method must be used.

For the case of non-uniform heat flux – and that is the reality – local heat flux must be determined at the point where wall temperature is measured. This is difficult for air cooling, because air's low thermal conductivity leads to high temperature gradients and high uncertainty. Even for liquids, typical techniques for mixing and measuring bulk fluid temperature can alter the wall temperature profile, which is undesirable. Another option to circumvent this local measurement is by creating models for heat flux on the air side [80, 81] and in some cases even modeling both wall temperature and heat flux [19]. However, models introduce additional uncertainty, and they can never be as accurate or informative as direct experimental measurement. Alternative techniques include measuring inner and outer wall temperature, as in [82], but the thin wall for this condenser makes this impractical. Other researchers have installed a heat flux block with a thicker wall [83], but this type of large metal heat exchanger is difficult and expensive to manufacture for this large tube geometry.

Considering all of these factors, this study attempts to improve upon the previous work by using a water-cooled, cross-flow, one-pass condenser to mimic the operating conditions of an air-cooled condenser and determine experimentally the mean HTC, while using a combination of experiment and computational fluid dynamics (CFD) to determine the local heat flux and local HTC. This technique can provide local HTC with sufficient accuracy at conditions close to that of

an operating ACC. A similar method was used by Kuhn *et al.* [84] to determine local heat flux and HTC, except that they used an analytical model to determine the local bulk temperature instead of CFD.

2.9 Pressure Drop during Internal Convective Condensation in Downwardly-Inclined and Flattened Tubes

Several experimental studies for inclined condensation pressure drop have been performed. For adiabatic flow in inclined, large-diameter tubes, Beggs and Brill [41] showed that correlations for predicting pressure drop in horizontal flow were not accurate when applied to their inclined tubes. Lips and Meyer [85] showed that increasing downward inclination angle decreases the pressure drop in comparison to a horizontal tube for all qualities and mass fluxes. The majority of this decrease occurs from 0^o to 30^o inclination, and the effect is more pronounced for low quality and mass flux. Adelaja *et al.* [86] showed that this relationship held for various saturation temperatures, and that the decrease in frictional pressure drop was a result of increased void fraction at higher downward inclination angles.

In a numerical study, Wen *et al.* [87] investigated the effect of aspect ratio on the pressure drop in small-diameter (< 1 cm) flattened tubes. They found that the film thickness reduced significantly as tube aspect ratio increased. However, they also found that the frictional pressure drop increased as aspect ratio increased due to the decreased cross-sectional area of the tube. Wilson *et al.* [60] arrived at this same conclusion experimentally.

Although many condensation pressure drop correlations exist for small, round-tube condensers, only a few exist for the case of large, flattened tubes. For this specific case with low mass flux, Groenewald and Kröger [88] numerically developed and experimentally validated a correlation for pressure drop that accounts for the suction rate of vapor towards the condensing wall, which affects the friction factor. Their model also finds that the effect of interfacial waviness is negligible due to the high aspect ratio and low mass flux of the tubes. For condensation in inclined tubes, Lips and Meyer [85] presented a pressure-drop model based on the correlation of Taitel and Dukler [38]. Developed based on experimental results in small-diameter round tubes, their model takes into account the curved shape of the vapor-liquid interface.

2.10 Effect of Non-Uniformities on Performance of Air-Cooled Condensers

Previous studies in both flattened-tube ACCs and in alternative condenser geometries have shown that system performance can be improved by condensate management. Li and Hrnjak [12, 89] showed that condensation rate can be increased by removing liquid from the condenser, taking advantage of the higher heat transfer coefficient (HTC) of condensing vapor. As one method of removing condensate, Cheng *et al.* [17] demonstrated numerically that drainage of condensate can be improved by increasing condenser inclination.

Another method of managing condensate is to consider its interaction with the condenser's air-side performance. Specifically, non-uniform air-velocity profile can be favorably aligned with the distribution of condensate in the condenser. The effect of non-uniform air distribution on various types of ACCs has been investigated at length; however, the majority of research has focused on the negative impact of airflow maldistribution. Looking at compact heat exchangers, Chiou [90] used a mathematical model to determine the effects of twelve typical airflow distributions on heat exchangers. It was determined that capacity could be significantly reduced under a number of commonly-occurring non-uniform distributions in comparison with a uniform airflow distribution. Following this study, Berryman and Russell [91] demonstrated numerically that as the non-uniformity (measured by standard deviation of the velocity) of the airflow velocity increases, condenser capacity decreases. They showed that with a 23% standard deviation in air velocity, condenser capacity would decrease by 3% compared to the case with no deviation in airflow velocity. Beiler and Kroger [92] experimentally measured airflow through air-cooled condensers, and analytically determined the condenser performance that would result. They calculated that the airflow non-uniformity would reduce condenser performance by less than 2%. Ng *et al.* [93] analytically studied the effect of flow maldistribution on automotive radiators, and found that the effect of non-uniform airflow was minor, except at the highest levels of non-uniformity, when it caused a decrease in radiator capacity. Hallqvist [94] also observed the detrimental effects of non-uniform airflow, showing that it decreased the capacity of a truck cooling system by 4.4%. Mao *et al.* [95] numerically studied four airflow distributions on a micro-channel condenser, and found that all non-uniform distributions reduced condenser capacity, with the largest reduction equaling 6%. Examining maldistribution on the liquid side, Lalot *et al*. [96] in an analytical study showed that condenser capacity could be reduced up to 7% versus a condenser with uniform steam distribution. Also investigating air and liquid-side distribution, Park and Hrnjak [97]

developed a numerical model for a microchannel condenser based on their experimental results. Using this model, they showed that the non-uniform air velocity from the fan caused a 1.4% decrease in condenser capacity, while refrigerant maldistribution caused a further 2.1% reduction in capacity. Kennedy *et al.* [98] investigated the effect of condenser inclination angle on airflow distribution both experimentally and numerically. They showed that increasing tube inclination increased the airflow non-uniformity. However, they showed that this change was offset by increased airflow caused by the increased plenum depth of the inclined condenser. Overall, they showed that increasing inclination angle increases condenser performance by 0.5%.

Looking specifically at power-plant ACCs, Wen *et al.* [99] used a numerical simulation to show that airflow distribution varies greatly among adjacent tubes in an A-frame condenser, due to radial velocity generated by the axial fans. Their simulation predicted that on average the highest air velocity would occur at the top of the A-frame. Walsh *et al.* [100] directly measured velocity through an A-frame condenser in a power plant for one entire fan-condenser cell. They also found that air velocity varies significantly from tube to tube, and they could not conclude a general pattern for airflow distribution. In their results, some tubes had higher airflow at the bottom and some had higher airflow at the top. Zhang *et al.* [101] showed experimentally that the air velocity profile for an operating ACC has highest velocity at the base, with velocity decreasing to a minimum at the peak of the A-frame. This result contradicts that of the previous two researchers. However, they only used twenty velocity measurement points, which may not provide a sufficiently-small standard error for a distribution with such high standard deviation. Nevertheless, they showed that their measured velocity distribution is unfavorable for condenser performance. Importantly, they also demonstrated experimentally that the opposite velocity profile – with maximum velocity at the peak and minimum at the base – is the most-favorable velocity distribution for condenser performance, with increased condenser effectiveness of 6%.

All of the above studies are for specific condenser geometries. To generalize the effects of non-uniformities, Guo et al. [102] introduced the field synergy principle. This principle provides a general analytical framework for investigating the effects of non-uniformities. For ACCs, it suggests aligning regions of maximum airflow and temperature gradient to improve condenser performance.

From these results, it can be seen that airflow profile has a significant effect on performance of ACCs, and that both favorable and unfavorable airflow profiles exist. One study has indicated

that increasing airflow at the top of the ACC A-frame (steam inlet) will increase condenser performance, although no study has been performed to explain the physical reason for this increase. This thesis compares the effect of several different air velocity profiles on condenser capacity. It compares these profiles with steam-side performance to provide a complete explanation of the effects of steam- and air-side maldistribution.

2.11 Thermal Modeling of Air-Cooled Condensers

Condenser thermal performance is commonly predicted using one-dimensional models (e.g. [89]). In instances where cold and hot-side heat transfer coefficients are independent of wall temperature and heat flux, they can be calculated along the length of the condenser as a function of Reynolds number or other parameters. In instances where condensation HTC is not independent of wall temperature, assumptions of constant heat flux or wall temperature are commonly made [103]. Corrections are then made for development lengths [104], or for changes in temperature difference [105]. This method is effective for cases where one or both HTCs are constant. However, Sparrow *et al.* [75] have found that when the HTC of both fluids is not constant, the assumptions of constant temperature difference or constant heat flux are invalid, and significant inaccuracy in prediction of the overall HTC can result. Qiao [106] also showed analytically that both traditional heat exchanger characterization methods – LMTD and effectiveness-NTU – are inaccurate when fluid temperatures are varying.

To solve this problem, models removing the assumptions of constant heat flux and wall temperatures have been developed. For ACCs, conjugate heat transfer models that simultaneously solve momentum and energy equations on the air and steam sides are becoming more common. These frequently include a numerical solution on one [18] or both sides [107]. Although physically accurate, these models are complicated and computationally expensive to implement. A simplified model with heat transfer correlations that account for the non-uniformities on the air and steam side is needed.

2.12 Summary of the Literature Review

Although the amount of research focused on air-cooled condensers has increased in recent years, the field lacks a fundamental characterization of the steam-side physics. There are no experimentally-validated models for flow regime, void fraction, and heat transfer coefficient for this

large-diameter flattened-tube condenser design. In the literature, these values are found by using CFD or by adopting round-tube-based correlations. These methods have drawbacks in computational time and lack of accuracy, respectively. Simple, experimentally-validated, condenser-specific correlations and models are needed for the basic steam condensation processes.

Looking at the field of condensation as a whole, the fundamental understanding of internal convective condensation is quite high, but the parameter space covered by ACCs has not been described in full. Large-diameter tubes (> 2.5 cm) have been investigated less than small-diameter tubes. Flattened tubes have been investigated mostly at the microchannel-scale. The effect of inclination on condensation was mostly ignored in the 20th century, although the research in this area has increased greatly in the last fifteen years.

For flow regimes, the diabatic maps were developed for small-diameter tubes, while the maps for large or inclined tubes were all developed adiabatically. There is no published experimental data for flow regimes in large flattened tubes. The available results indicate that stratified flow will extend to a greater range of qualities for tubes at low downward inclination angles than for horizontal tubes.

Void fraction in large-diameter tubes has been studied extensively in the oil and gas industry, with a focus on adiabatic flows. The models developed indicate that the gravitational force dominates over the shear force in determining void fraction for large diameter tubes. Open-channel-flow models can describe liquid levels in gravity-dominated flows. These models are dependent on inlet and outlet conditions, so experiments with realistic condenser inlet and outlet conditions are necessary. For inclination effects, the void fraction has been found to increase at slight downward inclination angles.

Pressure drop in downwardly-inclined tubes has been shown to not follow the models for horizontal tubes. Total pressure drop has been shown to decrease for downward inclinations. Two experimentally-validated correlations exist for downwardly-inclined tubes. That by Lips and Meyer [71] is for round tubes while that by Groenewald and Kroger [88] was developed specifically for flattened-tube ACCs.

Heat transfer coefficient, as with the other phenomena, has been well-studied in condensation. However, the exact parameters relevant to the flattened-tube ACC have not been covered in the literature. The inclination effect has been shown to be very dependent on flow conditions and geometry, and it has not been studied experimentally in large, flattened tubes. Prior

results indicate the existence of an optimal downward inclination angle for heat transfer. There is very limited work on the effects of non-uniform heat flux and wall temperature on condensation HTC. This is partly due to the difficulty in determining HTC experimentally under these conditions. Finally, there is limited work on the effect of tube aspect ratio on HTC. The most relevant study was an analytical investigation by Fieg and Roetzel [59] that indicated an increase in HTC for higher-aspect-ratio tubes.

The effect of airflow non-uniformities has been studied in many condenser designs, including in these ACCs. Non-uniform airflow has been shown to decrease condenser performance when steam-side performance is uniform. However, there has been less investigation of the interactions between air- and steam-side non-uniformities. A general understanding of these effects has been explained by the field synergy principle of Guo *et al.* [102] However, a proper optimization of air- and steam-side flow has not been performed for the flattened-tube ACC design.

Due to the maturity of the field of condensation, some extrapolation can be applied to existing studies to predict the phenomena in a flattened-tube air cooled condenser. However, extrapolation and modeling is not the same as experimental investigation and validation. This thesis seeks to provide the basic physics and understanding of the steam-side processes. Both adiabatic and diabatic visualization provide information about flow regimes and void fraction at varied inclination angles, as well as a qualitative understanding of the condenser physics. From these results, a void fraction model for stratified flow is developed. Heat transfer and pressure drop measurements provide the quantitative data to compare with existing correlations for flattened-tube condensers. Models for steam-side heat transfer coefficient and capacity are then developed to fill this lack in the literature.

Chapter 3 Effect of Inclination on Flow Regimes, Void Fraction, and Capacity in Air-Cooled Steam Condensers

3.1 Introduction

This chapter describes the facility used for visualization and for the evaluation of inclination on flow regimes, void fraction, pressure drop, and capacity. This initial facility was intended to provide a qualitative understanding of the steam-side condenser physics through visualization, as well as quantification of the effect of inclination. The description of the facility instrumentation and of the validation of heat transfer measurements is intended to provide support for the experimental results in the subsequent chapters in this thesis. In addition, complete descriptions of the observed flow regimes, measured void fraction, and the effect of inclination on condenser capacity are provided in this chapter.

3.2 Facility and Procedure

The facility is designed to test a flattened-tube, air-cooled steam condenser. The facility is used to determine capacity, steam-side HTC and pressure drop along with simultaneous visualization. Steam condensation occurs in one continuous 10.7 m test section, encompassing the full range of thermodynamic qualities, from 1 to 0 (although void fraction only reaches a minimum of 0.9). A schematic of the experimental setup is presented in Figure 3.1. The setup consists of two steam boilers (24 kW and 27 kW), an air-cooled condenser test section, a condensate receiver, and a condensate pump. The boiler is manually-controlled by a solid-state controller. An inlet heater and choke valve ensure that the steam enters the condenser in a slightly-superheated state. Inlet steam mass flow rate is measured by a Micromotion F050S coriolis mass flow meter, and outlet condensate flow rate is measured independently by a Micromotion CMF025 coriolis mass flow meter and by a digital scale. The condensate pump runs intermittently based on condensate volume, allowing for accurate mass flow rate measurement by the scale while the pump is off. Cooling air is provided by an array of 134 80-mm diameter axial fans. The fan speeds are individually-adjustable with 1 kΩ potentiometers. The condenser is a cross-flow heat exchanger, with the fans pulling air upwards, perpendicularly to the axial steam flow. The entire condenser is mounted on a hinged truss, allowing for lifting to the entire range of downward inclinations. Due to size limitations of the laboratory, all tests at

inclinations higher than 17° were performed outside, with the system raised and supported by a forklift (Figure 3.2).

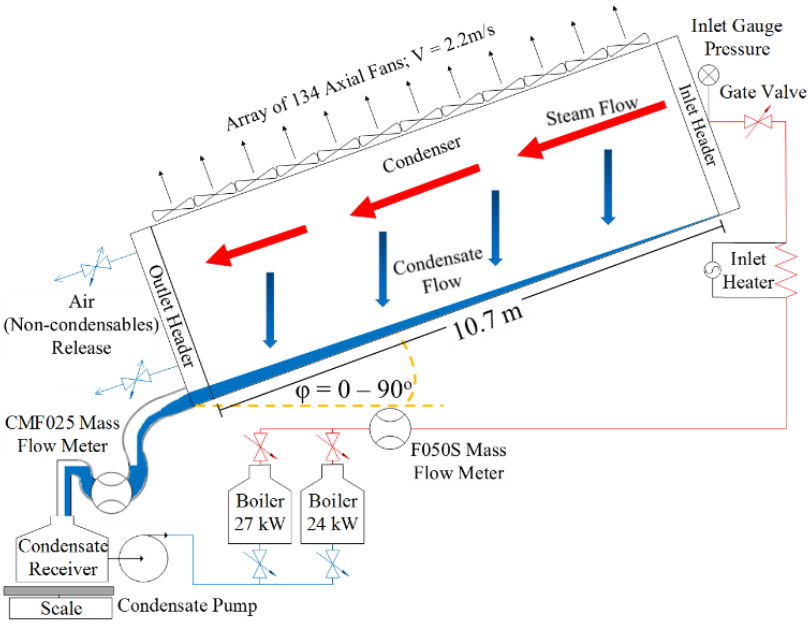

Figure 3.1: Diagram of condenser test facility

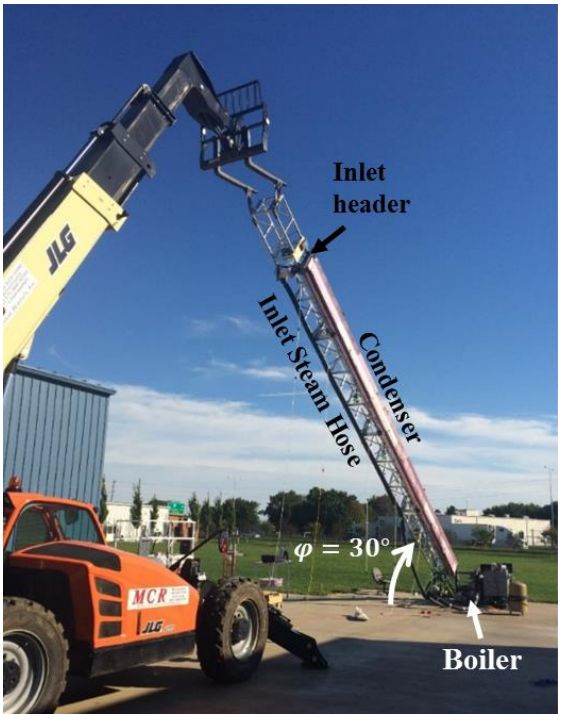

Figure 3.2: Facility located outdoors for higher-angle tests

3.2.1 Test Tube

The condenser tube in this experiment is 10.7 m in length, 0.214 m in inner height, and 0.016 m in inner width, as seen in Figure 3.3. This tube is used in air-cooled condensers for power plants. The tube is steel with aluminum cladding on the outside, and the wavy fins are aluminum. The fins are 200 mm x 19 mm, with a thickness of 0.25 mm and a fin pitch of 2.3 mm. For this experiment, the condenser tube is cut in half along the vertical center-line and a polycarbonate window is installed to allow visual access. This design leaves half of the heat transfer area intact, to allow in-situ visualization and void fraction measurement along with measurement of heat transfer. By cutting the tube on the line of symmetry, the modification is not anticipated to significantly affect the heat transfer results. Some possible effects of the polycarbonate window are suppression of waves in the condensate river, suppression of natural convection in the vapor, and increasing shear force on the vapor. The effect of increased vapor shear on the pressure drop is discussed in Chapter 6. In addition, the facility design is complicated by coupling metal with polymer in a high-temperature application.

In Figure 3.4.b, the cross-flow of air through the air duct can be seen. The air duct and polycarbonate surface are maintained adiabatic during measurements by using 50 mm-thick polystyrene foam insulation.

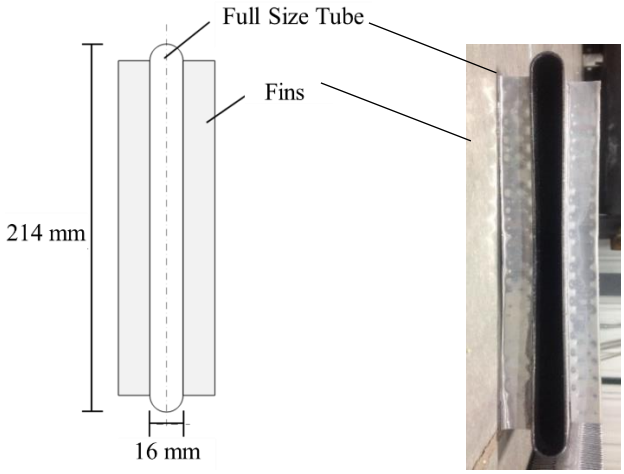

Figure 3.3: Full condenser tube cross-section view: (a) dimensioned schematic (b) actual

3.2.2 Instrumentation

Temperatures are measured at 1 m intervals along the test tube with T-type thermocouples, as seen in Figure 3.6. This provides local measurements of heat flux, heat transfer coefficient, and incremental quality determination. At each 1-m location, measurements include air inlet (T_{ai}) and outlet temperature (T_{ao}), steam temperature (T_{satt}), and wall temperature at x = 60 mm (T_{wb}) and x = 140 mm (T_{wt}). Wall temperature is measured by embedding a thermocouple bead in the outside of the condenser wall. This is covered with epoxy and aluminum tape, as shown in Figure 3.5. At z = 2 m and z = 10.7 m, a second steam temperature measurement is recorded at a lower x-position (T_{satb}). This sensor at 10.7 m allows verification of air removal from the system. The non-condensable air collects at the condenser outlet during system start-up, depressing the saturation temperature in the outlet portion of the condenser. When this bottom saturation temperature is equal to the top saturation temperature, the air is considered removed and data can be recorded. Since condenser pressure is above atmospheric, air is vented from the condenser tube and from the boiler, but is siphoned from the condensate receiver.

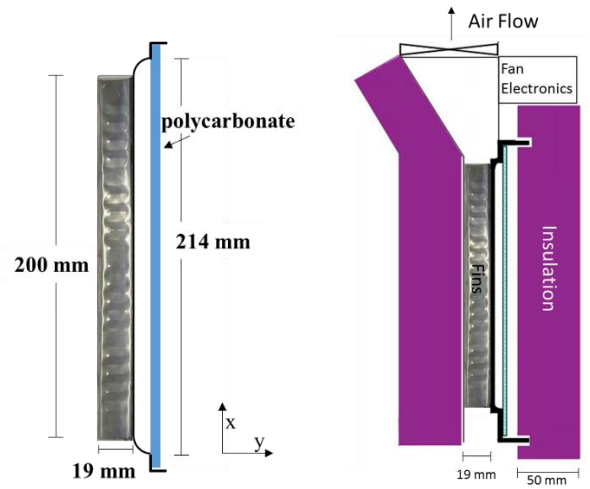

Figure 3.4: Half condenser tube with polycarbonate window: (a) Tube stand-alone (b) Tube installed in facility

Gauge pressure is measured at the condenser inlet and outlet with differential pressure sensors. Pressure drop is also measured in five 2.14 m sections. All the pressure sensors are calibrated within 1% accuracy against a standard manometer after being mounted onto the system. The gauge pressure sensors have ranges of 7.47 kPa. The full ranges of the five

differential pressure sensors are selected to be 497.7 Pa, 248.8 Pa, 248.84 Pa, 124.42 Pa, and 87.097 Pa, respectively for dP1 (steam inlet) to dP5 (steam outlet). The sensors are mounted on freely-rotating axles to allow them to hang vertically under the influence of gravity when the condenser is lifted to different inclination angles. Atmospheric pressure is measured locally with a mercury barometer.

Air velocity is measured using a handheld hot-wire anemometer. The anemometer is calibrated locally in a specially-designed facility [108]. Due to high local variation of air velocity, measurements are made at 5 cm intervals along the length of the condenser. At each measurement position, velocity is measured at the fin root, middle, and tip. Velocity measurements are made at the air inlet, as shown in Figure 3.7. These raw data, along with the condenser average are plotted in Figure 3.8.

In the design and instrumentation of the facility, emphasis is placed on visualization and on comparing performance at different inclination angles and airflow profiles. There is also a desire to maintain the facility as close to power-plant operating conditions as possible; for example, a full-length tube with air on the cold side of the condenser is used. This method provides crucial insight into the condenser physics, but also comes with limitations – most notably a decrease in the accuracy of determining heat transfer coefficient.

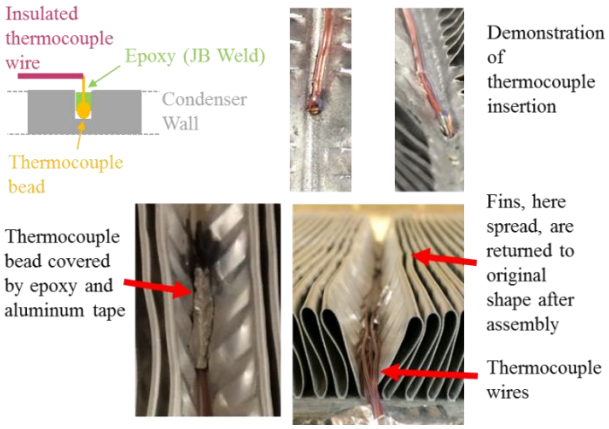

Figure 3.5: Diagram and picture of thermocouple installation for wall temperature measurements

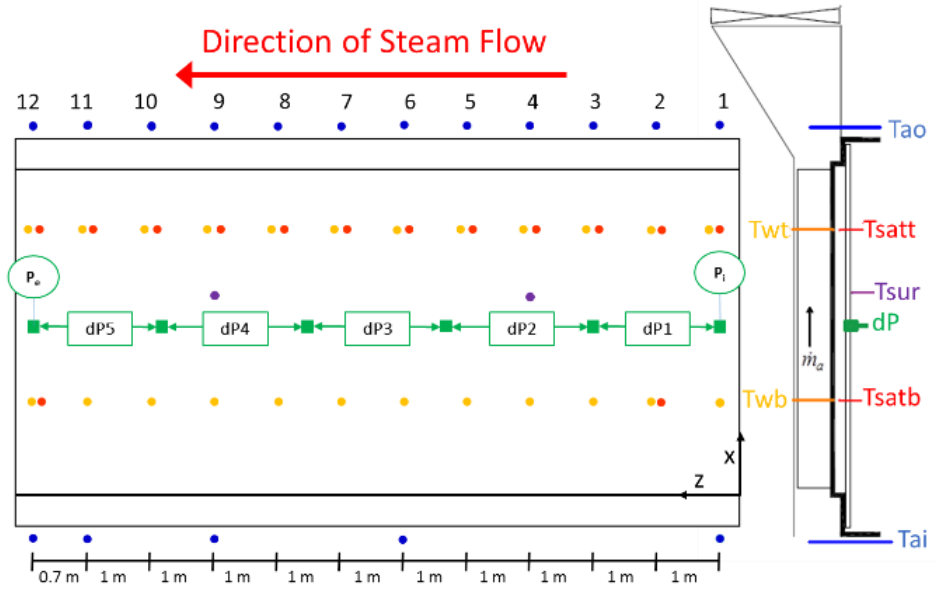

Figure 3.6: Diagram of sensor positioning

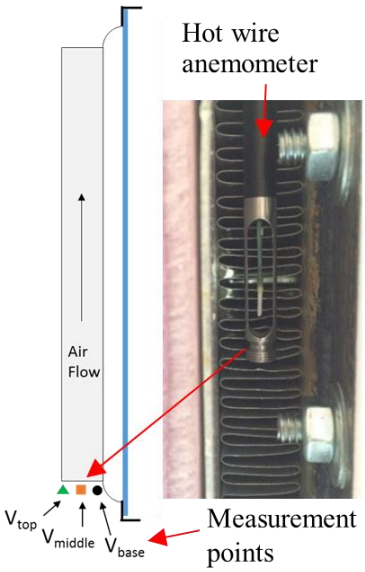

Figure 3.7: Air-velocity measurement using hand-held anemometer. Velocity is measured both between and behind the bolts.

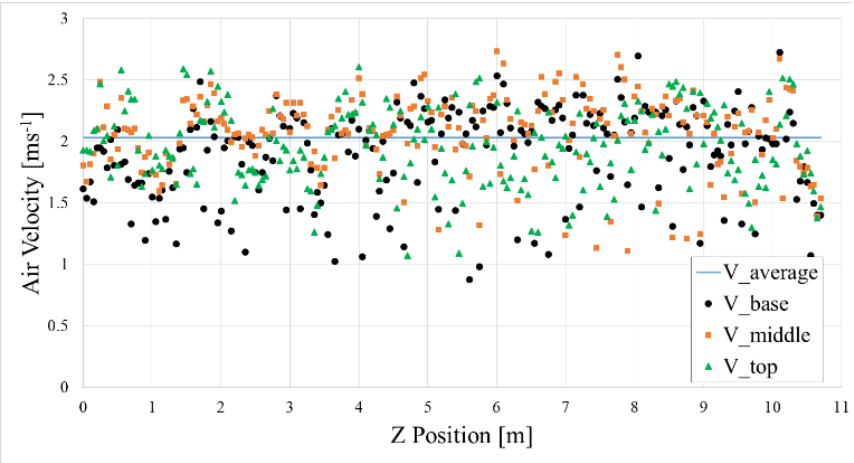

Figure 3.8: Air velocity measurements along the condenser

3.2.3 Measurement of Condensate Depth

Rulers (Figure 3.9) are placed on the polycarbonate window at five axial locations along the tube length, Z = 1.3 m, 4.5 m, 6.4 m, 8.7 m, and 10.6 m. Using these rulers, condensate depth along the polycarbonate window is measured directly. Due to the thickness of the polycarbonate

window, measurement error can occur if the eye level of the viewer is at a level other than horizontal with the depth of condensate. Therefore, a level is used to ensure that the line between the viewer's eye and the condensate depth is horizontal, as seen in Figure 3.10.

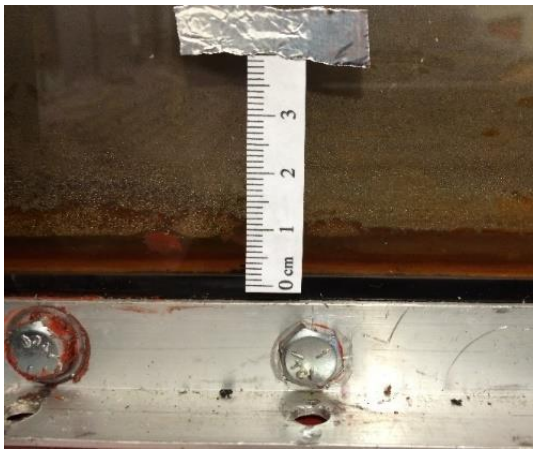

Figure 3.9: Ruler on polycarbonate viewing window for measurement of condensate depth

Figure 3.10: Level ensures horizontal measurement of the condensate depth through the polycarbonate window.

Once depth along the polycarbonate window is known, it is converted to depth along the steel wall. The height of the condensate river on the steel was determined by first assuming a triangular shape of the condensate along both walls. This can be seen in Figure 3.11. The contact angle of water on the rusted steel surface was measured by goniometer, as described in [108]. The capillary rise on both walls is then calculated by equating the forces of the water surface's line tension and buoyancy of liquid water in water vapor. The difference between the capillary rise on the steel and polycarbonate is then added to the measured condensate river height on the polycarbonate (equation (3.1)). The condensate height is determined to be 2 mm higher on the steel than that observed on the polycarbonate. This height on the steel is the reported condensate river depth.

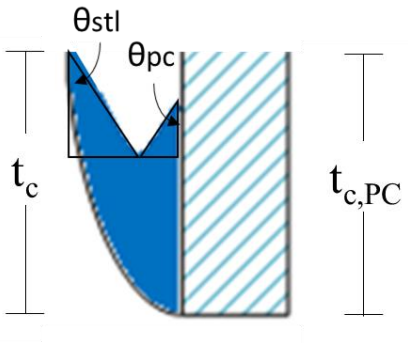

Figure 3.11: Model for converting measured condensate river depth on the polycarbonate window ($t_{c,PC}$) to condensate depth on the steel wall (t_c)

$$t_c = t_{c,PC} + \frac{2\sigma_c \cos(\theta_{st})}{g(\rho_l - \rho_v)\tan(\theta_{st})} - \frac{2\sigma_c \cos(\theta_{PC})}{g(\rho_l - \rho_v)\tan(\theta_{PC})} \tag{3.1}$$

The cross-sectional area of the condensate river is determined by a more complicated procedure that is described fully in Section 4.2.2. The inputs to the determination of condensate cross-sectional area are contact angles of water on the steel and polycarbonate, and measured condensate depth on the polycarbonate window.

3.2.4 Test Conditions

All measurements are performed slightly above atmospheric pressure. Test conditions are nearly identical across all tests, with condenser inclination being the primary variable. The range of test conditions can be seen in Table 3.1 below.

Table 3.1: Operating conditions and uncertainty

Parameter	**Range**	**Uncert.**
Steam mass flux [kg m^{-2} s^{-1}]	6.2 – 9.5	10%
Steam mass flow rate [g s^{-1}]	11 – 13.8	± 0.1
Condenser capacity [kW]	25.2 – 31	± 3%
Air velocity (average) [m s^{-1}]	2.2	± 7%
Vapor inlet pressure [kPa]	101 – 106	± 0.1
Vapor inlet superheat [°C]	0.1 – 0.7	± 0.1
Inclination angle [°]	0 – 75	± 0.1

3.3 Data Reduction

3.3.1 Capacity

Condenser capacity is determined on the air side and on the steam side. Air-side measurements are divided into eleven sections, and each section's capacity is:

$$Q_{a,j} = v_{a,j}\rho_{a,j}H_a\Delta z\left(c_{p,a,out,j}T_{ao,j} - c_{p,a,in,j}T_{ai,j}\right) + Q_{a,loss,j} \tag{3.2}$$

$Q_{a,loss,j}$ is the heat lost from the heated air to the atmosphere in the *j*-th measurement section. These values are negligible, representing about 0.1% of the air-side capacity.

$$Q_{a,loss,j} = UA_{a,loss}LMTD_{a,j} \tag{3.3}$$

Total air-side capacity is the sum of the sectional capacities:

$$Q_a = \sum_{j=1}^{11} Q_{a,j} \tag{3.4}$$

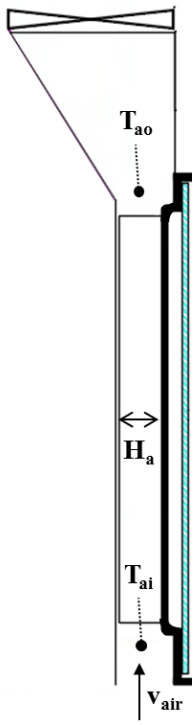

Figure 3.12: Cross-sectional diagram of test condenser, showing location of air-side measurements

Measurement of heat transferred along the condenser provides the opportunity to determine local quality along the condenser. Inlet steam enthalpy is determined from inlet temperature and pressure measurements, and local quality, x_j, is then determined in 1-m increments along the condenser by subtracting heat transferred over the previous meter, $Q_{a,j-1}$:

$$x_j = \frac{\dot{m}_s \left(i_{s,j-1} - i_{l,sat} \right) - Q_{a,j-1}}{\dot{m}_s (i_{v,sat} - i_{l,sat})} \tag{3.5}$$

Steam-side capacity is determined for the entire condenser from inlet and outlet enthalpies:

$$Q_s = \dot{m}_s \left(i_i - i_o \right) - Q_{s,loss} \tag{3.6}$$

$Q_{s,loss}$ is the heat lost through the polycarbonate window to the atmosphere. In an operating condenser, this surface would be the tube centerline, and would be adiabatic. For this test facility this value is negligible, representing about 0.3% of the condenser capacity. The effects on capacity of inlet superheat and outlet subcooling are also negligible, so steam-side capacity simplifies to:

$$Q_s = \dot{m}_s \left(i_{fg} \right) \tag{3.7}$$

Total system capacity is then taken as the uncertainty-weighted average of the air-side and steam-side capacities, as per the procedure recommended by Park, et al. [21]:

$$\bar{Q} = \frac{\left(\frac{1}{u_a^{\,2}} \right) Q_a + \left(\frac{1}{u_s^{\,2}} \right) Q_s}{\frac{1}{u_a^{\,2}} + \frac{1}{u_s^{\,2}}} \tag{3.8}$$

Here u_a and u_s are the uncertainties of the air-side and steam-side capacities, respectively.

3.3.2 Uncertainty Analysis

Uncertainty in capacity is calculated using the method of Taylor and Kuyatt [22] on equation (3.8). Uncertainties of measured quantities can be found in Table 3.1. For $\bar{Q}$, the main causes of uncertainty are the uncertainty in measured air outlet temperature, and in condensate flow rate. For all data points, the average difference in capacity between air- and steam-side measurements is 2%. Combined uncertainty for $\bar{Q}$ is 1.7%.

Uncertainty of depth of the condensate river is 0.6 mm.

3.4 Facility Validation in Single Phase

Important quantities such as capacity, temperatures and heat transfer coefficients are first verified by single-phase tests.

3.4.1 Heat Loss

Facility heat loss is measured via a single-phase test, with fans off and covered to prevent natural convection. Heat conducted through the insulation (Figure 3.4.b) can then be measured. Water is run through the system at different inlet temperatures, and capacity measured, in order to calculate a system UA_{loss} value by linear regression, using equation (3.9).

$$\bar{Q}_{loss} = UA_{loss} \times LMTD \tag{3.9}$$

UA_{loss} is found to be 16.1 WK^{-1}, representing less than 2% of condenser UA during fan operation. This can be seen graphically in Figure 3.13. The value of this loss term can then be divided between the air side, $Q_{a,loss}$, and steam side, $Q_{s,loss}$, via direct measurement of conduction through the insulation and summation of the areas. Once these components are determined, the heat transferred between steam and air, $\bar{Q}$, can be determined, as seen in Figure 3.14.

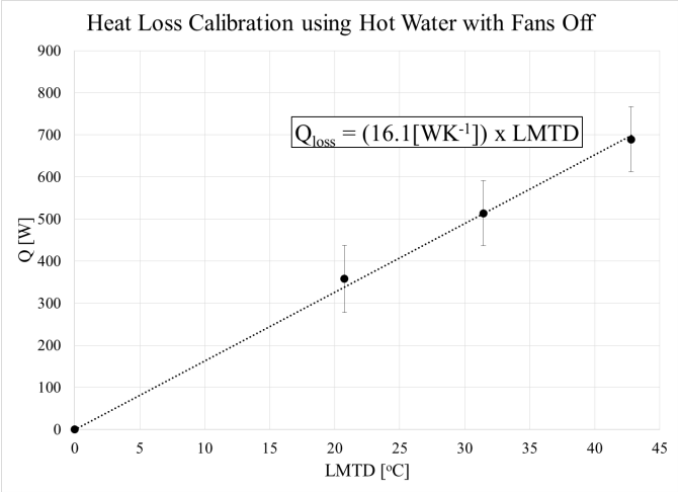

Figure 3.13: Heat loss calibration tests using single-phase water

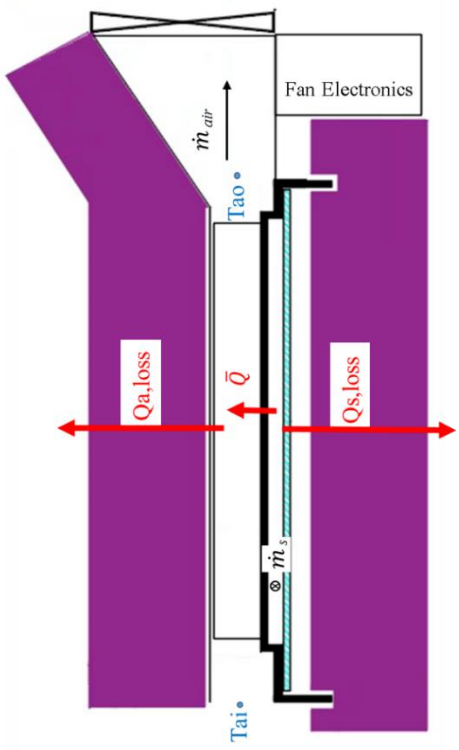

Figure 3.14: The losses of heat from air (Qa,loss) and steam (Qs,loss) to atmosphere are calibrated in order to determine heat transferred between steam and air (Qs-a)

3.4.2 Energy Balance

To verify the accuracy of the independent steam-side and air-side capacity measurements, an energy balance test is performed between the steam and air sides. Once again, single-phase hot water is used on the hot side. The fans are turned on, and the water-side capacity is calculated using equation (5). For all single-phase tests, the energy balance is within 10%, shown graphically in Figure 3.15. Note that the energy balance tests ensure that the mass flow rate measurements on both sides and the air-side temperature measurements are accurate, as well as ensuring the accuracy of the heat loss measurements. Accurate temperature measurements on the steam side must be further verified by comparing single-phase experiments and models.

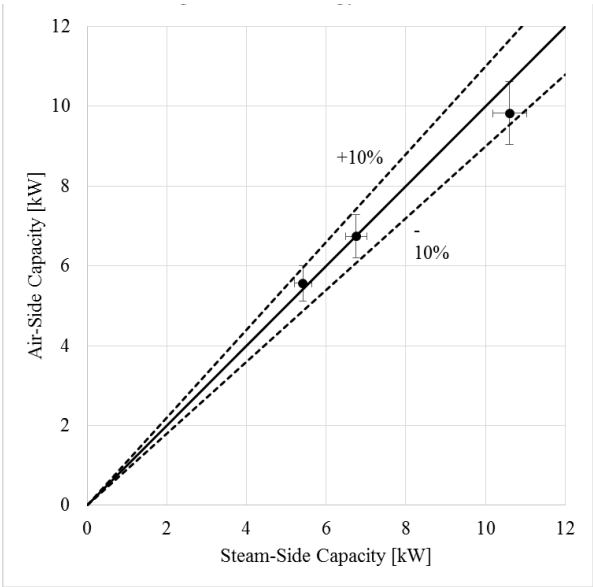

Figure 3.15: Energy balance verification using single-phase water

3.4.3 Verification of Temperature Measurements

To verify the accuracy of the temperature measurements, condenser temperatures are predicted using an analytical model for the single phase tests. Comparison is then made to the experimental results. For the predictive model, air-side heat transfer coefficient, $h_{a,}$ is predicted using the experimental correlation developed for this particular condenser by Creative Thermal Solutions:

$$Nu_a = .2329\,\mathrm{Re}_a^{0.5} \tag{3.10}$$

For the water side, the laminar flow, single-phase HTC is calculated using an average of uniform wall temperature and uniform heat flux predictions for parallel plates:

$$\overline{Nu} = 7.888 + \frac{0.065\left(D_h / L\right)\mathrm{Re}_D\,\mathrm{Pr}}{1 + .04\left[\left(Dh / L\right)\mathrm{Re}_D\,\mathrm{Pr}\right]^{2/3}} \tag{3.11}$$

This model uses inlet air temperature, inlet water temperature, and water mass flow rate from the experiments as boundary conditions. The results in Figure 3.16 show that the model accurately predicts air, water and wall temperatures along the condenser. This simple model assumes fully-developed flow, so it disagrees with experimental results near the condenser inlet. The model also predicts a similar water-side heat transfer coefficient to that found experimentally (380 W m^{-2} K^{-1} theory, 450 W m^{-2} K^{-1} experiment). Considering the acceptable energy balance and the close agreement of temperature measurements with the analytical model,

the facility is validated for evaluation of condenser performance.

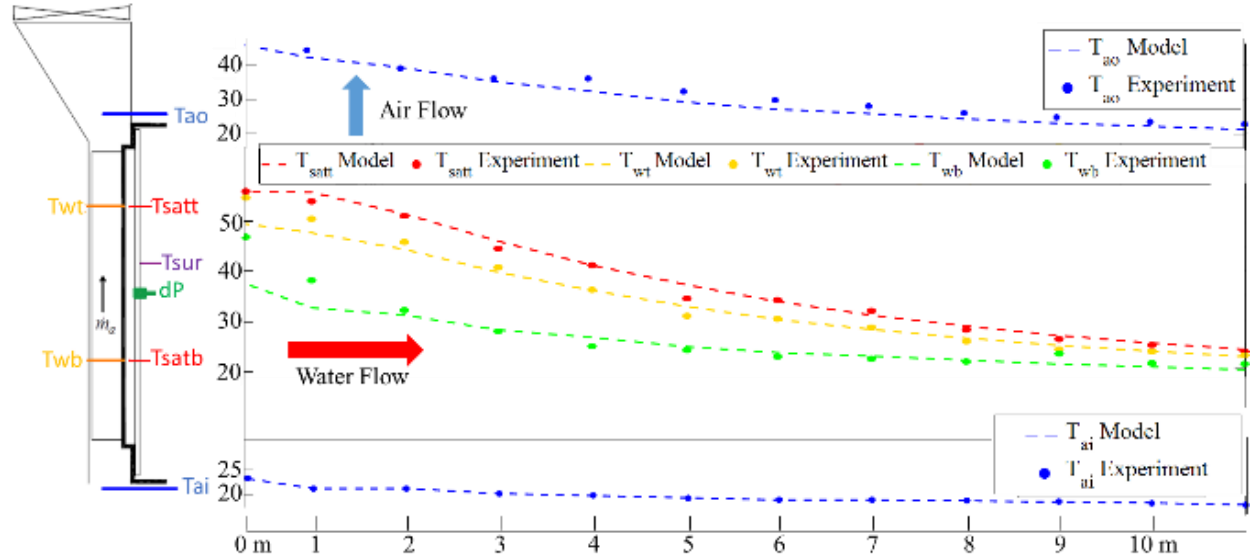

Figure 3.16: Predicted vs. measured temperatures along condenser for single-phase water tests

3.5 Results and Discussion

3.5.1 Flow Regimes

The flow regime is found to be stratified for almost all conditions, with mixed-mode dropwise and filmwise condensation along the condenser wall. For all but the inlet of the condenser, the flow is gravity-dominated. A condensate film on the wall falls downwards with gravity, and collects in a condensate river at the tube bottom. This river flows axially towards the condenser outlet, increasing in depth as it travels along the condenser length.

Figure 3.17 shows a picture of the condensation process near the tube bottom, for the horizontal inclination at z = 6.4 m. Droplets can be seen on the condenser wall, and the axial condensate river flow can be seen along the tube bottom. The film on the wall is not visible in the pictures due to its thinness.

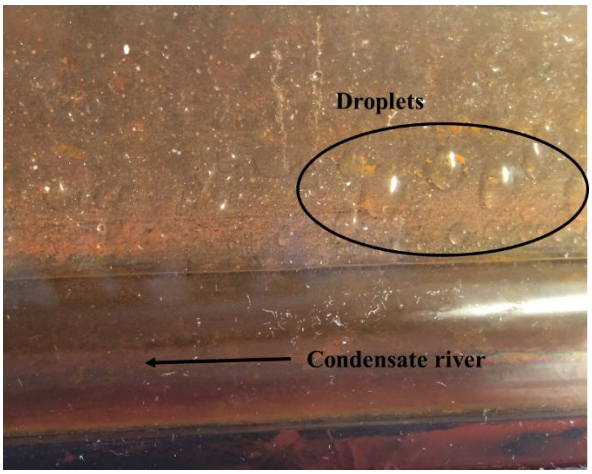

Figure 3.17: Flow during in-tube condensation in horizontal position (0º inclination), z = 6.4 m

For a horizontal tube, experimental results for flow regime are compared to the predictions of the flow regime map proposed by Xiao and Hrnjak [29], which is a modification of the widely-accepted flow-regime map by El Hajal *et al*. [27]. This map (Figure 3.18) predicts a stratified flow regime for over 98% of the condenser length, with the exception of very short annular and wavy sections near the condenser inlet. This is similar to the visualization results for this condenser. The results differ from the map in that the stratified-wavy section in the experiment extends approximately 2 m into the condenser (specific enthalpy = 2200 kJ kg^{-1}).

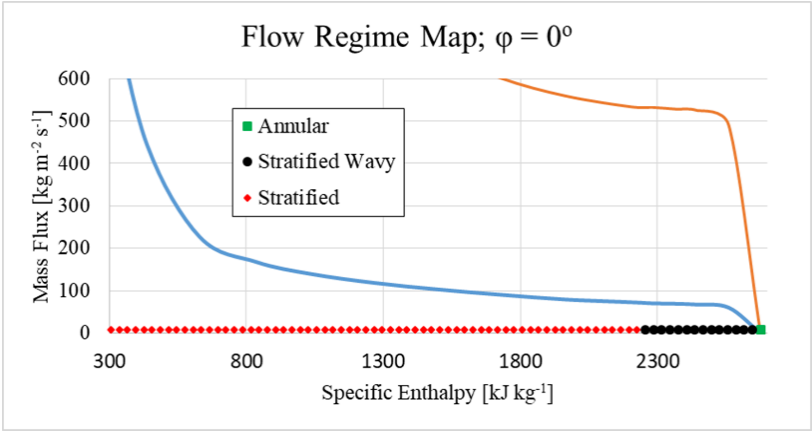

Figure 3.18: Experimental test conditions and observed flow regimes on the Xiao-Hrnjak [29] flow regime map. Experimental data is for a continuous visualization section along the length of the tube.

The primary effect of varying the inclination angle is to vary the flow regime. Therefore, a different map for inclined tubes is needed than for a horizontal tube. For inclined flow, Lips and Meyer [13] found Crawford *et al.*'s [35] flow map to be the most accurate. However, this flow map was developed for round tubes and for higher mass fluxes than those seen in the current study. Figure 3.19 shows this map at six different inclinations, plotted along with the test

conditions and observed flow regimes from the current experiment. For all the current test conditions and inclinations, this map predicts stratified flow. This is accurate for the majority of the test conditions, with a few notable exceptions. In the experiment, the inlet of the condenser is always in the annular flow regime. The condensation process always begins in the annular flow regime, because time and distance are required for the liquid to flow down the walls to the tube bottom and collect in the stratified regime. This phenomenon has been shown previously by Xiao and Hrnjak [29]. The Crawford *et al.* [35] map also fails to predict the stratified-wavy behavior in two separate instances – at the inlet of the horizontal condenser tube, and near the outlet of the high-inclination tubes (>60°). In the horizontal tube, from quality = 0.99 to quality = 0.81, the high vapor velocity creates sufficient shear force to form waves on the condensate layer at the tube bottom. At higher inclinations, the stratified condensate layer is very thin at this point of the condenser and waves are not formed. The third deviation from the map is near the outlet at high inclinations (>60°) in this study. Below quality 0.25, the flow becomes stratified-wavy near the tube outlet. In this case, the waves are caused by high condensate velocity.

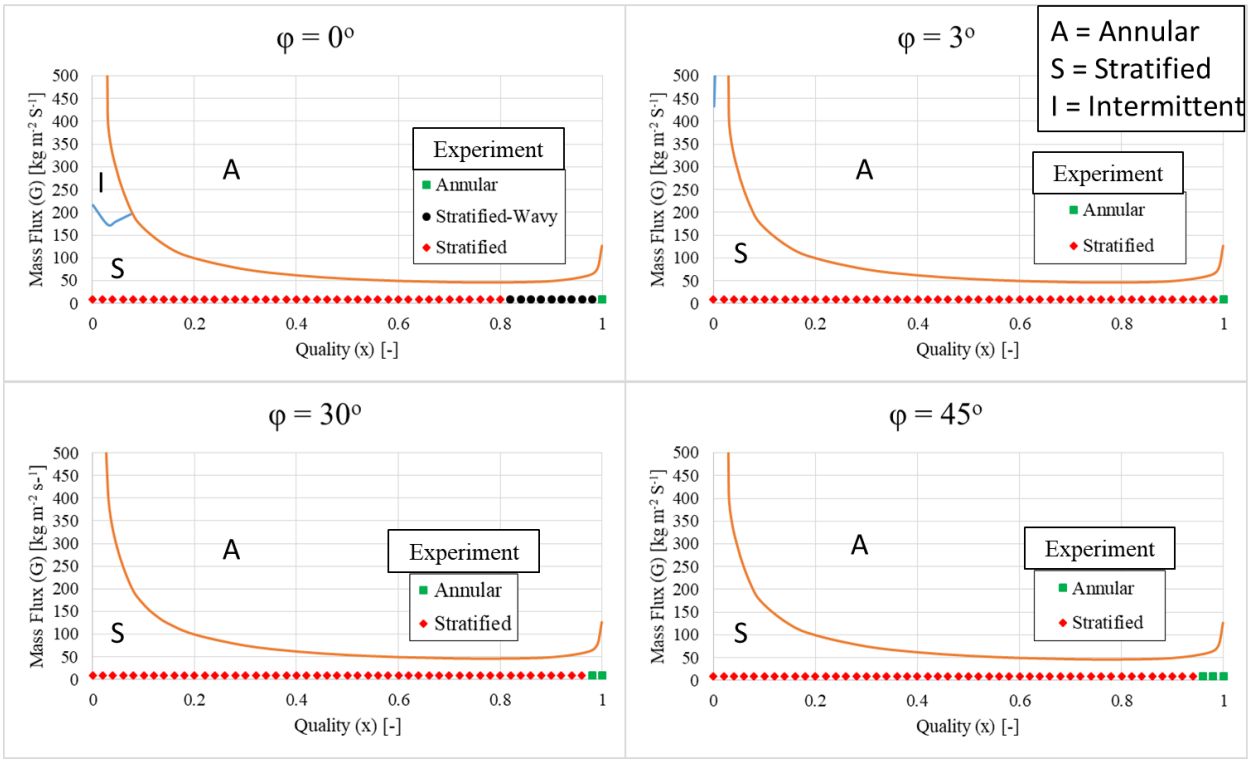

Figure 3.19 (cont.)

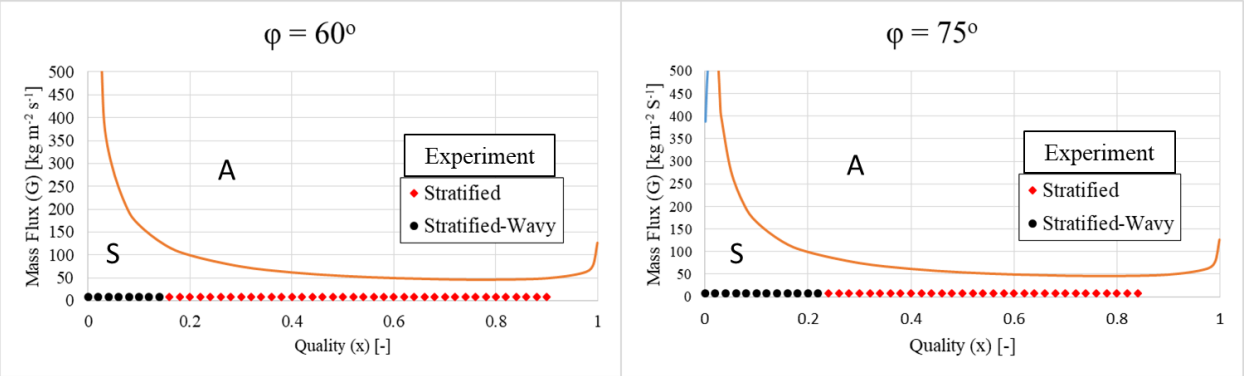

Figure 3.19: Results for flow regime from experiment at six different inclinations (φ = 0°, 3°, 30°, 45°, 60°, 75°), plotted on the Crawford et al. [18] flow pattern map (A = Annular, S = Stratified, I = Intermittent). Experimental data is for a continuous visualization section along the length of the tube. The inlet of the $\varphi \geq 60°$ tests were not observed experimentally. Quality is defined as the thermodynamic quality in a given cross section of the condenser tube

Near the tube inlet, as described in Figure 3.19, the flow is stratified-wavy for the horizontal inclination, but not for downwardly-inclined tubes. A comparison of these two flows is shown in Figure 3.20 and Figure 3.21. For the horizontal tube, high vapor shear and the thick condensate layer cause the formation of waves on the river surface. For inclined condensers, however, no waves are formed. This is shown for a condenser inclined at 3° in Figure 3.21. Despite similar magnitude of the vapor shear force, the shallower condensate river prevents the formation of waves in the inclined condenser. The shallower river would have waves of shorter wavelength [109]. Due to the shorter wavelength, surface tension becomes the important force to overcome in generating a Kelvin-Helmholtz instability [110]. In this case, the vapor velocity is not great enough to overcome the surface tension force.

Figure 3.22 and Figure 3.23 show a comparison of the flow regime near the tube bottom at Z = 10.6 m (near the condenser outlet) for inclinations of 0° and 70°. The most notable difference is the decrease in the depth of the condensate river for the steeper inclination angle. Compared to the horizontal tube, the river depth decreases from 2 cm to 0.7 cm for the 70° tube. In addition to the thinner river, the condensate river flow becomes wavy at this high inclination. The waves are not caused by vapor shear, as at the inlet of the condenser. At the outlet of the inclined tube, the waves are caused by the high river velocity creating turbulence. This turbulence-caused stratified-wavy flow was observed near the outlet of the tubes inclined at 60° or higher. At this location and tube inclinations, the river velocity exceeds 1 m s^{-1} and the Reynolds number based on tube width exceeds 20,000.

Figure 3.20: Stratified-wavy flow in horizontal condenser, Z = 1.1 m

Figure 3.21: Stratified (non-wavy) flow in condenser inclined at φ = 3º, Z = 0.7 m

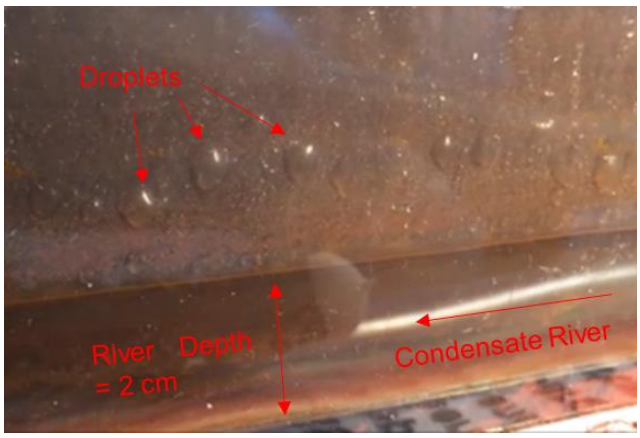

Figure 3.22: Flow characteristics during in-tube condensation in horizontal inclination, Z = 10.6 m

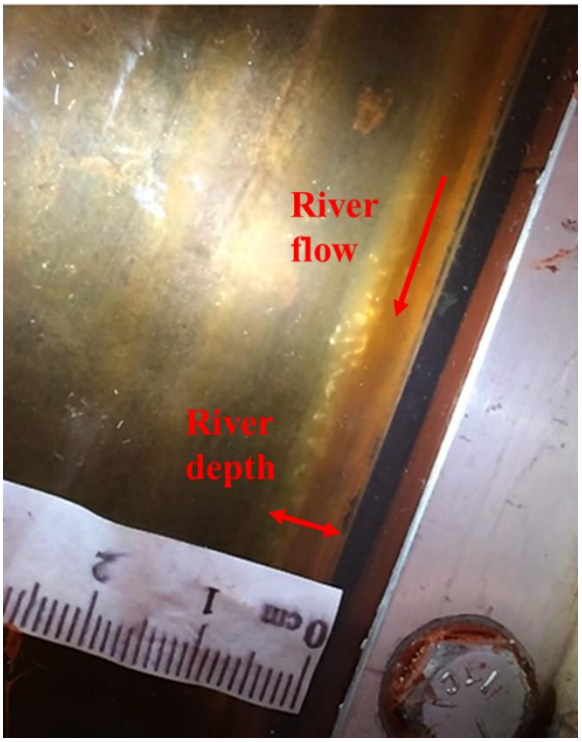

Figure 3.23: Flow during in-tube condensation in inclined position (70º inclination), Z = 10.6 m

3.5.2 Depth of the Condensate River

Figure 3.24 shows the change in depth of the condensate river along the condenser length. For inclined tubes, the condensate depth increases along the tube length, with the maximum depth found at the tube outlet. For the horizontal tube, the depth increases to a maximum around Z = 7 m, then decreases. This decrease in depth near the outlet for the horizontal orientation (0^o) is due to the condenser outlet geometry – the liquid falls down a 90^o pipe bend. The horizontal tube has a low-velocity subcritical flow of condensate. The depth of this type of flow is controlled by the downstream conditions. In this case, the flow accelerates out the end of the tube, with the increased velocity leading to a decreased flow depth. The inclined tubes have a higher-velocity, supercritical flow of condensate. The depth of this supercritical flow is unaffected by downstream flow conditions. Criticality is defined by the Froude number of the river flow:

$$Fr_c = \frac{v_c}{\sqrt{g d_{h,c}}} \tag{3.12}$$

$$d_{h,c} = \frac{A_{cs,c}}{Top\,Width} = \text{Hydraulic Depth} \tag{3.13}$$

When the inertia of a flow outweighs the gravitational force, it has a Froude number greater than one and is defined as a supercritical flow. A flow with gravitational force outweighing the inertial component has Froude number less than one and is defined as subcritical flow. The subcritical flow's dependence on outlet geometry means that the depth of the condensate river for the horizontal tube is dependent on the experimental conditions. It should be noted that an alternative outlet geometry, such as a trough, would create a different river surface profile near the condenser outlet for the horizontal tube. It is also important to emphasize that the local depth of the river depends on accumulation of condensate upstream, and is not an indicator of the local rate of condensate generation.

In addition to changing the depth profile, the increasing inclination angle decreases the condensate river depth for all positions along the condenser. When inclining the tube, the component of the gravitational force in the direction of the condensate flow increases. This increases the velocity of the condensate, which decreases its depth (for a constant mass flow rate).

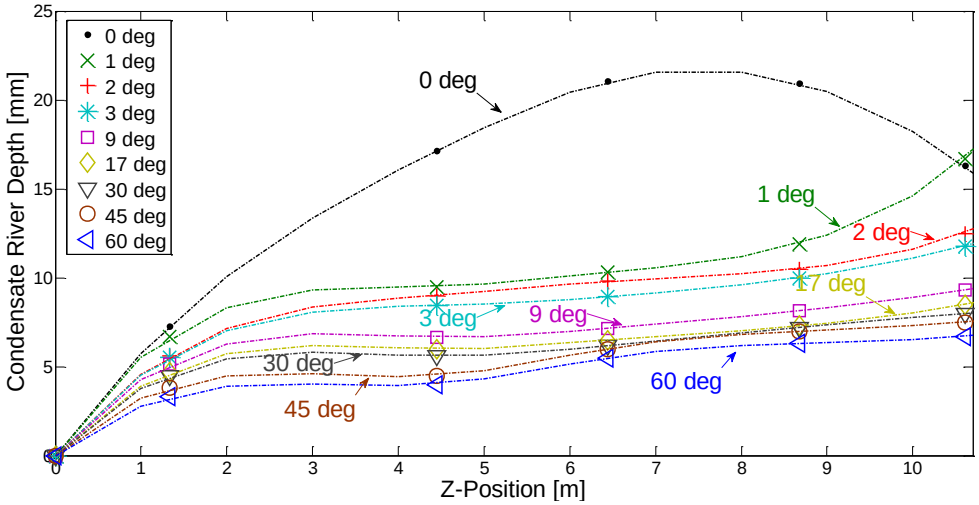

Figure 3.24: Depth of the condensate river along the condenser at various inclination angles

3.5.3 Effect of Inclination on Condenser Capacity

As expected, condenser capacity is a linear function of air inlet temperature difference, as shown in Figure 3.25. Air inlet temperature difference is defined as:

$$\Delta T_{in} = T_{sat} - T_{ai} \tag{3.14}$$

These results are for a horizontally-oriented condenser.

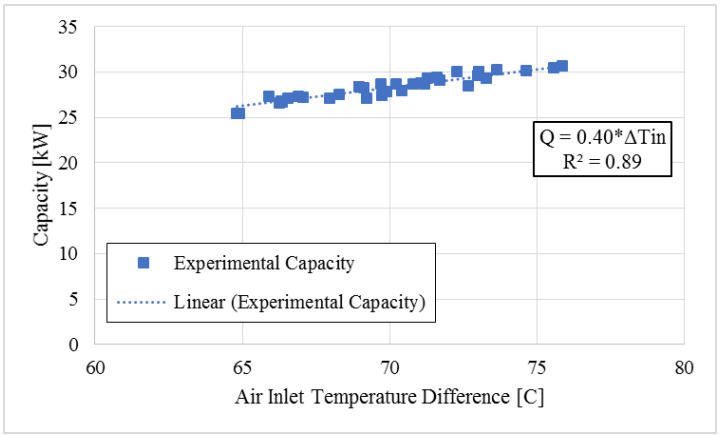

Figure 3.25: Condenser capacity as a function of inlet air temperature difference at φ = 0°

However, if air inlet temperature difference is held constant, it can be seen in Figure 3.26 that capacity is also a linear function of inclination. A linear regression of capacity as a function of ΔT_{in} and inclination finds both independent variables significant. After correcting for variations in ΔT_{in}, the variations in inclination account for 31% of the variation in capacity. This is a significant effect. As inclination increases, condenser capacity increases 0.041% for each

degree change in inclination from the horizontal, with a 3.1% expected improvement at the maximum inclination tested of 75°. This trend is similar to the modeled prediction of 3.4% improvement.

As discussed above, the increasing downward inclination angle causes condensate depth to decrease. This decreasing depth of condensate leaves more of the condenser wall available for condensation heat transfer, thereby increasing the condenser capacity.

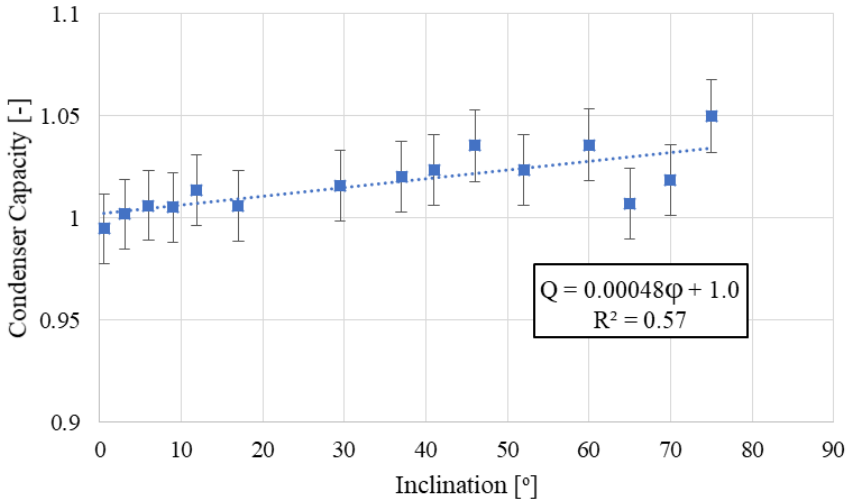

Figure 3.26: Effect of inclination on condenser capacity: ΔTin = 70 °C

3.6 Conclusion

An experimental facility has been developed to test the thermal performance of an air-cooled condenser at varied inclination angles. Providing pressure drop and capacity measurements along with visualization along the entire tube, the facility is designed to provide a complete picture of condenser performance at each operating condition tested.

Stratified flow has been observed for most of the condenser length for all test conditions, with the exception of a short annular section at the condenser inlet. The flow pattern deviates slightly from this trend at the extremes of inclination. The horizontal tube has a stratified-wavy section near the tube inlet, and the tubes inclined more than 60° have a stratified-wavy flow near the tube outlet. Both filmwise and dropwise condensation have been observed together along the condenser wall. This condensate falls vertically down the wall under the influence of gravity, and collects at the tube bottom and flows axially along the tube length. Depth of this condensate river has been found to increase along the length of the tube, and to decrease with increasing tube inclination angle.

The experimental results show an increase in condenser capacity for downwardly-inclined tubes versus the horizontal configuration. This increase is primarily a result of improved drainage of condensate for higher inclination angles. At the maximum tested inclination of 75^{o}, in the experimental half-tube, capacity increases 3.1% versus the horizontal and 0.6% versus 60^{o} inclination.

Chapter 4 Effect of Inclination on Heat Transfer in Air-Cooled Steam Condensers

4.1 Introduction

This chapter takes a deeper look at the effects of inclination on steam-side heat transfer in a 10.7 m long air-cooled condenser. The experiments shown here use the same facility and procedure as described in the previous chapter. All tests are performed slightly above atmospheric pressure. The main variation is the tube inclination angle. The range of test conditions can be seen in Table 4.1 below.

Table 4.1: Operating conditions and uncertainty

Parameter	Range	Uncert.
Steam mass flux [kg m^{-2} s^{-1}]	7 – 9.5	± 10%
Steam mass flow rate [g s^{-1}]	11 – 13.8	± 0.1%
Condenser capacity [kW]	25.2 – 31	± 3%
Air velocity (through fins) [m s^{-1}]	2.2	± 7%
Vapor inlet pressure [kPa]	101 – 106	± 0.1
Vapor inlet superheat [°C]	0.1 – 0.7	± 0.1
Air inlet temperature [°C]	23 – 35	± 0.1
Inclination angle [°]	0 – 75	± 0.1

4.2 Data reduction

4.2.1 Capacity and Overall Heat Transfer Coefficient

Condenser capacity is determined on the air side, and on the steam side, and is determined by the same method as in Chapter 3. Total system capacity is then taken as the uncertainty-weighted average of the air-side and steam-side capacities, as per the procedure recommended by Park, Liu and Jacobi [111]:

$$\bar{Q} = \frac{\left(\frac{1}{u_a^{\,2}}\right)Q_a + \left(\frac{1}{u_s^{\,2}}\right)Q_s}{\frac{1}{u_a^{\,2}} + \frac{1}{u_s^{\,2}}} \tag{4.1}$$

Air-side uncertainty is 7%, and steam-side uncertainty is 1.7%. The difference in air- and steam-side capacity measurements is less than 10% for all tests, with an average of 3% difference. This weighted capacity is then used to determine the overall condenser heat transfer coefficient, U, for a given steam-side area:

$$\overline{U} = \frac{\bar{Q}}{A_a \times LMTD} \tag{4.2}$$

$$LMTD = \frac{\left(T_s - T_{ai}\right) - \left(T_s - T_{ao}\right)}{\ln\left(\frac{T_s - T_{ai}}{T_s - T_{ao}}\right)} \tag{4.3}$$

For each 1 m measurement section, n, condenser HTC, U_n, is calculated from the air-side capacity:

$$U_n = \frac{Q_{a,n}}{A_{a,n} \times LMTD_n} \tag{4.4}$$

U is not constant along the condenser, due to nonlinear variations in h_a and h_s along the tube height. The $\overline{U}$ determined in equation (4.2) is therefore an area- and temperature-difference-weighted average of *U* along the condenser. This $\overline{U}$ cannot be used to determine a mean steam-side HTC, $\overline{h_s}$, as explained by Sparrow *et al.* [75]. Instead, h_s must be determined locally and averaged arithmetically to determine $\overline{h_s}$.

4.2.2 Determination of Steam-Side Heat Transfer Coefficient

Determination of steam-side heat transfer coefficient is complicated due to the non-linear variation in heat flux, wall temperature, and heat transfer coefficients in the condenser cross section. It is not valid to use an average heat flux and wall temperature to determine HTC. Local values of heat flux are needed, but it is difficult to experimentally measure local air-side heat flux. Therefore, a model of air and wall temperatures is developed, and this model is calibrated with the experimental wall temperatures to determine steam-side HTC, h_s. This is similar to the method of Sukhanov *et al.* [19], although this experiment measures wall temperature directly, while Sukhanov's did not. Abraham and Sparrow [112] explained the necessity of using local heat flux and temperatures to evaluate HTC during conditions of non-uniformity in a rectangular duct.

The condenser is first divided along the length into 11 cross sections, *n*, from the entrance to the outlet. Each section is 1 m long, except for the last section, which is 0.7 m long. Each cross section is then divided into 1 mm sections. For each 1 mm section, the heat transfer resistance network in Figure 4.1 must be solved. Steam temperature (T_s) is measured directly. Wall temperature is measured at two points (T_{wt}, T_{wb}). These measured wall temperatures are

used to calibrate the modeled wall temperature profile. Air temperature is only measured at the air inlet (T_{ai}) and outlet (T_{ao}) of each cross section, so the local air temperatures are determined by the model.

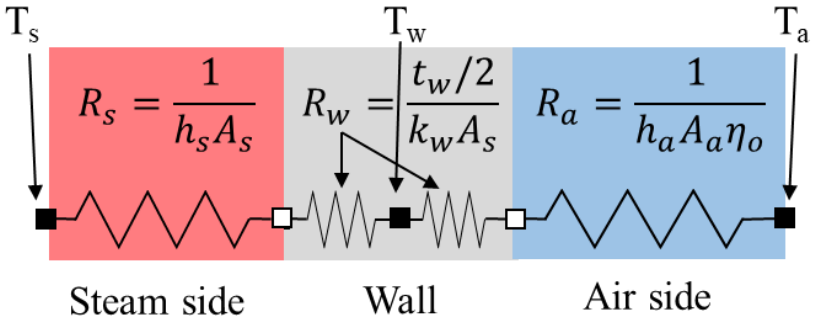

Figure 4.1: Heat transfer resistance network solved for each 1 mm segment in the model

Heat transfer coefficients must then be determined in three regions: in the stratified condensate layer at the bottom of the tube, in the condensing-vapor region, and on the air side, as shown in Figure 4.2.

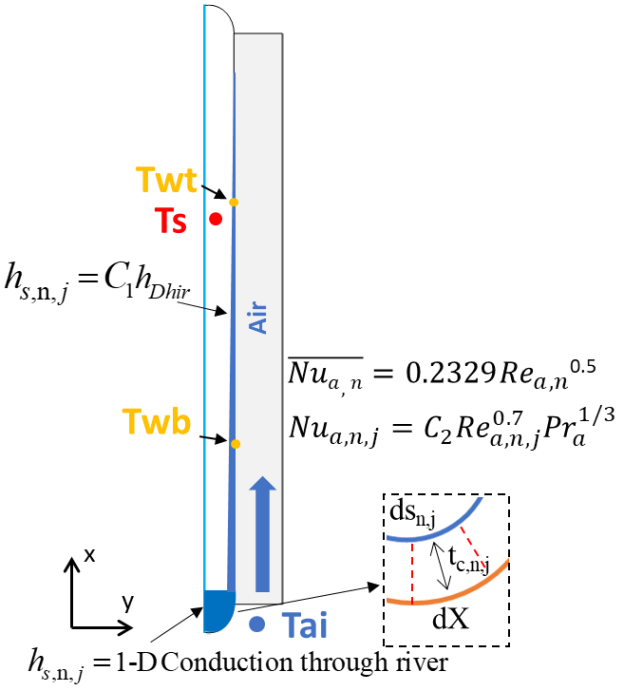

Figure 4.2: Scheme of the thermal model

To determine HTC in the stratified condensate layer, condensate river depth (t_c) must also be known. This is measured experimentally, as described in Chapter 3. For heat transferred

through this layer, 1-D conduction is assumed, as done by Lips and Meyer [71]. Their method is adapted to the flattened-tube geometry here:

$$h_{s,\mathrm{river,n,j}} = \frac{\left(dX - ds_j\right)k_f}{t_{c,\mathrm{n,j}}dX\ln\left(dX / ds_j\right)} \tag{4.5}$$

The stratified liquid layer is discretized into 1 mm intervals (dX) along the wall, as shown in Figure 4.3. The shape of the condensate surface is determined by a model similar to that used by Lips and Meyer [71], with the geometry adapted to match the condenser tube in this study. The local condensate thickness, $t_{c,n,j}$ is then determined for each interval. Apart from tube geometry, there are two inputs to the model for condensate river shape. The first is the depth of the condensate along the polycarbonate window, which is measured during the experiments. The second is the receding contact angle of water on the rusted steel wall, measured to be 0° with a goniometer in independent testing.

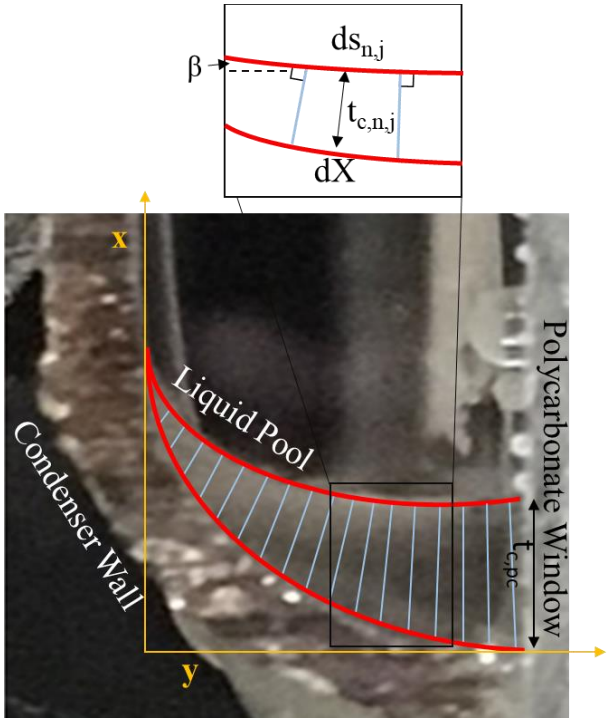

Figure 4.3: Condensate layer discretized for model of thermal conduction

For the model, shear forces are considered to be negligible, and the shape of the interface is controlled by gravitational and surface-tension forces.

The model proceeds by equating pressures. From the Young-Laplace equation describing the magnitude of the surface-tension force:

$$P_f(X) = P_g - \frac{\sigma}{r(X)} \tag{4.6}$$

Considering the effect of tube inclination ($\varphi = 0°$ for these experiments), the gravitational force is:

$$P_f(X) = -(\rho_f - \rho_g) g(\cos\varphi) X + P_f(X = t_{c,PC}) \tag{4.7}$$

Equating (4.6) and (4.7) and denoting the radius of curvature at the polycarbonate window as r_{pc}, yields:

$$\frac{\sigma}{r_{PC}} - \frac{\sigma}{r(X)} = -(\rho_f - \rho_g) g(\cos\varphi) X \tag{4.8}$$

Equation (4.8) can be simplified to:

$$r(X) = \frac{1}{\frac{2X}{b^2} + \frac{1}{r_{PC}}} \tag{4.9}$$

where b^2 is the capillary constant of the fluid:

$$b^2 = \frac{2\sigma}{(\rho_f - \rho_g) g \cos\varphi} \tag{4.10}$$

Geometry shows us that:

$$r(X) = \frac{dX}{(\sin\beta) d\beta} \tag{4.11}$$

Equating (4.9) and (4.11) yields:

$$\left(\frac{2X}{b^2} + \frac{1}{r_{PC}}\right) dX = (\sin\beta) d\beta \tag{4.12}$$

Integrating equation (4.12) from the polycarbonate window ($\beta = 0 \ @ \ X = t_{c,PC}$):

$$\left(\frac{X}{b}\right)^2 + \frac{X}{r_{PC}} = 1 - \cos\beta + \left(\frac{t_{c,PC}}{b}\right)^2 + \frac{t_{c,PC}}{r_{PC}} \tag{4.13}$$

The calculation is performed most easily by setting X = 0 at the top of the condensate along the polycarbonate ($t_{c,pc}$). The surface profile can then be solved in an iterative scheme, beginning at the polycarbonate window. An initial radius of curvature, r_{pc}, is assumed, and the initial parameters are:

$$Y_1 = .00636\text{m}; \ X_1 = 0\text{m}; \ \beta_1 = 0^o$$

The subsequent coordinates are found as:

$$Y_{j+1} - Y_j = \left(\cos\beta_j\right) ds_j \tag{4.14}$$

$$X_{j+1} - X_j = \left(\sin\beta_j\right) ds_j \tag{4.15}$$

$$ds_j = r\left(X_j\right) d\beta_j \tag{4.16}$$

Subsequent values of β are then found using equation (4.13). The calculation proceeds until the condensate surface intersects the condenser wall. The boundary condition at the wall is a contact angle of 0°. An iterative process is used to satisfy this boundary condition, whereby r_{pc} is varied until the condensate surface and the wall are tangent at the point of intersection. The bottom of the condenser wall is a circular arc that subtends an angle of 90°.

In the condensing-vapor region above the condensate river, natural-convection film condensation is assumed. Natural-convection film condensation can be considered a reasonable approximation for the condenser because the majority of the tube consists of high-void-fraction stratified flow with low vapor Reynolds number, ranging from 0 – 10,000. In addition, diabatic visualization (discussed in Section 3.5) found that vapor shear had little effect on the condensing film and droplets. Therefore, in the condensing-vapor region, HTC is determined from Dhir and Lienhard's equation for film condensation [4]. At a given cross section, *n*, and local section of the wall, *j*, HTC in the condensing vapor region is:

$$h_{\mathrm{s,n,j}} = \left[\frac{i_{fg} g_{eff} \left(\rho_f - \rho_g\right) {k_f}^3}{4 X_j \left(T_s - T_{w,\mathrm{n},j}\right) \nu_f}\right]^{1/4} \tag{4.17}$$

This is dependent on steam-wall temperature difference, which is unknown. Therefore, this set of equations must be solved iteratively. Care must also be taken at the top of the tube, where equation (4.17) goes to infinity. This behavior does not reflect reality, because surface tension causes liquid to coat the tube wall and yield a finite HTC. Therefore, film thickness is considered to be constant over the curved surface at the top of the tube for this model.

The third region where HTC must be determined is on the air side. In this region, the local HTC is determined from a CFD simulation in the current fin geometry. ANSYS Fluent software [113] is used for the simulation. The 3-D simulation is performed for one fin pitch and extending along the entire tube height. The result is found to be proportional to the Reynolds number along the fin length:

$$\mathrm{Nu}_{a,\mathrm{n,j}} \propto \mathrm{Re}_{\mathrm{a,n,j}}{}^{0.7}\,\mathrm{Pr}_{a,\mathrm{n,j}}^{1/3} \tag{4.18}$$

As verification of the air-side HTC, the result is compared with an empirical correlation for mean air-side HTC. The correlation was developed by Wilson plot for this particular condenser by Creative Thermal Solutions, Inc.:

$$\overline{\mathrm{Nu}_a} = 0.2329\,\mathrm{Re}_a^{0.5} \tag{4.19}$$

Here, Re_a is determined from experimentally-measured air velocity and inlet air temperature (T_{ai}). This correlation has an accuracy of 5% over the Reynolds number range of 300-1,200, with Reynolds number based on the hydraulic diameter of the channel between fins. The CFD results are found to slightly under-predict the empirical correlation, likely due to slight differences between the modeled and experimental fin geometries. Therefore, a gain, C_2, is applied to the local HTC in equation (4.18) so that it matches the empirical correlation in equation (4.19). To summarize, the profile of $h_{a,n,j}$ is determined by simulation, which is then scaled to match the average HTC determined by empirical correlation. The final equation for air-side HTC is:

$$h_{a,n,j} = C_2\,\mathrm{Re}_{a,n,j}^{0.7}\,\mathrm{Pr}_{a,n,j}^{1/3}\,\frac{k_{a,n,j}}{d_{h,a}} \tag{4.20}$$

Now that the inputs from the experiment (T_s, T_{wt}, T_{wb}, T_{ai}, T_{ao}, v_a, t_c) and the models for HTC in each of the three regions have been specified, the model can be solved in 1 mm increments in each condenser cross section as shown in Figure 4.4 (J steps of height $dx = 1\ mm$). The output of the model is h_s, the average HTC for each 1 m measurement section. The thermal model is run independently in each 1 m cross section.

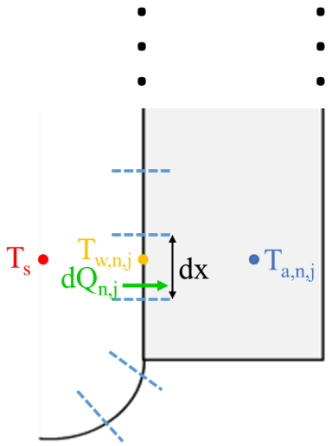

Figure 4.4: Diagram of model divisions along a condenser cross section, n; not to scale

The solution procedure is as follows, for each increment, j:

The local capacity is found first, using:

$$dQ_{n,j} = dUA_{n,j}\left(T_s - T_{a,n,j}\right) \tag{4.21}$$

$$\frac{1}{dUA_{n,j}} = \frac{1}{h_{a,n,j}\eta_{o,n,j}A_{a,n}} + \frac{t_w}{k_w A_{s,n}} + \frac{1}{h_{s,n,j}A_{s,n}} \tag{4.22}$$

The three terms on the right-hand side of equation (4.22) represent the air, wall, and steam heat transfer resistances, respectively. The wall resistance is constant. Air-side HTC, $h_{a,n,j}$ can be solved explicitly by equation (4.20). In the condensate river at the tube bottom, $h_{s,n,j}$ can also be solved explicitly, by equation (4.5). Higher along the tube wall, in the condensing film region, $h_{s,n,j}$ is a function of T_w, so the wall temperature from the previous section (j-1) is used to make a first approximation of $h_{s,n,j}$. Wall temperature is then determined by:

$$T_{w,n,j} = T_s - \frac{dQ_{n,j}}{h_{s,n,j}dA_{s,n}} \tag{4.23}$$

$$dA_{s,n} = dX * dL_n \tag{4.24}$$

Once the wall temperature is found, $h_{s,n,j}$ is re-calculated in an iterative process until the wall temperature and $h_{s,n,j}$ determinations converge.

The air temperature of the subsequent step, $j+1$, is then calculated by:

$$T_{a,n,j+1} = T_{a,n,j} + \frac{dQ_{n,j}}{c_{p,a,n,j}\dot{m}_{a,n}} \tag{4.25}$$

The process then continues from equation (4.21). Once the calculation for a given cross-section is complete, the wall temperature profile is compared to the measured wall temperatures, T_{wt} and T_{wb}. $h_{s,n}$ is then multiplied by a constant, C_1, in order to align the model and experimental wall temperatures. The model is then re-run, and wall temperatures re-checked, and the entire procedure is iterated until the modeled and experimental wall temperatures are equal:

$$\frac{abs(T_{w,model} - T_{w,exp})}{T_{w,exp}} \times 100\% < 0.1\% \tag{4.26}$$

The final average steam-side HTC for each condenser cross section is then:

$$h_s = C_1 * h_{s,model} \tag{4.27}$$

The ratio C_1 (between experimental HTC and model HTC) ranges from 0.8-2.8 depending on experimental conditions.

The circumferential mean HTC, h_s, is the mean of $h_{s,n,j}$ for a given cross-section, n, and $\overline{h_s}$ is the arithmetic mean of h_s for the entire condenser.

The model is validated by comparing the total condenser capacity from the model and from the experiment. Figure 4.5 shows that all experimental capacities were predicted to within 10% by the model. Similar verifications were performed with the capacity of each measurement section, and with condenser U, although they are not shown here.

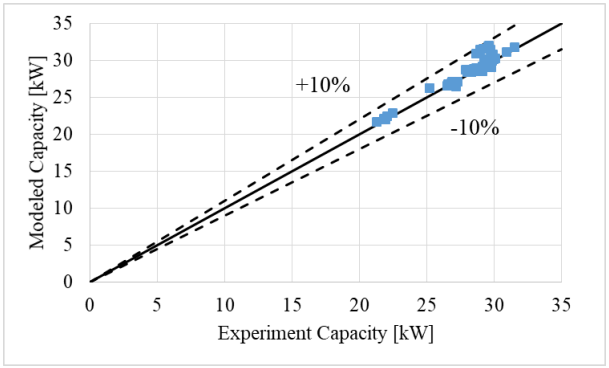

Figure 4.5: Modeled capacity compared to experiment capacity

An example of the modeled temperatures is presented in Figure 4.6. The non-linear temperature profile can be observed, as well as the correction required to match modeled and experimental wall temperatures. An example of $h_{a,n,j}$ and $h_{s.n.j}$ in a cross section are given in Figure 4.7. Air-side HTC decreases in the airflow direction as the boundary layer grows. Steam-side HTC decreases from tube top to bottom due to an increase in thickness of the condensate

film. The most significant decrease is seen at the bottom, due to the heat transfer resistance of the stratified condensate.

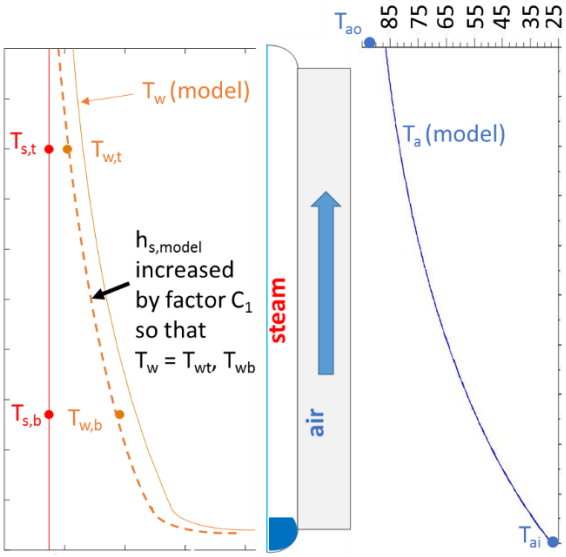

Figure 4.6: Modeled temperatures, T_w and T_a, and effect on T_w of adjusting $h_{s,model}$. Model values are presented by lines while dots are used for measured values

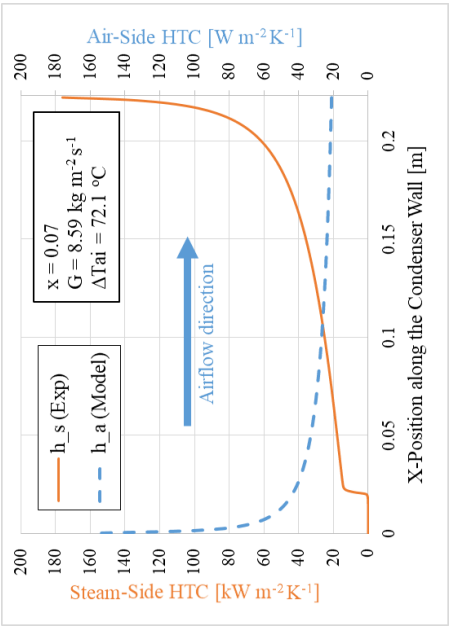

Figure 4.7: Calibrated model of air- and steam-side HTC along a vertical profile of the condenser tube; Z = 10.5 m

4.2.3 Uncertainty Analysis

Uncertainties in capacity and HTC are calculated using the method of Taylor and Kuyatt [114] on equations (4.1), (4.2) and (4.27). Uncertainties of measured quantities can be found in Table 4.1. For the method of local HTC, uncertainties in the modeled temperature profiles were

also considered. The model itself was verified by comparing modeled and experimental capacities, along with U values. For the entire condenser, the uncertainty in steam-side capacity is 1.7% and the uncertainty in air-side capacity is 7%. The majority of the uncertainty in air-side capacity is from measurement of the air outlet temperature, T_{ao}, and of air velocity, v_a. To reduce this uncertainty, T_{ao} is measured at 29 locations and v_a is measured at 645 locations. This yields an experimental uncertainty in capacity of 1.4% based on equation (4.1).

The error in U is 7% for the entire condenser, or 11% per section, n. The main cause of uncertainty is the uncertainty in measuring local air velocity and outlet temperature. The error in determining h_s is 20%. For h_s, the main causes of uncertainty are the small ΔT between wall and steam, and the uncertainty in the h_s profile near the top of the tube. Looking at Figure 4.7, the Dhir and Lienhard [4] approximation of h_s predicts an exponential increase in h_s near the top of the tube. In a practical condenser this is unlikely, especially with mixed-mode dropwise and filmwise condensation. In reality, the film thickness does not thin as drastically at the top of the tube as in theory. However, in this region, the temperature differences are small, and the air-side resistance is dominant, so even an order-of-magnitude change in h_s in this region does not have much effect on the condenser performance or even the wall temperature. Therefore, h_s in this region is very difficult to determine experimentally.

4.3 Analysis of the Effects of Inclination on Heat Transfer

4.3.1 Effect of Inclination on Filmwise and Dropwise Condensation

Both filmwise and dropwise condensation have been observed in this condenser, so it is important to understand the effects of varying inclination on both of these phenomena. Overall condensation HTC will be a combination of the HTC from both of these processes.

For filmwise condensation, inclination affects heat transfer by increasing the film thickness. For an inclined tube, the condensate film has a longer falling distance from the top of the tube until reaching the condensate river at the tube bottom. This increases the average thickness of the film. The magnitude of this increase is predicted from Nusselt condensation theory, which has been shown to vary with inclination by a factor of $cos(\varphi)^{-1/4}$:

$$t_{film,j} = \left[\frac{4\left(H_w - X_j\right)k_f \left(T_{sat} - T_{w,j}\right)\nu_f}{i_{fg} g \left(\rho_f - \rho_g\right)\cos\left(\varphi\right)} \right]^{1/4} \tag{4.28}$$

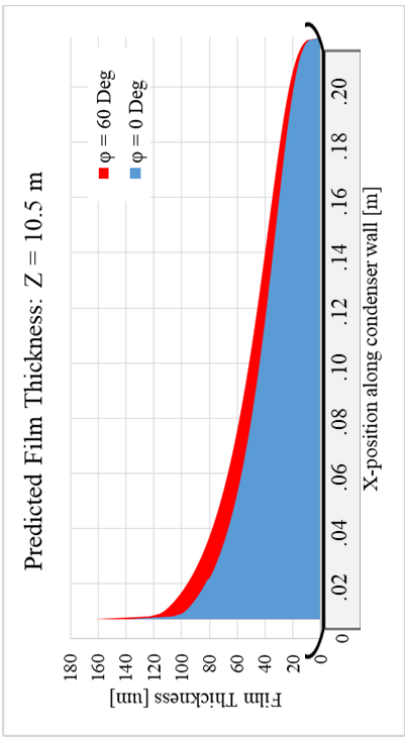

Figure 4.8: Prediction of condensate film thickness at outlet of condenser based on Nusselt theory (Z = 10.5 m) for two tube inclination angles, $\varphi = 0^{o}$ and $\varphi = 60^{o}$

The results in Figure 4.8 show that film thickness increases 26% on average for a given cross section. This thicker film would result in a decrease of 15% in condensation heat transfer coefficient for the 60^{o} inclination. Therefore, considering only the wall film, increasing inclination can be said to have a negative effect on film condensation heat transfer coefficient.

For dropwise condensation, the opposite effect is expected. As inclination of the surface increases, the dropwise heat transfer coefficient is expected to increase. As inclination increases, the falling length of the droplets increases. Falling droplets increase in size due to coalescence, and therefore the lower portion of the condenser wall is swept with a higher frequency than the upper portion. Sugawara and Michiyoshi [115] showed that the sweeping frequency varies as the cube root of the plate height. As a result, droplets on the lower surface of the plate have less time for growth, and are smaller. Dropwise condensation theory [116] and experiment [117] have shown that HTC increases as droplet radius decreases. Therefore, dropwise HTC increases as distance from the top of the condenser wall increases. Increasing tube inclination increases the effective height of the condenser wall. For the limit of a vertical tube, this height is equal to the entire condenser length. As a result, higher tube inclination is expected to increase dropwise heat transfer coefficient.

To describe the overall effect of inclination on condensation HTC as a result of the competing effects of filmwise and dropwise condensation first requires a knowledge of the distribution of dropwise and filmwise condensation throughout the condenser tube. This distribution may change from condenser to condenser, depending on local variations in surface conditions. However, the performance of the condenser for pure filmwise or pure dropwise condensation can be used as the limits for the expected performance of the ACC. For example, any decrease in HTC due to increased inclination must be less than or equal to the decrease predicted by Nusselt theory. In addition, the experimental HTC must be less than the theoretical HTC for pure dropwise condensation and greater than the theoretical HTC for pure filmwise condensation. For the experimental condenser in horizontal orientation with $\Delta T_{ai} = 73°C$ and $G = 7 \text{ kg m}^{-2} \text{ s}^{-1}$, Rose [118] predicts $\bar{h}_s$ of 50 kW $\text{m}^{-2}\,\text{s}^{-1}$ for pure dropwise condensation.

4.3.2 Prediction of Condenser Performance at Different Axial Positions and Inclination Angles

Performance of the experimental condenser is predicted using a similar model to that used for determining local HTC. In order to have a fully-predictive model, the uncorrected film-condensation model by Dhir and Lienhard [4], equation (4.17), is used to calculate steam-side HTC. To predict void fraction, the method from Kang *et al.* [119] is used. This method uses the correlation of Zivi [120] along with the superficial quality method of Xiao and Hrnjak [29] to predict void fraction. The void fraction is then converted to a condensate river depth by using tube geometry (Figure 3.24).

Figure 4.9 shows predicted condenser temperatures, heat transfer resistance, and heat flux for cross sections at Z = 0.5 m and Z = 10.5 m. In each cross section, steam-side heat transfer resistance decreases from condenser bottom to top. This is due to two effects – a decreasing temperature difference between steam and wall, and a decreasing condensate film thickness. This effect is especially pronounced at the tube bottom, where the stratified condensate layer creates a large heat transfer resistance. At the tube bottom, the steam-side heat transfer resistance is two orders of magnitude greater than the air-side resistance, causing the wall temperature to be nearly equal to the air temperature. Above this condensate layer, steam-side resistance reduces drastically and the air side provides the dominant heat transfer resistance – about 40 times greater than the steam-side resistance.

Air-steam temperature difference also decreases from condenser bottom to top. Following this temperature difference, heat flux decreases from condenser bottom to top. However, the tube bottom has low heat flux due to the large heat transfer resistance of the stratified condensate layer. Comparing along the condenser length, at Z = 10.5 m, the thicker condensate layer causes a higher steam-side heat transfer resistance, and a 3.5% lower heat flux than at the condenser inlet. In summary, heat flux is affected by the air-steam temperature difference and by the largest heat transfer resistance at each given location. The largest resistance is the condensate at the tube bottom and then becomes the air side when moving above the condensate layer.

Figure 4.10 shows predicted condenser behavior at the 60^{o} inclination at cross sections near the inlet and outlet. Comparing this inclination with the horizontal tube, the average heat flux at z = 0.5 m increases 0.3% at 60^{o} in comparison to 0^{o}. At Z = 10.5 m, average heat flux increases 3.9%. At 60^{o}, the stratified condensate layer along the tube bottom is thinner, leading to this improved performance. This effect is more pronounced near the condenser outlet, where void fraction is the lowest. In total, condenser capacity is expected to increase by 3% for the 60^{o} inclination vs the 0^{o} inclination. Condenser U value is expected to increase 9% for the 60^{o} inclination, or 0.15% per degree increase in downward inclination.

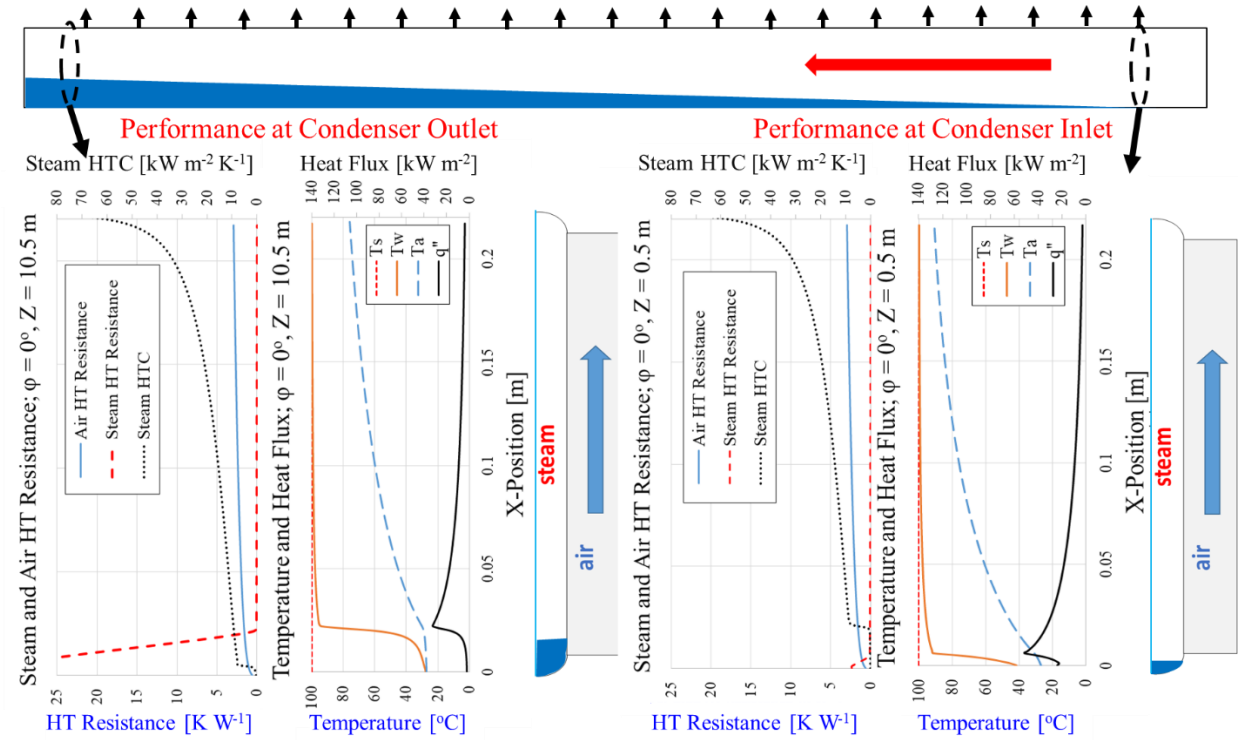

Figure 4.9: Prediction of steam and air heat transfer resistances, steam, wall, and air temperatures, and heat flux at cross sections at z=0.5m and z = 10.5m for the horizontal inclination. Steam-side area is 0.223 m^2 and air-side area is 3.56 m^2 per measurement section

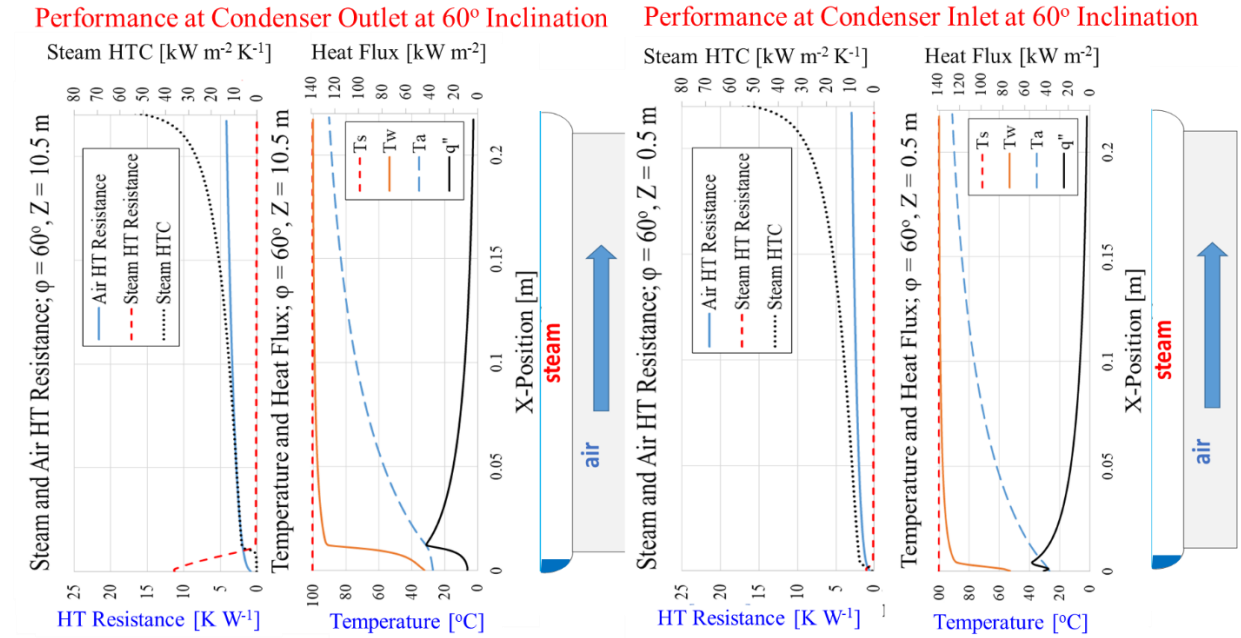

Figure 4.10: Prediction of steam and air heat transfer resistances, steam, wall, and air temperatures, and heat flux at cross sections at Z = 0.5 m and Z = 10.5 m for 60° inclination

4.4 Results and Discussion

4.4.1 Steam-Side Heat Transfer Coefficient along the Condenser

Heat transfer coefficient along the condenser, h_s, is constant within the limits of uncertainty, as seen in Figure 4.11. The results do not show an obvious increase in HTC, considering the high uncertainty in determining HTC. Here, h_s is the mean HTC for a given cross section of the condenser. Except for Shah's [121] correlation near the inlet, all of the correlations significantly underpredict the magnitude of the experimental data. The constant HTC demonstrates that quality and vapor velocity do not affect the steam-side performance significantly. As a result of the stratified flow, the majority of the condenser is unaffected by changes in quality. The vapor velocity is also low, around 11 m s^{-1} at condenser inlet, so vapor shear is negligible for much of the condensation process.

This constant HTC along the condenser contrasts with the predictions of Shah [121] and Chato [47]. Shah's correlation predicts a flow regime change near the tube inlet, leading to the sharp decline in h_s. Chato's [47] correlation predicts flooding near the tube outlet, leading to a sharp drop in h_s. These effects are not observed in this experiment, because the heat transfer for low mass flux in a large flattened tube is fundamentally different than that for traditional small, round tubes used in refrigeration. Due to the large cross-sectional area, vapor velocity is low and the effect of vapor shear is negligible for much of the condenser length. Due to these factors, parameters such as void fraction and HTC are not affected by Reynolds number, as they are for smaller, round tubes. In addition, void fraction is high for the entire length of the condenser tube, never reaching a value below 0.8. As a result, flooding is not encountered. This fact, coupled with a lack of dependence on steam Reynolds number, means that condenser performance changes very little along the length of the condenser. This is in great contrast to a refrigeration condenser, which has significantly higher heat flux near the condenser entrance.

Kroger's [69] correlation is the exception, in that it predicts no change in condenser performance along the length.

In comparing the experimental results to these correlations, the lack of applicability of these correlations to this ACC should be emphasized. All of the published stratified-flow correlations assume a constant wall-steam temperature difference (ΔT_w) for a given cross-section of the condenser tube. For the large ACC tube, this is not a valid assumption; the

temperature difference is nearly constant along the tube length, but varies around each cross-section as seen in Figure 4.9. Having both a non-linear variation in ΔT_w and correlations with a non-linear dependence on ΔT_w, it is highly inaccurate to use an average ΔT_w or a log mean temperature difference to predict $\bar{h}_s$. To accurately predict $\bar{h}_s$, a local, analytical calculation of h_s is needed, as done in the model explained above. Kroger's [69] correlation is the one exception to this problem, as it was developed specifically for the ACC, by applying Nusselt analysis to the ACC tube. However, even this correlation assumes a constant U value for a given tube cross section.

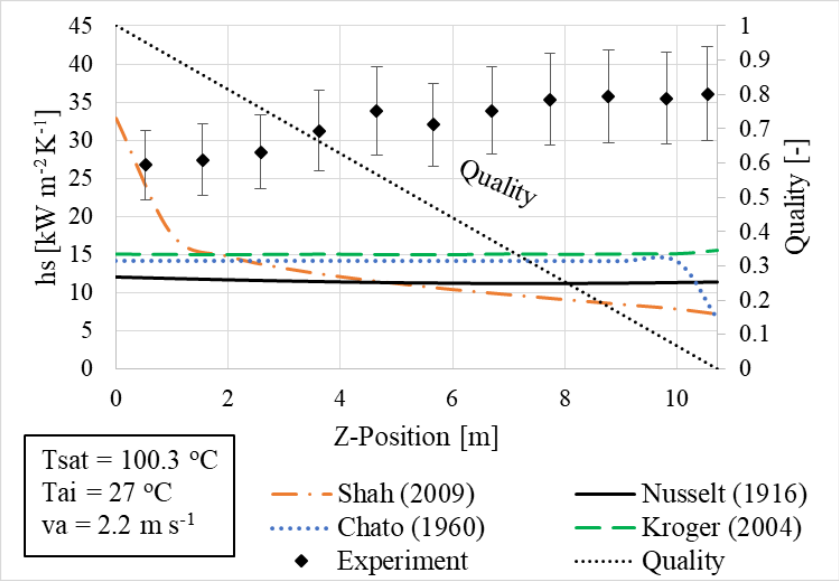

Figure 4.11: h_s measured from wall-steam temperature difference from condenser inlet to outlet at horizontal position (0° inclination)

As in the correlation of Chato [47] and model of Nusselt [3], h_s is strongly a function of wall-steam temperature difference. This comparison is shown in Figure 4.12. Figure 4.13 shows h_s plotted versus ΔT_w on a log-log scale, in order to see the relationship clearly. Nusselt analysis (equation (4.17)) predicts a slope of -0.25, but for this experiment, a slope of -0.77 is found to be the better predictor.

Figure 4.14 compares experimental results for h_s against ΔT_{ai}. A linear regression for h_s predicted by ΔT_{ai} shows a significant relationship between the two variables, at the 99% confidence level. As ΔT_{ai} increases, h_s decreases, which agrees with Kroger's [69] prediction.

However, significant scatter in the data makes a precise trend difficult to discern. More data over a wider range of ΔT_{ai} are necessary.

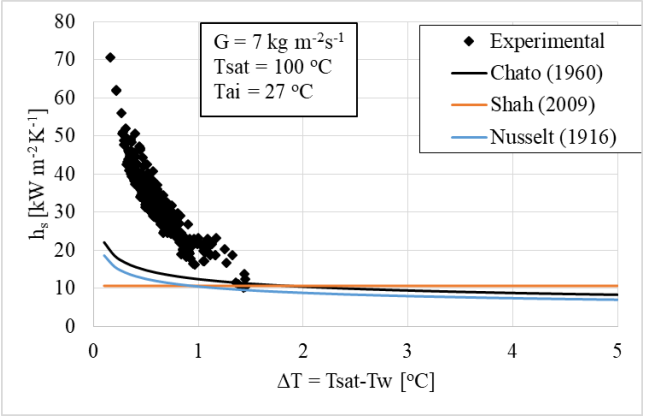

Figure 4.12: Experimental results and correlations plotted against $\Delta T_w = T_{sat} - T_w$

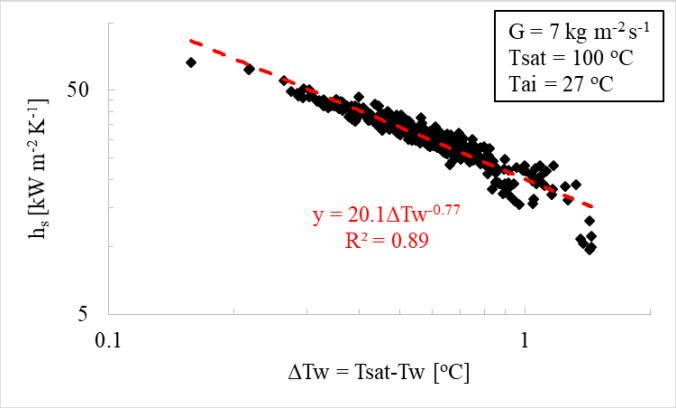

Figure 4.13: Film heat transfer coefficient h_s as in Figure 15 plotted on log-log axes as a function of heat flux ($\Delta T_w = T_{sat} - T_w$)

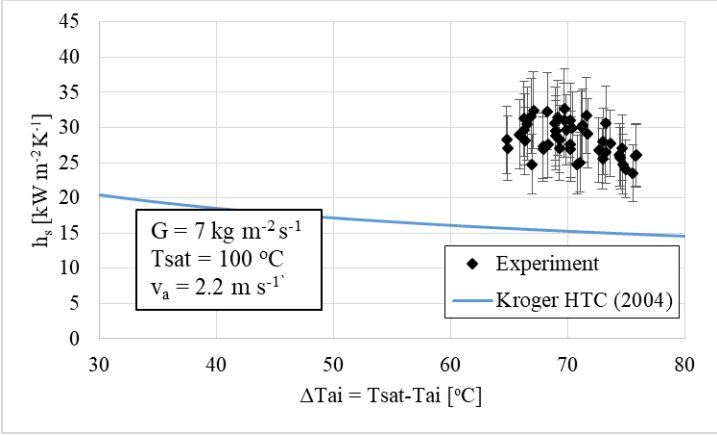

Figure 4.14: h_s vs. ΔTai, experimental results compared to Kroger correlation

Despite the lack of variation in h_s along the condenser, the overall condenser HTC does decrease, as seen in Figure 4.15. This U decreases due to an increase in depth of the condensate

river at the tube bottom. Referring back to Figure 4.9, the tube bottom is the most important region for heat transfer, due to the large air-steam temperature difference and the high air-side HTC in this region. The steam side is the largest heat transfer resistance in this region. Therefore, the increase in local h_s from the thicker condensate layer at the tube bottom has a large effect on condenser performance.

In contrast, higher along the flat tube wall, changes in h_s do not affect condenser performance. In this region, steam-side heat transfer resistance is much lower than air-side resistance. This upper wall region covers the majority of the condenser tube, so the average h_s in each cross-section remains nearly constant.

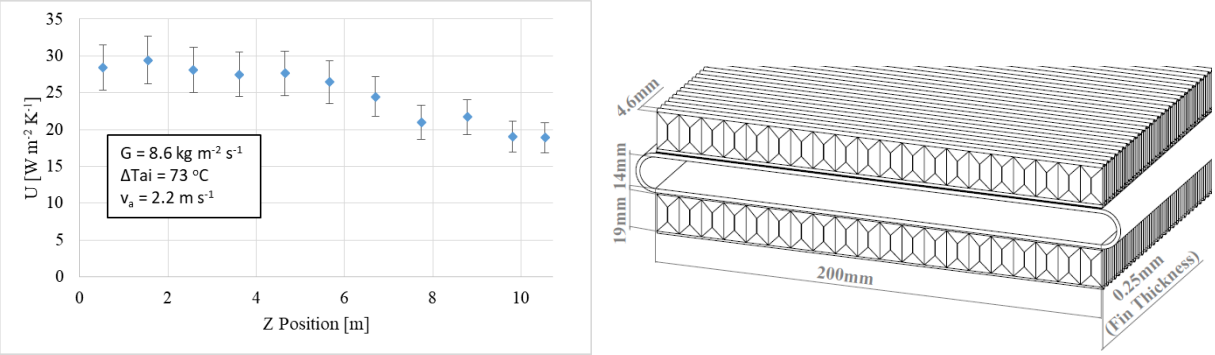

Figure 4.15: U (overall HTC, based on air-side area) along the condenser length; Air-side geometry depicted above for design reference; Current facility has 38 m^2 air-side area

Comparing Figure 4.11 and Figure 4.15, it is interesting how we have found that it is possible for *U* to vary independently of h_s. This can be investigated further through Figure 4.16, which shows the calibrated model for h_s and *U*. It is apparent that *U* at the condenser bottom (X-position < 0.03 m) is controlled by h_s. Above the condenser bottom, h_a is the dominant heat transfer resistance, so changes in h_s in this region do not affect condenser *U*. This air-controlled region covers the majority of the condenser, so it is possible for h_s to vary significantly in this region without causing a detectable change in condenser *U* or *Q*. It is this fact that makes accurate determination of h_s difficult in the current experimental setup.

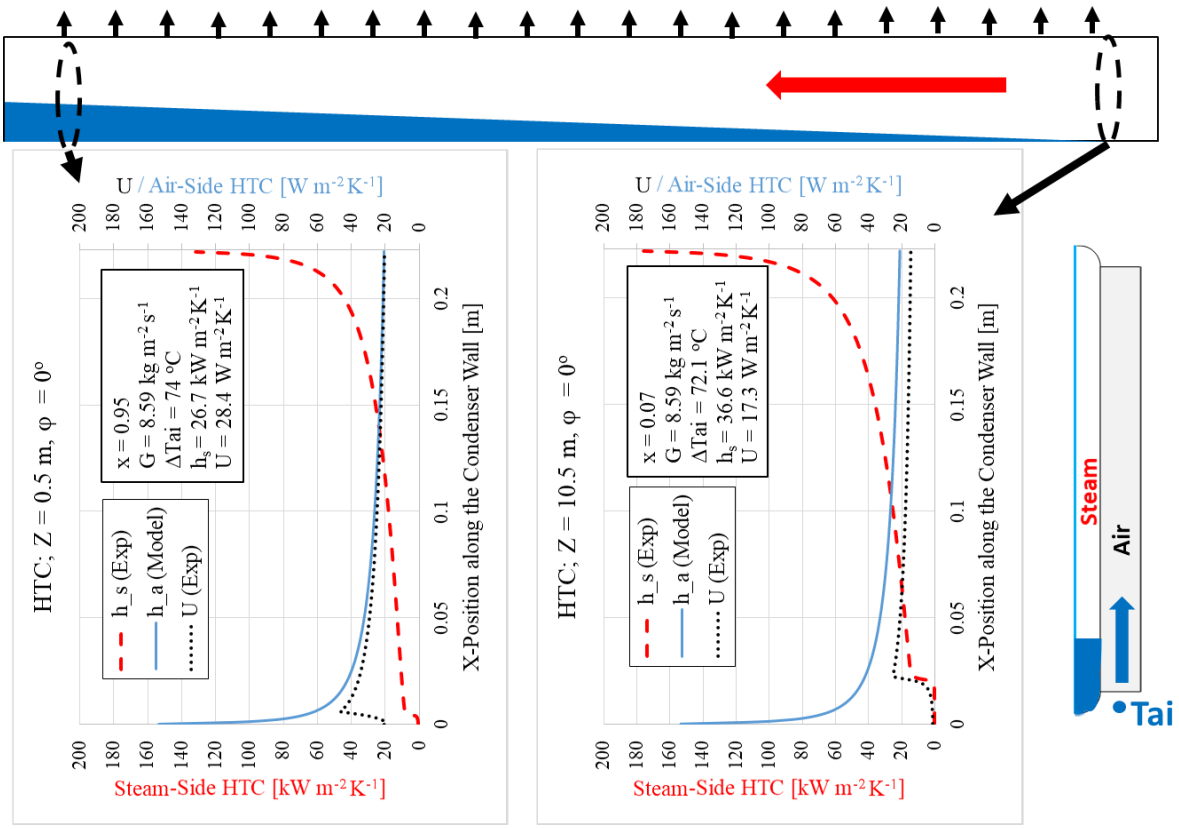

Figure 4.16: h_s and U determined from experiment, and h_a from model in cross sections of the condenser near the inlet and outlet; Note that units for h_s are kW m^{-2} K^{-1}, while for h_a the units are W m^{-2} K^{-1}

4.4.2 Condenser Heat Transfer Coefficient at Varied Inclination Angles

Overall condenser HTC, $\overline{U}$, increases slightly as inclination increases, as seen in Figure 4.17. An approximate 4% increase in $\overline{U}$ is found at 75° inclination compared to a horizontal tube. As inclination increases, the thickness of the condensate river at the tube bottom decreases. This reduces the overall heat transfer resistance. This increasing trend matches the trend of increasing capacity with increasing inclination that was discussed in Chapter 3. However, experimental uncertainty combined with the small increase in $\overline{U}$ make it impossible to draw a precise correlation between inclination and overall condenser HTC.

This increase in $\overline{U}$ is not reflected by a matching increase in mean steam-side HTC ($\overline{h_s}$), however. Figure 4.18 shows no trend for $\overline{h_s}$ versus inclination. In fact, as inclination increases, there are three competing effects on steam-side HTC. Depth of the condensate river decreases, which has a positive effect on $\overline{h_s}$. Falling length for droplets increases, which increases dropwise

HTC. However, film thickness along the wall increases, which has a negative effect on filmwise HTC. The results of the experiment show that these effects negate each other to yield no net change in $\overline{h_s}$ with inclination

The differing trends of $\overline{U}$ and $\overline{h_s}$ versus inclination further show that these two variables are not directly related, however counterintuitive this may seem. An area-averaged $\overline{h_s}$ can accurately predict $\overline{U}$ only when either h_s or ΔT is constant, as shown by Sparrow *et al.* [75]. Figure 4.9 and Figure 4.10 show that this is not the case for this condenser. Both h_s and ΔT vary non-linearly along each condenser cross-section. Therefore, $\overline{h_s}$ is not expected to follow the same trend as $\overline{U}$ in this study. $\overline{U}$ is most affected by regions of high ΔT, such as at the bottom of the condenser. Therefore, the thinning of the condensate river in this region causes the increase in $\overline{U}$.

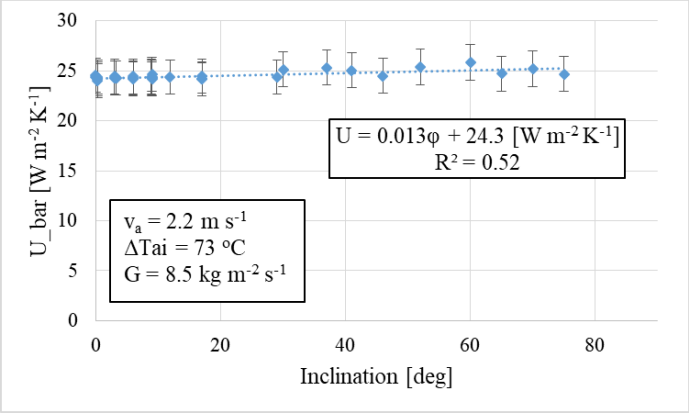

Figure 4.17: Condenser $\overline{U}$ (overall HTC) as a function of inclination angle φ

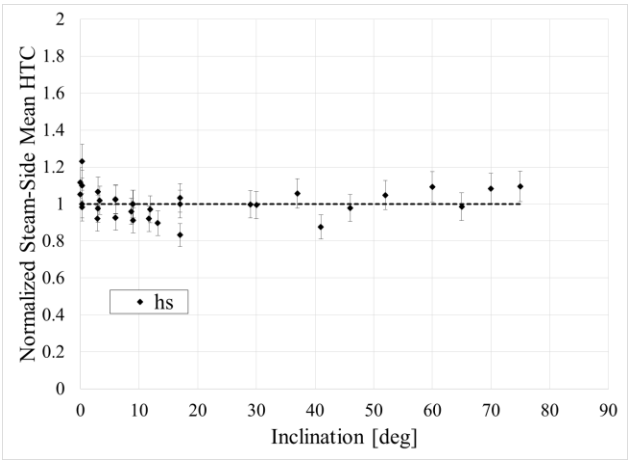

Figure 4.18: Mean steam-side HTC ($\overline{h_s}$) vs inclination. Results have been normalized by horizontal inclination (normalized $\overline{h_s} = \frac{\overline{h_s}}{h_{s,\varphi=0°}}$) to show percent change. A horizontal line is plotted to show that no trend is found vs inclination.

4.4.3 Effect of Inclination on Heat Transfer Coefficient at Different Qualities

Lips and Meyer [13] demonstrated that inclination has a greater effect on HTC at low qualities. This relationship does not hold for this condenser, based on the results shown in Figure 4.19. There is no significant trend for h_s vs inclination for any quality. The high void fraction, even at low qualities, means that the stratified condensate layer only covers a small portion of the condenser area. In addition the competing effects of dropwise and filmwise condensation may negate any changes in HTC due to the thinning of the condensate river. Therefore, even though the void fraction increases for increasing inclination angle, this does not have a significant effect on the mean HTC.

However, the local *U* value does change with inclination and quality, as seen in Figure 4.20. For low qualities, *U* increases linearly as inclination increases. As seen earlier, the removal of condensate at the tube bottom has a significant positive effect on the condenser performance. Although the heat transfer coefficient along the upper tube wall remains relatively unchanged, the removal of the heat transfer resistance at the tube bottom significantly improves the overall condenser performance. For quality = 0.02 (high quantity of liquid), *U* increases 10% at 75^o inclination (probably due to better drainage). At the highest quality shown (x = 0.85), there is no improvement in *U* with inclination. In this region, the depth of the condensate river is low for all

inclinations, and the effects of vapor shear are larger, so the variation in inclination angle has no effect on condenser performance.

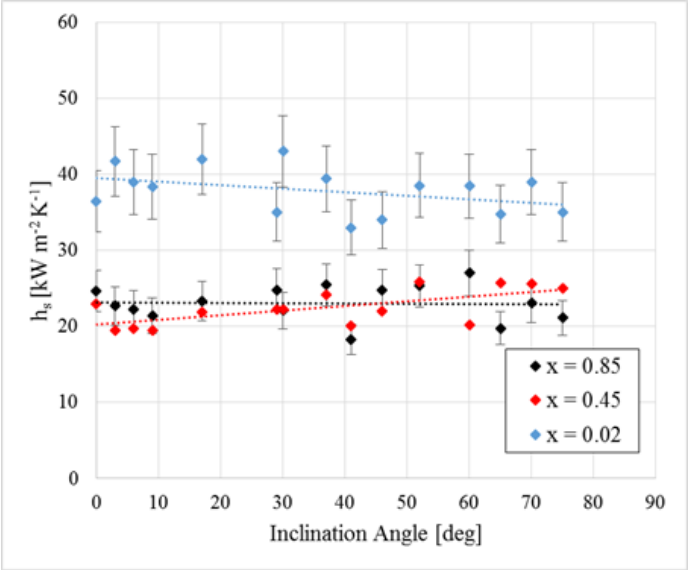

Figure 4.19: Effect of inclination angle φ on h_s at three different qualities x (average quality of each 1 m test section)

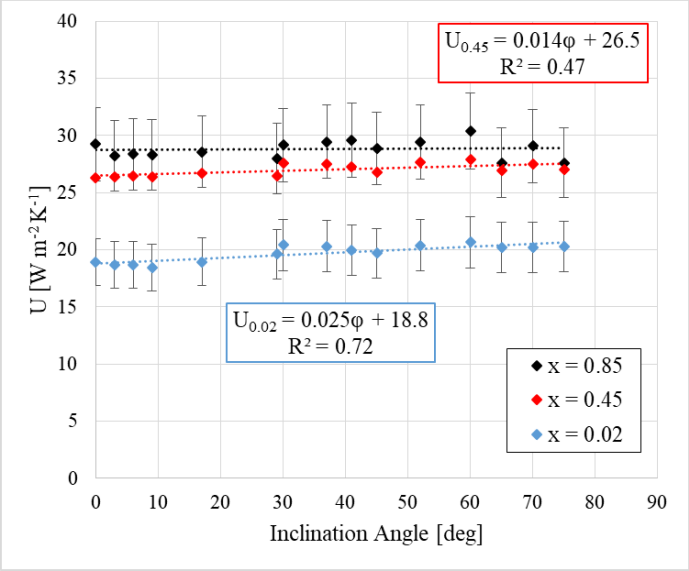

Figure 4.20: Effect of inclination angle φ on *U* value at three different qualities (average quality of each 1 m test section)

4.4.4 Effect of Inclination on Average Steam-Side Heat Transfer Coefficient

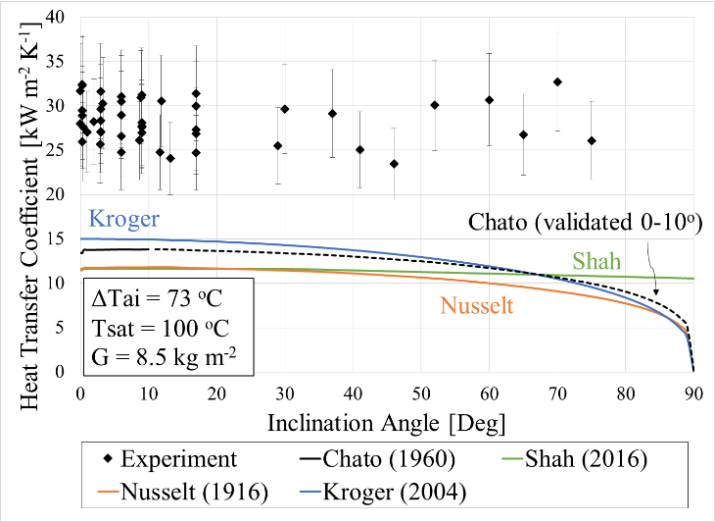

Figure 4.21: Steam-side heat transfer coefficient as a function of inclination angle; comparison of correlations and experimental results

In Figure 4.21, experimental results for $\bar{h}_s$ are compared to four published correlations. Chato's [47] and Kroger's [69] are for stratified condensation, with Kroger's correlation developed specifically for flattened-tube ACCs, although without experimental validation, to my best knowledge. Chato's correlation is experimentally validated in round tubes only for limited inclination angles (0-10°). Shah's [70] correlation is validated for a large range of experimental conditions, including low mass fluxes, large-diameter tubes, and high-aspect-ratio non-circular tubes. For the plotted correlations, a constant $\Delta T_w = 0.7\ °C$ and $\Delta T_{ai} = 73\ °C$ are assumed. At the horizontal inclination, the correlations vary $\pm 25\%$, with Kroger [69] providing the maximum prediction. The correlations under-predict the experimental results for all data points. Shah's correlation predicts only a slight decrease in HTC as inclination angle increases, which most closely matches the experimental results. However, the lack of decrease in HTC in the experiment is likely due to the presence of dropwise condensation, which is not addressed by Shah's correlation. Shah's correlation assumes that the continued influence of vapor shear will maintain the constant HTC.

4.4.5 Differences between Published Correlations and Experimental Results: Further Discussion

Figure 4.11, Figure 4.12 and Figure 4.14 compare experimental results for h_s to four published correlations. The correlations significantly under-predict the experimental results for

almost all data points. As these are the first published results for h_s in this geometry and condition in the open literature, this discrepancy warrants further discussion.

This under-prediction is caused by four main factors: the presence of mixed-mode dropwise and filmwise condensation in the experimental setup, the flattened-tube geometry, the variation in ΔT_w at each cross-section in the experimental tube, and the difficulty in determining accurate h_s in this experimental setup. These four factors can be explained. All correlations are for filmwise condensation, while dropwise condensation $\bar{h}_s$ is expected to be significantly higher. From the analysis of Rose [118], for the current experimental conditions, pure dropwise condensation $\bar{h}_s$ is expected to be 50 kW m^{-2} K^{-1}. This factor alone can explain the entire difference between experimental results and the correlations. Secondly, the flattened-tube shape may lead to a thinner average film thickness than for a round tube. As mentioned earlier, Fieg and Roetzel [59] found that this flattening of the tube increases condensation HTC. Thirdly, the correlations of Chato [47] and Shah [121] are for a constant ΔT_w in a round tube, and Kroger's [69] correlation assumes a constant U, which are not accurate assumptions for this condenser. Kroger's correlation is also not presented with supporting experimental data. Finally, the small ΔT_w and the necessity of using a calibrated model introduce the potential for additional error in the experimental determination of h_s. To mitigate these potential errors, the energy balances were found to be in good agreement (±3%), and the overall condenser HTC, *U*, was found to closely match the condenser model.

Despite these justifications for the results, it must be emphasized that this initial facility was built with a focus on the effect of inclination and evaluation of the real heat exchanger tube with inclusion of all real effects caused by air on the cooling side. This initial discussion of HTC is necessary, however, as a means of understanding and explaining the condenser physics, and it serves as a basis for further investigation of the steam-side HTC, which will be discussed in more detail in the upcoming chapters.

4.5 Conclusion

A model for the condenser thermal performance shows that h_s, h_a, and ΔT_w vary non-linearly in each condenser cross-section. This invalidates the assumptions of most conventional

condensation HTC correlations, and makes the experimental determination of h_s even more difficult.

Calibration of this thermal model with experimental results shows that h_s is constant along the condenser length within the limits of experimental uncertainty, which matches the prediction of Kroger [69] but disagrees with the prediction of other conventional correlations. The conventional correlations do predict the strong dependence of h_s on wall-steam temperature difference for stratified flow, which is seen in the experiment. All of the correlations significantly underpredict the magnitude of h_s found in this study. This underprediction is suspected to be the result of four factors: the presence of dropwise and filmwise condensation, the flattened-tube geometry, the variation in ΔT_w at each cross-section in the experimental tube, and high experimental uncertainty. In all, these factors require that both measurement and prediction of steam-side HTC be treated differently than for small, round tubes.

Finally, despite almost-constant h_s along the condenser, U has been shown to decrease along the condenser length. This decrease is caused by an increase in the depth of the condensate river at the tube bottom (air inlet). Therefore, the steam-side HTC significantly impacts heat transfer only at the tube bottom.

In considering the effects of tube inclination angle, the experimental results show a modest but clear increase in average overall heat transfer coefficient $\bar{U}$ for downwardly-inclined tubes versus the horizontal, with a maximum increase of 4% at 75^o inclination. This increase is primarily the result of improved drainage of condensate with increasing inclination angle. The majority of this performance improvement has been found to occur at low qualities.

In addition, steam-side HTC has been shown to be relatively constant with respect to inclination. This relationship holds at all qualities. The most widely-used correlations for inclined condensation under-predict steam-side HTC for this study.

Finally, this experiment has simulated the conditions of an operating condenser in many respects. However, one significant difference is the uniformity of the air flow rate in this study. In this experiment, in order to determine the effects of inclination angle on the steam condensation, air flow rate is maintained constant and uniform for all inclination angles. For an operating ACC, changing the condenser inclination angle will affect the airflow profile. Therefore, further study is required to examine the effect of inclination angle on airflow profile and the overall effect on condenser performance.

Chapter 5 Heat Transfer in a Full-Tube Air-Cooled Steam Condenser with 5.7 m Length

5.1 Introduction

This chapter describes the experimental determination of capacity and heat transfer coefficient in an air-cooled condenser tube of 5.7 m length at varied inclination angles. The work presented here is similar to that presented in Chapters 3-4. The most significant difference is the use of a full (uncut) tube, without a polycarbonate visualization window interfering with the flow of steam and condensate. In addition, the tube is significantly shorter – a geometry change suggested by industry partners. Finally, the parameter space is expanded to include lower condensing pressures.

5.2 Facility

5.2.1 Overview

The facility used in this study uses many of the components of the facility described in Chapter 3, although the tube is shorter. A schematic of the experimental setup is presented in Figure 5.1. The facility is designed to test a flattened-tube, air-cooled steam condenser, determining steam-side HTC, capacity and pressure drop along with adiabatic visualization. Steam condensation occurs in a continuous 5.7 m test section, encompassing the full range of thermodynamic qualities, from 1 to 0 (although void fraction only reaches a minimum of 0.9). On the air side, 48 120-mm axial fans are adjustable in 1 m lengths to allow for testing of varied air profiles. In the current experiment, uniform profiles of 2.5 m s^{-1} and 2.7 m s^{-1} velocities at the fin inlet are tested. Operating condensers have typical air-side velocities of 2-4 m s^{-1}. The condenser is mounted on a hinged truss, allowing for testing at various inclination angles.

The condenser tube in this experiment is 0.216 m in inner height and 0.016 m in inner width, as seen in Figure 5.2. The tube is steel with aluminum cladding on the outside, and the wavy fins are aluminum. The fins are 200 mm x 19 mm, with a thickness of 0.25 mm. The tube is installed in an air duct, with crossflowing air pulled upwards through the fins.

Air inlet and outlet temperatures are measured at 0.5 m intervals along the tube. Wall temperatures are measured at 1 m intervals along the tube, at the tube bottom, middle, and top. Steam temperature is measured at 2 m intervals along the tube. All temperatures are measured

using T-type thermocouples. Figure 5.3 is a diagram of the temperature locations. In total, these measurements allow for local determination of heat flux, heat transfer coefficient, and quality.

Air velocity is measured by a hand-held anemometer at the inlet of the fins. Air velocity has significant local variation due to fan and fin geometry, so velocity measurements have been made at 496 locations to ensure accurate average velocity. Steam mass flow rate is measured at the tube outlet by a MicroMotion CMF025 mass flow meter.

During condenser operation, steam passes through a pre-heating section and a choke valve to ensure that steam enters the test section in a slightly superheated state (<1 ^{o}C). Steam temperature and pressure are monitored at the condenser outlet to ensure that all non-condensables are removed during system start-up. During operation at vacuum pressures, the water-powered ejector loop at the condenser outlet is run intermittently to remove accumulated non-condensables. Condenser pressure is controlled via boiler power. The condensate pump is controlled to maintain a constant weight of condensate in the condensate receiver.

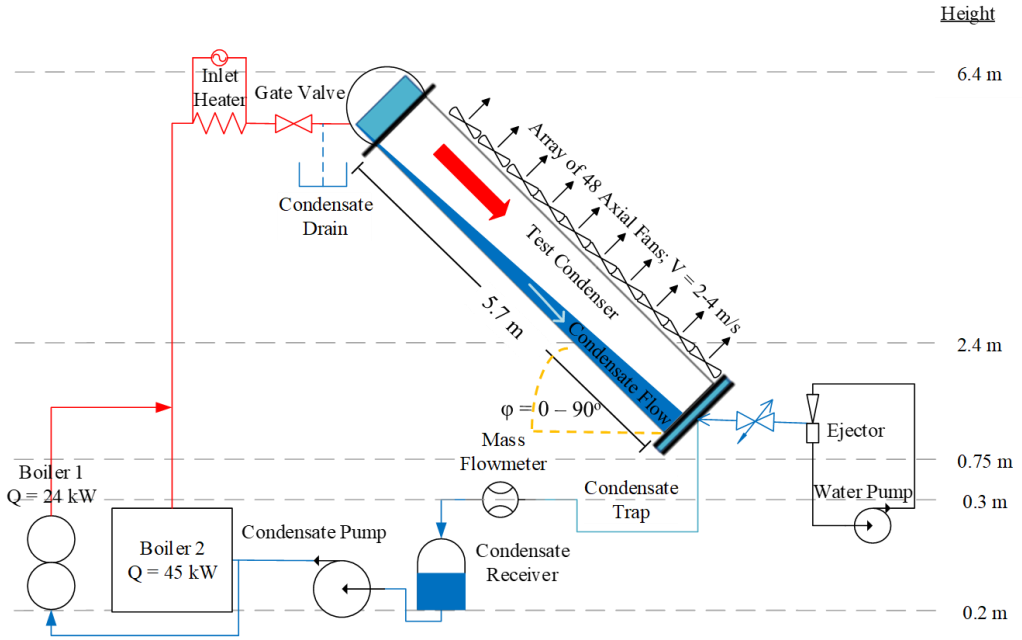

Figure 5.1: Diagram of the test facility

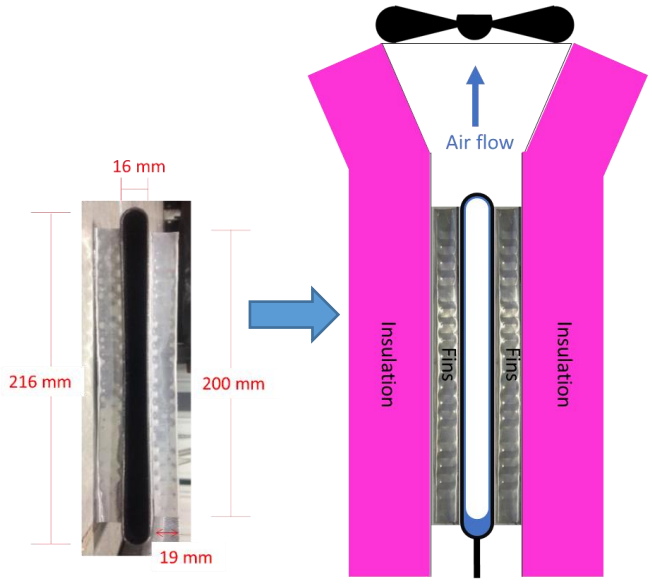

(a) (b)

Figure 5.2: Condenser tube cross-section view schematic: (a) tube stand-alone (b) tube installed in facility

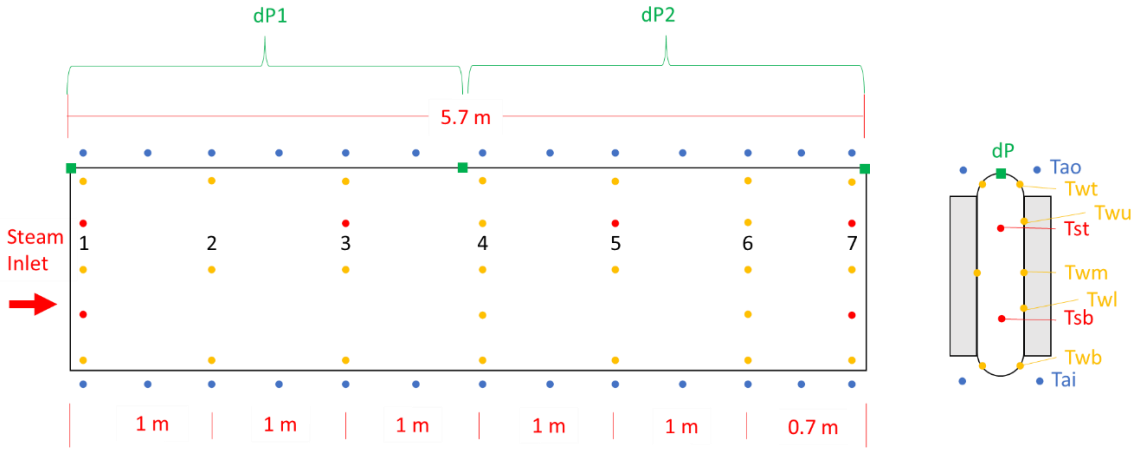

Figure 5.3: Location of temperature and pressure measurements along the tube

5.2.2 Test Conditions

The main variables in this study are condensation pressure, mass flux, and tube inclination. The range of test conditions can be seen in Table 5.1 below.

Table 5.1: Operating conditions and uncertainty

Parameter	Range	Uncert.
Steam mass flux [kg m^{-2} s^{-1}]	1.9 –4.0	± 10%
Steam mass flow rate [g s^{-1}]	7 – 13.6	± 0.1%
Condenser capacity [kW]	15.2 – 35.9	± 3%
Air velocity [m s^{-1}]	2.4 – 3.0	± 7%
Vapor inlet pressure [kPa]	70 – 106	± 0.1
Vapor inlet superheat [°C]	0.1 – 0.7	± 0.1
Air inlet temperature [°C]	31 – 50	± 0.1
Inclination angle [°]	0 – 49	± 0.1

5.3 Data Reduction

5.3.1 Capacity and Overall Heat Transfer Coefficient

Condenser capacity is determined on the air side and on the steam side. On the air side, the tube is divided into six 1 m-long sections, and in each section capacity is determined as:

$$Q_{a,j} = \mathrm{v}_{a,j}\rho_{a,j}H_a\Delta Z\left(c_{p,ao,j}T_{ao,j} - c_{p,ai,j}T_{ai,j}\right) + Q_{a,loss,j} \tag{5.1}$$

Qa,loss,j is the heat lost from the heated air to the atmosphere in the *j*-th measurement section. These values are negligible, representing about 0.1% of the air-side capacity.

$$Q_{a,loss,j} = UA_{a,loss}LMTD_{a,j} \tag{5.2}$$

Total air-side capacity is then the sum of the sectional capacities:

$$Q_a = \sum_{j=1}^{6} Q_{a,j} \tag{5.3}$$

On the steam side, capacity is determined for the entire tube from inlet and outlet enthalpies:

$$Q_s = \dot{m}_s\left(i_i - i_o\right) \tag{5.4}$$

Total system capacity is then taken as the uncertainty-weighted average of the air-side and steam-side capacities, as per the procedure recommended by Park, Liu and Jacobi [111]:

$$\bar{Q} = \frac{\left(\frac{1}{u_a{}^2}\right)Q_a + \left(\frac{1}{u_s{}^2}\right)Q_s}{\frac{1}{u_a{}^2} + \frac{1}{u_s{}^2}} \tag{5.5}$$

Air-side uncertainty is 7%, and steam-side uncertainty is 1.7%. The difference in air- and steam-side capacity measurements is less than 25% for all tests, with an average of 18% difference. This weighted capacity is then used to determine the overall condenser heat transfer coefficient, U, for a given steam-side area:

$$\overline{U} = \frac{\overline{Q}}{A_a \times LMTD} \tag{5.6}$$

$$LMTD = \frac{\left(T_s - T_{ai}\right) - \left(T_s - T_{ao}\right)}{\ln\left(\frac{T_s - T_{ai}}{T_s - T_{ao}}\right)} \tag{5.7}$$

For each 1 m measurement section, n, condenser HTC, U_n, is calculated from the air-side capacity:

$$U_n = \frac{Q_{a,n}}{A_{a,n} \times LMTD_n} \tag{5.8}$$

U is not constant along the condenser, due to nonlinear variations in h_a and h_s along the tube height. The $\overline{U}$ determined in equation (5.6) is therefore an area- and temperature-difference-weighted average of *U* along the condenser. This $\overline{U}$ cannot be used to determine a mean steam-side HTC, $\overline{h_s}$, as explained in [75]. Instead, h_s must be determined locally and averaged arithmetically to determine $\overline{h_s}$.

5.3.2 Determination of Steam-Side Heat Transfer Coefficient

The determination of steam-side heat transfer coefficient for the 5.7 m full tube closely follows the procedure described in Section 4.2.2 for the 10.7 m half tube. There are two notable differences for the 5.7 m tube, however, Firstly, wall temperature is measured at up to five locations in every meter length of tube, instead of in only two in the previous tube. The wall thermocouples are installed at heights of X = [8 mm, 54 mm, 108 mm, 164 mm, 208 mm] from the tube bottom, and are named [T_{wb}, T_{wl}, T_{wm}, T_{wu}, T_{wt}], respectively. The additional wall temperature measurements improve the accuracy of modeling the wall temperature profile, especially at the tube bottom where the temperature gradient is high. This change decreases the uncertainty of the HTC determination.

The second change is to the measurement of the condensate river depth, t_c. For the full tube, visual access is only possible at the tube inlet and outlet. Therefore, the condensate depth at the intermediate points must be determined by model. An open-channel-flow model is used. This model will be described in detail in the upcoming Section 7.3, which describes the condenser thermo-hydraulic model. This model determines the shape of the condensate interface, as well as the condensate depth. The results of this model are verified by comparison to experimental measurements at the condenser inlet and output. Inputs to the model of condensate river depth include mass flux, tube inclination angle, and condensation pressure.

The rest of the model proceeds as described for the 10.7 m tube, following the scheme shown in Figure 5.4. The thermal model is run independently in each cross section. Here, h_s is the average HTC for each 1 m measurement section, n, and $h_{s,n,j}$ is the local HTC over 1 mm height x 1 m length of condenser. Each cross section is discretized into J steps of height $dX = 1$ *mm.*

Once the calculation for a given cross-section is complete, the wall temperature profile is compared to the measured wall temperatures, $T_{wb,}$ $T_{wl,}$ $T_{wm,}$ $T_{wu,}$ and T_{wt}. $h_{s,n}$ is then multiplied by a constant, C_1, in order to align the model and experimental wall temperatures. The model is then re-run, and wall temperatures re-checked, and the entire procedure is iterated until the modeled and experimental wall temperatures are equal.

$$\frac{abs(T_{w,\mathrm{mod}el} - T_{w,\exp})}{T_{w,\exp}} \times 100\% < 0.1\% \tag{5.9}$$

The final average steam-side HTC for each condenser cross section is then:

$$h_s = C_1 * h_{s,model} \tag{5.10}$$

The ratio C_1 (between experimental HTC and model HTC) ranges from 0.8-2.8 depending on experimental conditions.

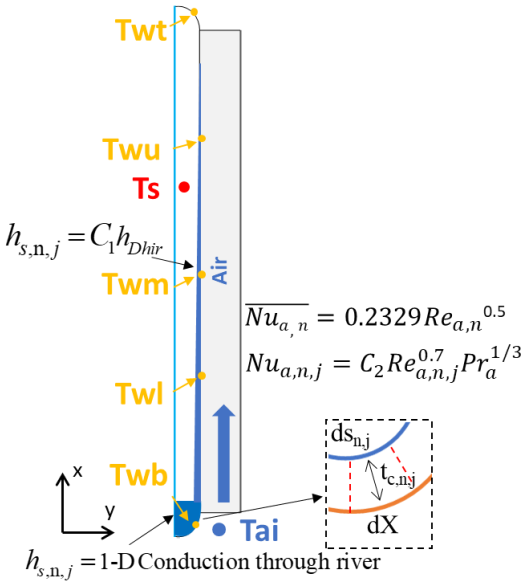

Figure 5.4: Scheme of the thermal model

The model is validated by comparing the total condenser capacity from the model and from the experiment. Figure 5.5 shows that all experimental capacities were predicted to within 10% by the model. Similar verifications were performed with capacity of each measurement section, and with condenser *U*, although they are not shown here.

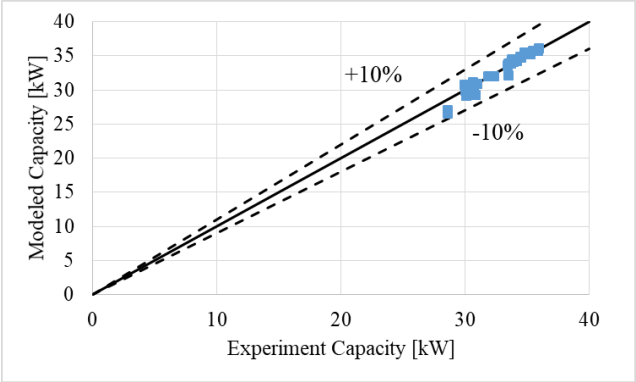

Figure 5.5: Modeled capacity compared to experiment capacity

An example of the modeled temperatures is presented in Figure 5.6. The non-linear temperature profile can be observed, as well as the correction required to match modeled and experimental wall temperatures. Wall temperature decreases significantly at the tube bottom due to cooler air and insulation provided by the stratified condensate layer.

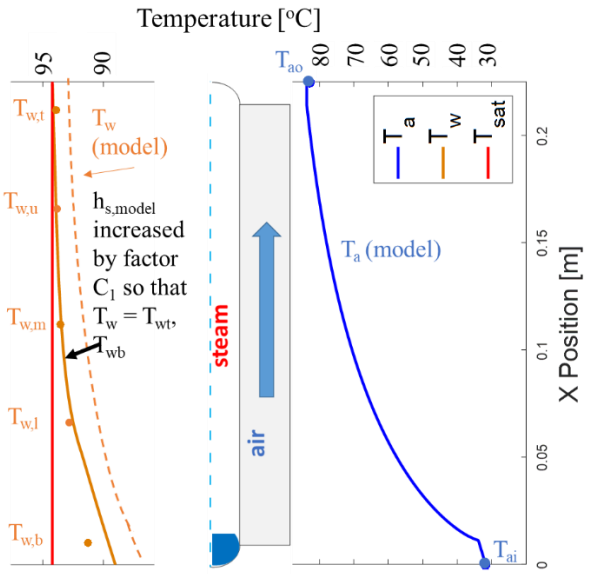

Figure 5.6: Modeled temperatures, T_w and T_a, and effect on T_w of adjusting $h_{s,model}$. Model values are presented by lines while dots are used for measured values

5.3.3 Uncertainty Analysis

Uncertainties in capacity and HTC are calculated using the method of Taylor and Kuyatt [114] on equations (5.5), (5.6) and (5.10). Uncertainties of measured quantities can be found in Table 5.1. For the method of local HTC, uncertainties in the modeled temperature profiles were also considered. The model itself was verified by comparing modeled and experimental capacities, along with *U* values. For the entire condenser, the uncertainty in steam-side capacity is 4% and the uncertainty in air-side capacity is 10%. The majority of the uncertainty in air-side capacity is from measurement of the air outlet temperature, T_{ao}, and of air velocity. To reduce this uncertainty, T_{ao} is measured at 29 locations and air velocity is measured at 645 locations. This yields an experimental uncertainty in capacity of 2.1% based on equation (5.5).

The error in *U* is 7% for the entire condenser, or 11% per section, n. The main cause of uncertainty is the uncertainty in measuring local air velocity and outlet temperature. The error in determining h_s is 20%. For h_s, the main causes of uncertainty are the small ΔT between wall and steam, and the uncertainty in the modeling assumptions – laminar film condensation, negligible convection in the condensate river at tube bottom, and the modeled air-side heat HTC profile.

5.4 Results and Discussion

5.4.1 Visualization

Experimentally-observed flow regimes are plotted on established in-tube condensation flow regime maps below for the lowest test pressure in this study – 70 kPa. Lower condenser pressures cause higher inlet vapor velocity, which increases the likelihood of wavy or annular flow in the tube. However, the below figures show that even at this lowest pressure, stratified flow is expected for almost the entire tube length. Figure 5.7 shows that the Xiao and Hrnjak [29] flow regime map accurately predicts annular flow at the tube inlet and stratified flow at the tube outlet. This map predicts a stratified flow regime for over 98% of the condenser length, with the exception of very short annular and wavy sections near the condenser inlet. The large tube cross-section and low mass flux causes the predominance of stratified flow. It should be noted that this map was developed for condensation of refrigerants at higher mass fluxes than were encountered in this study. For inclined flow, the Crawford *et al.* [35] flow regime map is used (Figure 5.8). Once again, this map was not designed specifically for the current experimental conditions. It was developed using condensing R113 in round tubes. This map accurately predicts the stratified flow at the condenser outlet but fails to predict the annular flow observed at the condenser inlet.

Figure 5.9 shows a picture of the stratified flow at the condenser outlet for a tube inclined at 3^o downwards. The flow is stratified. At the outlet, the vapor is nearly quiescent, so no waves are observed on the surface of the condensate. Figure 5.10 shows pictures of annular flow at the condenser inlet at two different condensing pressures – 80 kPa and 100 kPa. The tube is inclined at 2^o. Even at the inlet, droplets can be seen to collect on the tube wall and fall in a downward direction under the force of gravity. However, there has not been sufficient condenser length to collect a stratified layer on the tube bottom. Therefore, the liquid is fairly evenly distributed around the tube walls, and the flow regime is annular. In this case, the annular flow is a result of axial position, instead of shear force being dominant over the gravitational force. Identical flow regimes are observed for both condensing pressures.

The depth of this stratified layer was also measured in order to determine void fraction. Figure 5.11 shows void fraction at the tube inlet and outlet for three different tube inclinations. It can be seen that void fraction is very high (>95%) even at the condenser outlet. Therefore,

flooding never occurs in the condenser tube. It can also be seen that void fraction increases slightly as tube inclination increases.

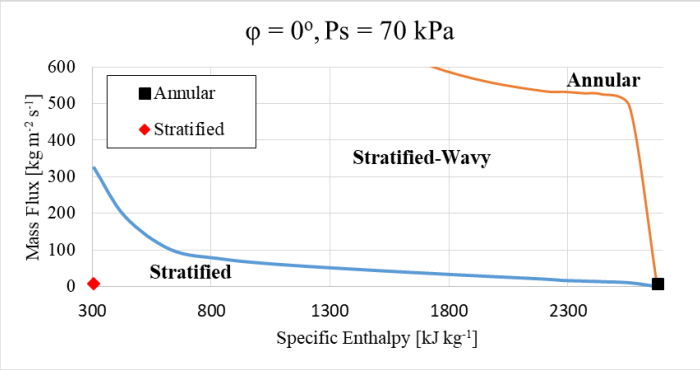

Figure 5.7: Observed flow regimes on the Xiao-Hrnjak [29] flow regime map for horizontal inclination and Ps = 70 kPa. Adiabatic visualization sections are located at the tube inlet and outlet.

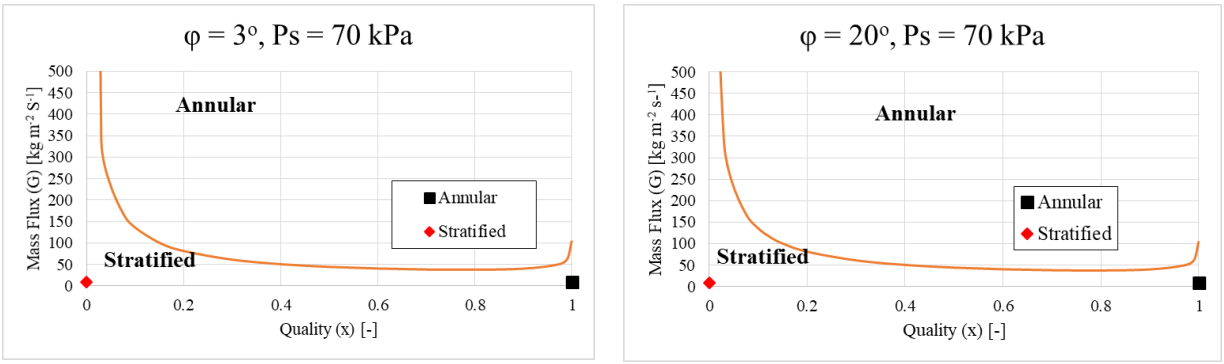

Figure 5.8: Crawford *et al.* [35] flow regime map for experimental conditions with Ps = 70 kPa plotted along with observed flow regimes at tube inlet and outlet. The annular-stratified transition is independent of inclination in the Crawford *et al.* [35] map.

Figure 5.9: Stratified Flow at outlet for 3° inclination; Ps = 70 kPa

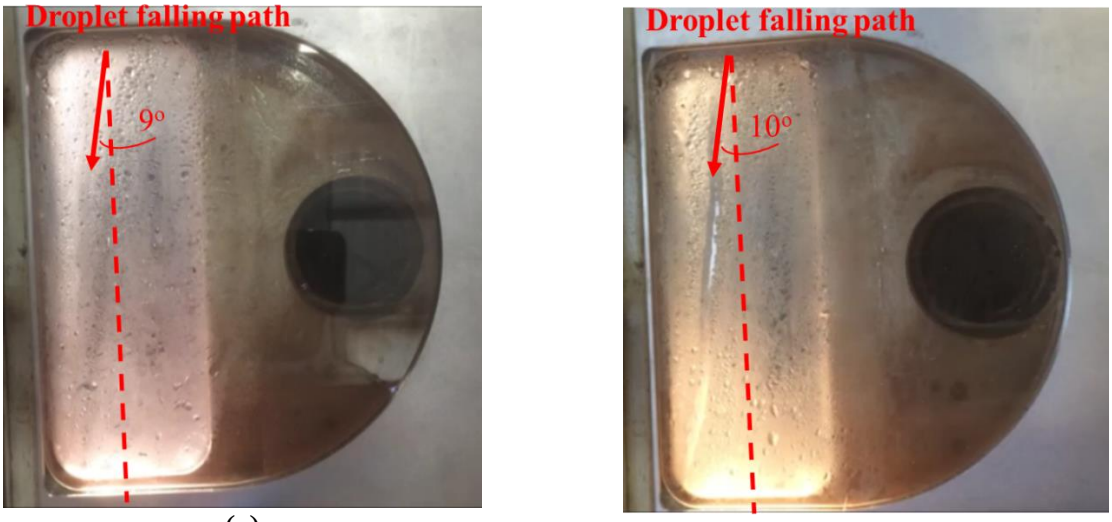

(a) (b)

Figure 5.10: Annular flow at inlet of condenser tube inclined at 2°. (a) P_s = 108 kPa, G = 3.7 kg m^{-2} s^{-1}; (b) P_s = 80 kPa, G = 2.8 kg m^{-2} s^{-1};

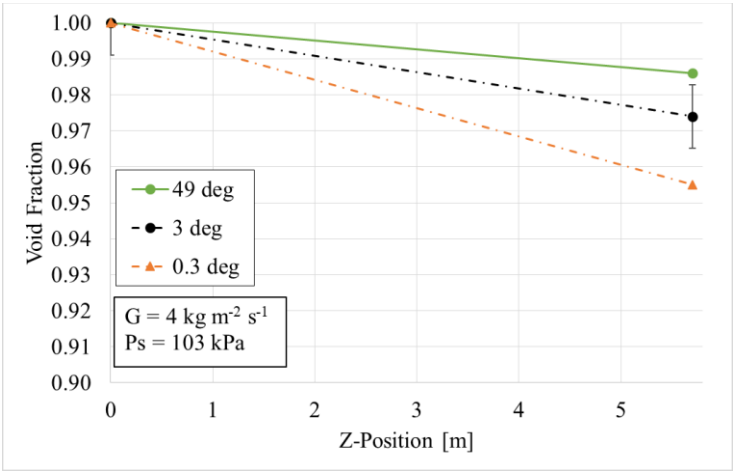

Figure 5.11: Void fraction at tube inlet and outlet for three tube inclinations

5.4.2 Steam-Side Heat Transfer Coefficient along the Condenser

Heat transfer coefficient along the condenser, h_s, is constant for the first four meters of the condenser, before decreasing by 15% over the last 1.7 m of condenser length. Figure 5.12 shows that the experimental results exceed the HTC predicted by the correlations with the exception of the Shah [121] correlation at the inlet, which over-predicts by 33%, and the Kroger [69] correlation, which over-predicts at all points by an average of 18%. It is interesting to note that the h_s predicted by the correlations varies by up 330% at the shown conditions.

The relatively-constant HTC demonstrates that quality and vapor velocity do not affect the steam-side performance significantly. As a result of the stratified flow and large condenser

cross section, the majority of the condenser is unaffected by changes in quality. In addition, the vapor velocity is also low – around 6 m s^{-1} at condenser inlet for the plotted condition – so vapor shear is negligible for much of the condensation process. At the tube outlet, an increase in depth of the stratified condensate layer causes the slight decrease in h_s.

The HTC is found to be lower than that in the 10.7 m tube. The main cause is the higher wall-steam temperature difference in the 5.7 m tube. This leads to higher heat flux, and may reduce the instances of dropwise condensation. Increased heat flux can lead to flooding of droplets on the surface, which creates a transition from dropwise to filmwise condensation [118]. The plotted correlations all assume pure filmwise condensation.

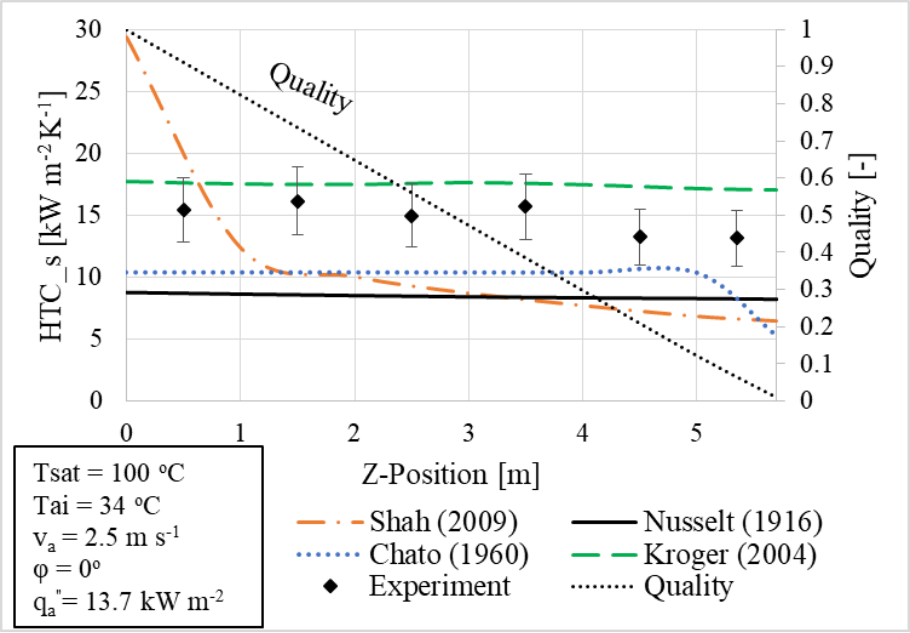

Figure 5.12: h_s measured from wall-steam temperature difference from condenser inlet to outlet at horizontal position (0° inclination)

Figure 5.13 shows that h_s is strongly a function of wall-steam temperature difference for small ΔT_w (< 2 °C), as in the correlations of Chato [47] and Nusselt [3]. At low temperature differences the condensate film thickness is low, which reduces the resistance to heat transfer. At higher ΔT_w, the dependence on temperature difference is reduced.

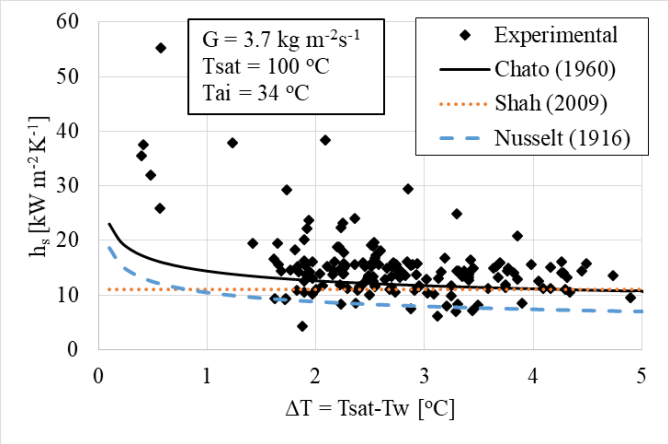

Figure 5.13: Experimental results and correlations plotted against $\Delta T_w = T_{sat} - T_w$

Figure 5.14 compares experimental results for h_s against ΔTai. The Kroger [69] correlation predicts that h_s is a function of ΔTai, as opposed to the other correlations, which formulate h_s as a function of ΔTw. Despite the uncertainty in the data, a linear regression for h_s predicted by ΔTai shows a significant relationship between the two variables, at the 99% confidence level. As ΔTai increases, h_s decreases, due to an increase in heat flux, which causes an increase in condensate film thickness. The Kroger correlation over-predicts the experimental data.

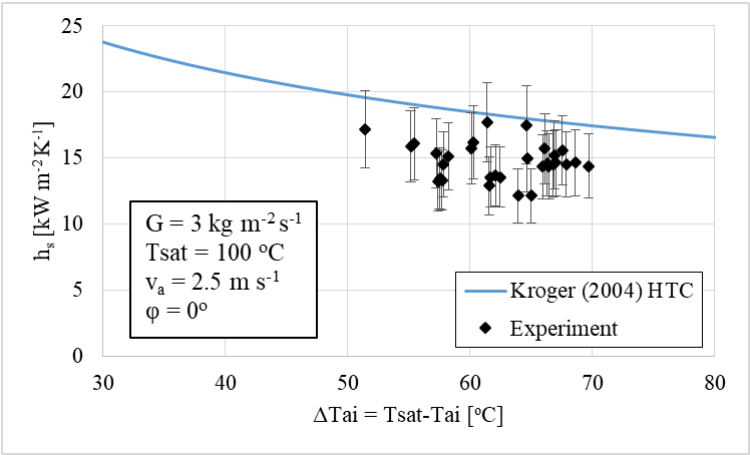

Figure 5.14: h_s vs. ΔTai, experimental results compared to Kroger correlation

Figure 5.15 shows that h_s increases as saturation temperature increases. This phenomenon has two main drivers. As temperature increases, liquid kinematic viscosity decreases, which causes the condensate film thickness on the vertical wall to decrease. The thinner film reduces the heat transfer resistance, causing an increase in h_s. Also, as temperature increases, thermal

conductivity of the liquid increases, which decreases the thermal resistance of the condensate film.

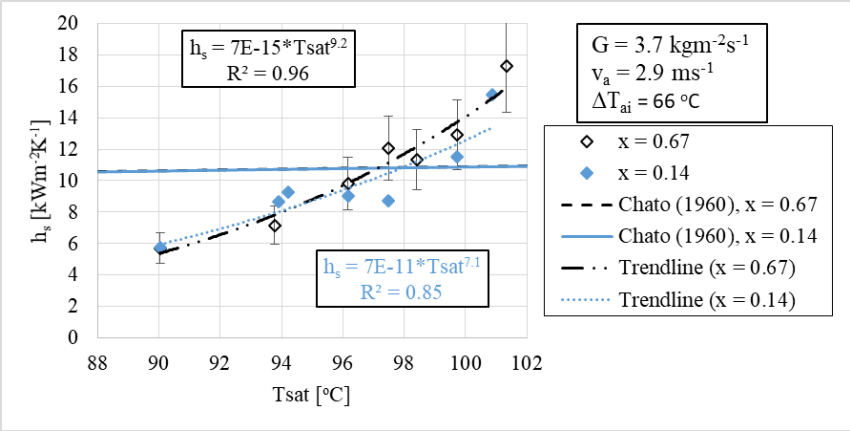

Figure 5.15: HTC vs. condensation temperature at two different qualities; HTC decreases as condensation temperature decreases. This matches the trend of the correlation ([47]) although the slope of the experimental data is significantly steeper

Despite the minimal variation in h_s along the condenser, the overall condenser HTC does decrease, as seen in Figure 5.16. Condenser U decreases due to an increase in depth of the condensate river at the tube bottom. As shown in Chapter 4, the tube bottom is the most important region for heat transfer, due to the large air-steam temperature difference and the high air-side HTC in this region. The steam side is the largest heat transfer resistance in this region. Therefore, the decrease in local h_s from the thicker condensate layer at the tube bottom has a large effect on condenser performance. Figure 5.16 also shows that as inclination angle increases, this decrease is less pronounced. The steeper inclination angle improves the drainage of condensate, which improves the heat transfer performance. This effect is less pronounced than was found previously in the longer, 10.7 m tube because the shorter tube contains less condensate. The longer tube was affected by condensate build-up predominantly in the last 5 m, which has been removed in the 5.7 m tube in the current study.

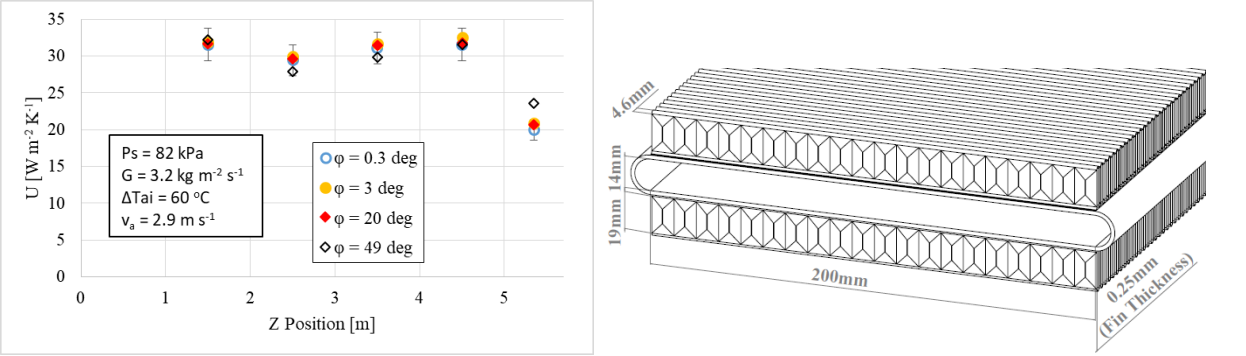

Figure 5.16: U (overall HTC, based on air-side area) along the condenser length at four different inclination angles; Air-side geometry depicted above for design reference; Current facility has 40 m^2 air-side area

5.5 Conclusion

Stratified flow has been observed at the tube outlet for all test conditions, with annular flow at the tube inlet. This result matches the prediction of the Xiao and Hrnjak [29] flow regime map for horizontal tubes, but in comparison with the Crawford [35] map for inclined tubes, the experimental results disagree with the map's prediction at the tube inlet.

Condensation HTC is determined by a combination of experiment and model. Calibration of this thermal model with experimental results shows that h_s is constant for the majority of the condenser length, with a slight decrease at the condenser outlet. The results fall between the predictions of Kroger [69] and Chato [47]. The experimental HTC is also lower than that found in previous experiments in a 10.7 m tube. This is caused by the greater wall-steam temperature difference in the current study. It is suspected that the higher temperature difference has reduced the instances of dropwise condensation in the current condenser. The strong dependence of h_s on wall-steam temperature difference is seen in the experiment, as the correlations predict for stratified flow. In addition, h_s is found to increase as saturation temperature increases.

Finally, despite almost-constant h_s along the condenser, U, has been shown to decrease at the condenser outlet. This decrease is caused by an increase in the depth of the condensate river at the tube bottom (air inlet). The steam-side HTC significantly impacts heat transfer only at the tube bottom.

Chapter 6 Pressure Drop in Inclined Air-Cooled Steam Condensers

6.1 Introduction

This chapter takes a brief step away from heat transfer to discuss the steam-side pressure drop in the condenser. In most heat transfer applications, gains in heat transfer coefficient are offset by an increase in pressure drop, and vice-versa, as explained by the Chilton-Colburn analogy [122]. Therefore, it is imperative to include a discussion of pressure drop when analyzing the heat transfer performance of a condenser. In a power-plant condenser, increasing pressure drop decreases the amount of power that can be generated by the turbine. This has a direct negative impact on the power-plant's bottom line. Therefore, pressure drop is also a crucial design parameter for power plant condensers.

Pressure drop was measured in both experimental facilities – the 10.7 m half tube and the 5.7 m full tube. The analysis of the pressure drop in the 10.7 m tube was led by Yu Kang, and his excellent paper [119] describing this work is borrowed from extensively here.

The pressure drop determination and analysis are much more straightforward than for the heat transfer coefficient. However, this makes it no less difficult to determine experimentally, as the small values of pressure drop and fluctuations in the steam generation process create significant uncertainty. The final results, as well as discussion of the method and uncertainty, can be found below.

6.2 Method: 10.7 m Tube

6.2.1 Instrumentation and Procedure

Gauge pressure is measured at the condenser inlet and outlet with differential pressure sensors. Pressure drop is also measured in five 2.14 m sections. All the pressure sensors are calibrated within 1% accuracy against a standard manometer after being mounted onto the system. The gauge pressure sensors have ranges of 7.47 kPa. The full ranges of the five differential pressure sensors are selected to be 497.7 Pa, 248.84 Pa, 248.84 Pa, 124.42 Pa, and 87.097 Pa, respectively for dP1 (steam inlet) to dP5 (steam outlet). The sensors are mounted on freely-rotating axles to allow them to hang vertically under the influence of gravity when the condenser is lifted to different inclination angles. Due to the condensation temperature being higher than the atmospheric temperature, steam vapor occasionally collects in the hoses leading

to the pressure gauges. To mitigate this effect, clear drains were installed in the pressure lines, and they are carefully monitored during data acquisition to ensure that no liquid remains trapped in them. Atmospheric pressure is measured locally with a mercury barometer.

Pressure drop is measured concurrently with heat transfer. During the measurement process, pressure drop fluctuates significantly due to churning flow in the boilers. The effect of these fluctuations is minimized by recording pressure drop over a sufficient length of time (> 10 minutes) to make the standard error of the pressure drop measurements negligible in comparison with the calibration and instrument error.

6.2.2 Data Reduction

Pressure drop is determined by two methods. The pressure drop of the individual 2.14 m sections is summed to find pressure drop along the entire tube length shown by equation (6.1):

$$\Delta P_{tot,sum,\text{half-tube}} = \Delta P_1 + \Delta P_2 + \Delta P_3 + \Delta P_4 + \Delta P_5 \tag{6.1}$$

As a second method, the difference between inlet and outlet gauge pressure is found by equation (6.2). This method is only valid for positive gauge pressures. For negative gauge pressures, the range of the sensors is too large to provide an accurate measurement of the small pressure drop.

$$\Delta P_{tot,\text{diff},\text{half-tube}} = P_i - P_o \tag{6.2}$$

The two methods are combined by equation (6.3) using the method of Park *et al.* [111] in order to reduce uncertainty:

$$\Delta P_{tot,half-tube} = \frac{\left(\frac{1}{u_{sum}{}^2}\right)\Delta P_{total,sum} + \left(\frac{1}{u_{diff}{}^2}\right)\Delta P_{tot,diff}}{\frac{1}{u_{sum}{}^2} + \frac{1}{u_{diff}{}^2}} \tag{6.3}$$

Once obtained, the total pressure drop can be into three components: the gravitational, momentum and frictional pressure drops:

$$\Delta P_{tot} = \Delta P_{gr} + \Delta P_{m} + \Delta P_{fr,half-tube} \tag{6.4}$$

As explained by Taitel and Dukler [38], for stratified flow, the pressure drop between the vapor and liquid phases will be equal. Therefore, in calculating the components of the total pressure drop, it is possible to consider the pressure drop in the vapor phase, only. The gravitational pressure drop is then the hydrostatic pressure in the vapor phase:

$$\Delta P_{gr} = \rho_g g L \sin(\varphi) \tag{6.5}$$

The gravitational pressure drop will be negative for a downwardly-inclined tube, indicating an increase in pressure along the tube length. In condensation, momentum pressure drop also increases the pressure. It is the result of the deceleration of the vapor flow, and is calculated by:

$$\Delta P_{m} = \frac{1}{2}\left[\left(\rho_g v_g^2\right)_o - \left(\rho_g v_g^2\right)_i\right] \tag{6.6}$$

Only condensate exits the tube, so the outlet vapor velocity is zero. In the experiment, mass flow rate of condensate is measured directly. The inlet quality and void fraction are approximately equal to one, so the inlet vapor velocity can be determined as:

$$\mathrm{v}_{g,\mathrm{i}} = \frac{\dot{m}_s}{\rho_g A_{\mathrm{cs}}} \tag{6.7}$$

Frictional pressure drop is then determined by subtracting the momentum and gravitational pressure drops from the measured total pressure drop.

Total mass flux is also determined from the measured condensate mass flow rate:

$$G = \frac{\dot{m}_s}{A_{cs}} \tag{6.8}$$

Inlet vapor Reynolds number is then determined from the mass flux and fluid properties:

$$\mathrm{Re}_{gi} = \frac{G D_h}{\mu_g} \tag{6.9}$$

Due to the stratified flow throughout the tube length (Chapter 3), and the constant heat flux leading to linear variation in vapor velocity (Chapter 4), a model for single-phase pressure

drop in the vapor can be assumed, and the pressure drop can be discretized along the length to determine an interfacial friction factor:

$$f_{half-tube} = \frac{2\Delta P_{fr} D_h}{\Delta Z v_g^2 \rho_g} \tag{6.10}$$

Surface roughness can then be determined by fitting Churchill's model [123] for friction factor to the experimental results for friction factor at various Reynolds numbers.

$$f = 8\left[\left(\frac{8}{\mathrm{Re}_g}\right)^{12} + \frac{1}{\left(B_1 + B_2\right)^{1.5}}\right]^{1/12} \tag{6.11}$$

$$B_1 = \left[-2.457 \ln\left(\left(\frac{7}{\mathrm{Re}_g}\right)^{0.9} + \frac{0.27\varepsilon}{D_h}\right)\right]^{16} \tag{6.12}$$

$$B_2 = \left(\frac{37530}{\mathrm{Re}_g}\right)^{16} \tag{6.13}$$

This friction factor and surface roughness are only applicable to the half-tube in this particular facility that has a polycarbonate window at the tube center-line. The effects of this polycarbonate must be removed in order to make a conclusion about the pressure drop in a full tube. Therefore, Kang *et al.* [119] devised a procedure to remove the effects of the shear force along the polycarbonate, and to determine interfacial friction factor on the liquid-vapor interface on the diabatic steel surface. Independent tests were run with nitrogen vapor to characterize the polycarbonate and steel surfaces. The model was then verified using nitrogen vapor in the condenser half-tube. Weighting factors were then assigned to the shear stress along each surface in the half tube – steel and polycarbonate:

$$f_{half-tube,1phase} = \omega_{stl} f_{stl} + \omega_{PC} f_{PC} \tag{6.14}$$

These weighting factors were determined with nitrogen vapor tests in the half tube, and they were nearly identical to the perimeter ratios of steel and polycarbonate. Once these quantities were known, the interfacial friction factor between steam vapor and the liquid condensing on the steel surface could be determined from the two-phase measurement of half-tube friction factor:

$$f_{half-tube,2\,phase} = \omega_{stl} f_i + \omega_{PC} f_{PC} \tag{6.15}$$

In this way, the interfacial roughness between condensate and steam vapor along the diabatic steel surface could be obtained.

Assuming the same vapor velocity profile in a full tube as in the half tube, the frictional pressure drop in a full tube could then be predicted from the half-tube results:

$$\Delta P_{fr,\,full-tube} = \frac{f_i \Delta Z \mathrm{v}_g^2 \rho_g}{2 D_{h,\,full-tube}} \tag{6.16}$$

More complete details on this process and validation are available in Kang *et al.* [119].

6.2.3 Uncertainty

There are three main causes of uncertainty of the pressure drop measurement: uncertainty of the pressure sensors, calibration uncertainty, and uncertainty caused by fluctuations in the system pressure. The published sensor uncertainty is 0.2% of the sensor range. Therefore, the differential pressure uncertainty is a maximum of 1 Pa for dP1 and a minimum of 0.17 Pa for dP5. Uncertainty of positive gauge pressure is 15 Pa, and uncertainty of negative gauge pressure is 248 Pa. The calibration uncertainty is 1%, which is five times greater than the sensor uncertainties. Additional uncertainty is added by the boiling process. The generation of steam is unsteady, so the condenser pressure undergoes significant variation with time. Taking the standard error of the measurements at the 95% confidence level, and combining with the instrument uncertainty, the measurement uncertainty of pressure drop over the full tube length is 5%. Additional uncertainty is then added by the model to convert from frictional pressure drop in the half tube to frictional pressure drop in the full tube. Final uncertainty of frictional pressure drop is 10%.

Uncertainty of the interfacial roughness depends on the uncertainty of the friction factor, as well as the uncertainty of fitting Churchill's model to the results. The uncertainty of the interfacial roughness is 20%.

6.3 Method: 5.7 m Tube

6.3.1 Instrumentation and Procedure

Pressure is measured at the condenser inlet, outlet, and halfway along the condenser length, as shown in Figure 5.3. Gauge pressure is measured at the condenser inlet and outlet with differential pressure sensors. Pressure drop is also measured in two 2.85 m sections along the condenser length. This provides two independent measurements of pressure drop along the tube length. Positive gauge pressure is measured by sensors with a maximum range of 7.47 kPa. When gauge pressure is negative, a sensor with a range of 124 kPa is used. The sectional pressure drops are measured by sensors with ranges of 498 Pa for positive pressure drop and 249 Pa for negative pressure drop. Pressure drop is occasionally negative due to pressure gain from deceleration and from decrease in elevation. The pressure sensors are mounted on axles to allow them to hang freely under the influence of gravity when the condenser is lifted to different inclination angles. Due to the condensation temperature being higher than the atmospheric temperature, steam vapor occasionally collects in the hoses leading to the pressure gauges. To mitigate this effect, clear drains were installed in the pressure lines, and they are carefully monitored during data acquisition to ensure that no liquid remains trapped in them. Atmospheric pressure is measured locally with a barometer.

Pressure drop is measured concurrently with heat transfer. During the measurement process, pressure drop fluctuates significantly due to the churning flow in the boilers. To minimize the effect of these fluctuations, pressure drop is recorded over a sufficient length of time (> 10 minutes) for standard error of the pressure drop measurements to be negligible in comparison with the calibration and instrument error.

6.3.2 Data Reduction

The data reduction for the 5.7 m tube is simpler than that for the 10.7 m tube, because the full-tube pressure drop is measured directly. The conversion process from half-tube to full-tube results in Equations (6.14) and (6.16) is not necessary. Otherwise, the data reduction is the same as explained in Section 6.2.2, with the exception of a reduced number of differential-pressure measurement sections in the 5.7 m tube. The pressure drop by summation is of just the two individual 2.85 m sections (equation (6.17)):

$$\Delta P_{total,sum} = \Delta P_1 + \Delta P_2 \tag{6.17}$$

All further data reductions proceeds as in equations (6.2)-(6.10) above.

6.3.3 Uncertainty

There are two main causes of uncertainty of the pressure drop measurement: uncertainty of the pressure sensors and uncertainty caused by fluctuations in the system pressure. The published sensor uncertainty is 0.2% of the sensor range. Therefore, the instrument uncertainty is 1 Pa when measuring positive pressure drop, and 0.5 Pa when measuring a negative pressure drop. However, significant uncertainty is added by the boiling process. The generation of steam is unsteady, so the condenser pressure undergoes significant variation with time. Taking the standard error of the measurements at the 95% confidence level, and combining with the instrument uncertainty, the final uncertainty of pressure drop over the full tube length is 10 Pa.

Uncertainty of the interfacial roughness depends on the uncertainty of the friction factor, as well as the uncertainty of fitting Churchill's model to the results. The uncertainty of the interfacial roughness is 20%.

6.4 Results and Discussion

6.4.1 Pressure Drop along the Tube

For the 10.7 m tube, with five pressure drop measurement sections, local interfacial roughness can be determined along the tube length. Figure 6.1 shows that the interfacial roughness close to the tube inlet – where the vapor flow is fully turbulent – is about 0.3 mm. This roughness increases in the second half of the tube. However, in this region, the vapor flow is in transition from turbulent to laminar due to the deceleration of the vapor, so the uncertainty of the model for interfacial roughness is much higher. In the fully-laminar region, the friction factor is independent of the interfacial roughness, so the roughness cannot be determined from the experimental results. The transitional Reynolds number from turbulent to laminar flow for this high-aspect-ratio tube is approximately 2800 [124]. The vapor Reynolds number decreases to 2800 around Z = 7 m along the tube length. In addition, the measured pressure drop is lower when vapor Reynolds number is low, so the uncertainty of the measurement is higher. Therefore, the interfacial roughness at Z > 6 m is not a reliable measurement. In addition, no dependence of

interfacial roughness on inclination angle is found. This indicates that inclination does not affect surface waviness of the condensate.

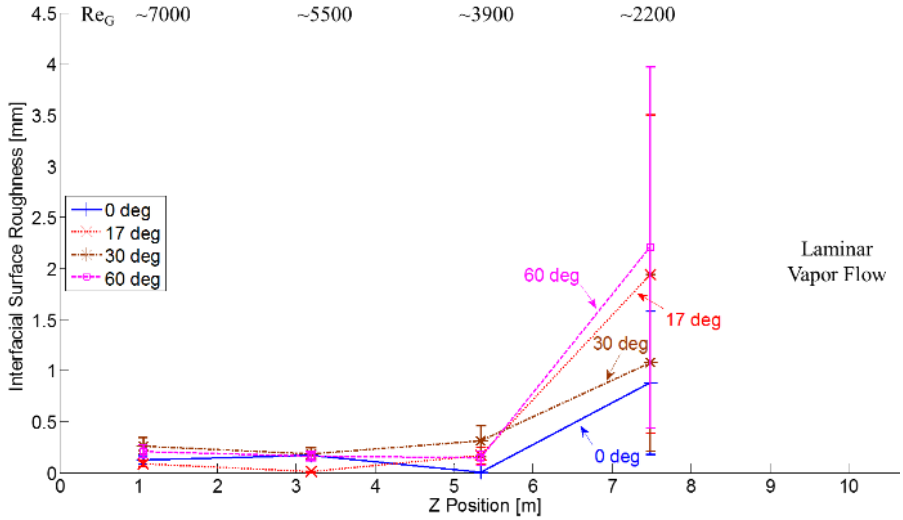

Figure 6.1: Interfacial surface roughness along the test tube at various inclination angles

For the 5.7 m tube, Figure 6.2 shows that interfacial friction factor decreases with Reynolds number in the laminar region, while remaining relatively constant in the turbulent region. This follows the behavior of relevant models for friction factor. However, the results exceed the predictions of the models. The interfacial friction factor determined by Kang *et al.* [119] for the 10.7 m tube most closely matches the friction factor in the 5.7 m tube. The higher friction factor may be the result of the low absolute pressure drop measured in the tube. As seen in Figure 6.1, the measured interfacial roughness was higher for low measured values of pressure drop. The experimental interfacial roughness can be determined for the 5.7 m tube by applying Churchill's model [123] to the results in Figure 6.2. The result of 0.94 mm is similar to the value of 0.85 mm found for the same rusted steel tube using nitrogen vapor [119].

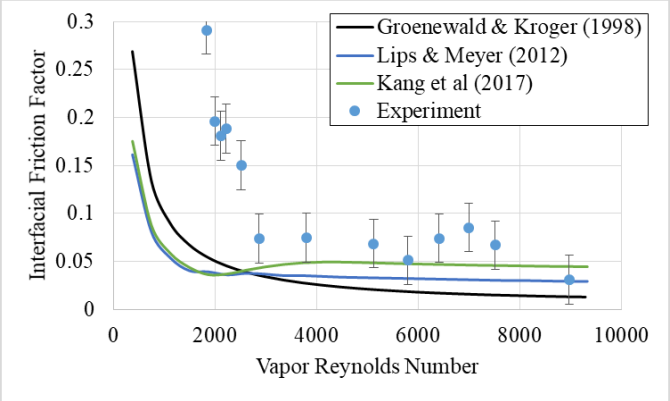

Figure 6.2: Experimental friction factor vs. vapor Reynolds number for the 5.7 m tube. The results exceed that of relevant models

Figure 6.3 and Figure 6.4 show that frictional pressure drop decreases along the tube length for both the 5.7 m and the 10.7 m tubes. This is the result of the decreased velocity as the two-phase density increases. Figure 6.3 also shows that the frictional pressure drop decreases as inclination increases. This is the result of increased void fraction, which decreases the vapor velocity. Figure 6.1 showed that inclination angle does not influence interfacial roughness, so the decrease in frictional pressure drop can only be a result of increased void fraction and decreased vapor velocity.

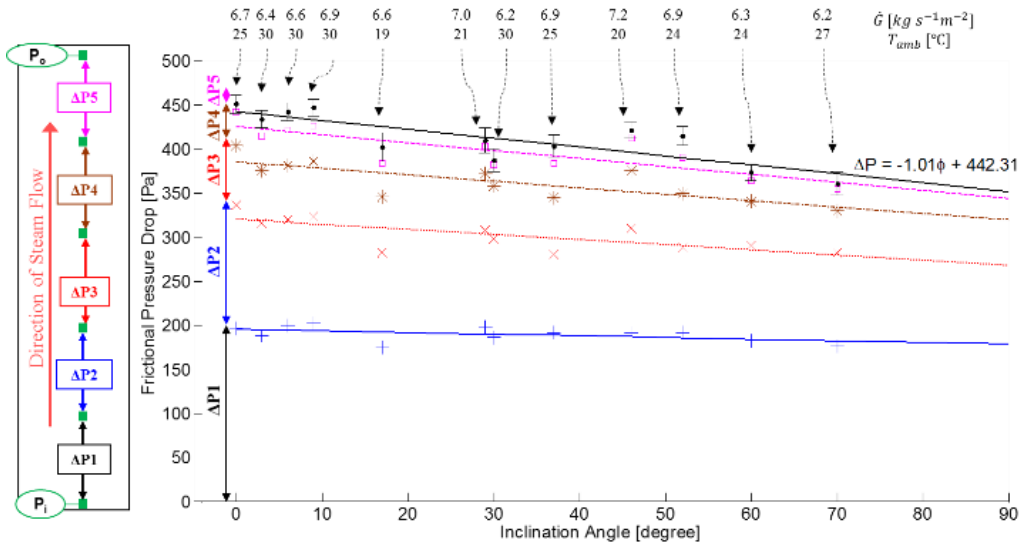

Figure 6.3: Frictional pressure drop along the 10.7 m tube at different inclination angles

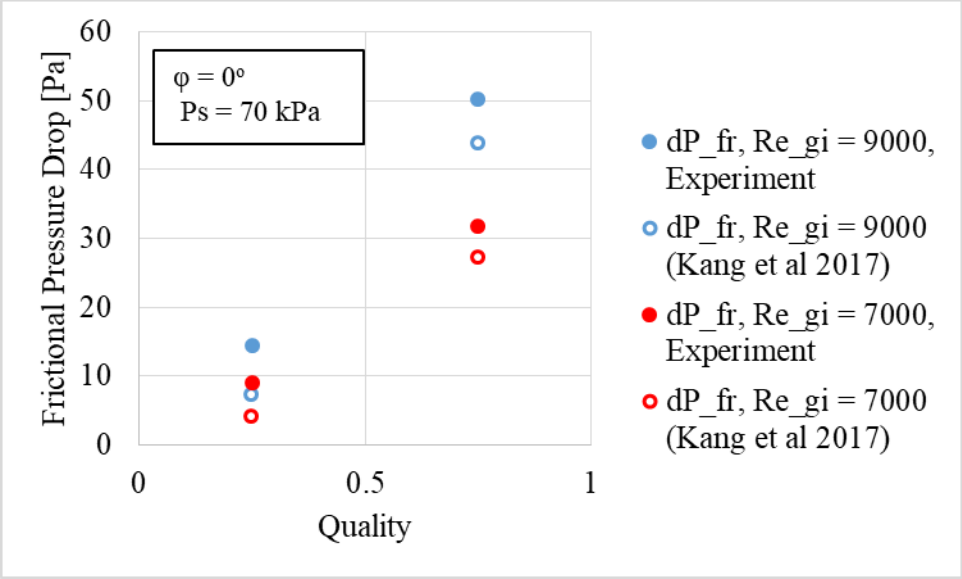

Figure 6.4: Frictional pressure drop vs. vapor quality in the 5.7 m tube

6.4.2 Overall Pressure Drop

For the 10.7 m tube, full-tube pressure drop results (converted from experimental measurements in the half tube) are shown in Figure 6.5. Total pressure drop can be seen to decrease as inclination increases. This is the result of increasing gravitational pressure recovery, as well as decreasing frictional pressure drop. The decreasing frictional pressure drop is the result of improved drainage of condensate due to gravity. With improved drainage of condensate, the void fraction increases, so the cross-sectional area for vapor flow is greater. This decreases the vapor velocity and decreases the frictional pressure drop.

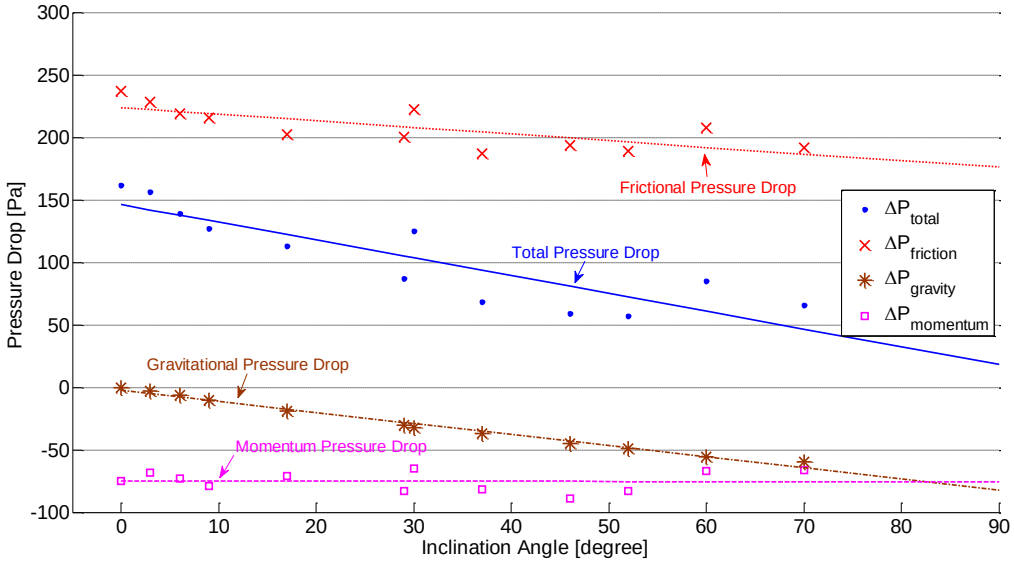

Figure 6.5: Full tube results for total pressure drop and components of pressure drop for the 10.7 m tube. These values have been converted from the half-tube measurements according to the procedure in Section 6.3.2

Figure 6.6 shows similar results for the 5.7 m tube: the total pressure drop decreases as tube inclination increases. This is a result of increased gravitational pressure recovery and a decrease in frictional pressure drop with increasing inclination. This agrees with the result in the 10.7 m tube that frictional pressure drop can decrease with increasing inclination due to improved condensate drainage.

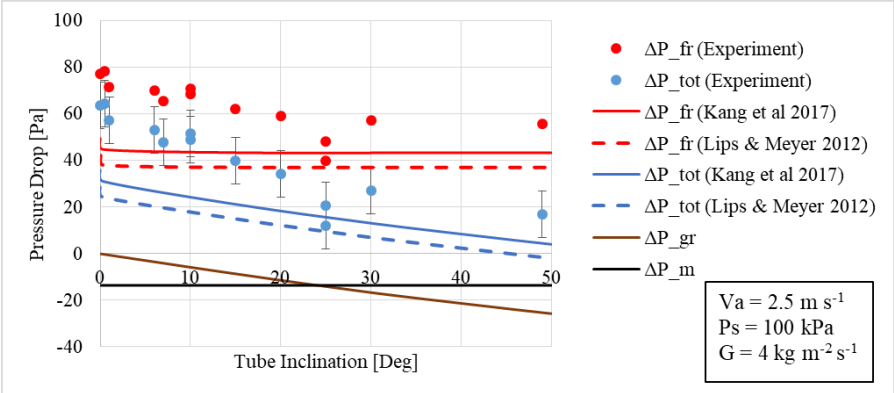

Figure 6.6: Total pressure drop vs. tube inclination angle, with experimental results compared to the models of Lips and Meyer [71] and Kang, Davies III, Hrnjak and Jacobi [119]

For the 5.7 m tube, frictional pressure drop in the tube is compared to the models of Lips and Meyer [71], Groenewald and Kröger [88] and Kang *et al.* [119] in Figure 6.7. Churchill's [123] model for frictional pressure drop is also shown, using the experimental surface roughness of 0.94 mm. Frictional pressure drop is very small in magnitude, so there is significant

experimental error. However, the experimental results exceed the predictions of all three models, with closest agreement to the models of Lips and Meyer [71] and Kang *et al.* [119]. Despite this under-prediction, the experimental results follow the trend of all three models in increasing frictional pressure drop as inlet vapor Reynolds number increases. This is the result of the increased vapor velocity increasing interfacial shear stress. Figure 6.8 shows the momentum and frictional components of pressure drop. These results are for a horizontal tube, so the gravitational pressure recovery is zero. The increase in overall pressure drop with inlet vapor Reynolds number is shown to be due to an increase in frictional pressure drop, which is partially offset by an increase in the momentum pressure recovery. As with frictional pressure drop, the experimental data follows the trend of the model, but exceeds the result predicted by the model. Figure 6.9 shows a very similar trend for the higher condensing pressure of 100 kPa. It can also be seen that frictional pressure drop is lower for a given Reynolds number at the higher condensing pressure. At higher condensing pressure, the vapor viscosity is lower. Therefore, the vapor velocity is lower for a given inlet Reynolds number. The lower vapor velocity yields a lower frictional pressure drop. This effect of condensation pressure agrees with the prediction of the models.

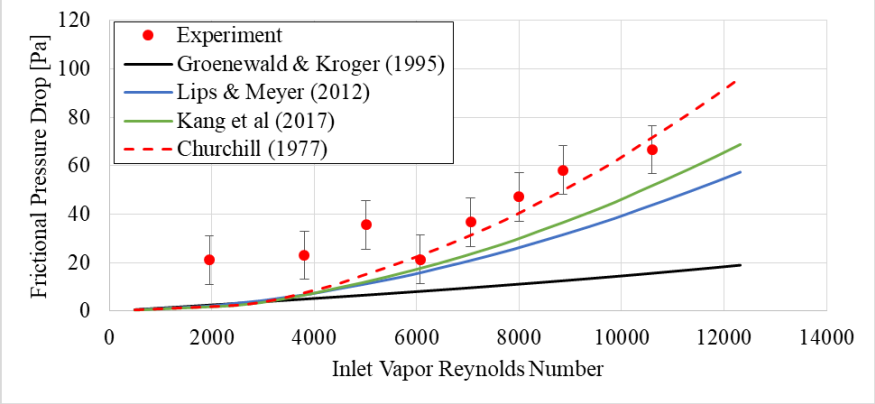

Figure 6.7: Experimental frictional pressure drop compared to the models of Kang, Davies III, Hrnjak and Jacobi [119], Groenewald and Kröger [88], Lips and Meyer [71] for a horizontally-inclined tube. The model of Churchill (1977) uses the roughness derived in the current experiment of 0.94 mm

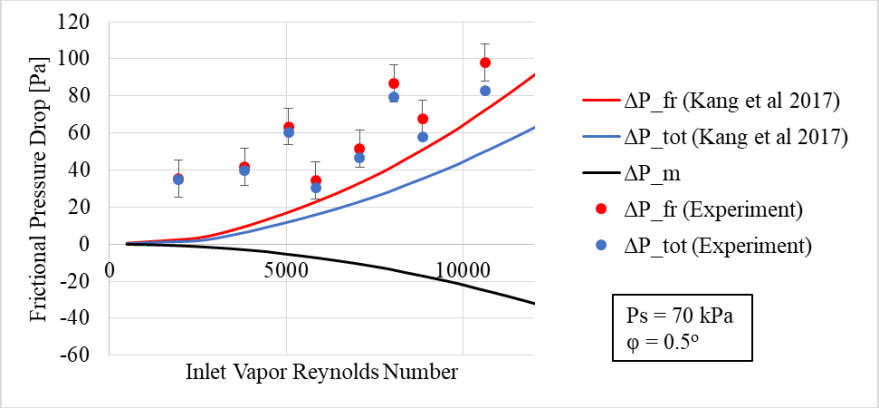

Figure 6.8: Pressure drop vs. mass flux, with experimental results compared to the frictional pressure drop model of Kang, Davies III, Hrnjak and Jacobi [119] for Ps = 70 kPa

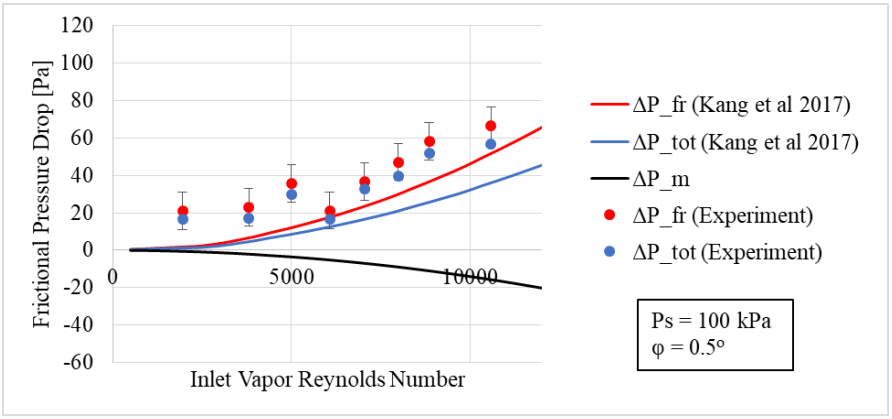

Figure 6.9: Pressure drop vs. mass flux, with experimental results compared to the frictional pressure drop model of Kang et al. (2017) for Ps = 100 kPa

6.5 Conclusions

Pressure drop has been measured during condensation of steam in 10.7 m and 5.7 m flattened-tube steam condensers. For both tubes, pressure drop has been found to decrease as inclination increases due to an increase in gravitational pressure recovery and decrease in frictional pressure drop. Frictional pressure drop has been found to decrease with increasing downward tube inclination due to an increase in void fraction. Interfacial surface roughness has been shown to be unaffected by inclination angle of the tube. Pressure drop has also been found to increase as inlet vapor Reynolds number increases, and as condensation pressure decreases. Total pressure drop is very low in magnitude, due to the low mass flux.

Interfacial roughness has been shown to be 0.3 mm in the 10.7 m tube when the vapor flow is turbulent. The interfacial roughness for Z > 6 m cannot be determined because the vapor flow transitions to laminar. In the 5.7 m tube, a higher interfacial roughness of 0.9 mm is found.

However, the measured pressure drop in the 5.7 m tube is much lower due to the shorter length and lower mass flux, so the uncertainty of this interfacial roughness is much higher than in the 10.7 m tube.

Chapter 7 Thermo-Hydraulic Model for Steam Condensation in a Flattened-Tube Air-Cooled Condenser

7.1 Introduction

This chapter describes the model for predicting void fraction, condensate river depth and velocity along the tube, and condenser capacity. Elements of this model are included in the determination of steam-side heat transfer coefficient in the air-cooled condenser, as discussed in Chapter 4. The results of the model are compared to the experimental results for condensate river depth and condenser capacity in both the 10.7 m and 5.7 m tubes.

7.2 Comparing Existing Condenser Models with Experimental Results

As described in Section 2.3, traditional void fraction models for in-tube condensation fail to capture the physics of a large, flattened-tube ACC. Traditional models, such as by Turner and Wallis [42], Zivi [120], Lockhart and Martinelli [23], Baroczy [125] and Thom [126] predict void fraction from quality, plus liquid and vapor densities and viscosities. They all neglect axial location in the tube, which is an important variable for an inclined tube where gravity is an important force. As the liquid moves along the tube, it accelerates due to gravity. This acceleration results in a decreasing cross-sectional area of the liquid in the tube, even with a constant liquid mass flux. Figure 7.1 also shows that all traditional void fraction correlations predict a sharp decrease in void fraction near the outlet of the condenser tube, which was not seen experimentally. In Figure 7.1, bulk quality is the same as the equivalent thermodynamic quality:

$$x_{bulk} = \frac{i - i_f}{i_{fg}} \tag{7.1}$$

Bulk quality neglects superheating of the vapor and subcooling of the liquid. Superficial quality is defined based on the onset and termination of condensation, to account for condensation during superheated or subcooled regions [29]:

$$x_{superficial} = \frac{i - i_{end\ of\ condensation}}{i_{onset\ of\ condensation} - i_{end\ of\ condensation}} \tag{7.2}$$

For this condenser, with subcooled liquid in the stratified condensate layer, superficial quality is better than bulk quality for calculating void fraction.

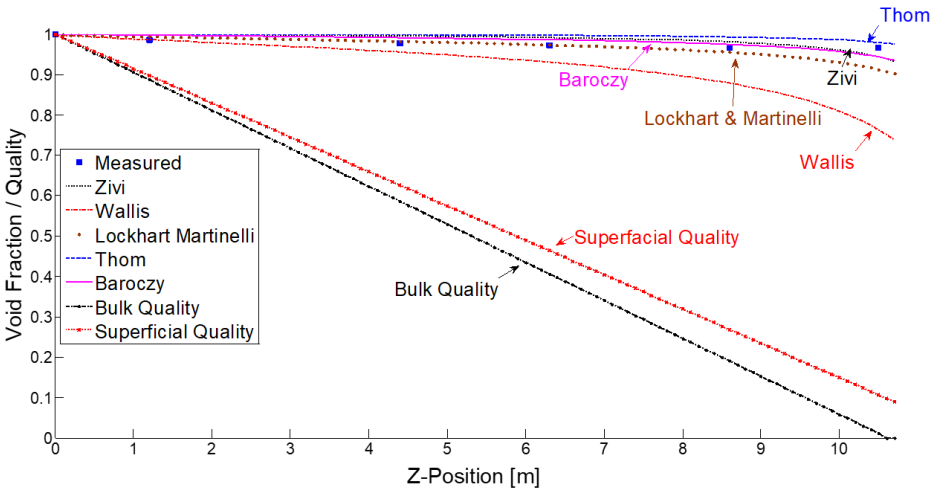

Figure 7.1: Measured void fraction compared to commonly-used void fraction correlations (reprinted from [119]).

In addition, as shown by Sparrow *et al.* [75], using an area-averaged HTC on the air and steam sides to calculate overall condenser HTC (U), is inaccurate under conditions of varying HTCs. To demonstrate this inadequacy, the results of a condenser model using area-averaged HTC on the air and steam sides is plotted in Figure 7.2 below, where

$$Q = UA \times LMTD \tag{7.3}$$

$$UA = \left[\frac{1}{\overline{h}_a \eta A_a} + \frac{t_w}{k_{st} A_s} + \frac{1}{\overline{h}_s A_s} \right]^{-1} \tag{7.4}$$

Steam-side HTC is determined from the model of Chato [47]. The area-averaged model over-predicts the condenser capacity by an average of 10%. This is outside the experimental uncertainty of 3%. To investigate statistically if this is an adequate condenser model, we can use the null hypothesis that equations (7.3) and (7.4) are an accurate model of condenser capacity. Taking the uncertainties of the correlations for air- and steam-side HTC, uncertainty of the model is 5%. Uncertainty of the experimental capacity is 1.7%. Given these uncertainties, the probability that this model is an accurate predictor (within 5%) of condenser performance is found to be less than 1%. For further comparison, the model of Kroger [69] is compared to the experimental results in Figure 7.3. This model overpredicts capacity by an average of 3%, with a maximum overprediction of 12%. Although this model is more accurate, it still shows a bias. Given the uncertainty of the model and experiment, the probability that this model is an accurate predictor (within 5%) of condenser performance is 1%.

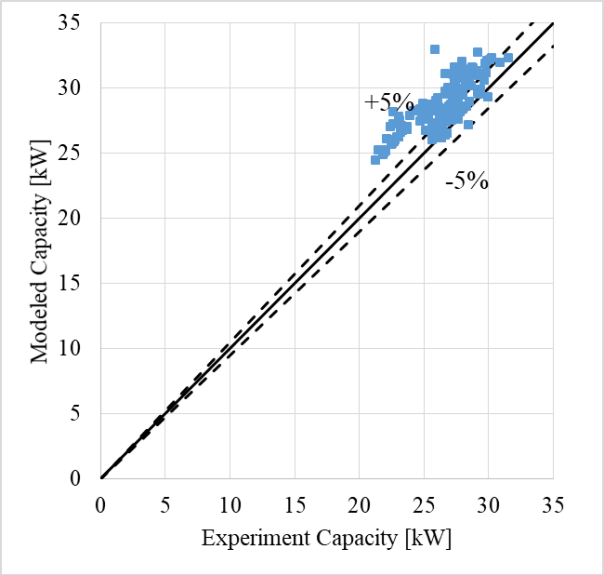

Figure 7.2: Experimental capacity compared to model using area-averaged HTC. The model with area-averaged HTC overpredicts the condenser capacity. Uncertainty of the experimental capacity is 3%.

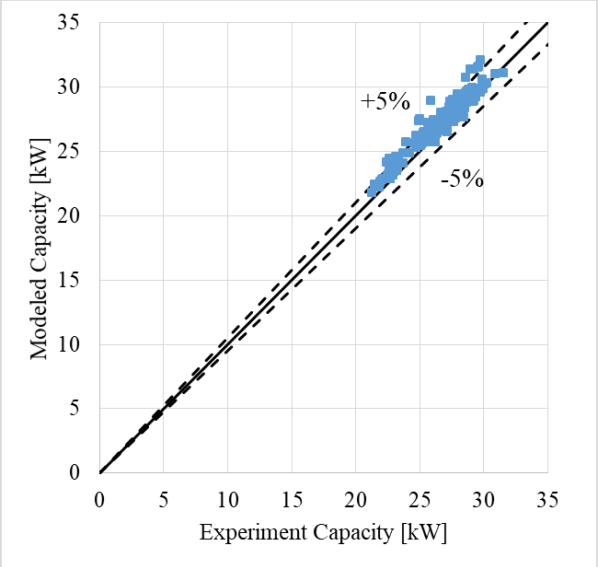

Figure 7.3: Experimental capacity compared to the model of Kroger [69]. The model overpredicts condenser capacity by an average of 3%. The experimental uncertainty is 3%.

7.3 Model of the Condensate River

The condenser model begins with a model of the condensate river. To accurately capture the physics of the flow, the axially-flowing condensate river is modeled as a spatially-varied open-channel flow. Due to the large cross-sectional area of the tube, the surface of the condensate river is unconstrained and is free to arrange itself based on the balance of gravitational, pressure, shear, and surface-tension forces. As discussed above, the flow has been found to be stratified flow for all experimental conditions.

To initiate the model, the flow must be characterized as sub- or super-critical. A subcritical flow is characterized by lower velocity and greater depth of the condensate river, and occurs at lower inclinations. The depth of subcritical flows is controlled by the downstream (outlet) conditions. Supercritical flows have greater velocity, and their depth is controlled by the upstream (inlet) conditions. The Froude number (equation (7.5)) is the criterion for determining criticality, with subcritical flows having Fr < 1 and supercritical flows having Fr > 1. This creates a potential difficulty in that the model will either begin at the upstream or the downstream end of the tube, depending on flow conditions.

At the condenser inlet, the condensate has not had time to collect at the tube bottom. Therefore, the condensate forms a falling film around the tube circumference. The initial depth of the condensate river is the thickness of this film at the at tube bottom, which can be predicted from Fieg and Roetzel's analysis for an inclined tube [59]. At the outlet of the experimental system, the condensate exits the tube via a free overfall (90^o pipe bend). At a free overfall, a subcritical flow (depth greater than critical) will decrease to its critical depth for a given tube inclination and flow rate. However, a supercritical flow will remain supercritical at a free overfall [44]. For the model, the river depth is initially assumed to be equal to the critical depth (Fr = 1) at the tube outlet. The river depth is then calculated for a short distance upstream. If the depth increases in the upstream direction, the flow is subcritical, and the calculation can continue in the upstream direction. If the depth decreases, then the flow is supercritical, and the calculation must begin from the tube inlet (supercritical flows are controlled by the upstream boundary condition).

In order to determine the critical depth at the tube outlet, the Froude number is set equal to one:

$$Fr_{critical} = \frac{\mathrm{v}_{f,critical}}{\sqrt{g d_{h,critical}}} = 1 \tag{7.5}$$

Re-arranging (7.5):

$$d_{h,critical} = \left(\frac{\dot{V}_f^{\,2}}{g W_{t,critical}^2} \right)^{1/3} \tag{7.6}$$

Hydraulic depth is defined as:

$$d_h = \frac{A_{f,cs}}{W_t} \tag{7.7}$$

$$v_f = \frac{\dot{V}_f}{A_{f,cs}} \tag{7.8}$$

The top width of the river, W_t, is defined as the width of the free surface at the top of the condensate river. For a semi-circular channel, this width is a function of the depth of the condensate. Therefore, the top width is initially assumed to be the maximum channel width, and equation (7.6) is solved iteratively.

The cross-sectional profile of the condensate surface is determined by a model similar to that used by Lips and Meyer [71], with the geometry adapted to match the condenser tube in this study. This portion of the model was described for the half tube in Section 4.2.2, so the full-tube boundary conditions are described here. For each river depth, the cross-sectional area, the top width, and the wetted perimeter of the river are calculated. For this river surface model, the receding contact angle of water on the rusted steel wall is assumed to be 0°. This was measured with a goniometer in independent testing. The cross-sectional profile (outlined in red) and a schematic of the discretization of this river are depicted in Figure 7.4.

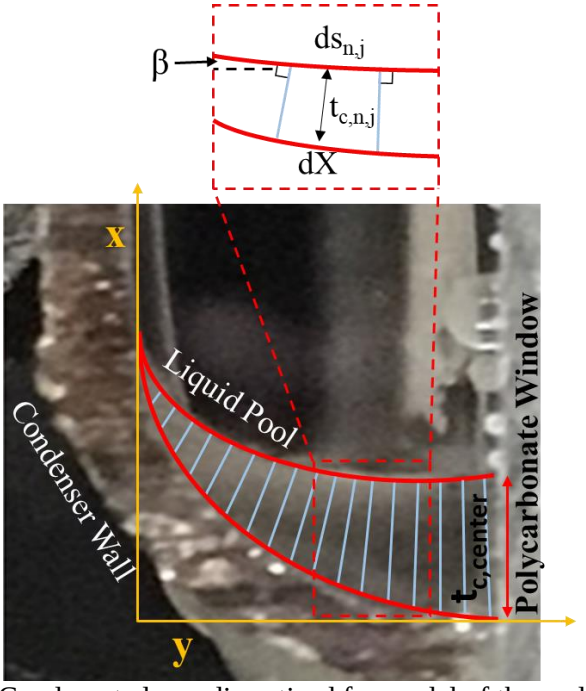

Figure 7.4: Condensate layer discretized for model of thermal conduction

For the model, the shape of the interface is controlled by gravitational and surface-tension forces only. The model proceeds by equating pressures. From the Young-Laplace equation describing the magnitude of the surface-tension force:

$$P_f(X) = P_g - \frac{\sigma}{r(X)} \tag{7.9}$$

Considering the effect of tube inclination, the gravitational force is:

$$P_f(X) = -\left(\rho_f - \rho_g\right) g(\cos\varphi) X + P_f\left(X = t_c\right) \tag{7.10}$$

Equating (7.9) and (7.10) and denoting the radius of curvature of the condensate surface at the tube centerline as r_{center}, yields:

$$\frac{\sigma}{r_{center}} - \frac{\sigma}{r(X)} = -\left(\rho_f - \rho_g\right) g\left(\cos\varphi\right) X \tag{7.11}$$

Equation (7.11) can be simplified to:

$$r(X) = \frac{1}{\frac{2X}{b^2} + \frac{1}{r_{center}}} \tag{7.12}$$

where b^2 is the capillary constant of the fluid:

$$b^2 = \frac{2\sigma}{\left(\rho_f - \rho_g\right) g \cos\varphi} \tag{7.13}$$

Geometry shows us that:

$$r(X) = \frac{dX}{(\sin\beta) d\beta} \tag{7.14}$$

Equating (7.12) and (7.14) yields:

$$\left(\frac{2X}{b^2} + \frac{1}{r_{center}}\right) dX = (\sin\beta) d\beta \tag{7.15}$$

Integrating equation (7.15) from the tube centerline ($\beta = 0 \; @ \; X = t_{c,center}$):

$$\left(\frac{X}{b}\right)^2 + \frac{X}{r_{center}} = 1 - \cos\beta + \left(\frac{t_{c,\text{center}}}{b}\right)^2 + \frac{t_{c,\text{center}}}{r_{center}} \tag{7.16}$$

The calculation is performed most easily by setting X = 0 m at the top of the condensate at the tube centerline ($t_{c,center}$). The surface profile can then be solved in an iterative scheme, beginning at the tube centerline. An initial radius of curvature, r_{center}, is assumed, and the initial parameters are:

$$Y_1 = W_{tube}/2; \; X_1 = 0 \text{ m}; \; \beta_1 = 0^o$$

The tube width is 16 mm for the full tube. The subsequent coordinates of the iteration are found as:

$$Y_{j+1} - Y_j = \left(\cos\beta_j\right) ds_j \tag{7.17}$$

$$X_{j+1} - X_j = \left(\sin\beta_j\right) ds_j \tag{7.18}$$

$$ds_j = r\left(X_j\right) d\beta_j \tag{7.19}$$

Subsequent values of β are then found using equation (7.16). The calculation proceeds until the condensate surface intersects the condenser wall. The boundary condition at the wall is a contact angle of 0^o ($\beta = 90^o$). An iterative process is used to satisfy this boundary condition, whereby r_{center} is varied until the condensate surface and the wall are tangent at the point of intersection. The bottom of the condenser wall is a circular arc that subtends an angle of 90^o for the half tube and 180^o for the full tube.

Once the shape of the river surface is determined at the outlet, the calculation proceeds upstream. The volumetric flow rate of condensate is assumed to increase linearly from condenser inlet to outlet, implying constant heat flux along the condenser length:

$$d\dot{V}_f = \frac{\dot{V}_{outlet}}{L / dZ} \tag{7.20}$$

Looking at a small length of the condenser, *dZ*, in Figure 7.5 the change in momentum along the river can be seen. Numerically, this is:

$$\Delta M_f = \rho_f \left(\dot{V}_f + d\dot{V}_f\right)\left(\mathrm{v}_f + d\mathrm{v}_f\right) - \rho_f \dot{V}_f \mathrm{v}_f \tag{7.21}$$

This can be equated with the sum of the axial forces on the river:

$$\Delta M_f = \sum F = F_{gravity} + F_{wall} + F_{pressure} + F_{vapor} \tag{7.22}$$

$F_{gravity}$ is the volumetric force due to gravity, F_{wall} is the shear force due to interfacial friction between the river and the condenser wall, $F_{pressure}$ is the sum of the hydrostatic forces on the condensate river from liquid in the adjacent sections of tube, *dZ*, and F_{vapor} is the shear force due to interfacial friction between the river and the vapor.

Assuming that $dA_{cs}dZ$ is small:

$$F_{gravity} \approx \rho_f g A_{f,cs} dZ \sin(\varphi) \tag{7.23}$$

$$F_{wall} = -\rho_f g A_{f,cs} f_w dZ \tag{7.24}$$

$$f_w = \frac{\dot{V}_f{}^2 n^2}{A_{f,cs}^2 R_h^{4/3}} \tag{7.25}$$

The *n* in equation (7.25) is Manning's roughness coefficient [127]:

$$n = \frac{KC_d^{1/2} R_h^{1/6}}{\sqrt{8g}} \tag{7.26}$$

This is related to the bulk drag coefficient, C_d, which resists the river flow. Here, $K = 1$ for SI units. Hydraulic radius is defined as:

$$R_h = \frac{A_{f,cs}}{p_{wetted}} \tag{7.27}$$

For the half-tube, the channel is made of two materials in parallel, (the steel condenser wall and the polycarbonate window), so Manning's roughness of the channel is a composite of Manning's roughness for the steel portion and for the polycarbonate portion. This composite roughness is calculated using the method of Einstein and Banks [128], which assumes that the total force resisting the flow is equal to the sum of the forces in the steel and polycarbonate sections:

$$n = \sqrt{\frac{p_{st} {n_{st}}^2 + p_{pc} {n_{pc}}^2}{p_{wetted}}} \tag{7.28}$$

For the full tube, the roughness of the steel tube is used directly. Bulk drag coefficient is calculated using Churchill's equation [123] for both the steel and the polycarbonate:

$$C_d = 8\left(\frac{\left(8/\mathrm{Re}_{dh}\right)^{1/12} + 1}{\left(B_1 + B_2\right)^{1.5}}\right)^{1/12} \tag{7.29}$$

$$B_1 = \left[-2.457 \log\left(\left(\frac{7}{\mathrm{Re}_{dh}}\right)^{0.9} + \frac{0.27\varepsilon}{R_h}\right)\right]^{16} \tag{7.30}$$

$$B_2 = \left(\frac{37530}{\mathrm{Re}_{dh}}\right)^{16} \tag{7.31}$$

$$\mathrm{Re}_{dh} = \frac{\rho_f \mathrm{v}_f d_h}{\mu_f} \tag{7.32}$$

The equivalent roughnesses, ε, of the steel and polycarbonate were found using pressure drop measurements of nitrogen vapor in separate steel and polycarbonate tubes [119]. The steel roughness was found to be 0.85 mm and the polycarbonate roughness was found to be 0 mm (i.e. smooth tube). The remaining forces are:

$$F_{pressure} = P_1 A_{f,cs} - P_2 A_{f,cs} = -\rho_f g A_{f,cs} dd_h \tag{7.33}$$

$$F_{vapor} = \tau_{in} s_{in} dZ \tag{7.34}$$

$$\tau_{in} = \frac{f_{in} \rho_g \left(\mathrm{v}_g - \mathrm{v}_f \right)^2}{2} \tag{7.35}$$

Interfacial friction factor, f_{in}, is calculated using Taitel and Dukler's [129] formula:

$$f_{in} = \begin{cases} \dfrac{16}{\mathrm{Re}_g} \, if \; \mathrm{Re}_g < 2000 \\ .046 \, \mathrm{Re}_g^{-0.2} \, if \; \mathrm{Re}_g \geq 2000 \end{cases} \tag{7.36}$$

$$\mathrm{Re}_g = \frac{\rho_g \mathrm{v}_g A_g}{\mu_g} \tag{7.37}$$

Equating the change in momentum (7.21) with these forces, and neglecting the $d\dot{V}dv$ term on the left, yields:

$$\rho_f \left(\dot{V}_f d\mathrm{v}_f + \mathrm{v}_f d\dot{V}_f \right) = -\rho_f g A_{f,cs} dd_h + \tau_{in} W_{in} dZ - \rho_f g A_{f,cs} f_w dZ + \rho_f g \sin(\varphi) A_{f,cs} dZ \tag{7.38}$$

Solving for the change in hydraulic depth yields:

$$dd_h = -\frac{1}{g} \left(\mathrm{v}_f d\mathrm{v}_f + \frac{\mathrm{v}_f}{A_{f,cs}} d\dot{V}_f \right) + \left(\frac{\tau_{in} s_{in}}{\rho_f g A_{f,cs}} - f_w + \sin(\varphi) \right) dZ \tag{7.39}$$

Further algebraic manipulation yields:

$$dd_h = -\frac{\mathrm{v}_f}{g} \left(\frac{2 A_{f,cs} d\dot{V}_f - \dot{V}_f dA_{f,cs} + dA_{f,cs} d\dot{V}_f}{A_{f,cs}^{\;2} + A_{f,cs} dA_{f,cs}} \right) + \left(\frac{\tau_{in} s_{in}}{\rho_f g A_{f,cs}} - f_w + \sin(\varphi) \right) dZ \tag{7.40}$$

Then, it is assumed that small incremental changes in $A_{f,cs}$ allows one to neglect $dA_{f,cs} d\dot{V}_f$ in the numerator and $A_{f,cs} dA_{f,cs}$ in the denominator (as suggested by Chow [44]). With some more algebra, and discretizing dd_h as Δd_h, this yields a final equation of:

$$\Delta d_h = -\frac{\dot{V}_{f,1} \left(\mathrm{v}_{f,1} + \mathrm{v}_{f,2} \right)}{g \left(\dot{V}_{f,1} + \dot{V}_{f,2} \right)} \left(\Delta \mathrm{v}_f + \frac{\mathrm{v}_{f,2} \Delta \dot{V}_f}{\dot{V}_{f,1}} \right) + \left(\frac{\tau_{in} s_{in}}{\rho_f g A_{f,cs}} - f_w + \sin(\varphi) \right) \Delta Z \tag{7.41}$$

Figure 7.5 shows a discretized section of the condensate river, with hydrostatic pressure force acting from adjacent sections of the river.

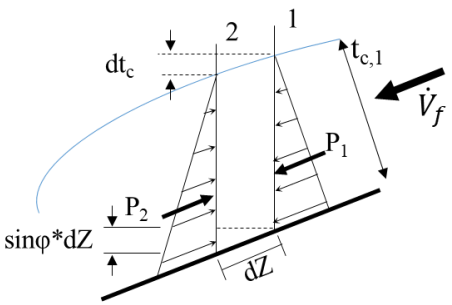

Figure 7.5: Differential step along the condenser length, showing change in river height

7.4 Thermal Model

For the thermal model, the steam side is divided into two sections: the stratified condensate river flowing axially, and the thin film falling down the condenser wall. In the condensate river, the heat transfer mechanism is approximated as one-dimensional conduction. In the falling film, HTC is predicted by the theory of Dhir and Lienhard [4].

Inputs to the model are the air inlet temperature (T_{ai}), air velocity (v_a), steam temperature (T_s), and river depth along the condenser, which is calculated from the river model described above. First, condenser capacity is estimated for the given input conditions, using a simple model such as equations (7.3) and (7.4) above. Using this capacity estimate, the river model is run. Then, the thermal model is run, taking this first iteration of river depth as an input. The capacity determined from the thermal model is compared to the initial capacity estimate. If the two values differ by greater than 0.1%, the river model is re-run, and the thermal model is then re-run with the new river depths. This iterative process is continued until the change in modeled capacity is less than 0.1%.

For the model in the 10.7 m tube, the condenser is divided along the length into 11 cross sections, denoted by subscript *n*. Each section is 1 m long, except for the last section, which is 0.7 m long. Outputs calculated for each 1 m section are T_w, T_{a,h_s}, h_a, U, and Q.

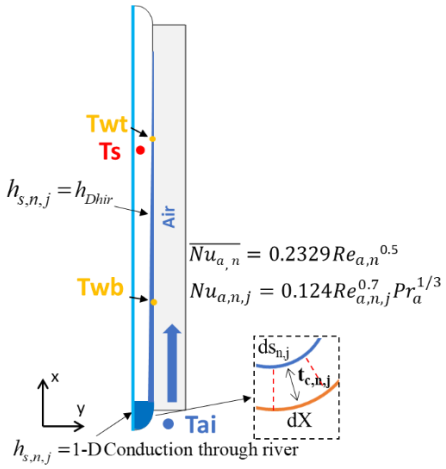

Figure 7.6: Scheme of the thermal model

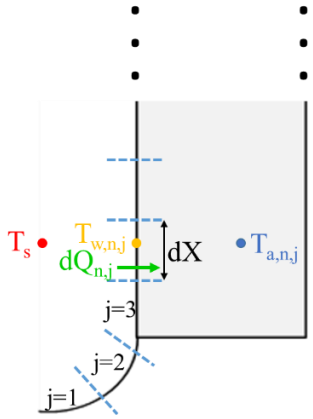

Figure 7.7: Diagram of model divisions along a condenser cross section, *n*; not to scale

The thermal model is run independently in each cross section. The scheme of the model is shown in Figure 7.6. Here, $\overline{h_s}$ is the area-averaged HTC for the entire condenser, h_s is the average HTC for each 1 m measurement section, and $h_{s,n,j}$ is the local HTC over a 1 mm height x 1 m length of condenser. The cross section is discretized into *J* steps of height $dX = 1\text{mm}$, as seen in Figure 7.7.

Beginning at the tube bottom, where air temperature, T_{ai}, is known, the air HTC is calculated. The profile for air-side HTC along the fin length is calculated from a CFD simulation in the current fin geometry. The simulation was performed on a 3-D domain over one set of fins (one fin pitch) using ANSYS Fluent [113] for laminar airflow at several of the experimental air velocities. A profile of steam-side HTC was applied as a boundary condition on the condenser wall to match that found experimentally. The simulation results were verified by comparing capacity with that found in the experiments, with error less than 9% for all simulations. Air-side HTC along the fin was extracted via equation (7.42):

$$h_{a,\mathrm{j},CFD} = \frac{Q_{a,\mathrm{j},CFD}}{\eta_{j,CFD}\left(T_{w,j,CFD} - T_{a,j,CFD}\right)} \tag{7.42}$$

The result is proportional to the Reynolds number along the fin length:

$$\mathrm{Nu}_{a,\mathrm{n,j}} \propto \mathrm{Re}_{\mathrm{a,n,j}}^{\ 0.7}\ \mathrm{Pr}_{a,\mathrm{n,j}}^{1/3} \tag{7.43}$$

$$\mathrm{Re}_{a,n,j} = \frac{\rho_a \mathrm{v}_{a,n} X_j}{\mu_a} \tag{7.44}$$

This profile is then calibrated to match the mean air-side HTC, h_a, for each cross section, as determined from an experimental correlation developed by Wilson plot for this particular condenser by Creative Thermal Solutions, Inc.:

$$\overline{\mathrm{Nu}_a} = 0.2329\,\mathrm{Re}_a^{0.5} \tag{7.45}$$

$$\mathrm{Re}_{a,\mathrm{n}} = \frac{\rho_a \mathrm{v}_{a,n} D_{h,\,fin}}{\mu_a} \tag{7.46}$$

$$D_{h,\,fin} = \frac{4A_{fin,cs}}{p_{fin}} = \frac{4(W_{fin} - t_{fin})(\mathrm{H}_{fin} - \mathrm{t}_{fin})}{2(W_{fin} - t_{fin} + \mathrm{H}_{fin} - \mathrm{t}_{fin})} \tag{7.47}$$

In developing this experimental correlation, an identical flattened-tube with identical fins as in the current experiment was tested. Water was run inside the tube, and experimental uncertainty of h_a was 5%.

$h_{s,n,j}$ is calculated by one-dimensional conduction through the condensate river by equation (7.48), as explained in detail in [71]:

$$h_{\mathrm{s,river,n,j}} = \frac{\left(dX - ds_j\right)k_f}{t_{c,\mathrm{n,j}}\,dX \ln\left(dX / ds_j\right)} \tag{7.48}$$

Local capacity is then found by equation (7.49):

$$dQ_{n,\,j} = dUA_{n,\,j}\left(T_s - T_{a,n,\,j}\right) \tag{7.49}$$

$$\frac{1}{dUA_{n,\,j}} = \frac{1}{h_{a,n,\,j}\eta_{n,\,j}A_{\mathrm{a},n}} + \frac{t_w}{k_w A_{s,n}} + \frac{1}{h_{s,n,\,j}A_{s,n}} \tag{7.50}$$

The three terms on the right-hand side of equation (7.50) represent the air, wall, and steam heat transfer resistances, respectively. The wall resistance is constant. From the local capacity, the wall temperature and subsequent air temperature can be calculated by equations (7.51) and (7.52):

$$T_{w,n,\,j} = T_{a,n,\,j} + dQ_{n,\,j}\left(\frac{1}{h_{a,n,\,j}A_{a,n}\eta_{n,\,j}}\right) \tag{7.51}$$

$$T_{a,n,\,j+1} = T_{a,n,\,j} + \frac{dQ_{n,\,j}}{C_{p,a,n,\,j}\dot{m}_{a,n}} \tag{7.52}$$

When the model reaches the condensing film region above the condensate river, steam-side HTC is determined from Dhir and Lienhard's [4] modification to Nusselt analysis [3] for

round-tube condensation. Wall temperature is necessary for calculating this HTC, so the wall temperature from the previous 1 mm section is used:

$$h_{s,n,j} = \left[\frac{i_{fg} g_{eff} \left(\rho_f - \rho_g\right) {k_f}^3}{4 \frac{X_j}{\cos\varphi} \left(T_s - T_{w,n,j-1}\right) \nu_f} \right]^{1/4} \tag{7.53}$$

where the effective acceleration due to gravity, g_{eff}, is due to the gravitational force in the vertical direction:

$$g_{eff} = g \cos\theta \tag{7.54}$$

To summarize, the profile of $h_{a,n,j}$ is determined by simulation, which is then scaled to match the average HTC determined from independent experiments. $h_{s,n,j}$ is determined in two distinct regimes – by conduction through the condensate river at the condenser bottom, and by natural convection higher along the condenser wall.

Overall, the model is calculated by stepping in 1 mm increments from tube bottom to top along the condenser wall (in the X-direction). Steam and air HTC, air and wall temperatures, and capacity are calculated at each increment. At the tube bottom, $h_{s,n,j}$ is determined from a 1-D conduction model through the condensate river (equation (7.48)). The shape of the condensate river is calculated using the model described in section 7.3. Above the condensate river, $h_{s,n,j}$ is modeled in the natural-convection film-condensation regime using equation (7.53).

7.5 River Model Results

7.5.1 Comparison with Experimental Results

Figure 7.8 shows the predicted river depth vs the measured depth along the condenser length for three different inclination angles. The model closely matches the experimental results. The efficacy of the model can be noted in the ability to predict the unusual profile of the river when the condenser is inclined at $\varphi = 0.3°$. Conventional void fraction correlations cannot predict this void fraction behavior (increase in void fraction near the condenser outlet) that is dependent on the tube outlet condition.

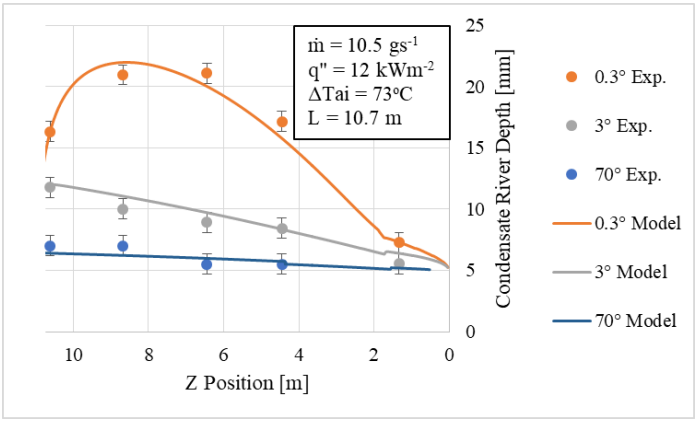

Figure 7.8: Modeled vs experimental depth of the condensate river along the 10.7 m length of the condenser for three different inclination angles

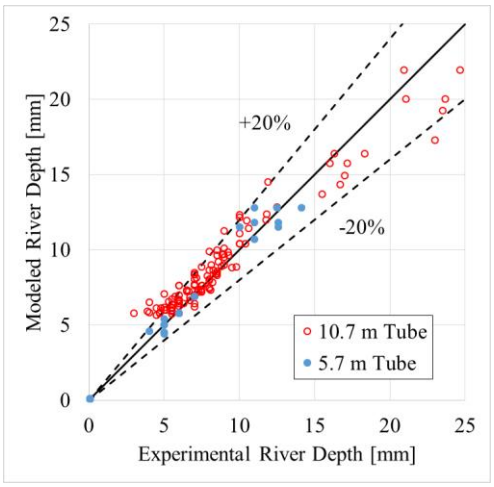

Figure 7.9: Comparison of modeled condensate river depth to experimental river depth for both tube lengths

Figure 7.9 compares modeled condensate river depth against the experimental data for both tube lengths. For the 10.7 m tube, the model predicts 79% of the data within 20%. The model tends to under-predict the experimental results at high river depths, and over-predict at low river depths. For the 5.7 m tube, the model predicts all experimental data to within 20%.

7.5.2 Forces on the Condensate River

From the model, the relative importance of the four forces (gravitational, hydrostatic pressure, vapor shear, wall friction) on the condensate flow can be determined. Figure 7.10 and Figure 7.11 show the relative strength of the forces for 10.7 m condenser tubes inclined at 0.3° and 3°, respectively. The condensate in the 0.3° tube is propelled primarily by vapor shear over the first 3 m of length. Over the final 6 m, gravity is the dominant force driving the liquid flow. Wall friction provides the force opposing liquid flow. For the tube with slightly higher inclination (3°), gravity is the primary force driving river flow for nearly the entire tube length. Only for the first 1 m of tube length does vapor shear play a significant role. Figure 7.11 also shows the effect of lowering condensation pressure. Lowering the condensation pressure to 10 kPa increases the vapor shear force. At 3° inclination, vapor shear is significant for the first half of the condenser length. However, when considering the entire condenser length, the average gravitational force is still larger than the average force from vapor shear.

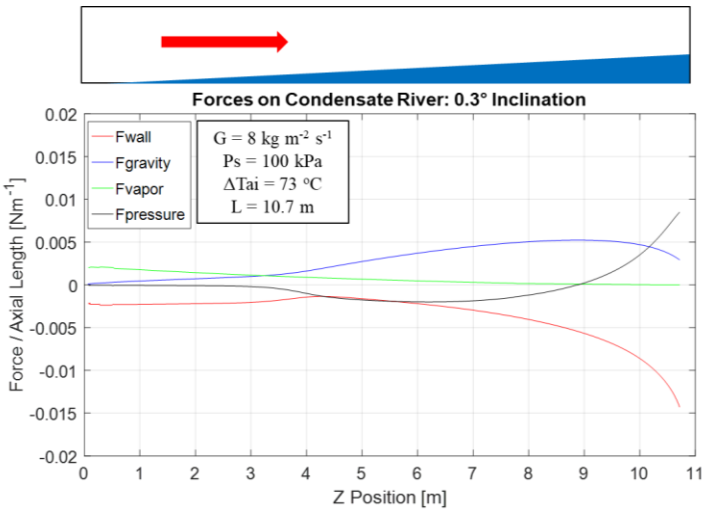

Figure 7.10: Modeled forces on the condensate river along the length of a condenser tube inclined at 0.3°. Vapor shear and wall friction dominate over first 3 m of length, while gravity and wall friction dominate over the last 6 m of length

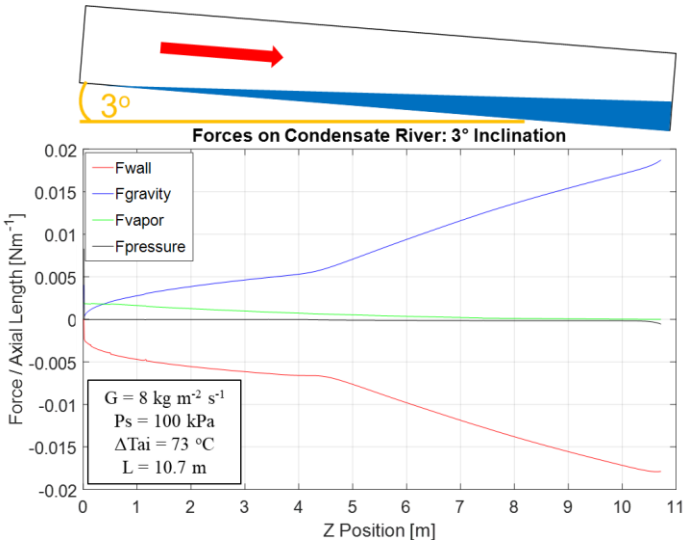

(a)

Figure 7.11 (cont.)

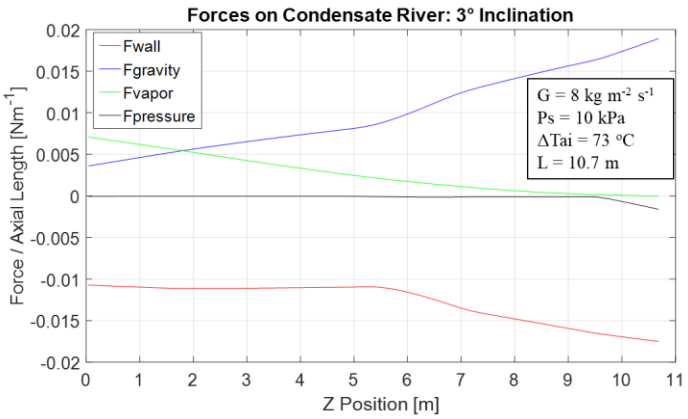

(b)

Figure 7.11: Modeled forces on the condensate river along the length of a condenser tube inclined at 3º, for (a) Ps = 103 kPa and (b) Ps = 10 kPa. Gravity and wall friction are the dominant forces for nearly the entire condenser length

7.5.3 Velocity of the Condensate River

Figure 7.12 shows the slip ratio along the condenser tube at three different tube inclination angles for the 10.7 m tube. Slip ratio is defined as:

$$\text{slip ratio} = \frac{v_g}{v_f} \tag{7.55}$$

For all cases, the vapor velocity is significantly higher than the liquid velocity for nearly the entire condenser tube. The slip ratio is a maximum at the condenser inlet and decreases along the length of the tube. At the condenser inlet, the vapor velocity is 14 m s^{-1}, and the model assumes that liquid velocity is 0 m s^{-1}. The average slip ratio decreases as tube inclination increases, due to the effect of gravity increasing the liquid velocity. As the tube inclination increases, the liquid flow direction becomes more closely aligned with the direction of the gravitational force, thereby increasing the acceleration due to gravity.

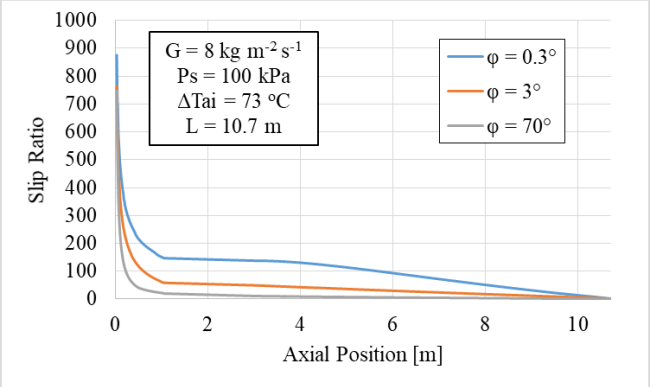

Figure 7.12: Modeled slip ratio along the condenser tube at three inclination angles

Figure 7.13 shows the modeled velocity of the condensate at Z = 10.5 m at varied inclination angles. The velocity is shown to increase as the tube inclination angle increases, due to the increased gravitational force along the tube length. The model results match well with the experiment except at two points, which may be due to experimental error. Experimental river velocity was determined from measurement of condensate river depth, mass flow rate, and quality at Z = 10.5 m.

$$v_{river,\text{experiment}} = \frac{\dot{m}(1-x)}{A_{f,cs}\rho_f} \tag{7.56}$$

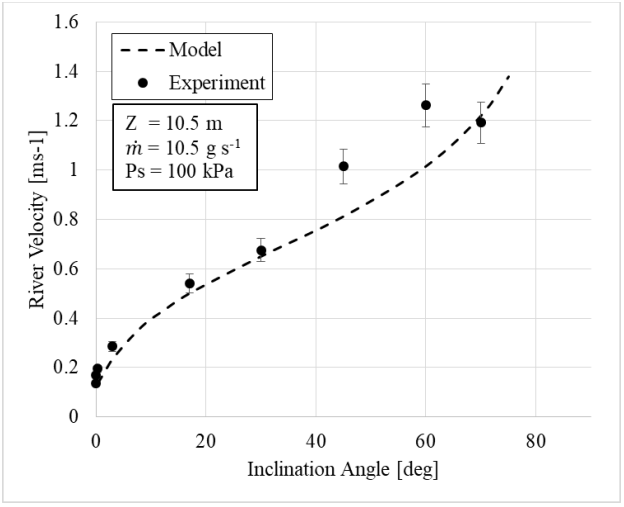

Figure 7.13: Modeled and experimental velocity of the condensate river near the tube outlet for various tube angles; Ps = 100 kPa

7.6 Thermo-Hydraulic Model Results

7.6.1 Capacity

The thermal model is validated by comparing the total condenser capacity from the model and from the experiments. Figure 7.14 shows that all experimental capacities for the 10.7 m tube were predicted to within 5% by the model. For the 5.7 m tube, 95% of the data was predicted to within 5%, with all predictions falling within 7% of the experimental results. In comparison to the area-averaged model in Figure 7.2, the new model has greater precision and greater accuracy, with an average error of 0.6% and a mean absolute percent error (MAPE) of 1.9%.

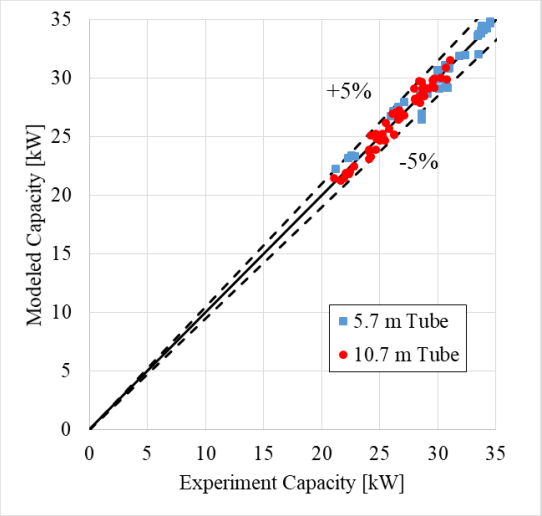

Figure 7.14: Modeled capacity compared to experimental capacity for 10.7 m tube and 5.7 m tube. The model was developed using data from the 10.7 m tube. Uncertainty of the experimental capacity is 3%

7.6.2 Temperature and Overall Heat Transfer Coefficient

An example of the modeled temperatures is presented in Figure 7.15 for the 10.7 m tube at $\varphi = 0.3^{o}$. The non-linear temperature profile can be observed. Experimental wall, air, and steam temperatures are also plotted for comparison. The model under-predicts the wall temperature, which indicates that the steam HTC is higher than that assumed in the model. This is expected, as the natural-convection model used is a lower bound for HTC in pipe flow. An example of $h_{a,n,j}$ and $h_{s.n.j}$ in a cross section are given in Figure 7.16. Air-side HTC decreases in the airflow direction (tube bottom to top) as the boundary layer grows. Steam-side HTC decreases from tube top to bottom due to an increase in thickness of the condensate film. The most significant decrease is seen at the bottom, due to the high heat transfer resistance of the

condensate river. Figure 7.16 also shows that as air inlet temperature difference increases, steam-side HTC decreases. The increased temperature difference causes higher heat flux, which results in greater generation of condensate. This condensate acts as a resistance to heat transfer, which decreases steam-side HTC.

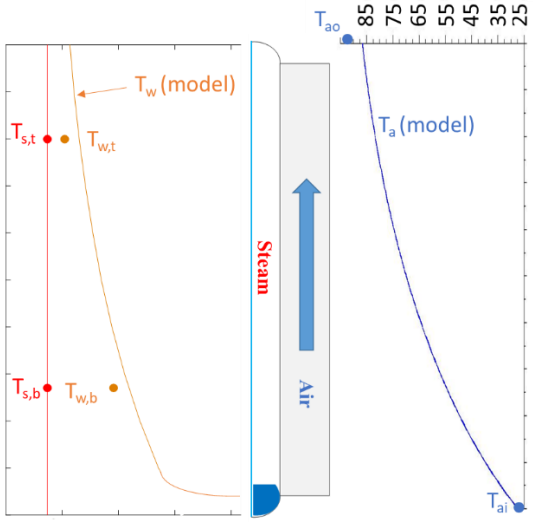

Figure 7.15: Modeled temperatures, T_w and T_a compared to measured values. Model values are presented by lines while dots are used for measured values

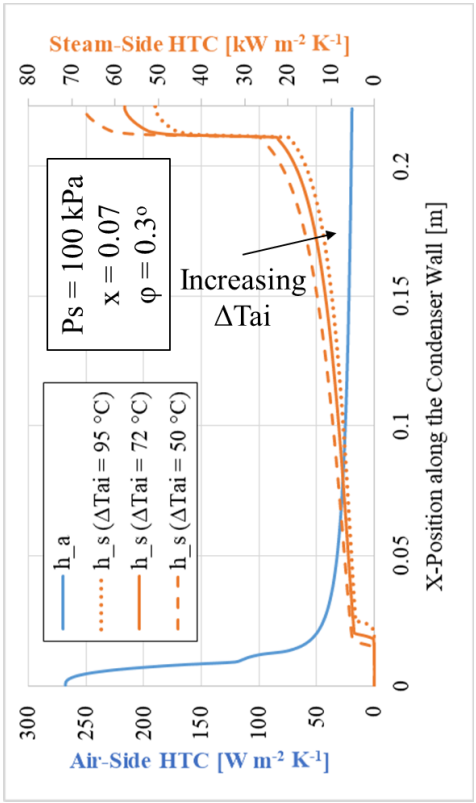

Figure 7.16: Calibrated model of air- and steam-side HTC along a vertical profile of the condenser tube for three air inlet temperature differences (ΔTai = Ts-Tai); Z = 10.5m

Figure 7.17 shows the effect of air inlet temperature difference on overall capacity. As air inlet temperature difference increases, capacity increases. Capacity also increases as air velocity increases.

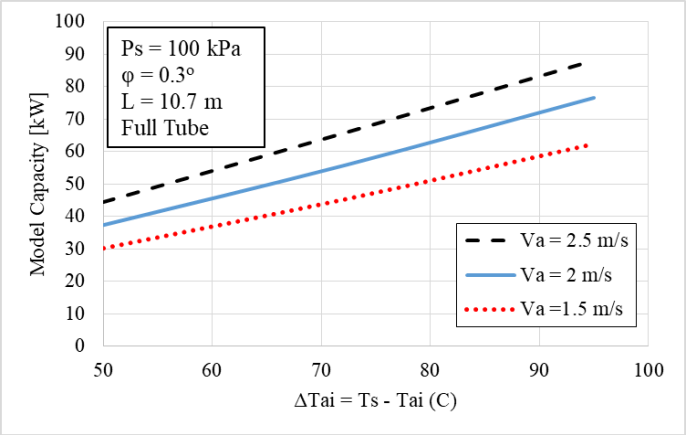

Figure 7.17: Modeled capacity of the full condenser tube (no polycarbonate window) increases as air inlet temperature difference increases and as air velocity increases

7.7 Conclusions

A thermo-hydraulic model has been developed to predict capacity, void fraction, and overall heat transfer coefficient of a flattened-tube air-cooled condenser. The model has been developed based on experiments in a tube of 10.7 m length, and validated by comparison to experiments in a 5.7 m-long tube. The hydraulic model accurately predicts the depth of the stratified condensate layer using open-channel-flow theory. The model is particularly accurate at predicting the decrease in condensate depth near the tube outlet of the horizontal condenser. For heat transfer, the model predicts 98% of experimental capacities to within 5%. The model also provides insight into the local temperature distributions on the air and steam sides. From a hydraulic standpoint, the model shows that the vapor shear force is only important for condensate flow in near-horizontal tube inclination angles of less than 3^{o}. For higher inclination angles, the gravitational force dominates. For heat transfer, the model predicts that the resistance of the condensate river acts as a significant barrier to heat transfer at the bottom of the tube, with this resistance increasing as mass flow rate of the condensate increases.

Chapter 8 Effects of Airflow Profile and Condensation Pressure on Performance of Air-Cooled Condensers

8.1 Introduction

From initial investigations of steam-side condenser performance, significant non-uniformities in steam-side heat transfer coefficient and condenser heat flux were found. This indicated a potential benefit in matching non-uniformities on the air and steam sides of the condenser. This chapter explores this possibility by experimentally comparing the effect of several air velocity profiles on condenser capacity. Combining these experimental results with the model developed in Chapter 7, an in-depth look at the effects of air- and steam-side maldistribution is provided.

In addition to investigating the effects of airflow profile, this chapter examines the effect of condensation pressure on condenser capacity for a power-plant ACC. Condensation pressure is an important system-level parameter. Decreasing condensation pressure improves power-plant performance by increasing the Carnot efficiency, as shown by O'Donovan and Grimes [21]. Only a few previous experimental parametric studies of ACC performance have been performed and only one in a flattened-tube geometry. Of the previous studies, O'Donovan and Grimes [21] showed through thermodynamic modeling of a power plant that decreasing condensation pressure decreases the capacity of an ACC, due to decreased steam-ambient temperature difference. In a combined experimental and numerical study of air-steam condensation inside an ACC, Sukhanov *et al.* [19], found that condensation HTC increased as inlet steam-air velocity increased (velocity increases as pressure decreases). However, they found that condensation HTC decreased as subcooling of the condensate decreased. Condensate subcooling is expected to decrease as condensation pressure decreases. From these results, it is expected that the predominant effect of decreasing condensation pressure is to decrease air-steam temperature difference, but the effect on heat transfer coefficient is less clear. This study examines the effect of condensation pressure on condenser capacity.

8.2 Facility

The experiments were conducted on the two previously-described facilities: one with a 10.7 m long condenser tube, and the other with a 5.7 m long tube. The tube can be inclined at the full range of angles from 0 – 90^{o} with steam and condensate flowing co-currently downward.

Cooling air is provided by 134 axial fans of 80 mm diameter. The fans are controlled by individual potentiometers to allow for variation of velocity and airflow profile. In this paper, six different airflow profiles are examined, including: uniform upward flow at three different velocities, two non-uniform upward flow profiles, and uniform downward flow.

8.3 Method

8.3.1 Experimental Procedure

Fan power is adjusted and air velocities are measured by a hand-held anemometer before system start-up. Air velocity is measured at 645 locations for the 10.7 m tube, and at 496 locations for the 5.7 m tube. An iterative procedure is used in adjusting fan power and measuring air velocity in order to achieve the desired velocity profile.

For the 10.7 m tube, four velocity profiles are tested:

1. Uniform upward airflow of 1.6 m s^{-1} (face velocity)
2. Non-uniform upward airflow, with average velocity at the tube inlet (Z = 0 – 5 m) of 1.92 m s^{-1} (face velocity), average velocity at the tube outlet (Z = 5 – 10.7 m) of 1.28 m s^{-1}, and overall average velocity of 1.6 m s^{-1} (face velocity)
3. Uniform upward airflow of 2.0 m s^{-1} (face velocity)
4. Uniform downward airflow (air flowing from top of tube to bottom, towards the ground) of 2.0 m s^{-1} (face velocity)

For the 5.7 m tube, two velocity profiles are tested:

5. Uniform upward airflow of 2.5 m s^{-1} (face velocity)
6. Non-uniform upward airflow, with average velocity at the tube inlet of 2.02 m s^{-1} (Z = 0 – 3 m), average velocity at the tube outlet (Z = 3 – 5.7 m) of 3.06 m s^{-1}, and overall average velocity of 2.5 m s^{-1} (face velocity)

For the downward air flow, the fans are physically flipped face-down to push air downward through the fins.

For the current study, test conditions and uncertainties are presented in Table 8.1.

Table 8.1: Operating conditions and uncertainty

Parameter	Range	Uncert.
Steam mass flux [kg m^{-2} s^{-1}]	2.1 – 9.5	± 10%
Steam mass flow rate [g s^{-1}]	11 – 13.8	± 0.1%
Condenser capacity [kW]	21.2 – 35.2	± 3%
Air velocity [m s^{-1}]	1.6, 2.0, 2.5	± 7%
Vapor inlet pressure [kPa]	70 – 106	± 0.1
Ambient temperature [°C]	23 – 35	± 0.1
Inlet air temperature difference [°C]	56 – 76	± 0.1
Inclination angle [°]	0	± 0.1

8.3.2 Data Reduction

Condenser capacity is determined on both the air and steam sides. On the air side, capacity is determined by equation (8.1):

$$Q_a = v_a A_{a,\,face} \rho_a \left(c_{p,ao} T_{ao} - c_{p,ai} T_{ai} \right) + UA_{a,loss} \left(LMTD_{a-atm} \right) \tag{8.1}$$

On the steam side, capacity is determined by equation (8.2):

$$Q_s = \dot{m}_s \left(i_{si} - i_{so} \right) - UA_{s,loss} \left(T_s - T_{atm} \right) \tag{8.2}$$

For both tubes, the loss terms are less than 1% of total condenser capacity. These values of heat lost to the atmosphere were determined by testing of the systems with single-phase hot water and the fans off and covered.

For the 10.7 m tube's energy balance, the difference in steam- and air-side capacities were less than 10% for all tests, with an average difference of 3%. For the 5.7 m tube's energy balance, the difference in steam- and air-side capacities were less than 25% for all tests with an average difference of 16%. To minimize the experimental uncertainty, the capacities were combined into an average capacity using equation (8.3), based on the method of Park *et al.* [111]:

$$\bar{Q} = \frac{\left(\frac{1}{u_a^{\,2}} \right) Q_a + \left(\frac{1}{u_s^{\,2}} \right) Q_s}{\frac{1}{u_a^{\,2}} + \frac{1}{u_s^{\,2}}} \tag{8.3}$$

Here, u_a and u_s are the air-side and steam-side uncertainties in the capacity determination.

8.3.3 Uncertainty

Uncertainty of capacity is determined by the method of Taylor and Kuyatt [114] on equation (8.3). Uncertainty of the steam-side capacity is dominated by the measurement of the mass flow rate of condensate. Uncertainty of the air-side capacity is dominated by uncertainty in the outlet air temperature and in the air velocity measurement. For the 10.7 m tube, uncertainty of air-side capacity is 7%, of steam-side capacity is 4%, and combined uncertainty of condenser capacity is 1.7%. For the 5.7 m tube, uncertainty of air-side capacity is 10%, of steam-side capacity is 4%, and combined uncertainty of condenser capacity is 2.1%.

8.4 Results

8.4.1 Non-Uniform Airflow Profile

Non-uniform airflow profiles were compared to uniform airflow profiles for both the 10.7 m and 5.7 m tubes. For the 10.7 m tube, the non-uniform profile had increased velocity near the tube inlet. The uniform and non-uniform profiles had an average velocity of 1.6 m s^{-1} at the fin inlet as shown in Figure 8.1.

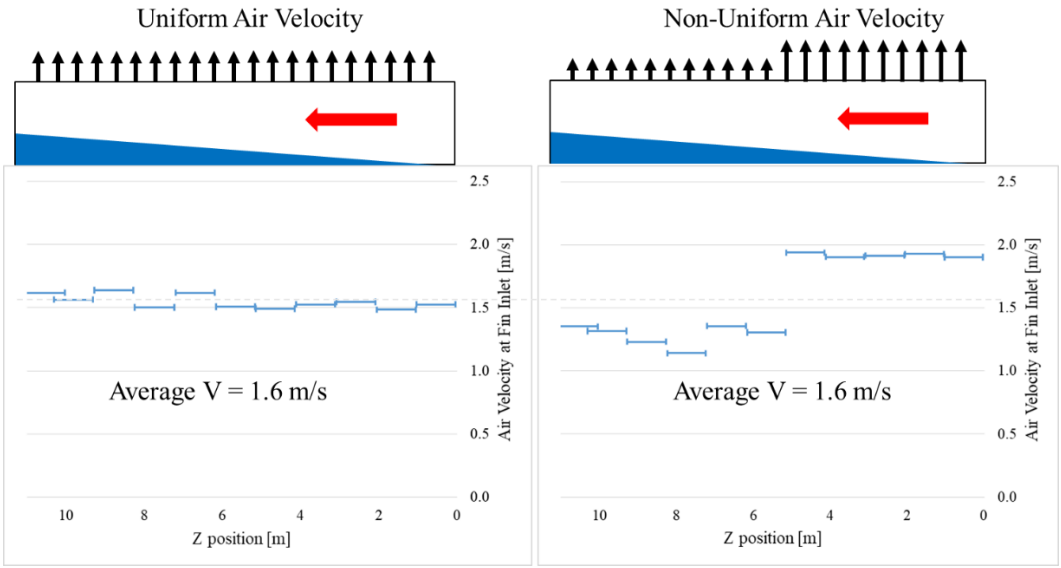

Figure 8.1: Uniform and non-uniform velocity profiles along the tube length for 10.7 m tube

Results for capacity for both airflow profiles are shown in Figure 8.2 below. The non-uniform airflow profile has 3.1% higher capacity than the uniform profile. This increase occurs because the steam-side has a non-uniform distribution of HTC. The steam condenses as it moves through the tube, resulting in a build-up of condensate along the condenser length. This

condensate increases the thermal resistance of the condenser. Therefore, the steam-side thermal resistance is higher near the tube outlet than near the tube inlet. As a result, the airflow at the inlet has more efficacy than the airflow near the tube outlet. Therefore, it is beneficial to increase airflow at the tube inlet and decrease airflow at the tube outlet. This trend matches the results of Zhang *et al.* [101]. Figure 8.2 also compares the results to the thermo-hydraulic model that was described in Chapter 7. The model predicts a 2% increase in capacity from the favorable airflow profile.

Figure 8.3 shows the effect on pressure drop of the non-uniform airflow profile. For a given mass flux, pressure drop is lower for the non-uniform airflow profile in comparison to the uniform profile. The non-uniform profile increases the condensation rate near the tube inlet, which lowers the average steam velocity in the tube. This decreases the frictional pressure drop.

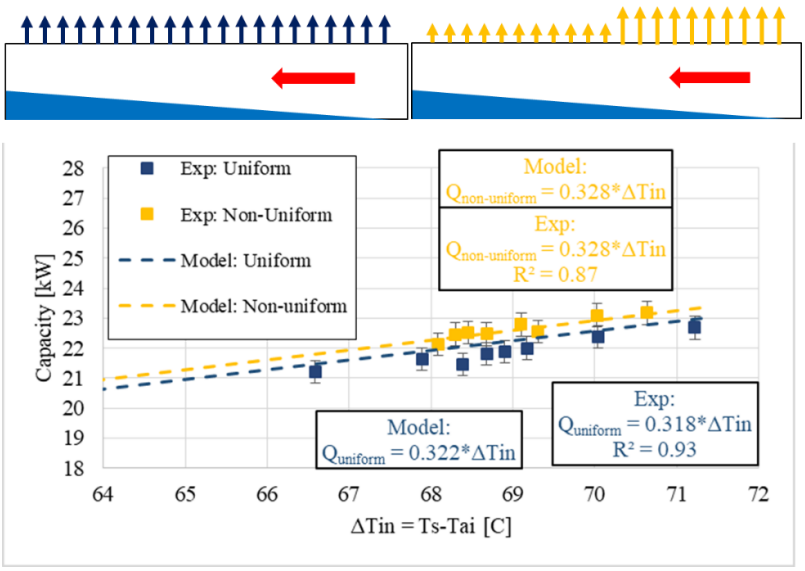

Figure 8.2: Capacity vs. inlet air - steam temperature difference for two different velocity profiles for the 10.7 m tube. Increasing airflow at the condenser inlet increases capacity.

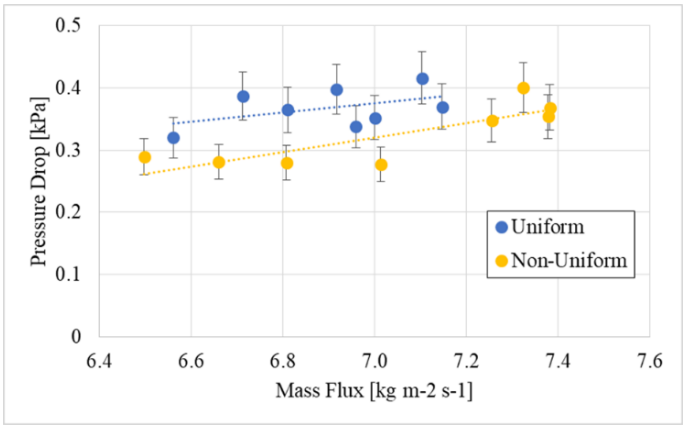

Figure 8.3: Pressure drop is lower when airflow at the tube inlet is increased versus a uniform airflow profile, for a given mass flux

For the 5.7 m tube, the non-uniform profile had increased airflow near the tube outlet, which is the reverse of the profile tested on the 10.7 m tube. This profile is expected to be unfavorable, because it aligns the most airflow with the highest steam-side thermal resistance. Figure 8.4 shows the two velocity profiles tested in the 5.7 m tube. The profiles have equivalent average air velocity of 2.5 m s^{-1} at the fin inlet. Figure 8.5 shows the capacity plotted against inlet air-steam temperature difference. The results show no difference in capacity for the two velocity profiles. This demonstrates the advantage of the shorter tube length. The shorter tube does not accumulate as much condensate as the longer tube, and therefore the increase in steam-side thermal resistance is negligible along the tube length. Therefore, there are no significant non-uniformities on the steam side, so there is no benefit to attempting to match air- and steam-side non-uniformities.

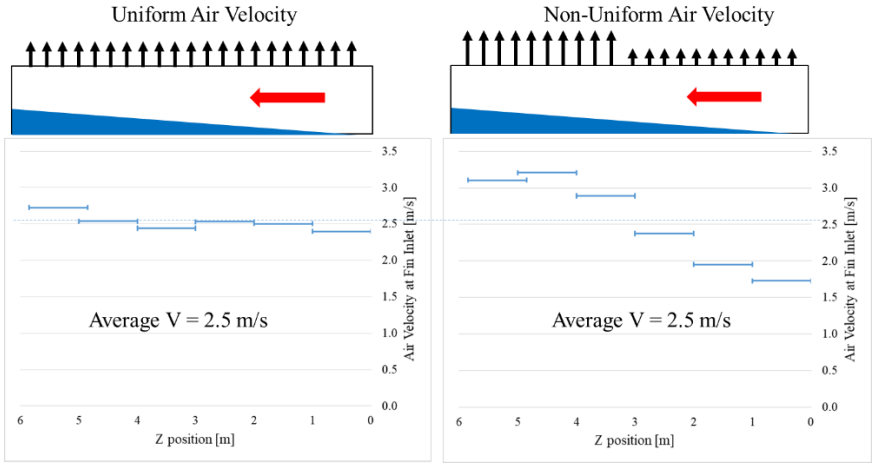

Figure 8.4: Uniform and non-uniform velocity profiles for the 5.7 m tube

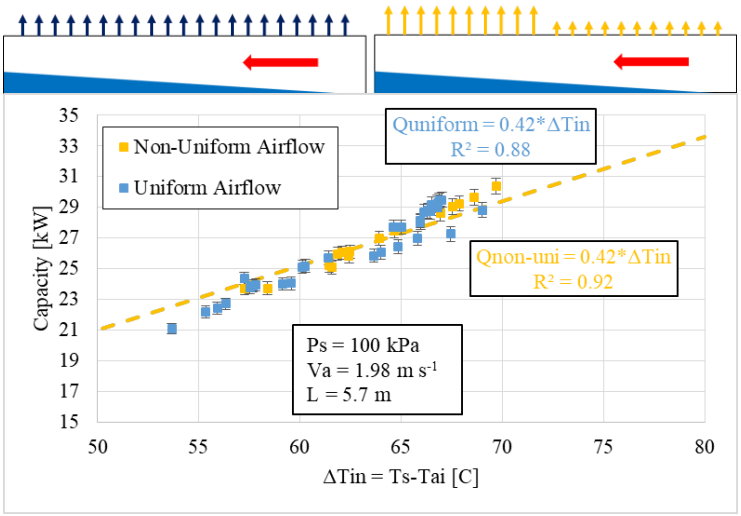

Figure 8.5: Capacity vs. inlet air - steam temperature difference for two different velocity profiles. Decreasing airflow at the condenser inlet has no effect on condenser capacity for the shorter condenser, L = 5.7 m

8.4.2 Reversed Airflow Direction

The effect of airflow direction on condenser capacity is presented in Figure 8.6 below for the 10.7 m tube. Conventional condensers have air flowing upwards. The reversed airflow direction is an attempt to avoid the negative impact on thermal resistance of the stratified condensate layer at the bottom of the condenser tube. Both profiles had equivalent average air velocity of 2.0 m s^{-1} at the fin inlet. The condenser with air flowing downwards has increased capacity in comparison to the condenser with air flowing upwards. At all inlet air – steam temperature differences, the downward-air condenser had 3.5% higher capacity than the upward-air condenser.

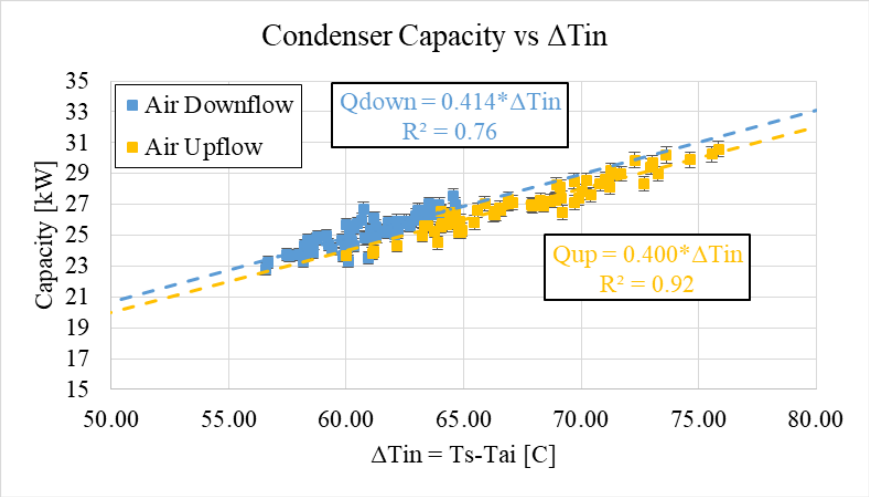

Figure 8.6: Capacity vs. inlet air - steam temperature difference for air flow upwards and downwards. A condenser with downward air flow has higher capacity than a condenser with upward air flow

The reversal of airflow direction increases capacity by rendering negligible the heat transfer resistance of the condensate layer at the tube bottom. This can be clearly described by the condenser model. As shown in Figure 8.7, the condensate layer significantly decreases heat flux at the tube bottom when air is flowing upwards. When air is flowing downwards, the heat flux at the tube bottom is low regardless of the presence of condensate, so the decrease due to the added resistance of the condensate is not important to the overall capacity. On the air side, the inlet is the most important region for heat transfer, due to the high ΔT and high HTC. Therefore, it is beneficial to locate this region in a corresponding region of high steam-side HTC. The region of highest steam-side HTC is the tube top (due to the thin film at the tube top). Capacity is affected by the sum of the air, steam, and wall resistances, as shown in equation (8.4):

$$Q = AU * \Delta T = A_s \frac{1}{R_a + R_{wall} + R_s}\left(T_s - T_a\right) \tag{8.4}$$

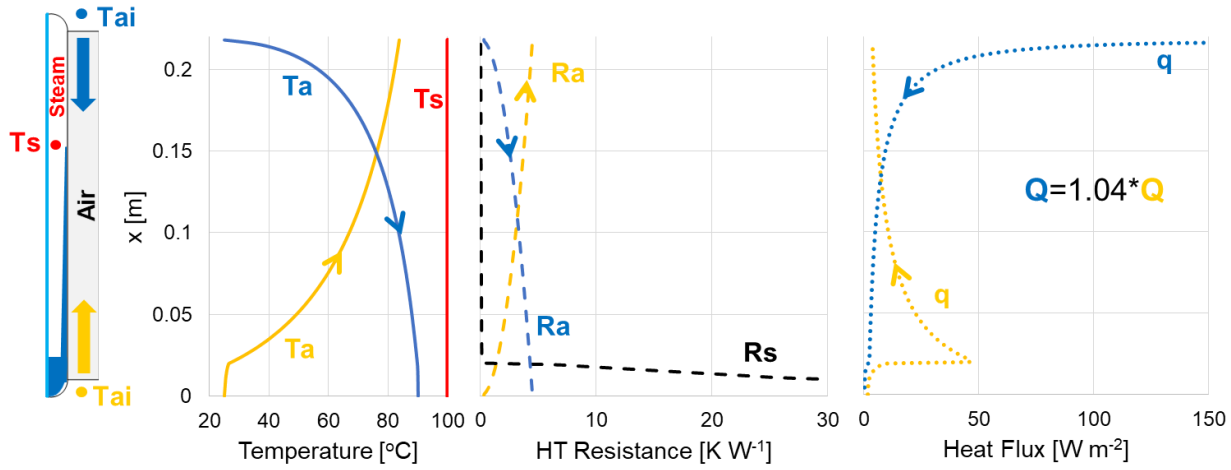

Figure 8.7: Model for system performance in upward and downward airflow. The resistance of the condensate river has a significant negative effect for the case of upward airflow, but is negligible for the case of downward airflow

8.4.3 Discussion of Non-Uniformities in Air-Cooled Condensers

This paper presents examples of the effects of non-uniformities in two different ACC geometries. To generalize these results to other condenser designs, the field synergy principle of Guo *et al.* [102] can be used. This principle lays out the mathematical basis for aligning condenser non-uniformities. According to the principle:

$$Nu_j = \mathrm{Re}_j \,\mathrm{Pr} \int_0^1 \bar{\mathrm{v}} \bullet \nabla \bar{T} d\bar{x} \tag{8.5}$$

$$\bar{\mathrm{v}} = \frac{\mathrm{v}}{\mathrm{v}_{ref}} \tag{8.6}$$

$$\nabla \bar{T} = \frac{\nabla T}{\Delta T_{ref} / L_{ref}} \tag{8.7}$$

$$\bar{\mathrm{v}} \bullet \nabla \bar{T} = \left|\bar{\mathrm{v}}\right| \left|\nabla \bar{T}\right| \cos\beta \tag{8.8}$$

where L is the characteristic length, Nu_j and Re_j are the local Nusselt and Reynolds numbers, respectively, and θ is the angle between the temperature gradient (∇T) and the velocity (v). The integral in equation (8.5) has been named the field synergy number, *Fc*, and can range between 0 and 1.

As shown by equations (8.5)-(8.8), enhancement of convective heat transfer occurs when: 1) the angle between the temperature gradient and the velocity are as small as possible; 2) The

local values of the velocity, the temperature gradient, and cosθ are simultaneously large; 3) the velocity and temp profiles at each cross section are as uniform as possible. This is the synergy of the velocity and temperature fields [102], and it is the analytical basis for matching non-uniformities on the air and steam sides of the condenser.

For an ACC, the air-side velocity and temperature gradient are parallel, so condition (1) is already optimized. Condition (3) can be met on the steam side by removing or limiting the accumulation of condensate. However, if this is not possible, it is best to align the highest air velocity with the location with the least amount of condensate, as proposed by condition (2). The accumulated condensate in the condenser reduces heat flux, which decreases the local temperature gradient. For an ACC, it is therefore important to maximize the product of the air-side velocity and temperature gradient over the entire condenser area:

$$Q \sim \int \mathrm{v}_a \nabla T_a dA \tag{8.9}$$

Guo *et al.* [102] further showed that the field synergy principle is more important when the Peclet number is greater than 100:

$$Pe = \mathrm{Re}\,\mathrm{Pr} = \frac{L\mathrm{v}\rho\mathrm{c}_p}{k} \tag{8.10}$$

L is the characteristic length. For the air-side of the ACC designs used in this paper, the Peclet number (based on condenser height) is approximately 20,000. This shows that air-side non-uniformity will be a significant factor to consider regardless of the ACC geometry. For the steam side, the importance of non-uniformities will increase as the tube length increases, which we have seen for the 10.7 m tube vs. the 5.7 m tube.

A complete quantitative optimization of condenser non-uniformities requires the solution of a complete condenser model, because the temperature gradients are a function of the air- and steam-side flow rates. The optimum alignment of non-uniformities will occur when the integral in equation (8.9) is maximized for all potential airflow profiles. Figure 8.8 shows the effect on condenser capacity of increasing airflow over the first half of the condenser length while decreasing airflow over the second half of the length in a 10.7 m tube. The model shows that a peak in capacity occurs when the air velocity over the tube length from Z = 0 to Z = 5.35 m is about 0.6 m s^{-1} higher than the air velocity over Z = 5.35 m to Z = 10.7 m.

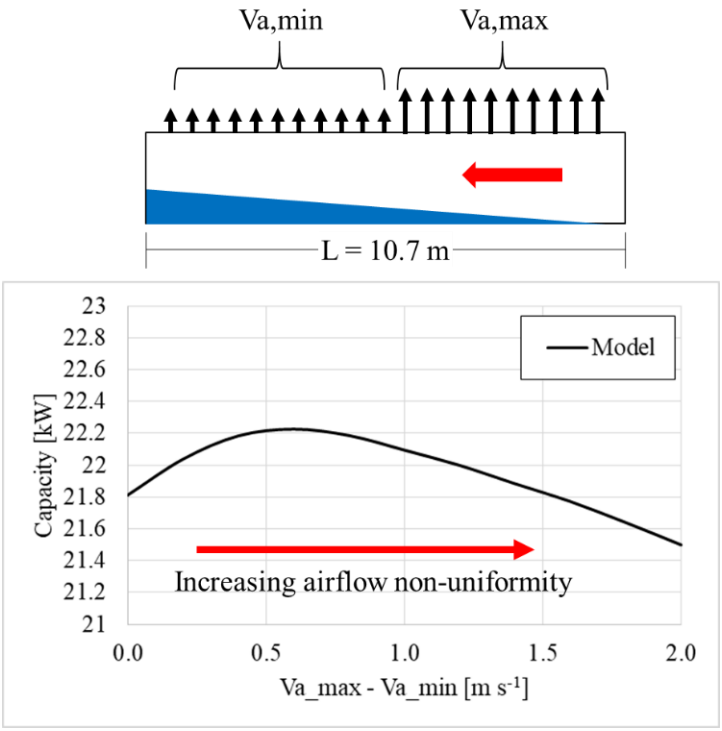

Figure 8.8 Model results show that there exists an optimum non-uniform airflow profile for maximizing condenser capacity. Airflow is arranged in a step profile with $v_{a,max}$ in the region Z = 0 m to Z = 5.35 m and $v_{a,min}$ in the region Z = 5.35 m to Z = 10.7 m along the condenser length

8.4.4 Effect of Condensation Pressure on Condenser Capacity

The effect of condensation pressure on tube capacity at a constant inlet air-steam temperature difference is shown in Figure 8.9. Condensation pressure is found to have a slight positive effect on capacity for both tube lengths. Although the larger heat transfer resistance – the air side – is not affected by the steam pressure, this result is not unexpected. As pressure increases, steam-side HTC is expected to increase, as shown in Section 5.4.2. Two changes in properties drive this increase. Steam viscosity decreases, which decreases the film thickness. Also, steam thermal conductivity increases. Figure 8.10 shows the practical effects of reducing condensation pressure – ΔTin is reduced in addition to the reduction in overall condenser HTC. As pressure decreases, condensing temperature must decrease, so for a constant ambient temperature, the driving temperature difference for heat transfer is reduced. Combined with the decreases in steam-side HTC, the overall result is a significant reduction in condenser capacity as pressure decreases.

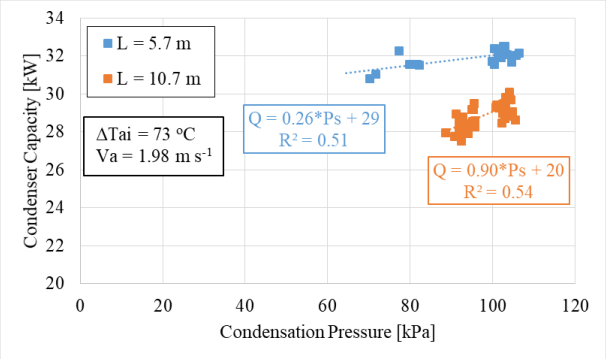

Figure 8.9: Condenser capacity decreases slightly as condensation pressure decreases

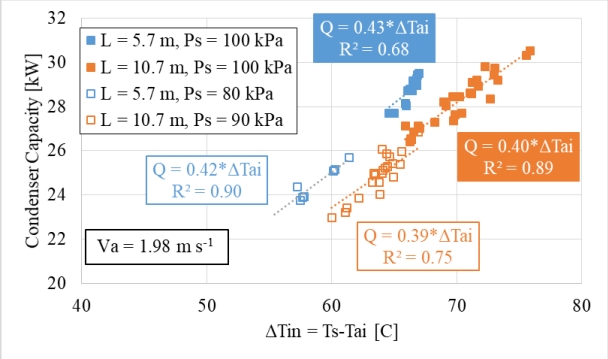

Figure 8.10: Condenser capacity decreases as condensation pressure decreases due to decreased ΔTin and decreased U

8.5 Conclusions

Through experiment, it has been found possible to increase air-cooled condenser capacity by modifying the airflow profile. These modifications match non-uniformities on the air and steam sides of the condenser. Adjusting the air velocity profile so that more of the airflow is concentrated at the condenser inlet increases capacity. For the tested non-uniform velocity profile in a 10.7 m tube, capacity increases by 3.1% in comparison to a uniform velocity profile. Reversing the airflow direction also increases condenser capacity by 3.5%. These gains are achieved by diminishing the negative effect of the high heat transfer resistance of the stratified condensate layer. For a 5.7 m tube, the effect of airflow profile was found to be negligible. This was attributed to the minimal non-uniformities on the steam side for this shorter tube.

In addition to these designs, the effect of condensation pressure on condenser capacity has been tested. Decreasing condensation pressure has been found to decrease capacity by two mechanisms. First, temperature difference between steam and cooling air is decreased when pressure decreases. Second, overall condenser HTC decreases when condensing pressure decreases. However, this decrease in capacity must be balanced with system-level performance, which increases as condensation pressure decreases, due to higher Carnot efficiency.

Chapter 9 Local Heat Transfer Coefficient during Stratified Flow in Flattened-Tube Steam Condensers with Non-Uniform Heat Flux and Wall Temperature: Experimental Results and Correlation

9.1 Introduction

This chapter describes the experimental method and results for determining local heat transfer coefficient during condensation in the flattened-tube condenser. A water-cooled test section is designed to match the non-uniform heat flux and wall temperature found in an operating air-cooled condenser while significantly improving accuracy of the HTC determination. Results are shown for the effects of several parameters on the local HTC. From these results, two regions for heat transfer are identified – the stratified condensate layer flowing axially along the tube bottom, and the condensing-film region along the tube walls. Additional experiments are then run to artificially vary the depth of the stratified condensate layer and determine its effect on HTC in that region. Correlations for HTC in both the stratified-condensate and condensing-film regions are developed, and a circumferentially-averaged correlation for HTC is presented as the perimeter-weighted average of the HTC in both regions.

In addition to the HTC results and correlations, experimental results for condensate subcooling along the tube length are presented.

9.2 Facility and Test Section

9.2.1 Overview

The facility used in this study is similar to that described in Chapter 5 for the 5.7 m tube, although with several significant modifications. A schematic of the experimental setup is presented in Figure 1. The setup contains two consecutive test sections: an air-cooled condenser tube of 5.7 m length, and a water-cooled condenser tube of 0.12 m length. Steam is generated by two boilers (24 kW and 45 kW), following which it passes through a pre-heater and a choke valve into an adiabatic visualization window and then into the air-cooled test section. At the outlet of the air-cooled section, the steam and collected condensate flow directly into the water-cooled test section. These tubes are connected directly via flange in order to assure that no disruption is made to the flow regime. After these two test sections, the collected condensate passes through a Micromotion CMF025 coriolis mass flow meter and into a condensate receiver for return to the boilers. The remaining steam passes to a secondary condenser, where it is

condensed completely. This secondary condensate is pumped back into the boilers via a CMF010 coriolis mass flow meter. The boiler is manually-controlled by a solid-state controller. An inlet heater and choke valve ensure that the steam enters the condenser slightly-superheated. The condensate pumps run intermittently based on condensate volume. This intermittency does not affect the steadiness of the steam exit condition.

Cooling air is provided by an array of 48 120-mm diameter axial fans. The fan speeds are adjustable to control the cooling capacity in the air-cooled section, and therefore control the inlet quality of the water-cooled test section. Both condensers are cross-flow heat exchangers, with cooling fluids flowing perpendicularly to the axial steam flow direction. Fans pull air upwards in the first condenser and cooling water is pumped upwards in the second. The entire condenser is mounted on a hinged truss, allowing for lifting to the entire range of downward tube inclinations.

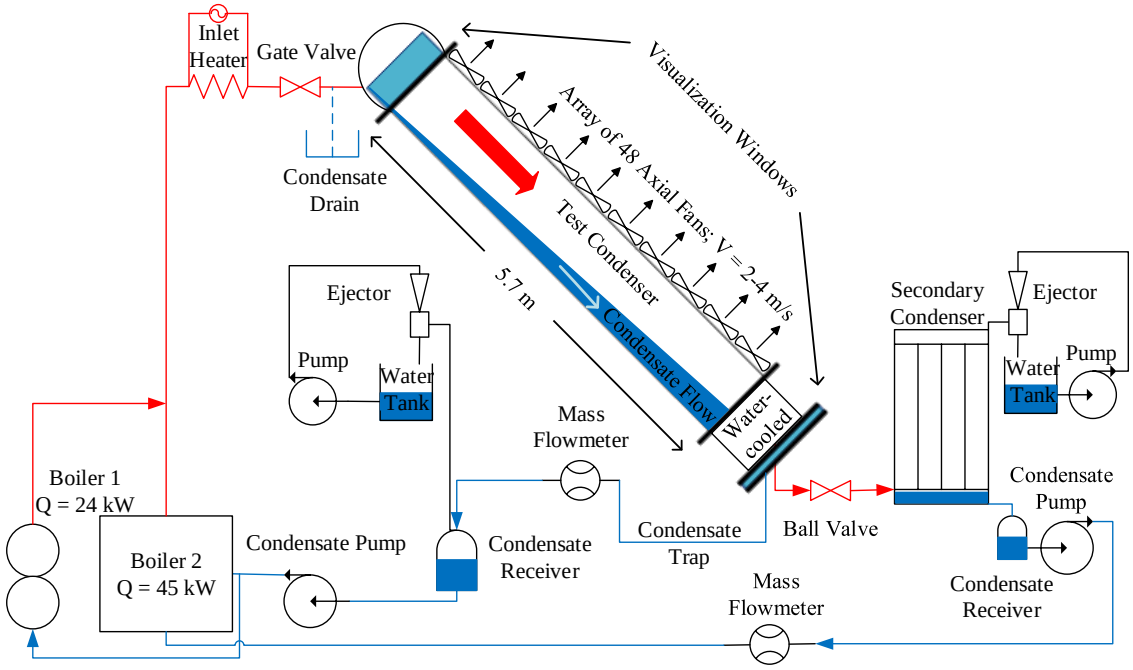

Figure 9.1: Diagram of condenser test facility

9.2.2 Test Tube

The condenser tube in this experiment is 0.216 m in inner height and 0.016 m in inner width, as seen in Figure 9.2. The tube is steel with aluminum cladding on the outside, and the wavy fins are aluminum. The fins are 200 mm x 19 mm, with a thickness of 0.25 mm. The tube is installed in an air duct, with crossflowing air pulled upwards through the fins. The water-cooled tube has the same geometry, but the fins are not present.

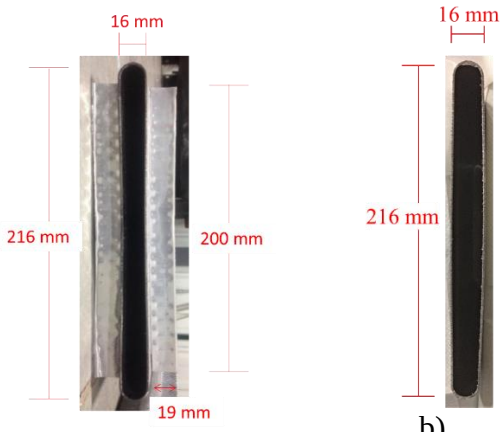

Figure 9.2: Condenser tube cross-section views: a) air-cooled tube; b) water-cooled tube (no fins)

9.2.3 Air-Cooled Test Section

Air-side capacity is determined in the air-cooled test section, along with steam temperature and pressure. Air inlet and outlet temperatures are measured at 0.5 m intervals along the test tube with T-type thermocouples. Temperature of the stratified condensate layer is also measured at Z = 2 m and Z = 4 m along the tube. Air velocity is measured by a handheld hot-wire anemometer at 496 points along the tube. Gauge pressure is measured at condenser inlet and outlet with differential pressure sensors. Atmospheric pressure is measured locally with a barometer.

9.2.4 Water-Cooled Test Section

The water-cooled test section is cooled via a polycarbonate water jacket that was manufactured using the fused deposition modeling 3-D printing process. A diagram of the water-cooling loop is presented in Figure 9.3.

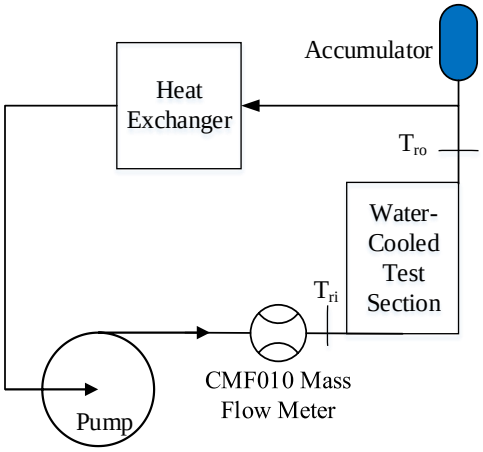

Figure 9.3: Diagram of water-cooling loop

The water-cooled tube is attached via flange to the air-cooled section in order to ensure continuous development of flow regime. A schematic of the test section is presented in Figure 9.4. The polycarbonate water jacket is presented in Figure 9.5. The configuration of the two test sections (air-cooled and water-cooled) as well as the inlet and outlet visualization sections is shown in Figure 9.7.

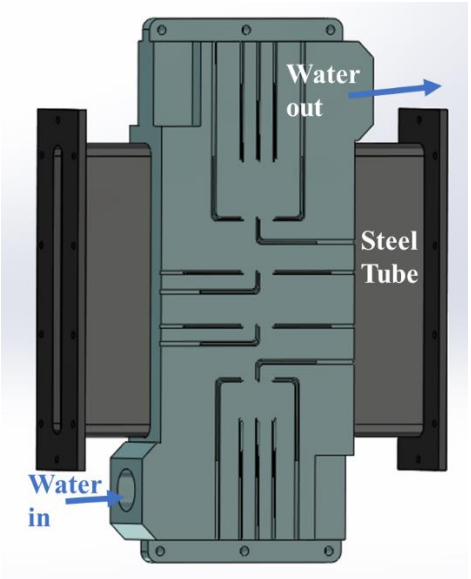

Figure 9.4: Diagram of water-cooled test section, with water jacket covering tube

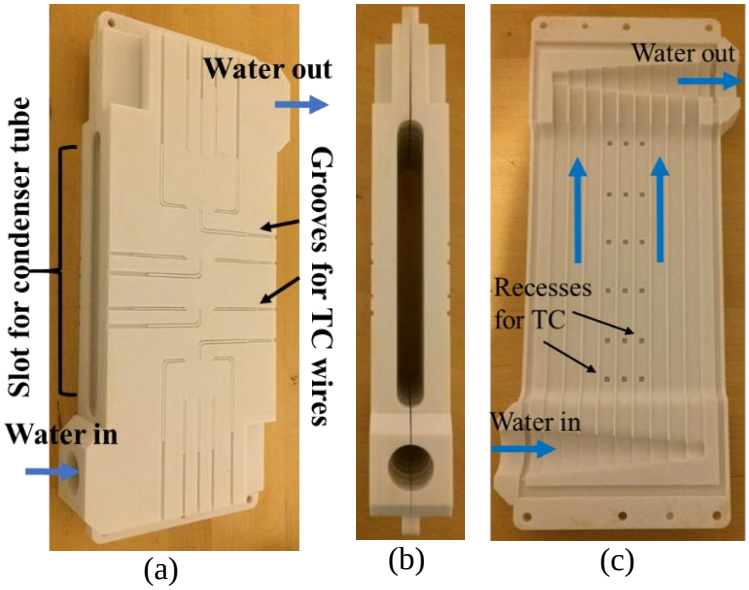

Figure 9.5: Polycarbonate water jacket, (a) External view of jacket, matching the view in Figure 9.4; (b) End view showing water inlet and space for tube; notches on sides are for thermocouple wires. (c) View of inside one half of the jacket. Recesses for water thermocouples (T_r) can be seen in the middle three channels.

The water jacket and test tube form a single-pass counter-flow heat exchanger. The water jacket channels are designed to mimic the large temperature variation present in an air-cooled

condenser. The steam-side flow is in the stratified regime, so the condensation HTC depends on wall-steam temperature difference. That was an important reason to mimic the ACC conditions in order to develop a useful understanding and HTC correlation.

The jacket is clamped around the conventional tube, replacing the fins. Water is in direct contact with the outer wall of the tube. A groove around the outer edges of the jacket is filled with high-temperature silicone sealant in order to create a seal directly on the steel tube, preventing leaks. The jacket is insulated on all sides with 12.5 mm thick Armaflex insulation.

Channel geometry and instrumentation are shown in Figure 9.7. Water temperature is measured at the inlet and outlet to the jacket, as well as at six locations in each of the three middle channels, on each side of the condenser tube. A flow mixer is installed before the inlet water thermocouple (T_{ri}) in order to ensure that an accurate mixing cup temperature is measured at this point.

The thermocouples along each channel ($T_{r\_j,k}$) are positioned in recesses directly above the water channels, in order to measure the water temperature at the top of the channel, while not disturbing the water flow. The thermocouple wires exit the jacket through holes and channels on the top of the jacket (Figure 9.5.a), with insulation removed in order to prevent leaking along the wire. In order to determine the mixing-cup temperature of the water flow, a CFD simulation was performed, and results were compared to the temperature measurements. Details of the CFD simulation are contained in section 9.3.2. The decision to measure the unmixed water temperatures along the channels was an intentional one. The water-cooling system was designed with the goal of matching the temperature glide of air through the fins in the air-cooled test section, as shown in Chapters 5-7. Due to the high heat capacity of water in comparison to air, this requirement compelled the use of thin (1.4 mm height) water channels. These channels were too thin to build a polycarbonate mixing structure along the length of the channel. An alternative option would be to pull the water away from the tube into separate mixing chambers before each temperature measurement. However, this would interrupt the thermal boundary layer and expose the tube to intermittent doses of cooler water – once again failing in the requirement to match the temperature glide of the air-cooled section. Therefore, a combined experimental and CFD approach was chosen to maintain this uninterrupted temperature glide. This method introduces increased uncertainty in the determination of water temperatures along the channel, and therefore

in the determination of local condensation HTC. However, the mixing-cup temperatures of the inlet and outlet water were measured directly, so the uncertainty of the mean HTC is unaffected.

In following the water temperature measurements, wall temperature ($T_{w\_j,k}$) is measured in six locations at each of the three middle channels on both sides of the tube. The thermocouples are embedded in the 1.7 mm-thick steel wall of the tube, as diagrammed in Figure 9.7. The thermocouple beads are covered with Omegabond 101 high thermal conductivity epoxy (published thermal conductivity of 1.0 W m^{-1} K^{-1}) before insertion to ensure proper thermal contact with the wall. The thermocouple wires are passed outside of the water channels through grooves cut in the steel wall of the tube, in order to avoid leaks and disturbance of the flow. These grooves for the wires are also filled with thermal epoxy after insertion in order to affix the thermocouples and ensure proper heat conduction through the wall. The wall thermocouples after installation are shown in Figure 9.8. All temperatures are measured with T-type thermocouples.

Water mass flow rate ($\dot{m}_r$) is measured using a Micromotion CMF010 Coriolis mass flow meter. The polycarbonate heat exchanger was designed to minimize pressure drop in the headers in order to ensure a uniform flow distribution among all of the channels. Therefore, flow rate through each channel can be determined by simply dividing the total flow rate by the number of channels. The validity of this assumption is investigated and confirmed in section 9.3.3. In addition, the uncertainty caused by this assumption is reduced by averaging the temperature measurements in three channels.

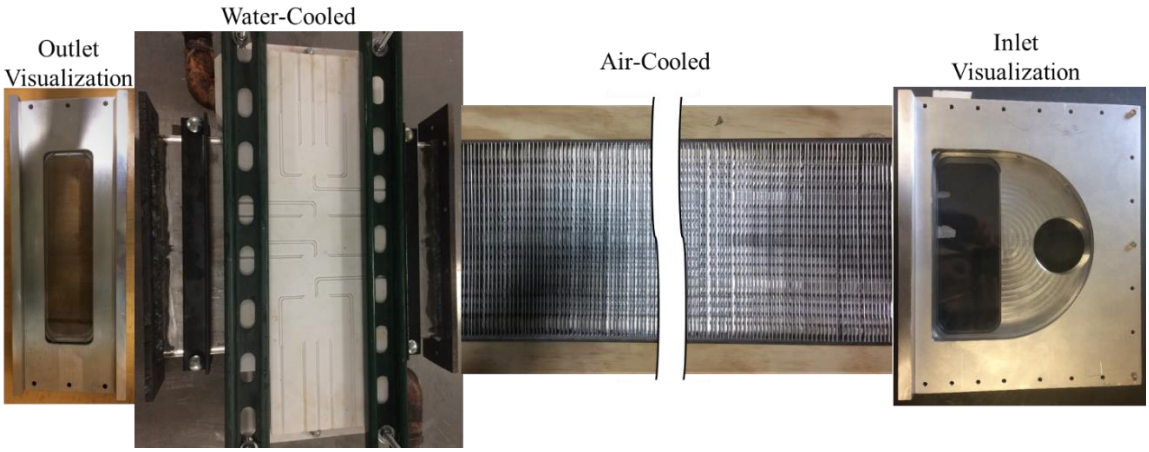

Figure 9.6: Picture of test and visualization sections

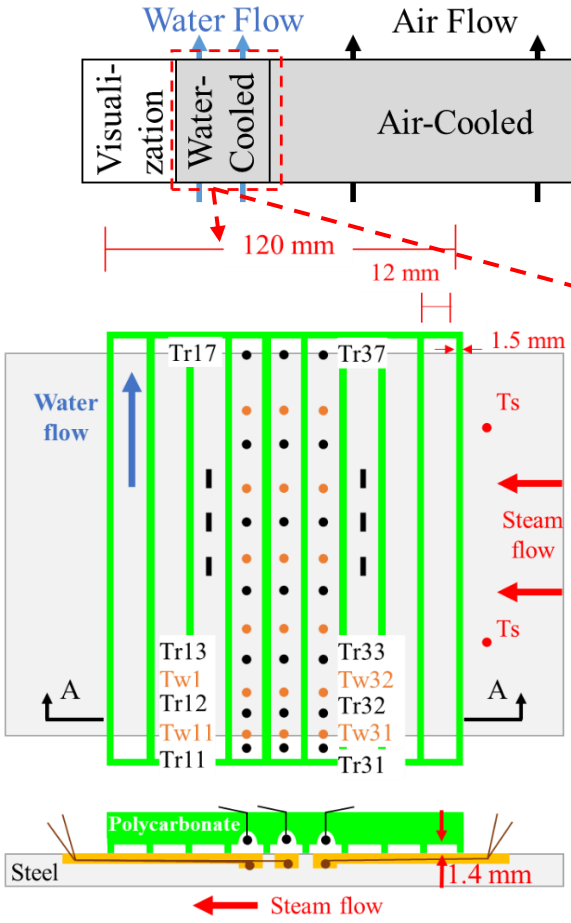

Figure 9.7: Diagram of water-cooled section; Wall (Tw_{jk}) and water (Tr_{jk}) temperatures are measured in the three center channels along the channel length. Polycarbonate depicted in green for visibility

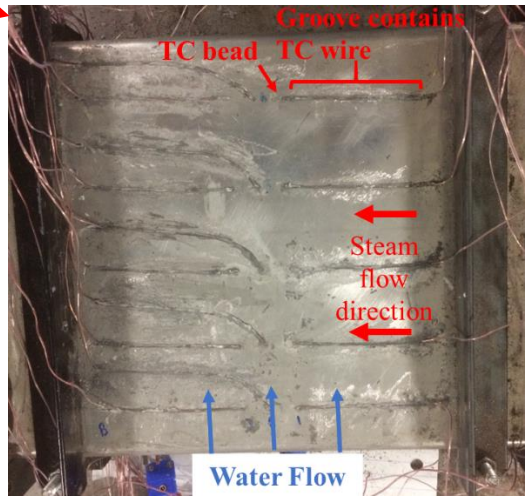

Figure 9.8: Water-cooled test section (steel tube) with wall thermocouples installed. TCs are installed in three adjacent channels on each side of the tube. The TC wires run through channels cut into the steel wall perpendicularly to the channel direction. TCs are affixed with Omegabond 101 high-conductivity thermal epoxy

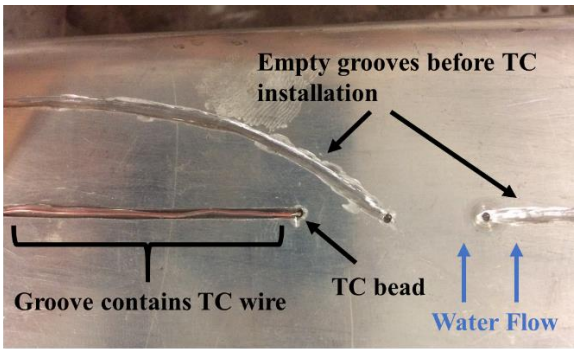

Figure 9.9: Close-up picture of grooves for wall thermocouples before installation with Omegabond 101, in order to demonstrate TC placement

9.2.5 Measurement of Condensate Subcooling

To measure the condensate temperature, T-type thermocouple probes are placed with their tips 1 mm above the bottom condenser wall, in order to measure condensate temperature as close to the condenser wall as possible. These thermocouples were positioned at 2 m and 4 m along the tube length in the air-cooled section, as well as at the condenser outlet. A diagram of the condensate thermocouples (T_c) is shown in Figure 9.10.

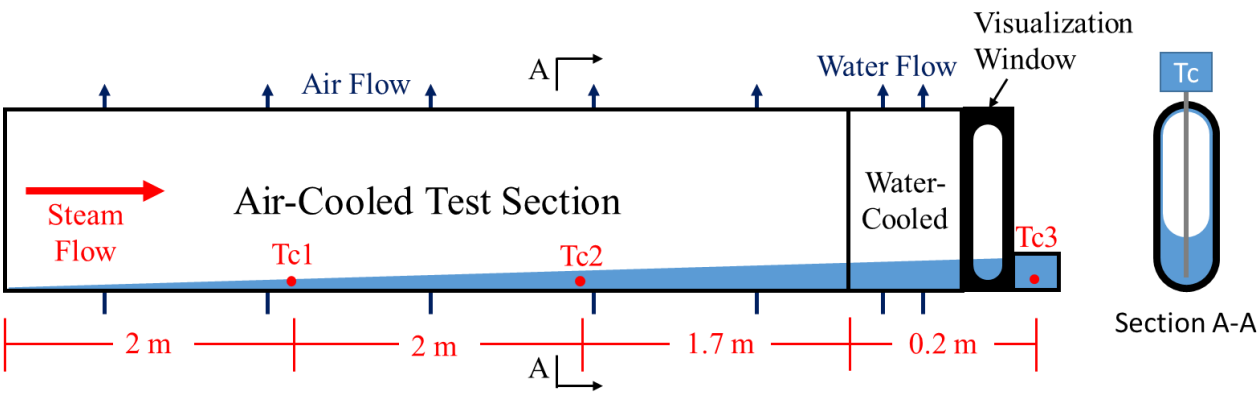

Figure 9.10: Diagram of condensate subcooling measurements in the two test sections. Two subcooling measurements, *Tc1* and *Tc2*, are made in the air-cooled test section, and one, *Tc3*, is made at the condenser outlet

9.2.6 Experimental Procedure

The system is run with steam pressure above atmospheric at startup to expel all non-condensables from the system. When the temperature in the secondary condenser indicates that all non-condensables have been removed, the release valve is closed. Boiler power is then reduced in order to create a vacuum in the system. Due to the large size of the system, ingress of non-condensables at vacuum conditions is inevitable. These collect in the secondary condenser and are removed via a water-powered ejector. Quality in the water-cooled section is controlled

by adjusting fan power in the air-cooled condenser and by adjusting system mass flow rate. Mass flow rate is controlled via boiler power. The flow rate of cooling water is controlled to maintain a constant water temperature difference between the inlet and the outlet. This control allows imitation of the temperature glide across the fins in the air-cooled condenser. Flow regime and depth of the stratified condensate layer are observed and measured via an adiabatic visualization window at the outlet of the water-cooled test section. This outlet visualization window is shown in Figure 9.11.

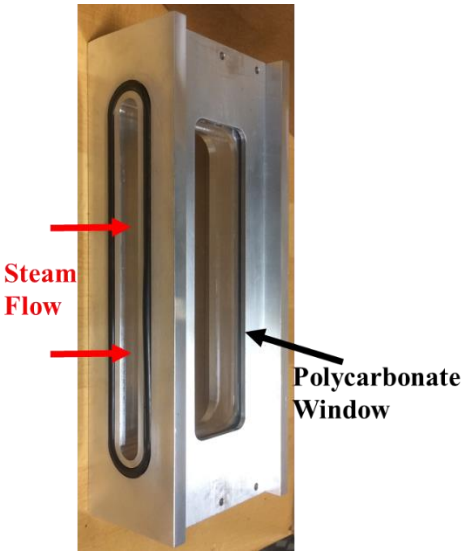

Figure 9.11: Outlet visualization window

9.2.7 Experimental Procedure: Heat Transfer Coefficient in the Stratified Condensate Layer

To determine HTC through the condensate at various depths, the valve at the outlet to the condenser is closed, and the condenser tube is flooded to the desired depth of condensate. The tube is kept at 0.5^{o} inclination, to ensure a near-constant depth of condensate through the test section. Depth of the condensate is measured via the visualization window directly downstream of the test section. Once the depth reaches the desired level, the outlet valve is opened just enough to maintain the condensate depth constant. Once the depth and the flow rate of condensate are constant, data are recorded. This method makes it possible to measure a wide range of condensate depths and velocities.

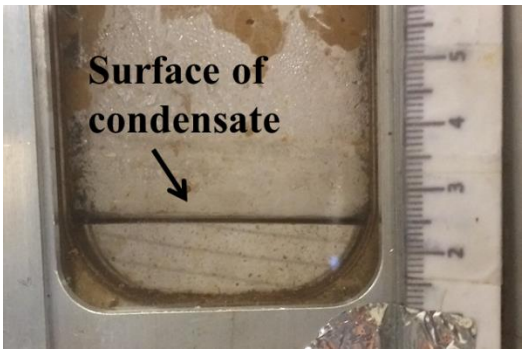

Figure 9.12: Flow regime and condensate depth are observed and measured in the visualization window directly downstream of the water-cooled test section

9.2.8 Test Conditions

The test conditions in Table 9.1 describe the conditions at the inlet of the water-cooled test section. The primary variables are steam mass flux, steam quality, tube inclination angle, condensation pressure, water-side temperature difference, and heat flux (although these last two are dependent on each other).

Table 9.1: Operating conditions and uncertainty

Parameter	**Range**	**Uncert.**
Steam mass flux [kg m^{-2} s^{-1}]	0.75 – 5.3	± 10%
Steam mass flow rate [g s^{-1}]	2.5 – 18	± 0.1
Mean heat flux [kW m^{-2}]	2 – 67	± 3%
Steam quality [-]	0 – 0.74	± 0.1
Condensation pressure [kPa]	52 – 108	± 0.1
Inlet water-steam temp. difference [^{o}C]	32 – 77	± 0.2
Vapor superficial Reynolds number [-]	0 – 7000	± 10%
Liquid Reynolds number (based on hydraulic depth of condensate) [-]	10 – 4100	± 10%
Inclination angle [^{o}]	0 – 38	± 0.1

9.3 Method

9.3.1 Data Reduction

Total steam mass flow rate, $\dot{m}_s$, is the sum of the condensate mass flow rates leaving each of the water-cooled test section ($\dot{m}_{c1}$) and the secondary condenser ($\dot{m}_{c2}$).

$$\dot{m}_s = \dot{m}_{c1} + \dot{m}_{c2} \tag{9.1}$$

Steam mass flux, G_s, is the total steam mass flow rate, $\dot{m}_s$, divided by the inner cross-sectional area of the condenser tube, A_{cs}:

$$G_s = \frac{\dot{m}_s}{A_{cs}} \tag{9.2}$$

Steam quality at the inlet to the water-cooled test section (x_r) is determined by two methods.

For the first method, condensate generated by the water-cooled section is subtracted from mass flow rate of condensate leaving the primary condenser. The result is divided by the system mass flow rate.

$$x_{r,method1} = \frac{\dot{m}_{c1} - Q_r / i_{lv}}{\dot{m}_s} \tag{9.3}$$

Capacity of the water-cooled test section, Q_r, is determined by equation (9.4):

$$Q_r = \dot{m}_r \left(T_{ro} c_{p,ro} - T_{ri} c_{p,ri} \right) \tag{9.4}$$

The second method to determine quality is by using the capacity of the air-cooled test section, measured via heat transferred to the cooling air (equation (9.5)):

$$x_{r,method2} = \frac{Q_a / i_{lv}}{\dot{m}_s} \tag{9.5}$$

Air-side capacity, Q_a, is determined via air velocity and air-side temperature difference. A complete description of this determination is available in section 3.3.

Final steam quality is determined by an uncertainty-weighted average, as described by Park et al. [111]:

$$x_r = \frac{\left(\frac{1}{u_{method1}^{\ 2}} \right) x_{r,method1} + \left(\frac{1}{u_{method2}^{\ 2}} \right) x_{r,method2}}{\frac{1}{u_{method1}^{\ 2}} + \frac{1}{u_{method2}^{\ 2}}} \tag{9.6}$$

Equation (9.7) shows that heat flux of the water-cooled section is determined by water-cooled capacity divided by the total steam-side heat transfer area of the water-cooled section, which totals 0.0547 m^2:

$$q''_r = \frac{Q_r}{A_{s,r}} \tag{9.7}$$

Local capacity of the water-cooled section is determined from change in local water temperature, $T_{bulk,r,jk}$, in each channel, as in equation (9.8):

$$Q_{r,jk} = \frac{\dot{m}_r}{\#\text{of channels}}\left(T_{bulk,r,j,k+1}c_{pr,j,k+1} - T_{bulk,r,j,k}c_{pr,j,k}\right) + Q_{loss} \tag{9.8}$$

$$Q_{loss} = U_{loss}A_{s,k}LMTD_{r-atm,j,k} \tag{9.9}$$

$$LMTD_{r-atm,j,k} = \frac{\left(T_{bulk,j,k+1} - T_{atm}\right) - \left(T_{bulk,j,k} - T_{atm}\right)}{\ln\left[\frac{\left(T_{bulk,j,k+1} - T_{atm}\right)}{\left(T_{bulk,j,k} - T_{atm}\right)}\right]} \tag{9.10}$$

The local water mass flow rate is determined by assuming equivalent mass flow rate in each of the 18 channels. This was achieved through careful design of the header (assisted by CFD) and maintaining higher pressure drop through the channels than in the header. This assumption was verified by comparing temperature measurements in adjacent and opposing channels. The value of Q_{loss} – the heat lost from the cooling water to the atmosphere – varies from <1% at the bottom of the tube to about 10% at the top of the tube (where the water temperature is highest). Uloss

Local heat flux is then determined by the local water-side heat transfer area, with the subscripts *j* and *k* in equations (9.8) and (9.11) denoting the channel number (1-9) and axial location along the channel (1-6) respectively:

$$q''_{r,j,k} = \frac{Q_{r,j,k}}{A_{s,k}} \tag{9.11}$$

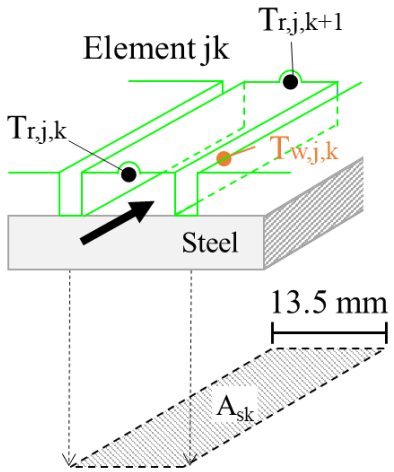

Figure 9.13: Depiction of area and temperature measurements for local HTC determination

The local area and temperature measurements for determination of $h_{s,j,k}$ are shown in Figure 9.13. The local condensation heat transfer coefficient is then determined by local heat flux

and temperature difference between the steam and the wall, and then accounting for the heat transfer resistance of the wall (equations (9.12) and (9.13)):

$$h_{j,k} = \frac{q''_{r,j,k}}{T_s - T_{w,j,k}} \tag{9.12}$$

$$h_{s,j,k} = \left(\frac{1}{h_{j,k}} - \frac{t_w}{k_w} \right)^{-1} \tag{9.13}$$

9.3.2 CFD Method for Determining Local Water Temperature

In order to determine the local water bulk temperature ($T_{bulk,r,j,k}$), a 2-D CFD simulation using the ANSYS Fluent software [113] is performed for the flow of cooling water through a channel of the polycarbonate jacket. The problem is assumed to be two-dimensional, steady, incompressible turbulent flow. The water is assumed to be Newtonian with constant properties. The computational domain and mesh are shown in Figure 9.14.

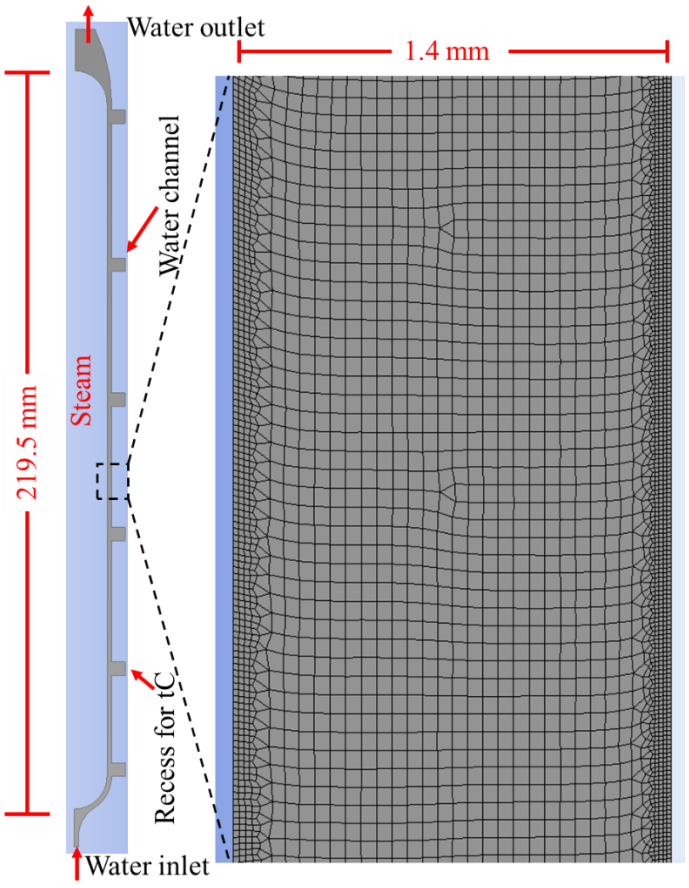

Figure 9.14: Computational domain and enlargement of one section of the mesh for the CFD simulation

Boundary conditions include a constant, uniform inlet velocity and temperature, with a pressure outlet with gauge pressure of 0 kPa. Inlet velocity and temperature are input from experimentally-measured mass flow rate and inlet temperature, respectively. Temperature of the condenser wall (left wall) follows the experimental profile, which is input via a user-defined function. The right wall has a 3.8 cm insulation thickness with thermal conductivity of 0.2 W m^{-1} K^{-1}, as in the experiment.

Mesh independence is verified using the temperature difference between water inlet and outlet temperature:

$$\Delta T_r = T_{ro} - T_{ri} \tag{9.14}$$

The results for mesh independence can be seen in Figure 9.15. The selected mesh has 440,000 elements with an element size of 50 μm, with 10 μm sizing in the boundary layer.

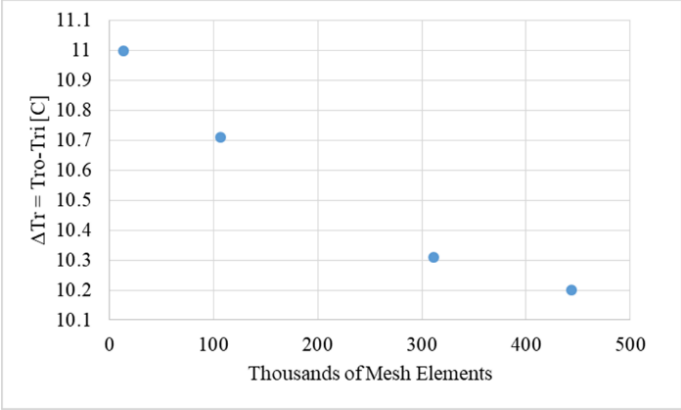

Figure 9.15: Mesh independence of increase in water temperature. The software limit is 500,000 mesh elements.

To validate the CFD results, comparison is made to the outlet water temperature that was measured in the experiment, as well as to the water temperature along the length of the channel. A comparison of water temperature results for one data point is shown in Figure 9.16. A comparison of experimental vs. CFD capacity of the cooling water for all data points is shown in Figure 9.17. The average error in the CFD calculation is -1%. As can be seen, the CFD capacity matches the experimental capacity within 10% for the majority of the data points. However, this 10% error is still unacceptable for HTC determination. Therefore, the CFD capacity is scaled to ensure that it equals the experimental capacity. The scaling is performed by equation (9.15). In this way, the mean HTC is fully validated by the experimental results, while only the local HTC is apportioned by the CFD results.

$$T_{bulk,r} = \left(T_{bulk,r,CFD} - T_{ri}\right)\frac{T_{ro} - T_{ri}}{T_{ro,CFD} - T_{ri}} + T_{ri} \tag{9.15}$$

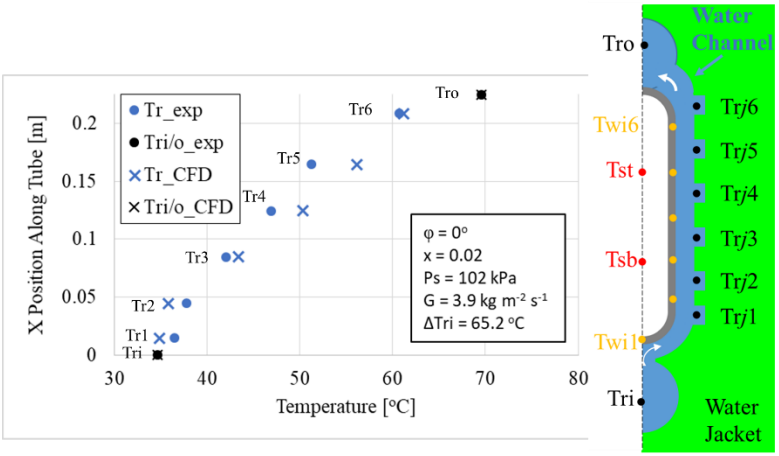

Figure 9.16: CFD cooling water temperatures compared to experimental temperature results for one data point. The inlet water temperature is a boundary condition for the CFD.

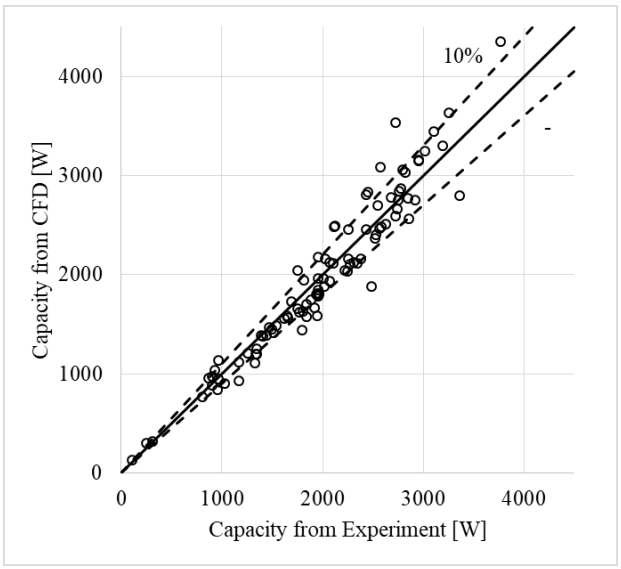

Figure 9.17: Comparison of capacity of the water-cooled test section calculated by CFD with the capacity of the water-cooled test section determined experimentally

9.3.3 Validation with Single-Phase Water

To further verify the accuracy of this method and to provide a manner of calibration, hot water was run through the test section and cooled by the water loop. The experimentally-determined HTC could then be verified by the analytical result for developing laminar flow heat transfer. In addition, this allowed verification of another assumption: uniform flow rate among all of the cooling-water channels. To verify the validity of this assumption, the temperature

measurements in adjacent (along the same side of the tube) and opposite (at the same Z-position but opposite sides of the tube) channels are compared. Figure 9.18 shows good agreement in water and wall temperature measurements between the adjacent and opposite channels. This confirms the uniform flow rate among these three channels.

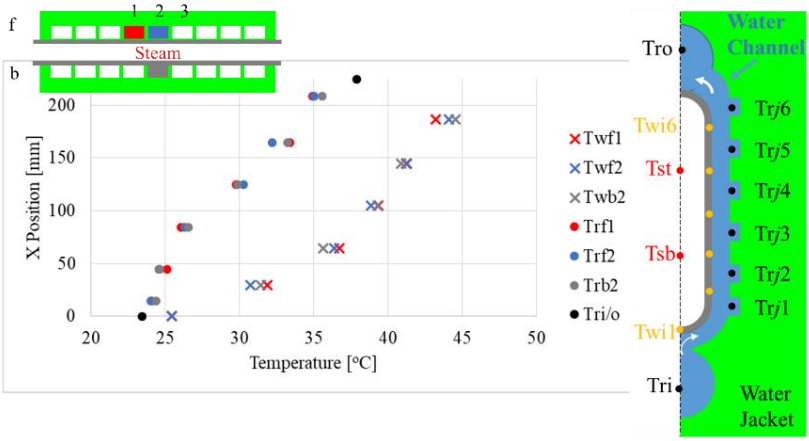

Figure 9.18: Wall and water temperature measurements in three channels during a single-phase test

Figure 9.19 shows the HTC validation for single-phase laminar flow of water. The theoretical value is calculated based on Shah's correlation for thermally-developing laminar flow through parallel plates [130]. This correlation does not precisely fit the current situation – non-uniform wall temperature and heat flux, and a tube instead of parallel plates. However, it is able to provide a rough estimate of the HTC. More importantly, the results shows that the local experimental HTC is constant within the limits of uncertainty from tube bottom to top, which serves to validate the method.

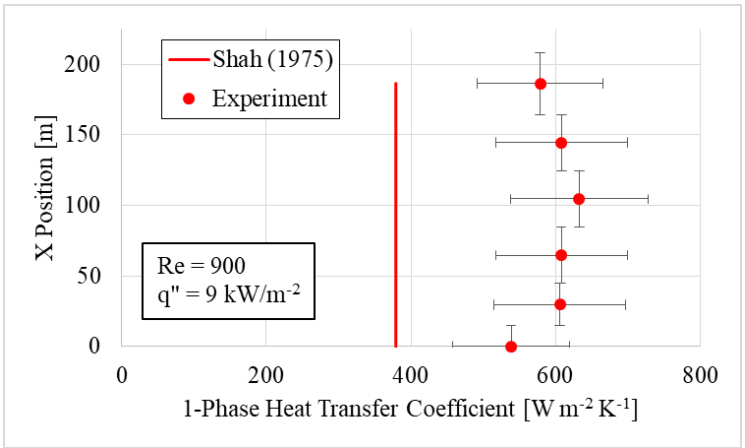

Figure 9.19: HTC for 1-phase laminar water flow in the condenser tube;

9.3.4 Verification of Water Outlet Temperature

To ensure accurate measurement of the outlet water temperature, two thermocouples are installed in the outlet water line. One is installed directly at the outlet of the heat exchanger, while the second is installed after a flow mixer and a pipe bend. The comparison between the two measured outlet temperatures shown in Figure 9.20 shows agreement within the calibrated T-type thermocouple accuracy of 0.1 °C.

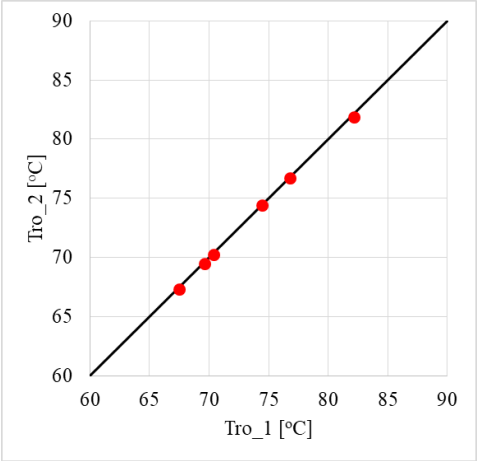

Figure 9.20: Comparison of measured water outlet temperature before (Tro_1) and after (Tro_2) a flow mixer shows agreement within the thermocouple accuracy

9.3.5 Data Reduction: Condensate Depth, Condensate Velocity, and Void Fraction

The receding contact angle of water on polycarbonate is about 80° [131], which means the condensate in the visualization section has a nearly-flat surface (see Figure 9.12 and Figure 9.21). This makes determination of the cross-sectional area of the condensate in the visualization section simple: the condensate has a semi-circular shape at the tube bottom, and a rectangular shape above the bottom.

$$A_c = A_{semi-circle} + A_{rectangle} \tag{9.16}$$

$$A_{semi-circle} = \begin{cases} R^2 \cos^{-1}\left(\frac{R-t_c}{R}\right) - \left(R-t_c\right)\sqrt{2Rt_c - t_c^2} & \text{if } t_c < R \\ \pi R^2 / 2 & \text{if } t_c > R \end{cases} \tag{9.17}$$

$$A_{rectangle} = \begin{cases} 0 & \text{if } t_c < R \\ \left(t_c - R\right) * W & \text{if } t_c < R \end{cases} \tag{9.18}$$

The radius of curvature of the tube bottom, R, is 8 mm, and the tube width, W, is 16 mm. The hydraulic depth of the condensate is determined by:

$$d_h = \frac{A_c}{W_{top}} \tag{9.19}$$

$$W_{top} = \begin{cases} 2\sqrt{R^2 - (R - t_c)^2} & t_c < R \\ W & t_c > R \end{cases} \tag{9.20}$$

In the test section, however, the condensate contacts the (rusted) steel tube wall, which has a receding contact angle close to 0° [108]. In this case, the precise shape of the condensate surface can be determined via the procedure described in Section 7.3. However, the difference in hydraulic depth and cross-sectional area between the two methods is less than 3% for all cases, so this surface curvature could be neglected.

The void fraction is calculated by area ratio:

$$\alpha = \frac{A_{cs} - A_c}{A_{cs}} \tag{9.21}$$

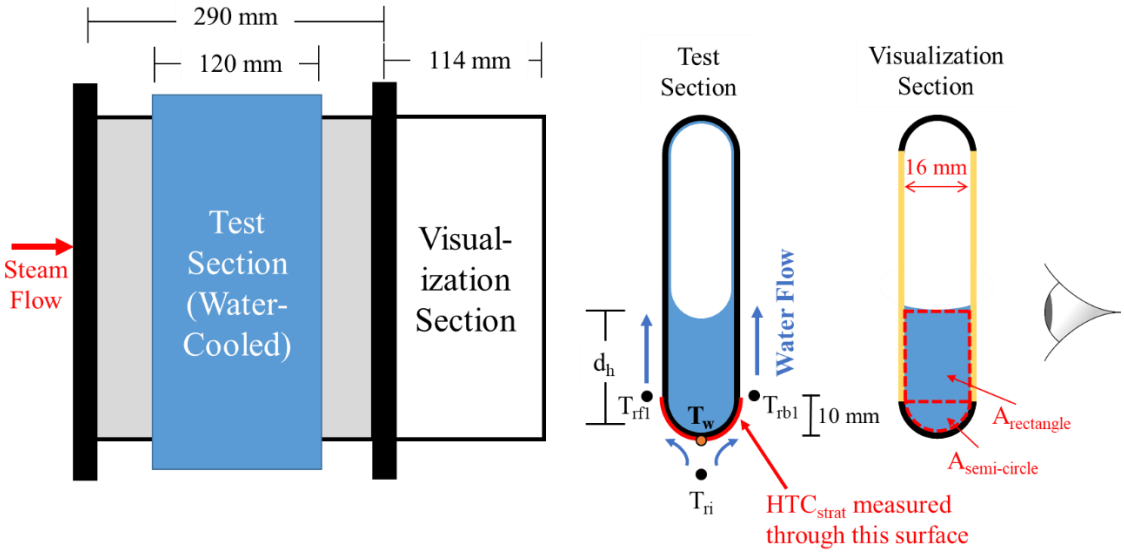

Figure 9.21: Schematic of water-cooled test section and visualization section, along with shape of condensate in each section, and description of measurement location in test section

9.3.6 Uncertainty

To determine the uncertainty of the local HTC, the uncertainty of the modeled local q_r'' must first be determined. Using the method of Rebba *et al.* [132], uncertainty of each $q''_{r,j,k}$ is determined to be 10%. The greatest contributors to this uncertainty are the uncertainty of the

wall-temperature profile input to the model, and discretization uncertainty. Uncertainty in local HTC is then calculated using the method of Taylor and Kuyatt [22] on equation (9.13). This method takes the square root of the sum of the squares of the deviation caused by the uncertainty in each of the component measurements. The main component of the uncertainty of this local HTC is the uncertainty of the local capacity, as determined by the CFD. A secondary cause of the uncertainty is the measurement uncertainty of the temperature difference between the wall and steam. The relative magnitude of these two contributions varies with test conditions. For example, the uncertainty of each thermocouple is 0.1 ^{o}C and the temperature difference varies from 0.4 ^{o}C – 56.7 ^{o}C, meaning the uncertainty of the temperature difference varies from 35% - 0.2%. Despite the variation in the individual contributions to the overall uncertainty, uncertainty of local HTC is nearly 12% for all tests. Uncertainty of overall HTC, determined as the average of the local HTCs, is 5%. The uncertainty of the mean HTC is much lower because the mean heat flux is measured experimentally. This eliminates the added uncertainty of the CFD simulation that is present in the determination of local HTC.

Uncertainty of the hydraulic depth of the stratified condensate layer has three main contributors: uncertainty in measuring the depth of the condensate layer (t_c), uncertainty in measuring the tube dimensions, and uncertainty in approximating the cross-sectional area of the condensate. The uncertainty of the condensate depth measurement is ± 0.3 mm. The uncertainty of measuring the tube width is significant because the tube width increases as operating pressure increases due to the non-circular shape of the tube. This uncertainty is ± 1 mm. The uncertainty in approximating the condensate area is 7%, although this increases when the depth of the condensate layer is less than 10 mm. For example, when the condensate depth is 5 mm, the uncertainty of the area is 28%. The final uncertainty of the hydraulic depth (d_h) of condensate is 9% when hydraulic depth is greater than 7 mm. The uncertainty increases when hydraulic depth is shallower than 7 mm.

9.4 Results and Discussion

9.4.1 Organization of Results and Proposal of New Correlations

Sections 9.4.2 – 9.4.4 present the results for local heat flux and HTC along the tube wall and describe the basis for defining two regions for heat transfer. Sections 9.4.5 – 9.4.7 discuss heat transfer through the stratified condensate layer at the tube bottom. Section 9.4.5 describes

the subcooling of the condensate layer. Section 9.4.6 presents results for heat transfer coefficient in the stratified condensate layer. Section 9.4.7 presents a new correlation for HTC in the stratified condensate layer. Sections 9.4.8 and 9.4.9 describe HTC in the condensing-film region, with 9.4.8 presenting results and 9.4.9 discussing a new correlation for HTC. Finally, sections 9.4.10 and 9.4.11 combine these previous discussions to present the results and model for circumferentially-averaged HTC for a given condenser cross section.

9.4.2 Local Temperature and Heat Flux

Figure 9.22 shows the measured wall, steam, inlet water and outlet water temperatures, as well as the local water temperatures determined using CFD for one experimental point. These are compared to modeled temperatures, which are determined using the equation of Dhir and Lienhard [4] to calculate condensation HTC for points 2-6 (X > 10 mm), and that of Dobson and Chato [2] to determine HTC at point 1 (X < 10 mm) at the bottom of the tube. The experiment finds equivalent wall temperatures to the model, but greater water temperature for all points. This indicates higher heat transfer and higher heat transfer coefficient than that predicted by the experiment.

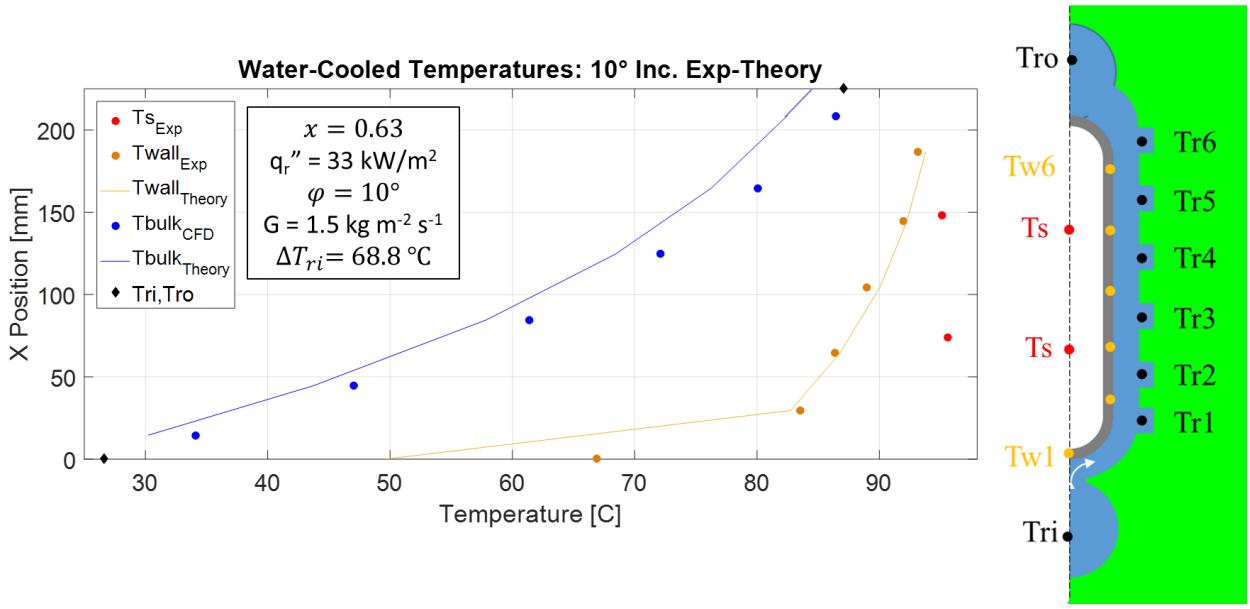

Figure 9.22: Measured and CFD temperatures vs. temperatures determined using the Dhir & Lienhard [4] and Dobson and Chato [2] correlations for HTC

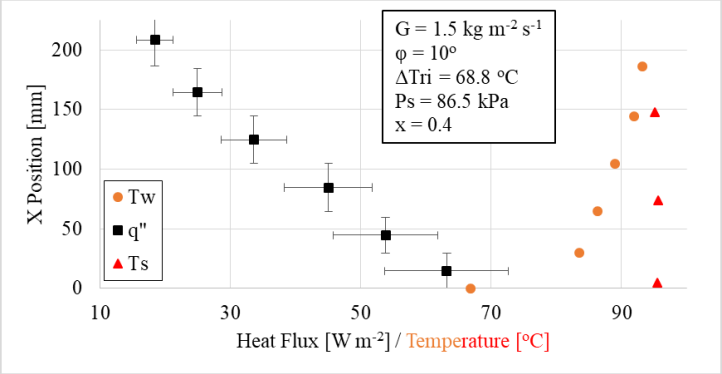

Figure 9.23: Local heat flux, and wall, steam and condensate temperatures for condenser inclined at 10°

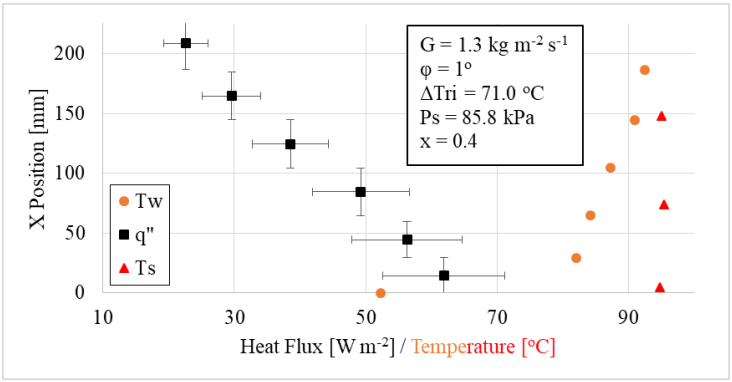

Figure 9.24: Local heat flux, and wall, steam and condensate temperatures for condenser inclined at 1°

Figure 9.23 shows the local heat flux, wall temperature, steam temperature, and condensate temperature for the same test point as in Figure 9.22. For this point, with low mass flux and the condenser inclined at 10°, negligible subcooling is observed. The heat flux decreases from the condenser bottom to the top. The linear decrease in heat flux is mainly the result of increasing water temperature (seen in Figure 9.22). The parabolic increase in water temperature is offset by a decrease in HTC, resulting in a linear increase in heat flux. The wall temperature increases from tube bottom to top as a result of three factors: increasing water temperature, decreasing heat flux, and increasing steam-side HTC.

Figure 9.24 shows the same measurements for a tube inclined at only 1°. The other conditions are held constant, to allow for comparison of the effect of tube inclination angle. For this point, some subcooling of the condensate is observed, as the bottom T_s measurement records condensate temperature 0.4 °C lower than the steam temperature. In addition, the wall temperature at the bottom of the 1° tube is 14.6 °C lower than for the tube with 10° inclination. This increase in subcooling and decrease in bottom wall temperature is the result of increased condensate build-up for the shallower inclination. The condensate has a lower velocity due to

decreased gravitational acceleration. As a result, for the same mass flow rate, the stratified condensate layer on the tube bottom is thicker. The lower velocity and greater surface area of this condensate leads to increased subcooling. In addition, the greater depth of condensate and lower velocity increases the heat transfer resistance. This greater resistance causes a slight decrease in heat flux at the tube bottom compared to the linear trend of the 10^o inclined tube. For the 1^o inclined tube, the heat flux at the tube bottom is 6% less than a linear trend line would predict.

9.4.3 Local Heat Transfer Coefficient

Figure 9.25 (a) displays local HTC for the tube inclined at 10^o. The HTC is lowest at the tube bottom, as expected due to the build-up of condensate at the tube bottom. Condensation HTC then increases along the tube height due to the lower film thickness at the higher positions. The lower film thickness is due to reduced heat flux (reduced local condensate generation) and the higher position along the wall (lower flow rate of condensate from above). Experimental HTC closely follows the model prediction all along the condenser wall. In the condensing film region (X > 10 mm), the modeled HTC is calculated from the natural-convection model of Dhir and Lienhard [4]. In the stratified condensate layer at the tube bottom, the correlation of Dobson and Chato [2] is used. When used for stratified flow, the correlation of Dobson and Chato [2] divides the flow into two regions – the condensing film on the tube wall, and the stratified liquid layer at the tube bottom. For the stratified liquid, the correlation assumes convective single-phase heat transfer, and uses a correlation similar to that of Dittus and Boelter [56]. This HTC can be extracted from the correlation to provide an estimate of the HTC at the tube bottom. In the case of the experimental points shown here, the observed condensate level does not cover the entire bottom measurement section. As a result, the model prediction at the tube bottom is an area-averaged result of condensing-film HTC (Dhir and Lienhard [4]) and stratified-condensate HTC (Dobson and Chato [2]). This method carries significant uncertainty, but it can provide a rough estimate of HTC in this region.

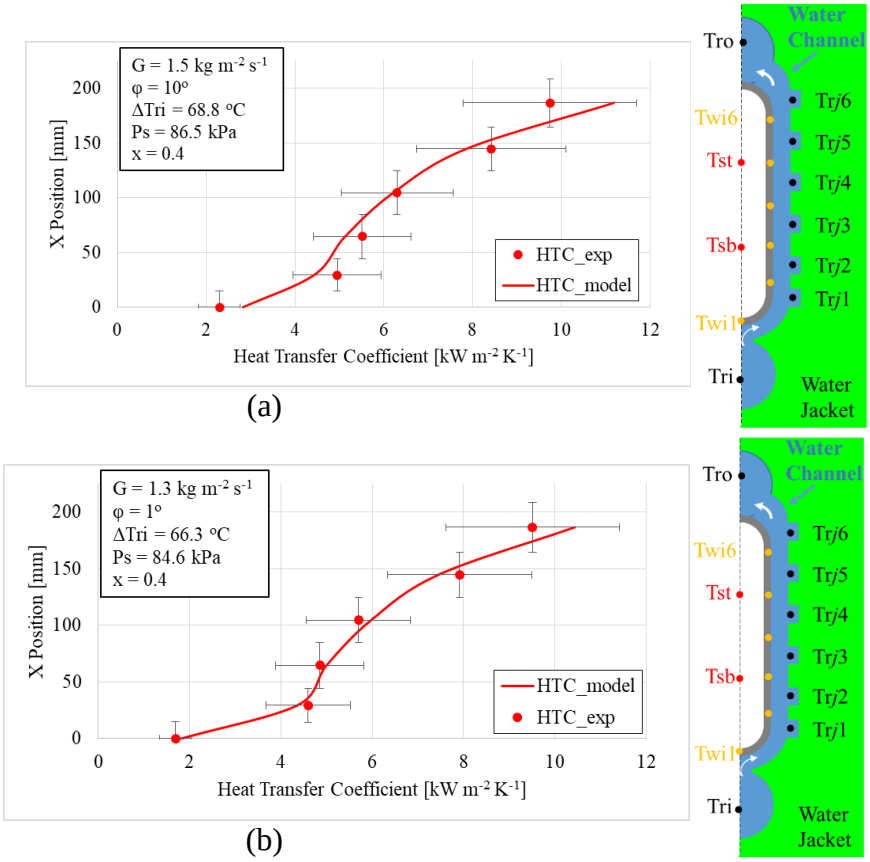

Figure 9.25: Local condensation HTC for the tube inclined at 10° (a), and 1° (b) compared to the correlation of Dobson & Chato [2] in the stratified condensate at the tube bottom and to the analytical model of Dhir & Lienhard [4] in the condensing film region along the tube wall

Figure 9.25 (b) displays the local HTC for the tube inclined at 1°. The HTC is relatively unchanged in the condensing-film region in comparison to the 10° tube. However at the tube bottom, the HTC is reduced by 25%, due to the thicker condensate layer. Once again, the experimental HTC agrees well with the HTC predicted by the model.

Further examination of the effect of inclination can be seen in Figure 9.26. At the condenser bottom, HTC increases 25% from a horizontal condenser to a condenser inclined at 38°. The majority of that increase in HTC occurs between 0° and 10°, with a plateau at higher inclination angles. As shown in Chapter 3, the depth of the stratified condensate layer decreases significantly from 0° to 3° inclination, with more gradual change at higher inclination angles. This is the primary cause of the increase in HTC at the bottom of the tube. In the condensing-film region higher along the wall, there is a slight decrease in HTC as inclination angle increases. This is likely due to an increase in film thickness on the condenser wall due to the film's falling path increasing as inclination angle increases.

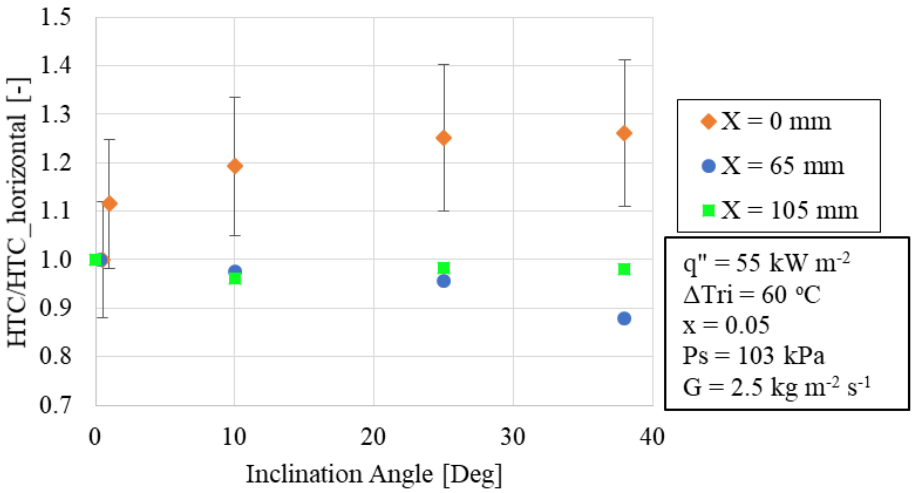

Figure 9.26: The effect of inclination angle on heat transfer coefficient is shown for three different positions on the condenser wall

The effect of temperature difference between the wall and steam is shown in Figure 9.27. Here, the temperature difference is averaged over all six measurement points. As expected, the HTC increases as temperature difference decreases. Decreasing the wall-steam temperature difference decreases the thickness of the condensate film, which reduces the resistance to heat transfer. This can be seen directly in the analysis of Nusselt [3]. The most drastic change is seen at the top of the condenser for the smallest wall-steam temperature difference. At this uppermost point, the temperature difference is only 0.4 °C. According to Nusselt's [3] theory, as temperature difference goes to zero, the HTC will tend towards infinity. Therefore, this uppermost point sees the most drastic increase.

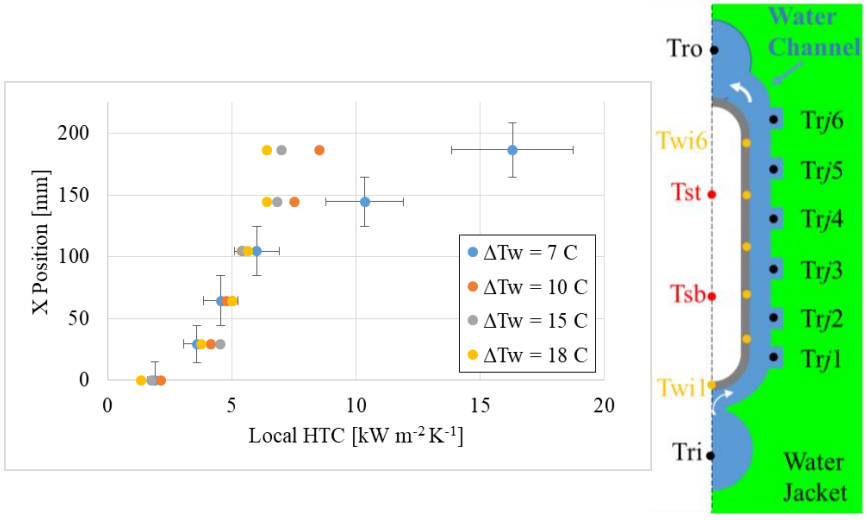

Figure 9.27: Local HTC for different average wall-steam temperature differences ($\Delta T_w = T_s - T_w$)

A similar trend is shown in Figure 9.28, although the temperature difference shown here is between the steam and the inlet of the cooling water. Temperature difference is proportional to the heat flux at the water inlet. Once again, for lower temperature difference, HTC increases, with most of this increase occurring near the top of the condenser. The cause once again is the lower temperature difference yielding lower heat flux, resulting in a thinner condensate film. This plot is of more practical use to engineers, since the inlet water (or air)-steam temperature difference is known at the design stage.

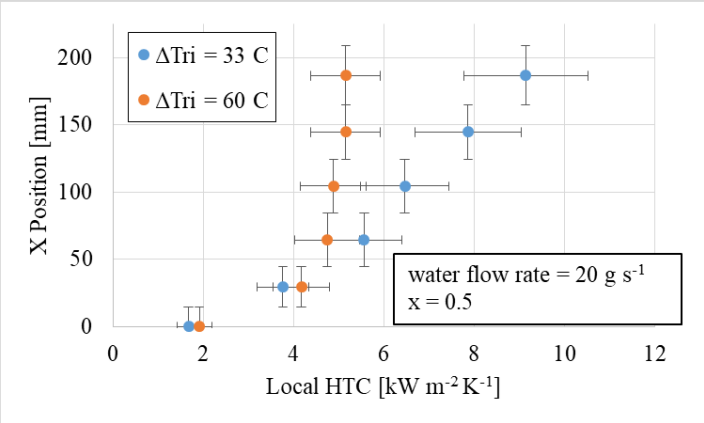

Figure 9.28: Local HTC for two temperature differences between steam and inlet cooling water ($\Delta T_{ri} = T_s - T_{ri}$)

Finally, the effect of vapor quality on local HTC is shown in Figure 9.29. In the condensing-film region, HTC is not affected by quality within the limits of uncertainty. In this region, the only effect of decreasing quality is to decrease the vapor velocity. The lack of a corresponding decrease in HTC indicates that vapor shear has no effect on the HTC. This is not surprising, due to the low mass flux. At the highest measured quality of 0.74, the vapor velocity is only 4 m s^{-1}. With regards to quality, the only significant effect is seen at the bottom of the condenser tube. In this region of the stratified condensate layer, the HTC decreases as quality decreases. As vapor quality decreases, the amount of collected condensate at the bottom of the tube increases. This decreases the HTC.

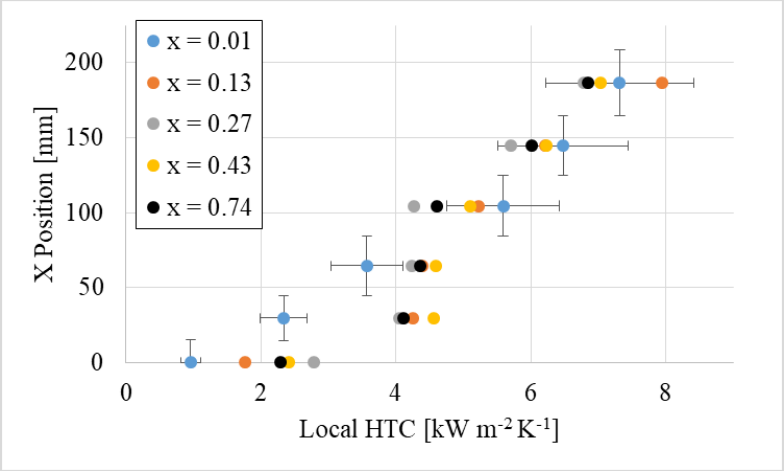

Figure 9.29: Local HTC at five different vapor qualities

9.4.4 Effect of Temperature Glide in the Air- and Water-Cooled Sections

Increasing the temperature glide on the cooling side has a strong effect on steam-side HTC, especially for cases of high temperature glide. Figure 9.30 shows that as temperature glide increases, HTC increases at the top of the tube. This occurs because the increasing water temperature on the cold side of the condenser causes the wall temperature to increase. This elevated wall temperature decreases the local rate of condensation, which leads to a thinner condensate film and a higher HTC. According to Nusselt [3] theory, this increase is proportional to $\Delta Tw^{-0.25}$. Therefore, there is negligible effect at higher ΔTw, but the increase in HTC trends towards infinity as ΔTw goes to zero. For this reason, there is a notable effect of ΔTw at the top of the tube only. For reference, Figure 9.22 shows the decreasing ΔTw along the wall height.

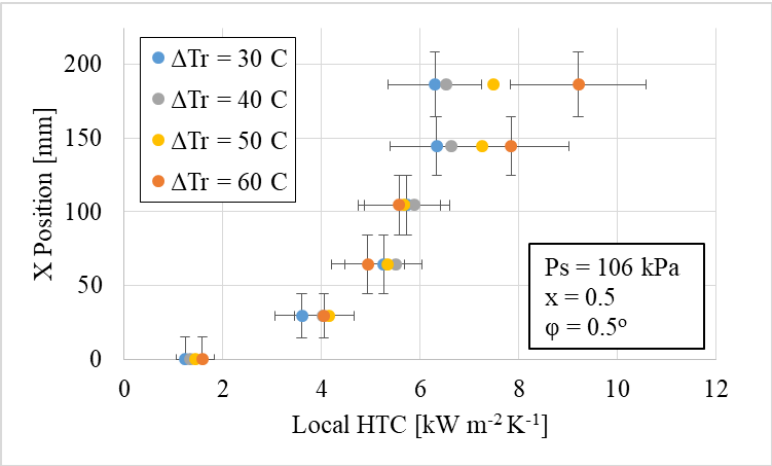

Figure 9.30: Effect of temperature glide (ΔTr = Tro-Tri) on the steam-side HTC

Figure 9.31 demonstrates that for a given temperature glide, heat flux also has an effect on HTC. Decreasing heat flux increases HTC, with the most pronounced change occurring at the

top of the tube. The cause is the same as that stated above: the decreased heat flux decreases the condensation rate and the film thickness, which enhances the HTC. Figure 9.31 also compares the HTC profile in the air-cooled test section and the water-cooled test section. This comparison shows a similar trend between HTC in both the air- and water-cooled test sections. The low heat flux in the air-cooled test section yields a high HTC, as seen in the water-cooled test section. This indicates that the HTC determined in this water-cooled test section is an accurate representation of the HTC in an operating ACC. In addition, it suggests that the steam-side HTC in an air-cooled condenser can be directly determined based on the air-side temperature glide and heat flux.

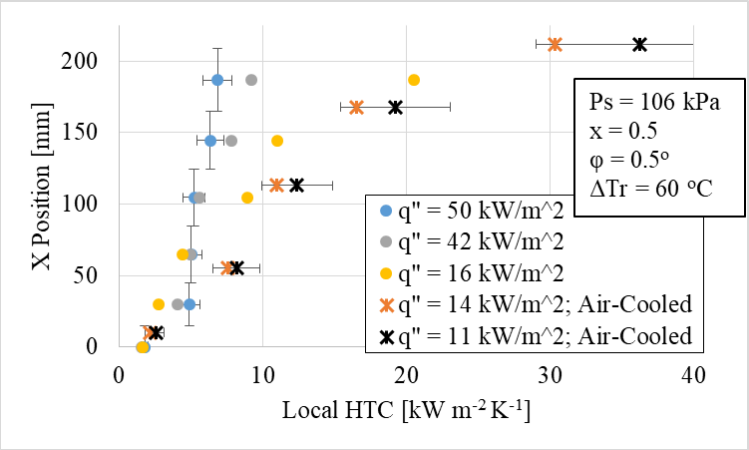

Figure 9.31: Comparison of the effect of heat flux on the local HTC profile. The lowest heat flux was determined in the air-cooled test sections

9.4.5 Condensate Subcooling along the Condenser Length

Figure 9.32 shows condensate temperature in comparison to vapor temperature along the condenser length for a tube inclined at 0.5°. Condensate depth at the tube outlet is varied artificially by varying the opening of a valve at the outlet of the condenser. This variation in condensate depth is created solely to show the effect of condensate depth on subcooling and HTC of the condensate. The varying outlet depth of the condensate is not a reflection of varying condenser operating conditions, such as inclination or air-side flow rate.

The results show that condensate subcooling increases along the condenser length, and increases as condensate depth increases. Subcooling is negligible at Z = 2 m except for the condition with condensate depth equal to 112 mm at the condenser outlet (the maximum depth tested). In this deepest case, the condensate fills nearly half of the condenser tube at the outlet. For the other conditions, subcooling is less than 1.5 °C at Z = 2 m. There is significant

subcooling at the condenser outlet for all conditions, with subcooling at the outlet increasing as condensate depth increases. Increased subcooling indicates a decrease in temperature gradient at the tube bottom, which should decrease the conductive heat transfer rate.

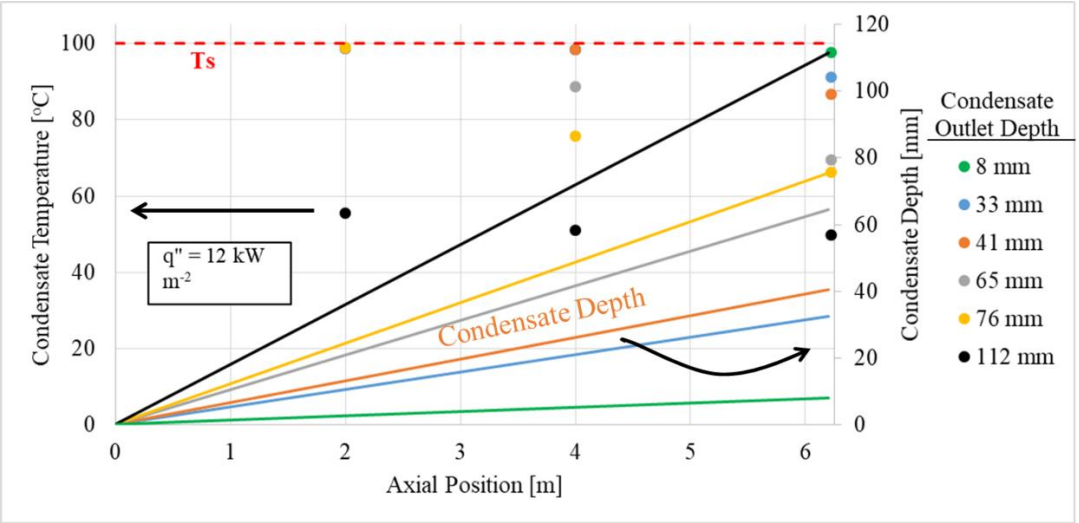

Figure 9.32: Condensate temperature along the condenser at several different condensate depths. Condensate depth is measured at the condenser inlet and outlet, and is plotted on the right ordinate

9.4.6 Results for Heat Transfer Coefficient in the Stratified Condensate Layer

Figure 9.33 shows the heat transfer coefficient at the bottom of the tube (over the area highlighted in red and labeled 'HTC_{strat}' in Figure 9.21). The local bulk heat transfer coefficient at the tube bottom decreases as depth of the condensate increases for a constant mass flow rate. The primary cause for the decreasing HTC is a decrease in temperature gradient, which is inversely proportional to the condensate depth (Figure 9.32). The HTC in this region also exceeds that predicted by the correlation of Dobson and Chato [2]. The experiment also exceeds the lower-bound assumption of one-dimensional conduction through the liquid layer. This conduction model neglects any convective heat transfer.

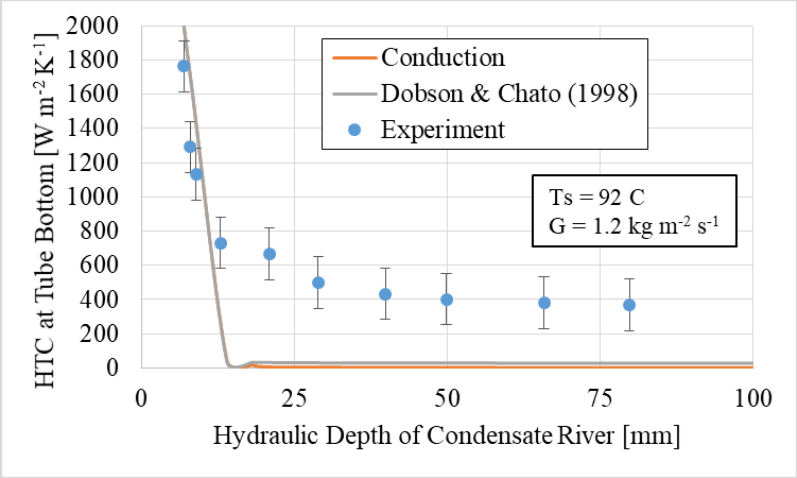

Figure 9.33: HTC through stratified condensate layer decreases as hydraulic depth of the condensate increases. For depths < 15 mm, HTC encompasses both the film-condensing and stratified-condensate regions

Figure 9.34 shows that HTC through the stratified layer increases as a function of the ratio between Prandtl number of the saturated liquid, $Pr_{f,sat}$ (top of the condensate layer) and Prandtl number of the liquid evaluated at the wall temperature, $Pr_{f,w}$. The Prandtl number evaluated at the wall temperature was as much as three times greater than the Prandtl number evaluated at saturation temperature for the experimental points. This ratio is inversely related to the subcooling of the liquid. Miropolski [133] suggested this ratio as a factor affecting single-phase convective heat transfer coefficient, and results show that it is a strong predictor of HTC.

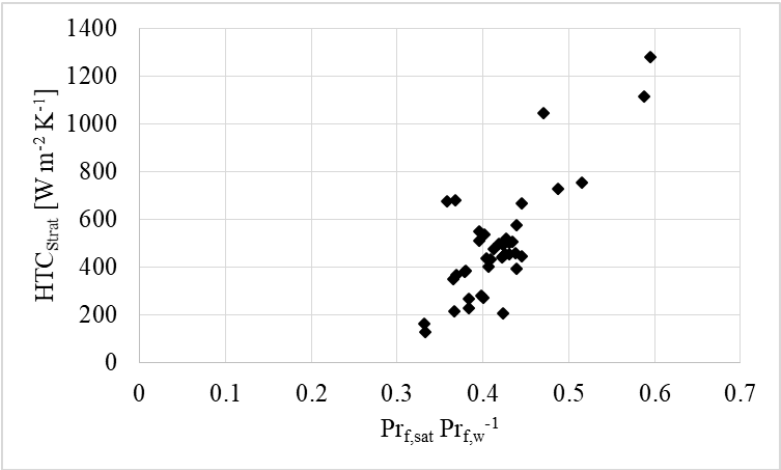

Figure 9.34: HTC through the stratified layer is shown to increase as the ratio of liquid Prandtl numbers at saturation temperature and wall temperature increases

For this low-Reynolds-number laminar flow, there is no dependence of HTC on velocity of the condensate. Figure 9.35 shows that the measured velocities are below 0.04 m s^{-1}, and HTC

does not increase as velocity increases. This result is expected for convective laminar flow heat transfer, where Nusselt number is a function of channel geometry only [134].

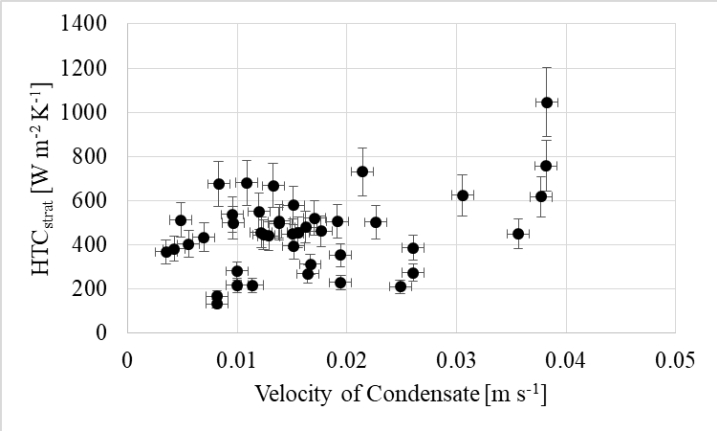

Figure 9.35: Heat transfer coefficient through the stratified condensate shows no dependence on velocity of the condensate

9.4.7 Correlation for Heat Transfer Coefficient in the Stratified Condensate Layer

The correlation for HTC in the stratified layer is modeled after the correlations by Miropolski [133] and Dobson and Chato [2]. The proposed correlation for HTC through the stratified condensate layer is presented in equation (9.22).

$$HTC_{strat} = 200\,\mathrm{Pr}_{f,sat}^{-3.4}\left(\frac{\mathrm{Pr}_{f,sat}}{\mathrm{Pr}_{f,w}}\right)^{0.36}\left(\frac{d_h}{\mathrm{W}}\right)^{0.42}\left(\frac{k_{f,sat}}{d_h}\right) \tag{9.22}$$

The first factor ($Pr_{f,sat}$) indicates that HTC increases as thermal conductivity increases, or as fluid viscosity decreases. The second factor ($Pr_{f,sat}/Pr_{f,w}$) is an indicator of the liquid subcooling, to which it is inversely proportional. The third factor (d_h/W) is the aspect ratio of the stratified layer. For laminar convective heat transfer, Nusselt number increases as this aspect ratio increases from one to infinity [135]. The correlation was developed for the range of conditions listed in Table 9.2.

Table 9.2: Range of variables used to develop the correlation for HTC in the stratified condensate layer

Variable	**Range**
Tsat [^{o}C]	91.7 – 104.0
Tw [^{o}C]	30.4 – 57.7
d_h [mm]	13 – 132
Re_{dh} [-]	810 – 4100

Comparison with experimental results, as well as with previous correlations and a one-dimensional conduction model is presented in Figure 9.36. The correlations of Dobson and

Chato [2], Rosson and Meyers [1], and the conduction model show no relation to the experimental data over the range of experimental conditions. The correlations, in particular, are insensitive to the hydraulic depth of the condensate. The new correlation predicts 61% of the data to within 20% error, with a mean absolute percent error (MAPE) of 21%. Figure 9.36 also shows additional experimental points that were recorded in order to verify the repeatability of the correlation. The correlation predicts 80% of these points to within 20% error, with a mean absolute percent error of 16%.

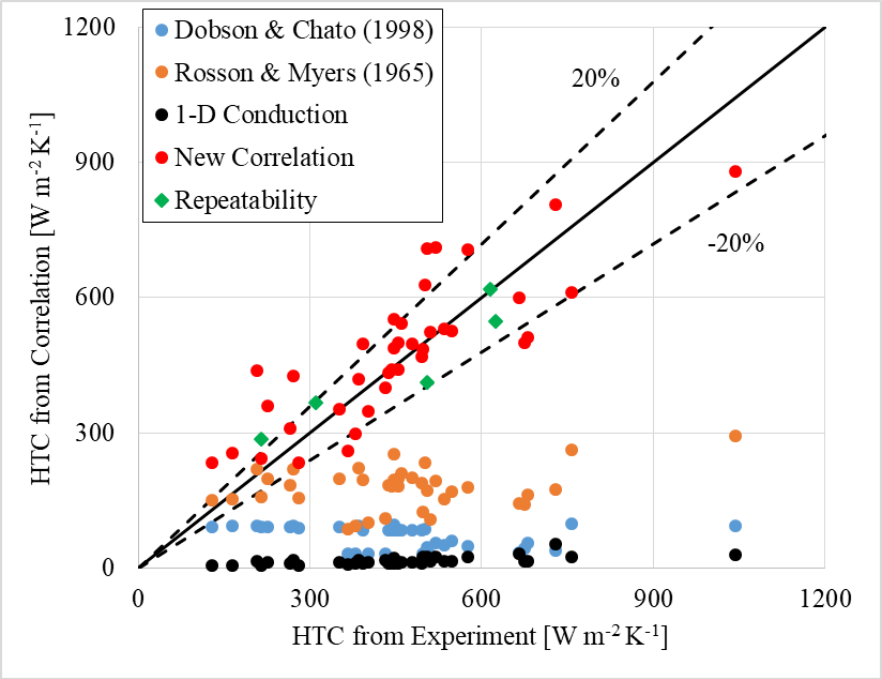

Figure 9.36: A comparison of experimentally-determined HTC through the stratified condensate layer with prediction by one-dimensional conduction and three correlations, including a new correlation proposed in this paper

9.4.8 Results for Heat Transfer Coefficient in the Condensing Film Region

This section presents results for the average HTC in the condensing film region, above the stratified condensate layer. In this region, the film is thin (~40 um), so condensation is the predominant mode of heat transfer. Figure 9.37 shows that HTC in this region is not affected by quality. Decreasing quality has two main effects in this condenser: vapor velocity decreases, and depth of the stratified condensate layer increases. Decreasing vapor velocity decreases the shear force on the liquid film. Vapor shear can increase HTC by creating waves on the liquid film, but in this condenser, vapor shear is too low to have any effect. Increasing depth of the condensate has no effect on the film-condensation region. This agrees with the model of Dhir and Lienhard

but disagrees with the film-condensation models of Rosson and Myers [1] and Dobson and Chato [2].

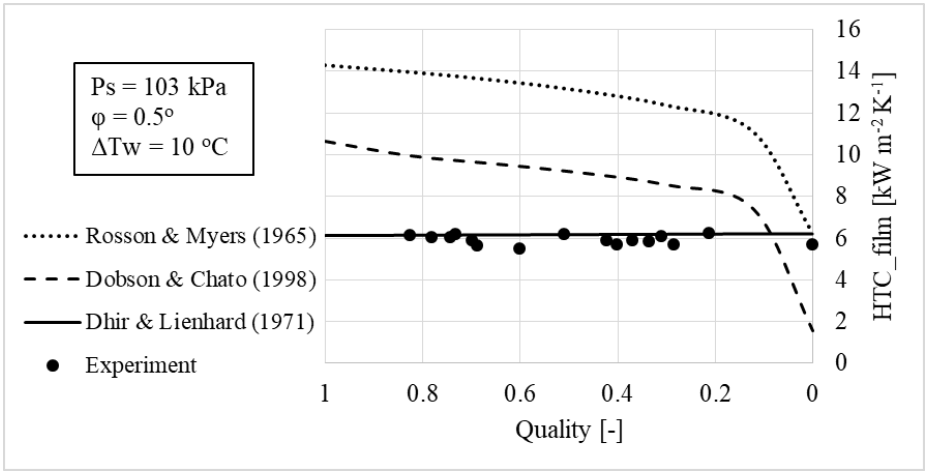

Figure 9.37: Heat transfer coefficient in the condensing-film region does not vary with quality

Figure 9.38 shows that HTC decreases as the wall-steam temperature difference increases. The increasing temperature difference increases the thickness of the condensate film, which decreases the HTC. The correlations shown in the figure all predict a power-law relationship between $T_{w,film}$ and film HTC, with $HTC_{film} \sim T_{w,film}^{-0.25}$. The experimental results show a relationship of $HTC_{film} \sim T_{w,film}^{-0.55}$

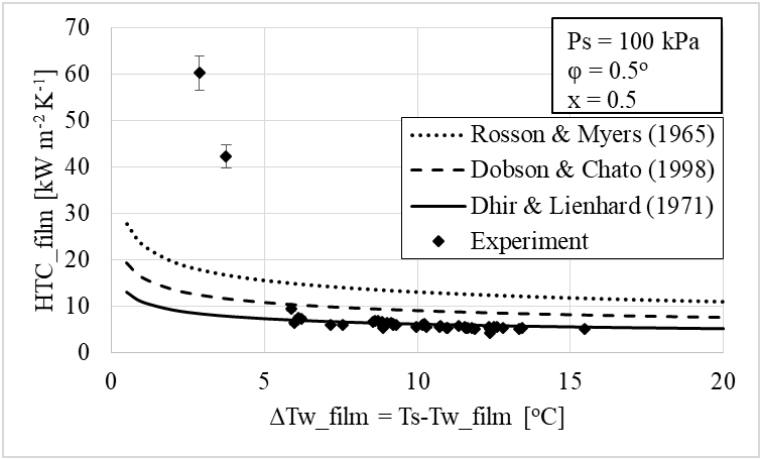

Figure 9.38: HTC in the condensing film region has a power-law increase as wall-steam temperature difference decreases

Figure 9.39 shows that film HTC increases as temperature glide of the cooling water (ΔT_r) increases. This trend can be explained in two manners. An increased ΔT_r is caused by decreased water flow rate. This decreased flow rate decreases the heat flux, which increases the HTC. Additionally, as ΔT_r increases, the average wall-steam temperature difference (ΔT_w) decreases. This also leads to an increase in HTC, as seen in Figure 9.38.

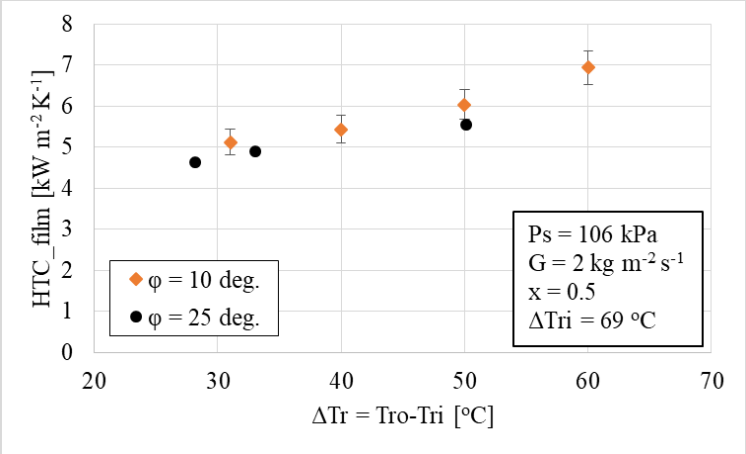

Figure 9.39: Heat transfer coefficient in the condensing-film region increases as air-side temperature glide increases

Figure 9.40 shows that the mean HTC decreases as the inlet temperature difference (ΔT_{ri}) increases. Increasing inlet temperature difference leads to increased heat flux. As heat flux increases, HTC decreases.

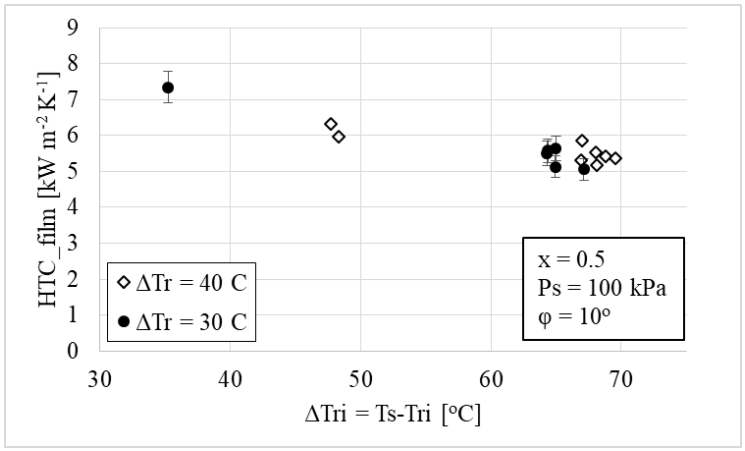

Figure 9.40: Heat transfer coefficient in the condensing-film region decreases as inlet air-steam temperature difference increases

Figure 9.41 shows that HTC in the condensing-film region decreases as inclination angle increases. This agrees with the prediction of Chato [47]. In the condensing-film region, increasing inclination angle increases the falling path of the condensing film. This increases the mean film thickness, which decreases the mean HTC. According to the theory of Nusselt, the mean HTC is proportional to $Length^{-1/4}$, so HTC is proportional to $(cos\varphi)^{1/4}$.

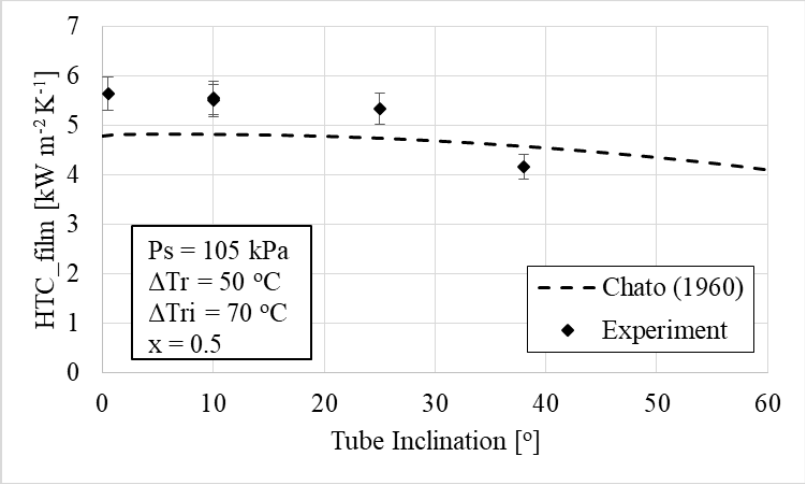

Figure 9.41: Heat transfer coefficient in the condensing-film region decreases as inclination angle increases

Figure 9.42 shows that film HTC increases as steam temperature increases. This is predominantly the result of two changes in properties. Thermal conductivity of the liquid film increases as temperature increases, which increases conduction through the condensing film. Viscosity of the liquid film also increases as temperature increases, which decreases the thickness of the condensing film. Both of these changes have a positive effect on film HTC. Both the direction and magnitude of this change in HTC agree with the model of Dhir and Lienhard [4].

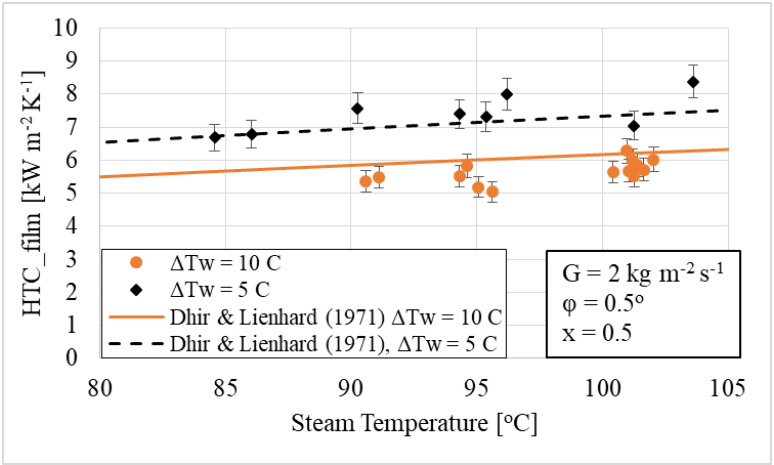

Figure 9.42: Heat transfer coefficient in the condensing-film region increases as steam temperature increases

9.4.9 Correlation for Heat Transfer Coefficient in the Condensing Film Region

Based on the experimental data for HTC in the condensing-film region determined in both the water-cooled and air-cooled test sections, a new correlation is proposed. In this

condensing-film region, Nusselt-type condensation is assumed, but an extra factor is introduced to account for the tube inclination angle. The correlation requires input of the average wall temperature of the entire tube cross-section. The correlation is fit to two-thirds of the data points, and validated with the remaining one-third of data points, to avoid overfitting and provide validation of the model. The range of vapor superficial Reynolds numbers included in the model development is 0-7,000. The proposed correlation (version 1) for film HTC is given in equation (9.23).

$$HTC_{film} = 0.75\left(\frac{k_f}{p/2}\right)\left[\frac{g\rho_f\left(\rho_f-\rho_g\right)i'_{fg}\left(\frac{p}{2}\right)^3\cos\varphi}{\mu_f\left(T_s-T_w\right)k_f}\right]^{0.25} \tag{9.23}$$

$$i'_{fg} = i_{fg} + 0.68c_{p,f}\left(T_s-T_w\right) \tag{9.24}$$

The correction to latent heat (i_{fg}) accounts for effects of subcooling and convection in the condensate film. For all conditions, the correction to latent heat is less than 3%, with a resulting correction to HTC_{film} of less than 1%. Sadasivan and Lienhard [136] suggested an alternative correction to account for the effects of inertia in the film. This correction on latent heat is less than 0.5% for all conditions and is neglected. The correlation is compared to experimental results and three existing models in Figure 9.43. The new correlation more accurately captures the trend of the experimental data than do the existing models.

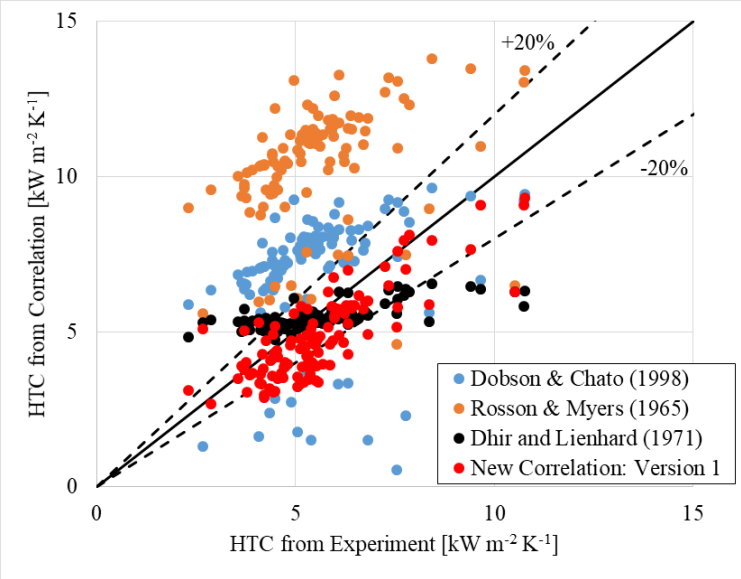

Figure 9.43: Comparison of experimental data with three existing correlations, as well as with a new proposed correlation for HTC in the condensing film region

Despite its accuracy, this correlation requires an accurate model of the wall temperature in order to be applied. To determine this wall temperature accurately, the condenser cross-section must be discretized into small sections, due to the varying heat flux and HTCs on the steam and air sides. This discretization requires knowledge of the local air-side HTC. The local air-side HTC can usually be found only by performing CFD for the air side. Unfortunately, less computationally-expensive models can be significantly less accurate. As an example, a simple condenser model can be created by assuming constant air-side and steam-side HTCs to determine an average wall temperature in each cross section. Using this average wall temperature, the accuracy of the new correlation is drastically reduced, as shown in Figure 9.44.

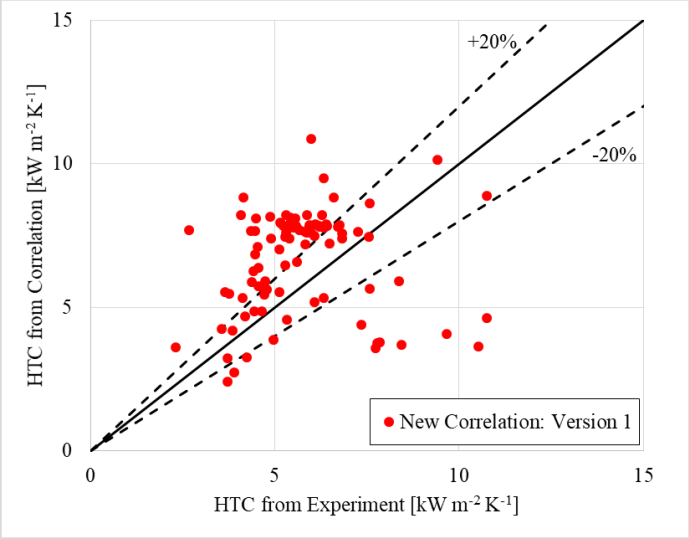

Figure 9.44: Accuracy of the proposed correlation decreases significantly if the wall temperature is not accurately predicted

The added uncertainty in determining the wall temperature profile makes the uncertainty of this correlation unacceptable. Therefore, if the wall temperature profile cannot be accurately predicted, an alternative correlation – without wall temperatue – is required. Kroger [69] developed such a correlation analytically for an ACC by assuming a constant air-side HTC. By fitting his analytical correlation to the current experimental data, an alternative correlation (version 2) is proposed that does not require estimation of the wall temperature:

$$h_{film} = 4.5\times10^{-4}\frac{k_f}{H}\left(\cos\varphi\right)^{0.25}\left[\frac{H^3\rho_f^2 g\, i_{fg}\, dZ}{\mu_f \dot{m}_a c_{pa}\left(T_s - T_{ai}\right)\left[1-\exp\left\{-UdZH/\left(\dot{m}_a c_{pa}\right)\right\}\right]}\right]^{0.62} \tag{9.25}$$

This correlation more accurately predicts the experimental data when the wall temperature is unknown, as seen in Figure 9.45.

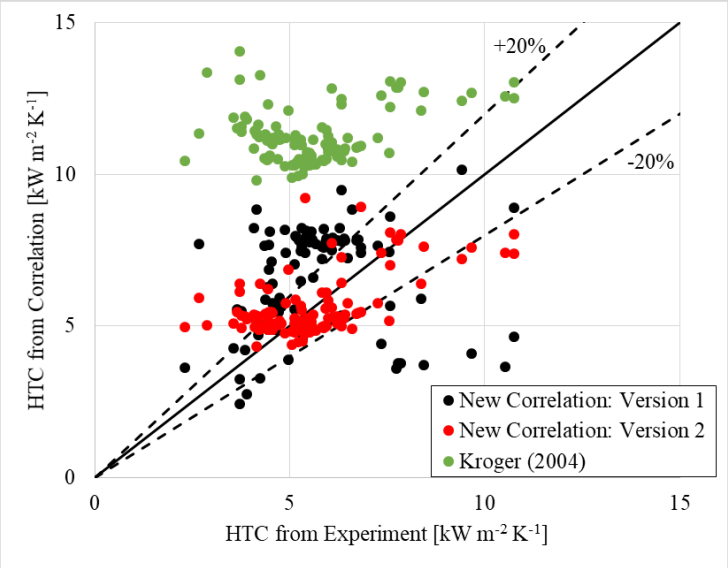

Figure 9.45: A comparison of correlations for HTC in the condensing film region, applied when the wall temperature is unknown. The correlation of Kroger [69] and version 1 (equation (9.23)) of the new correlation proposed here over-predict the experimental data. Version 2 of the new correlation (equation (9.25)) does not required prior knowledge of the condenser wall temperature and is the most accurate in this situation

9.4.10 Results for Circumferentially-Averaged Heat Transfer Coefficient

Mean (circumferentially-averaged) HTC is dominated by film-condensation effects, because the majority of the wall is in the condensing-film region. For nearly all conditions, the void fraction is greater than 0.9, so the stratified condensate layer accounts for less than 10% of the area-averaged HTC. Therefore, the circumferentially-averaged HTC closely resembles the film HTC presented in section 9.4.8. Figure 9.46 shows that mean HTC is not significantly affected by quality. This closely matches the results for the condensing-film region in Figure 9.37. This contrasts with the prediction of Shah [70], but agrees with the prediction of Chato [47]. Although decreasing quality has no effect in the condensing-film region, it increases the depth of the stratified condensate layer. Increasing depth of the condensate decreases HTC through the tube bottom, however, the overall effect of quality is minimal – less than the uncertainty of the HTC measurements.

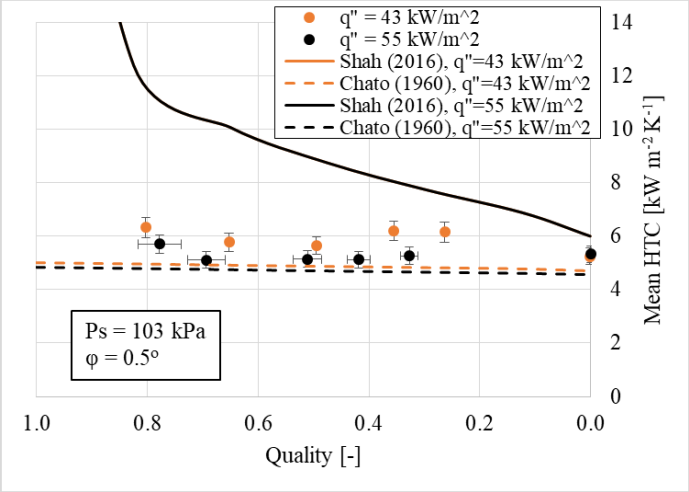

Figure 9.46: Effect of quality on circumferentially-averaged HTC is negligible

Figure 9.47 and Figure 9.48 show the effects of heat flux and wall-steam temperature difference on the mean HTC. These charts also compare the HTC determined in the water-cooled section with the HTC determined in the air-cooled section, as explained in Chapters 4 and 5. The results show that mean HTC is a function of heat flux and wall temperature, with the strongest effect in the lower range of both variables. The general trend agrees with the predictions of Dobson and Chato [2] and Chato [47]. However, the experimental HTC exceeds that of the correlations when heat flux is less than 17 kW m^{-2} or ΔT_w is less than 10 °C for all of the experimental data sets. One possible explanation is the presence of dropwise condensation, which was observed during the diabatic visualization in the air-cooled tube.

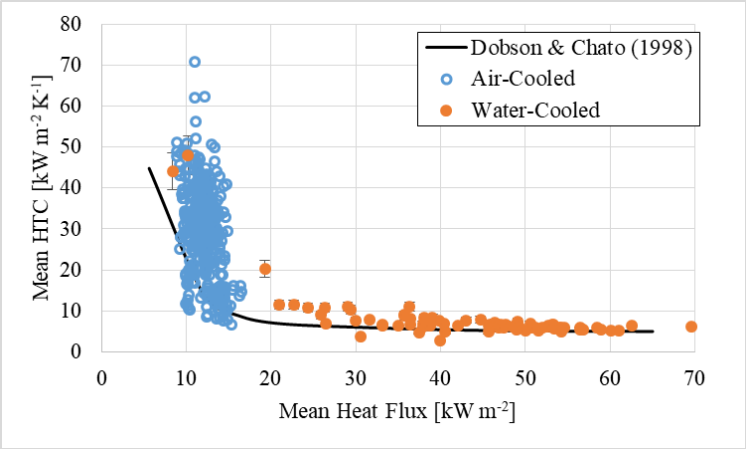

Figure 9.47: Mean HTC decreases as heat flux increases for all experimental data

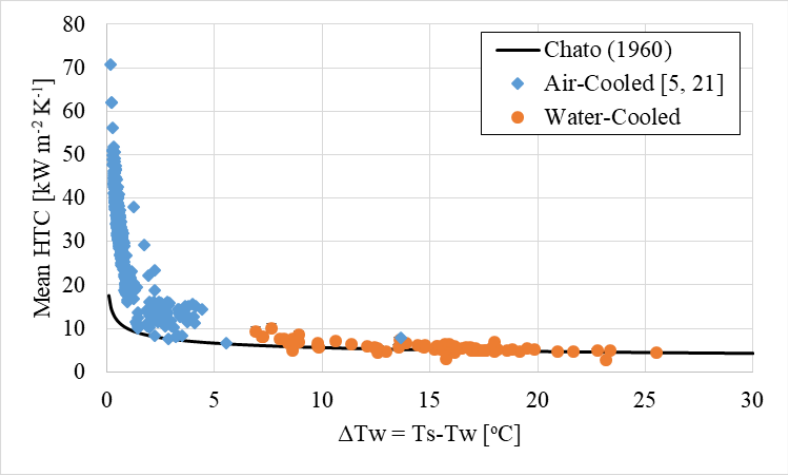

Figure 9.48: Circumferentially-averaged HTC decreases as wall-steam temperature difference increases

Figure 9.49 and Figure 9.50 show that mean HTC increases as temperature glide of the cooling water (ΔT_r) increases. This closely follows the trend of the condensing-film HTC, seen in Figure 9.39. These charts also show that the circumferentially-averaged HTC decreases as inclination increases.

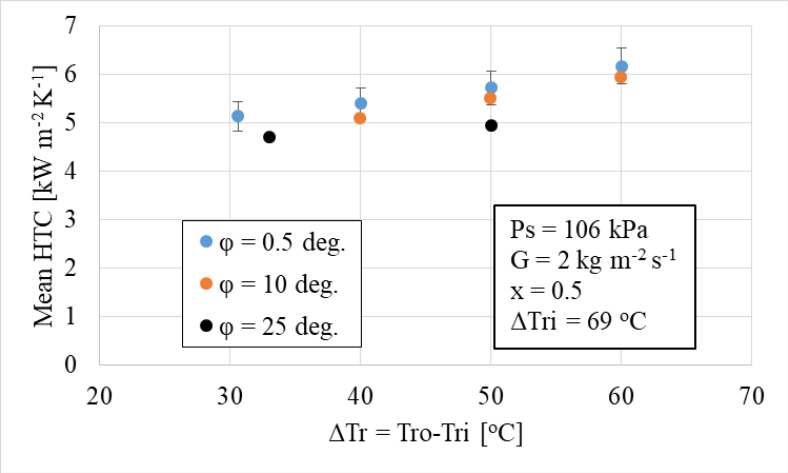

Figure 9.49: Circumferentially-averaged HTC increases as temperature glide on the cooling side increases

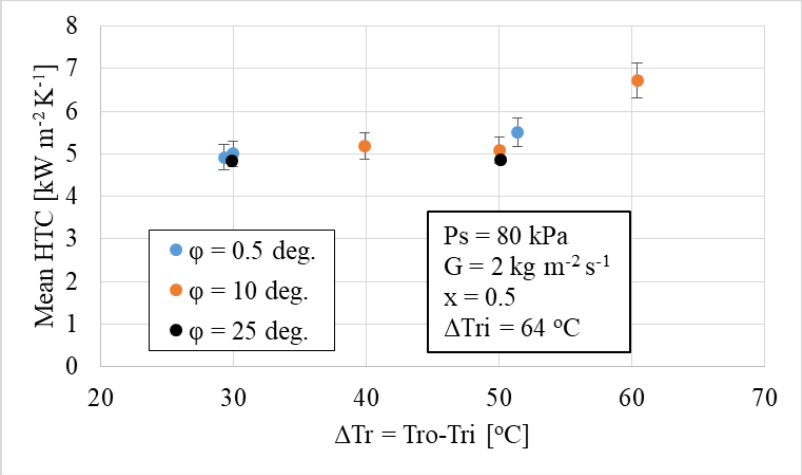

Figure 9.50: Circumferentially-averaged HTC increases as temperature glide on the cooling side increases

Figure 9.51 shows that the mean HTC decreases as the inlet temperature difference (ΔT_{ri}) increases. Increasing inlet temperature difference leads to increased heat flux. As heat flux increases, HTC decreases in the condensing-film region, and therefore circumferentially-averaged HTC also decreases. This agrees with the correlation of Kroger [69].

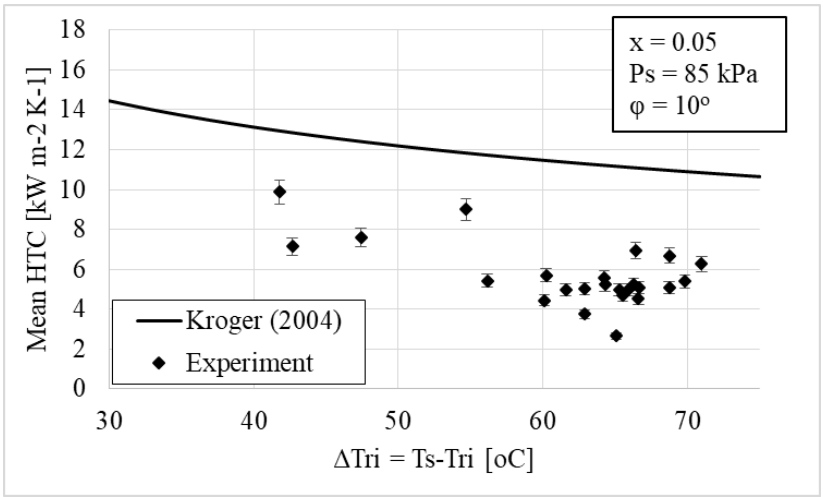

Figure 9.51: Circumferentially-averaged HTC decreases as inlet temperature difference increases

Figure 9.52 shows the effect of inclination angle on mean HTC. The HTC decreases slightly as inclination angle increases. This agrees with the predictions of Chato [47] and Kroger [69]. As discussed above, in the condensing-film region, increasing inclination angle decreases the HTC. A counteracting effect is a decrease in thickness of the stratified condensate layer as tube inclination increases. This causes the HTC in the stratified layer to increase. However, this increase only affects a small proportion of the condenser area, so the effect on mean HTC is negligible.

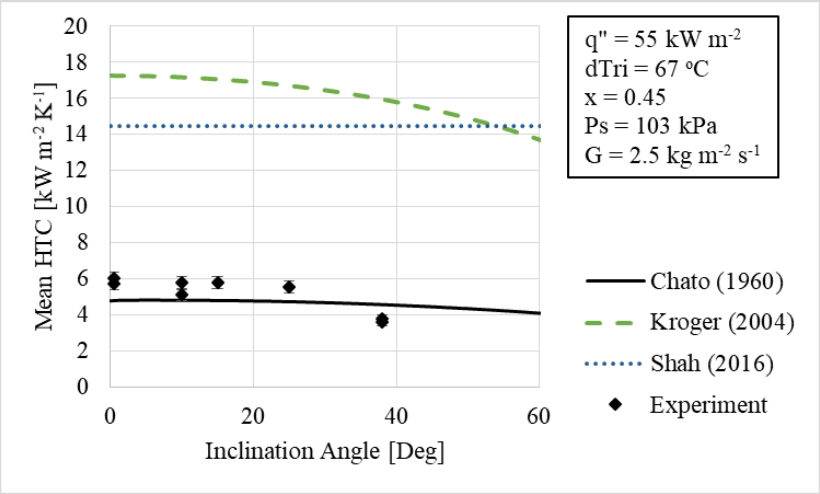

Figure 9.52: Circumferentially-averaged HTC decreases slightly as inclination increases

Figure 9.53 shows that circumferentially-averaged HTC increases as condensation temperature increases, while Figure 9.54 shows the same effect in terms on condensation pressure. This increase in HTC is predominantly the result of two changes in properties. Thermal conductivity of the liquid increases as temperature increases, which increases conduction through the condensing film and through the stratified liquid layer. Viscosity of the liquid also increases as temperature increases, which decreases the thickness of the condensing film and increases mixing in the stratified condensate layer. All of these changes have a positive effect on circumferentially-averaged HTC. Both the direction and magnitude of this change in HTC agrees with the prediction of Chato [47].

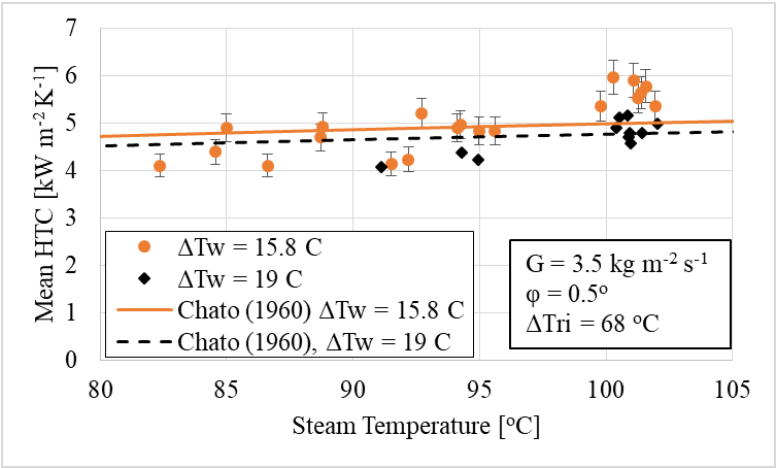

Figure 9.53: Mean HTC increases as condensation temperature increases due to higher thermal conductivity and lower viscosity of the condensate film

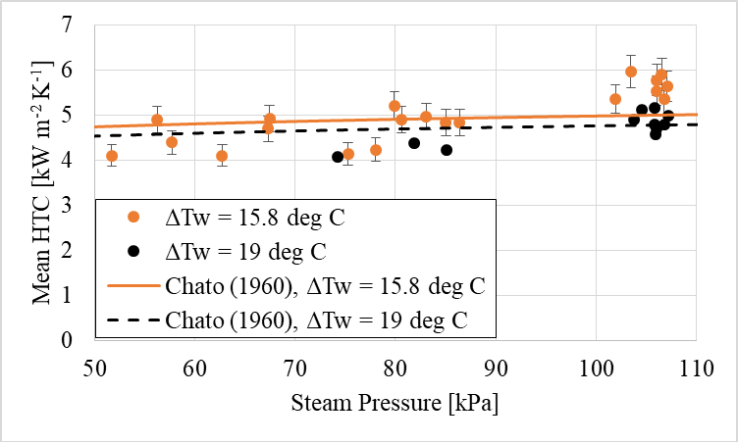

Figure 9.54: Mean HTC increases as condensation pressure increases due to higher thermal conductivity and lower viscosity of the condensate film

9.4.11 Correlation for Circumferentially-Averaged Heat Transfer Coefficient

The correlation for circumferentially-averaged HTC combines the correlations for the stratified condensate layer and the condensing-film region, as with the correlations of Dobson and Chato [2] and Rosson and Myers [1]. In the film region, equation (9.23) can be used if the average wall temperature can be estimated accurately. If a local model for wall temperature is not available, then equation (9.25) should be used in the condensing-film region. In the stratified liquid layer, equation (9.22) is used. The correlation is fit to two-thirds of the data points, and validated with the remaining one-third of data points, to avoid overfitting and provide validation of the model. The correlation (equation (9.26)) is valid for condensation in a stratified flow regime in inclined tubes under conditions of non-uniform heat flux and wall temperature. The range of vapor superficial Reynolds numbers included in the model development is 0-7,000, and liquid Reynolds number (based on hydraulic depth of the liquid) ranges from 800-4,100.

$$h_{mean} = \left(\frac{p_{wetted}}{p} \right) h_{strat} + \left(1 - \frac{p_{wetted}}{p} \right) h_{film} \tag{9.26}$$

To apply this correlation, an estimation of the depth of the stratified condensate layer is needed. The most accurate method is to use an open-channel-flow model, as proposed by Chato [47] and adapted to this condenser geometry in Chapter 7 of this thesis. However, previous results have shown that for most qualities (x > 0.1), conventional round-tube correlations can accurately predict the void fraction, with the correlation of Thom [126] fitting the experiments most accurately. Figure 9.55 shows that either the void fraction model of Thom [126] or the open-channel-flow void fraction model presented here is suitable for use with the model for

quality > 0.05. Below this quality, the void fraction model of Thom predicts condenser flooding, which causes a drastic decrease in HTC that was not seen experimentally. In order to avoid this error, if using one of the conventional void-fraction models designed for round tubes, assumption of constant void fraction when x < 0.05 will provide suitable results.

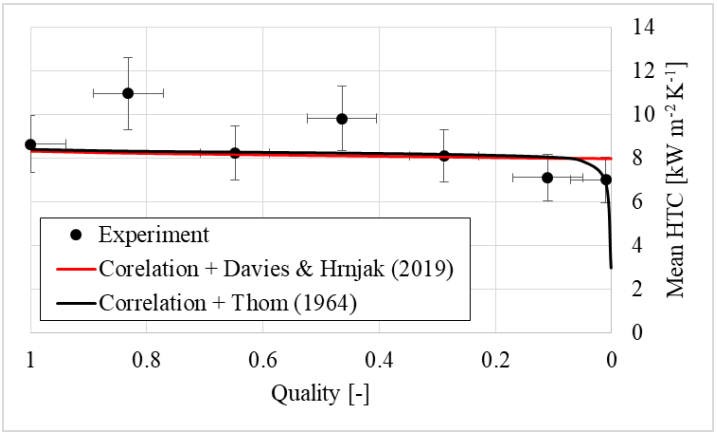

Figure 9.55: Mean HTC predicted by the correlation using two different void fraction models: the open channel-flow model presented in Chapter 7 (Davies & Hrnjak 2019) and that of Thom [126]. Predictions are compared to experimental results

Once the void fraction and the condensate cross-sectional area (A_c) are calculated, the wetted perimeter of condensate can be estimated by the following equations [137]:

$$P_{wetted} = \begin{cases} \sqrt{W_{top}^2 + \frac{16}{3}t_c^2} & A_c < \frac{\pi W^2}{8} \\ \frac{\pi W}{2} + 2\left(\frac{A_c - \pi W^2/8}{W}\right) & A_c > \frac{\pi W^2}{8} \end{cases} \tag{9.27}$$

$$W_{top} = \begin{cases} 2\sqrt{R^2 - (R - t_c)^2} & A_c < \frac{\pi W^2}{8} \\ W & A_c > \frac{\pi W^2}{8} \end{cases} \tag{9.28}$$

$$t_c \approx 0.8 R^{-0.34} A_c^{0.68} \quad \text{if} \quad A_c < \frac{\pi W^2}{8} \tag{9.29}$$

Figure 9.56 shows a comparison of several correlations for HTC with the new correlation (using the average wall temperature from the experiments). Of the previous correlations, that of Chato [47] is able to predict the experimental data most accurately. The new correlation is able to predict 77% of the data within 20%. Table 9.3 shows that the mean absolute percent error of

the new correlation is 14% if using the void fraction correlation presented in this thesis (Davies and Hrnjak 2019), and 15% if using the void fraction correlation of Thom [126]. Among the other correlations for HTC, that of Chato [47] is by far the most accurate in predicting the current data, with a MAPE of 27%.

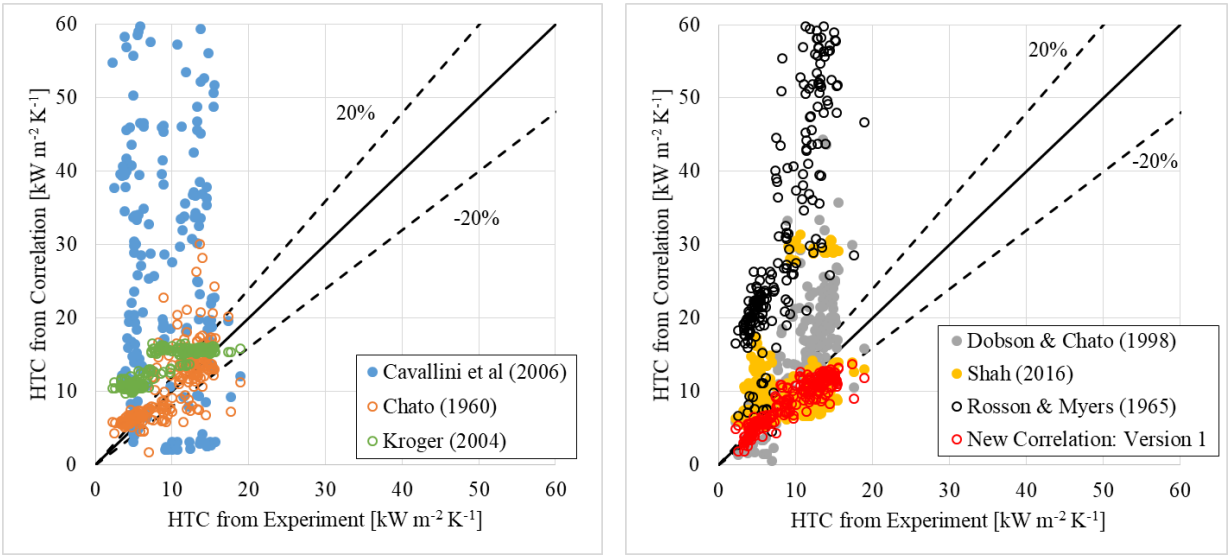

Figure 9.56: a) Comparison of experimental data (air-cooled and water-cooled) to previous correlations; b) Comparison of experimental data (air-cooled and water-cooled) to previous and new correlations

Table 9.3: Mean absolute percent error (MAPE) of predictions by several HTC correlations in comparison with experimental data from both the air and water-cooled sections

HTC Correlation	**Void Fraction Correlation**	**MAPE**
New Correlation	Davies & Hrnjak (2019)	14%
New Correlation	Thom (1964)	15%
Chato (1960)	Davies & Hrnjak (2019)	27%
Rosson & Myers (1965)	Davies & Hrnjak (2019)	318%
Dobson & Chato (1998)	Davies & Hrnjak (2019)	52%
Cavallini *et al.* (2003)	Davies & Hrnjak (2019)	416%
Kroger (2004)	Davies & Hrnjak (2019)	71%
Shah (2016)	Davies & Hrnjak (2019)	64%

Figure 9.57 shows that if the wall temperature profile is unknown, the alternative correlation (equation (9.25)) provides nearly-equivalent accuracy to the correlation requiring input of wall temperature.

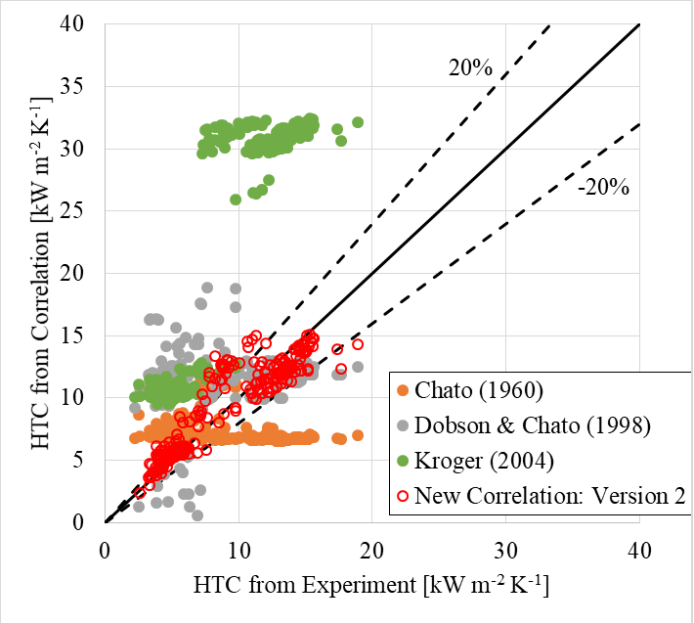

Figure 9.57: If the wall temperature profile is unknown, the alternative correlation provides higher accuracy than existing models

9.5 Conclusions

A method of determining heat transfer coefficient for condensation under the conditions of varying heat flux and wall temperature has been presented and shown to be accurate. The combined experimental and computational method has produced a heat transfer coefficient that has been validated with single-phase measurements, and that matches the analytical prediction during steam condensation. The condensation heat transfer coefficient has been shown to be affected by tube inclination, wall-steam temperature difference, inlet water-steam temperature difference, and vapor quality. In addition, two distinct heat transfer regions have been identified: the stratified-liquid region at the tube bottom and the condensing-film region along the tube wall. Increasing tube inclination increases the heat transfer coefficient at the tube bottom. Increasing vapor quality also increases heat transfer coefficient at the tube bottom. Increasing wall-steam temperature difference or inlet water-steam temperature difference has been shown to decrease heat transfer coefficient in the condensing-film region along the tube wall. In addition, condensation heat transfer coefficient in the condensing-film region has been shown to agree well with the analytical prediction of Dhir and Lienhard [4] if accounting for the local wall-steam temperature difference.

Further results and analysis for heat transfer coefficient in the two regions have then been presented. HTC in the stratified layer has been shown to vary with depth and subcooling of the

condensate, but not with velocity. HTC in the condensing-film region has been shown to vary with heat flux, wall-steam temperature difference, cooling-side temperature glide, inlet temperature difference, condensation temperature and inclination, but remain constant with changes in quality. These results have followed the general trends proposed by the Nusselt model for film condensation. Circumferentially-averaged HTC has been shown to closely follow the film condensation results, due to this region occupying the majority of the condenser area.

In comparing these results to existing correlations, HTC correlations designed for round tubes have been unable to accurately predict the experimental data. To improve the prediction, a new correlation for circumferentially-averaged HTC during stratified-flow condensation in large-diameter inclined, flattened tubes has been proposed. The new correlation accounts for heat flux through the stratified condensate layer as well as in the condensing-film region. Variations for use when the wall temperature is known (equation (9.23)) and unknown (equation (9.25)) are presented. In addition, a simple void fraction correlation (Thom [126]) is shown to provide sufficient accuracy for use with the correlation. The correlation accurately predicts the experimental data both from the current paper with a water-cooled condenser and from a previous experiment with an air-cooled condenser.

There are several additional considerations when applying this correlation to designing an air-cooled condenser. The correlation is presented here for a circumferentially-averaged HTC, because this is the standard practice in the literature. However, assuming a constant steam-side HTC will result in an inaccurate capacity prediction when modeling an air-cooled condenser as shown in Chapter 7. This is the result of the large variations in air-side temperature and heat transfer coefficient in each condenser cross section. A local model for heat transfer in each condenser cross section is recommended for accurate capacity prediction. It is best to use the correlation presented here for HTC in the stratified condensate layer, and then use the model of Dhir and Lienhard [4] to predict the local HTC in the condensing-film region. As shown in this thesis, the HTC in the stratified condensate layer is the most important for condenser design, even though it occupies a small area of the condenser. In this region, the steam-side HTC is the lowest, and therefore the heat flux is controlled by the steam-side HTC. Errors in estimating HTC in this region will significantly affect the accuracy of the condenser model, while errors in the condensing-film region will only have a minor effect. This proposed correlation, with two

heat transfer regions, provides the basis to create a local condenser model using the stratified portion of the HTC correlation.

Chapter 10 Conclusions and Recommendations for Future Work

10.1 Conclusions

Prior to this dissertation, very few experimental results existed for steam-side performance of flattened-tube air-cooled condensers. The complete lack of validated models for flow regime, void fraction, pressure drop and heat transfer coefficient created significant uncertainty in the condenser design. The majority of previous studies on air-cooled condensers were focused on air-side performance of the condenser. However, the steam side design has a significant effect on condenser and system performance. Steam-side pressure drop has a direct effect on power plant efficiency. In addition, the steam-side thermal resistance has been shown to be a significant contribution to the overall thermal resistance. This dissertation has addressed this gap in knowledge by characterizing the steam-side condensation in downwardly-inclined, co-current flattened-tube steam condensers.

The characterization of steam-side performance was completed through visualization and measurement of pressure drop, capacity and heat transfer coefficient in tubes with lengths of 10.7 m and 5.7 m. The 10.7 m facility provided diabatic visualization of the entire length of the condenser. The vast majority of prior visualization studies in any tube geometry were of short, adiabatic sections discrete qualities. In addition, these were the first published visualization results for large-diameter flattened-tube steam condensers. The results showed stratified flow along the majority of the condenser, with high void fraction (> 90%) over the entire condenser length and no flooding of liquid. In addition, stratified-wavy flow was shown to exist near the tube outlet for high tube inclination angles. This contrasts with condensation in horizontal tubes, where waves on the stratified liquid are caused by vapor shear and stratified-wavy flow always occurs before stratified-smooth flow. Tube inclination angle was also shown to have a significant effect on void fraction, as increasing the inclination angle increased condensate drainage and increased void fraction.

Pressure drop was measured in both the 10.7 m diabatic visualization section and in the 5.7 m full (un-cut) tube. A method was developed to characterize interfacial roughness in the 10.7 m tube that consisted of both diabatic steel and adiabatic polycarbonate surfaces. The results showed that increasing the tube inclination angle decreased the pressure drop due to increased

gravitational pressure recovery as well as decreased frictional pressure drop. The frictional pressure drop decreased due to increased drainage of liquid.

Two methods were then developed to determine steam-side HTC experimentally – an air-cooled method and a water-cooled method. The methods combined experiment with analytical modeling (air-cooled) and CFD (water-cooled) in order to determine local heat flux. These specialized techniques were necessary due to the large variations in heat flux, wall temperature and HTC (both air- and steam-side) along each condenser cross-section. Both methods were inexpensive and provided insight into local HTC under realistic condenser operating conditions. The water-cooled method improved the accuracy of the measurement while maintaining the same local heat flux as in an operating condenser. The results showed significant variation in steam-side HTC in each condenser cross-section (HTC increases from bottom-top by 4-30 times, depending on conditions). Two regimes for heat transfer were identified – the stratified liquid layer flowing axially at the tube bottom, and the condensing-film region along the tube wall. In the condensing-film region, the film condensation model of Dhir and Lienhard [4] was found to be accurate if accounting for the local wall-steam temperature difference. In the stratified liquid layer, the depth of the condensate was found to be the most significant factor in determining the HTC, and existing correlations for HTC in this region were found to under-predict the experimental results. From these results, a new correlation for HTC during steam condensation in large-diameter flattened tubes was developed. The correlation is a perimeter-weighted average of HTC in both the condensing-film and stratified-liquid regions. The correlation predicts the experimental results with a mean absolute percent error of 14%.

Once an understanding of the HTC was established, it was possible to understand the effects of the steam side on condenser capacity. The capacity was measured in both tube lengths at varying tube inclination angles, air velocity profiles, condensation pressures, and air inlet temperature differences. The capacity was shown to be negatively affected by condensate build-up at the bottom of the tube. Therefore, when increasing the inclination angle and draining the condensate, capacity in the 10.7 m tube increased at a rate of 0.041% for every degree increase in angle. This effect was negligible in the 5.7 m tube due to less accumulation of condensate. The effect of this condensate build-up could also be mitigated by arranging the airflow and air-steam temperature difference to be greater in regions with less accumulated liquid. These improved

airflow profiles – increased flow rate near the steam inlet, or reversed airflow direction – were shown to increase condenser capacity by more than 3% while maintaining fan power constant.

From these experimental results, a model for condenser capacity was created. The model accounted for circumferential variations in air and steam-side temperatures and heat transfer coefficients. In addition, the void fraction model developed for this condenser was implemented. This model significantly improved upon the accuracy of a model using circumferentially-averaged temperature and HTCs. The model was able to predict 98% of the experimental data to within 5% accuracy.

Overall, the work presented in this dissertation has an impact in three areas: the engineering design of air-cooled condensers, the understanding of condensation in uncommon duct shapes, and the experimental methods for determining HTC in air-cooled condensers.

From the engineering design standpoint, models were provided for void fraction, steam-side HTC and capacity. These models will reduce the uncertainty in condenser design. In addition, the effects of tube inclination angle on flow regimes, void fraction, pressure drop and capacity were quantified. Finally, a demonstration was performed of two improved airflow profiles.

For condensation specifically, this work expands the parameter space of existing condensation studies. This work provides the first experimental results for large flattened tubes with non-uniform heat flux and wall temperature. In addition, it extends the recent work in inclined condensation to large-diameter flattened tubes. In addition, the heat transfer through the stratified condensate layer has been quantified, and incorporated into a new correlation for HTC. This is the first experimentally-validated correlation for HTC in this (the most common) ACC design.

Finally, the development of two new, inexpensive experimental methods for determining local HTC under realistic operating conditions in an ACC provides additional tools to experimentalists. The close agreement between the two methods and to analytical predictions serves as a measure of validation of the methods. Experimental determination of HTC for ACCs is difficult due to the non-uniform heat flux and wall temperature, as well as the difficulty in measuring air-side flow rate and temperature. Therefore, experimental methods tend to be complex, and experimental studies are rare. This is the first study to provide two independent methods for determining HTC in the same ACC facility.

In addition, a method for full-length diabatic visualization was developed and demonstrated. The method was able to provide insight into realistic development of flow regimes while simultaneously measuring pressure drop and heat transferred.

In all, the results presented here provide the basic understanding of steam-side physics that are necessary for improving the flattened-tube air-cooled condenser design. These results – including for flow regimes, void fraction, pressure drop, capacity and heat transfer coefficient – show distinct differences to models developed for round tubes or refrigerant condensers. The condenser-specific models developed for void fraction, heat transfer coefficient and capacity can significantly reduce the uncertainty in condenser design.

10.2 Recommendations for Future Work

In regards to understanding of the fundamental physics on the steam side of flattened-tube air-cooled condensers, there are several gaps that future work must address. For example, this dissertation only addressed co-current downward flow. However, approximately 20% of the tubes in an operating condenser are configured for reflux condensation. Although reflux condensation is well-studied for thermosiphon and distillation applications, it has not been studied for this design of flattened-tube air-cooled condensers. Similar work in visualization and measurement of pressure drop and heat transfer coefficient as done here must be completed for the tubes during reflux condensation. In addition, reflux condensation brings the added concern of tube flooding – when vapor shear prevents the downward flow of condensate. A study of the onset of flooding is necessary for this condenser.

This work has also not addressed the effects of non-condensables on condenser performance. These effects can be quite significant for condensation. Prior research has shown that a 5% mass fraction of air could reduce steam-side HTC by 40% for these condensers [138]. This reduction in HTC can make the steam side thermal resistance much larger than the air side resistance. This further increases the importance of the steam side on condenser design. Once again, several studies on the effect of non-condensables have been made for other applications (such as nuclear reactors), but the conclusions from those studies need to be verified in this tube design.

Further work is also necessary in developing a model for steam-side pressure drop. Two factors limited the accuracy of pressure drop measurements in this study. The 10.7 m tube was

modified for visualization, so a model was developed to apply the results to an un-modified tube. This model adds uncertainty to the results. The 5.7 m tube had very low pressure drop due to the shorter length and lower mass flux. These small values of pressure drop were difficult to measure accurately. Therefore, pressure drop measurements at higher mass flux (higher condenser capacity) are necessary to accurately model the two-phase friction factor.

Additional work could be done in performing experiments at lower condensation pressure. The current experiments reached a minimum operating pressure of 50 kPa. This is towards the upper range of condenser operating pressures. Industry guidelines suggest that operating pressure reaches a minimum of 10 kPa. Therefore, it would be beneficial to further extend the experimental parameters to this low pressure. In particular, it is important to verify the flow regimes as the conclusions and models developed here are for stratified flow only.

Finally, investigating the combined effects of inclination angle on air- and steam-side performance is necessary. This work showed the effects of inclination angle on steam-side performance for a uniform air-side flow rate. However, varying the inclination angle will affect the uniformity of flow rate on the air side. By combining the results of this study with that of prior research on air-side non-uniformities, modeling work could be carried out to evaluate the overall effects of inclination on condenser performance.

REFERENCES

[1] H. Rosson, J. Myers, Point values of condensing film coefficients inside a horizontal tube, in: Chemical Engineering Progress Symposium Series, Vol. 61, 1965, pp. 190-199.
[2] M. Dobson, J. Chato, Condensation in smooth horizontal tubes, J. Heat Transfer, 120 (1998) 193-213.
[3] W. Nusselt, Die Oberflachenkondesation des Wasserdamffes the surface condensation of water, Zetrschr. Ver. Deutch. Ing., 60 (1916) 541-546.
[4] V. Dhir, J. Lienhard, Laminar film condensation on plane and axisymmetric bodies in nonuniform gravity, J. Heat Transfer, 93 (1971) 97-100.
[5] W.E. Forum, Global Risks 2015, in, 2015.
[6] M.A. Maupin, Kenny, J.F., Hutson, S.S., Lovelace, J.K., Barber, N.L., and Linsey, K.S., Estimated use of water in the United States in 2010, U.S. Geological Survey Circular 1405 (2014) 56.
[7] E. Shuster, Estimating freshwater needs to meet future thermoelectric generation requirements, in, National Energy Technology Laboratory, 2007.
[8] S. Fleischli, B. Hayat, Power plant cooling and associated impacts: the need to modernize US power plants and protect our water resources and aquatic ecosystems, in: Natural Resources Defense Council (https://www.nrdc.org/sites/default/files/power-plant-cooling-IB.pdf), 2014.
[9] EPRI, Power Plant Cooling System Overview: Guidance for Researchers and Technology Developers, in, Palo Alto, CA, 2015.
[10] K. Wilber, J. Maulbetsch, Air-Cooled Condenser Design, Specification, and Operation Guidelines, EPRI, Palo Alto, CA2005, (2005).
[11] V. Dorjets, Many newer power plants have cooling systems that reuse water, in: Today in Energy, epub, Energy Information Agency, 2014.
[12] J. Li, P. Hrnjak, Improvement of condenser performance by phase separation confirmed experimentally and by modeling, International Journal of Refrigeration, 78 (2017) 60-69.
[13] S. Lips, J.P. Meyer, Experimental study of convective condensation in an inclined smooth tube. Part I: Inclination effect on flow pattern and heat transfer coefficient, Int. J. Heat Mass Transfer, 55 (2012) 395-404.
[14] J.A. van Rooyen, D.G. Kröger, Performance trends of an air-cooled steam condenser under windy conditions, Journal of Engineering for Gas Turbines and Power, 130 (2008).
[15] Z. Ge, X. Du, L. Yang, Y. Yang, Y. Li, Y. Jin, Performance monitoring of direct air-cooled power generating unit with infrared thermography, Appl. Therm. Eng., 31 (2011) 418-424.
[16] V. Gadhamshetty, N. Nirmalakhandan, M. Myint, C. Ricketts, Improving air-cooled condenser performance in combined cycle power plants, Journal of energy engineering, 132 (2006) 81-88.
[17] T. Cheng, X. Du, L. Yang, Y. Yang, Co-current Condensation in an Inclined Air-cooled Flat Tube with Fins, Energy Procedia, 75 (2015) 3154-3161.
[18] K. Kekaula, Y. Chen, T. Ma, Q.W. Wang, Numerical investigation of condensation in inclined tube air-cooled condensers, Appl. Therm. Eng., 118 (2017) 418-429.
[19] V. Sukhanov, A. Bezukhov, I. Bogov, V. Tolmachev, Numerical-Experimental Studies of the Heat Transfer in an Air-Cooled Condenser Model, Power Technology and Engineering, 50 (2016) 318-322.

[20] V. Sukhanov, A. Bezukhov, I. Bogov, N. Dontsov, I. Volkovitsky, V. Tolmachev, Experimental study of condensate subcooling with the use of a model of an air-cooled condenser, Thermal Engineering, 63 (2016) 17-23.
[21] A. O'Donovan, R. Grimes, A theoretical and experimental investigation into the thermodynamic performance of a 50 MW power plant with a novel modular air-cooled condenser, Appl. Therm. Eng., 71 (2014) 119-129.
[22] A. O'Donovan, R. Grimes, Pressure drop analysis of steam condensation in air-cooled circular tube bundles, Appl. Therm. Eng., 87 (2015) 106-116.
[23] R. Lockhart, R. Martinelli, Proposed correlation of data for isothermal two-phase, two-component flow in pipes, Chem. Eng. Prog, 45 (1949) 39-48.
[24] H. Kim, T.-S. Kwon, D.E. Kim, Experimental study of air-cooled water condensation in slightly inclined circular tube using infrared temperature measurement technique, Nucl. Eng. Des., 308 (2016) 38-50.
[25] M. Owen, D.G. Kröger, A numerical investigation of vapor flow in large air-cooled condensers, Appl. Therm. Eng., 127 (2017) 157-164.
[26] A.J. Mahvi, A.S. Rattner, J. Lin, S. Garimella, Challenges in predicting steam-side pressure drop and heat transfer in air-cooled power plant condensers, Appl. Therm. Eng., 133 (2018) 396-406.
[27] J. El Hajal, J.R. Thome, A. Cavallini, Condensation in horizontal tubes, part 1: two-phase flow pattern map, Int. J. Heat Mass Transfer, 46 (2003) 3349-3363.
[28] J.R. Thome, J. El Hajal, A. Cavallini, Condensation in horizontal tubes, part 2: new heat transfer model based on flow regimes, Int. J. Heat Mass Transfer, 46 (2003) 3365-3387.
[29] J. Xiao, P. Hrnjak, A new flow regime map and void fraction model based on the flow characterization of condensation, Int. J. Heat Mass Transfer, 108 (2017) 443-452.
[30] H. Dong, H.-Q. Zhang, C. Sarica, An experimental study of low liquid loading gas-oil-water flow in horizontal pipes, in: 14th International Conference on Multiphase Production Technology, BHR Group, 2009.
[31] X. Chen, X. Cai, J. Brill, Gas-liquid stratified-wavy flow in horizontal pipelines, TRANSACTIONS-AMERICAN SOCIETY OF MECHANICAL ENGINEERS JOURNAL OF ENERGY RESOURCES TECHNOLOGY, 119 (1997) 209-216.
[32] P. Andreussi, L. Persen, Stratified gas-liquid flow in downwardly inclined pipes, Int. J. Multiphase Flow, 13 (1987) 565-575.
[33] B.D. Woods, E.T. Hurlburt, T.J. Hanratty, Mechanism of slug formation in downwardly inclined pipes, Int. J. Multiphase Flow, 26 (2000) 977-998.
[34] A.R. Hasan, C.S. Kabir, Predicting multiphase flow behavior in a deviated well, SPE Production Engineering, 3 (1988) 474-482.
[35] T. Crawford, C. Weinberger, J. Weisman, Two-phase flow patterns and void fractions in downward flow Part I: Steady-state flow patterns, Int. J. Multiphase Flow, 11 (1985) 761-782.
[36] J. Weisman, D. Duncan, J. Gibson, T. Crawford, Effects of fluid properties and pipe diameter on two-phase flow patterns in horizontal lines, Int. J. Multiphase Flow, 5 (1979) 437-462.
[37] D. Barnea, A unified model for predicting flow-pattern transitions for the whole range of pipe inclinations, Int. J. Multiphase Flow, 13 (1987) 1-12.
[38] Y. Taitel, A. Dukler, A model for predicting flow regime transitions in horizontal and near horizontal gas-liquid flow, AlChE J., 22 (1976) 47-55.

[39] Y. Taitel, D. Bornea, A. Dukler, Modelling flow pattern transitions for steady upward gas-liquid flow in vertical tubes, AlChE J., 26 (1980) 345-354.
[40] J.W. Coleman, S. Garimella, Two-phase flow regimes in round, square and rectangular tubes during condensation of refrigerant R 134a, International Journal of Refrigeration, 26 (2003) 117-128.
[41] D.H. Beggs, J.P. Brill, A study of two-phase flow in inclined pipes, Journal of Petroleum technology, 25 (1973) 607-617.
[42] J. Turner, G. Wallis, The separate-cylinders model of two-phase flow, paper no, NYO-3114-6Thayer's School Eng., Dartmouth College, Hanover, NH, USA, (1965).
[43] J. Xiao, O. Shonham, J. Brill, A comprehensive mechanistic model for two-phase flow in pipelines, in: SPE Annual Technical Conference and Exhibition, Society of Petroleum Engineers, 1990.
[44] V.T. Chow, Open channel hydraulics, (1959).
[45] T. Kao, Spatially varied subcritical and supercritical flow in gullies, (1974).
[46] B.C. Yen, Spatially varied open-channel flow equations, (1971).
[47] J.C. Chato, Laminar condensation inside horizontal and inclined tubes, in, Massachusetts Institute of Technology, 1960.
[48] L. Liebenberg, J.P. Meyer, A review of flow pattern-based predictive correlations during refrigerant condensation in horizontally smooth and enhanced tubes, Heat Transfer Engineering, 29 (2008) 3-19.
[49] A. Cavallini, G. Censi, D. Del Col, L. Doretti, G. Longo, L. Rossetto, C. Zilio, Condensation inside and outside smooth and enhanced tubes—a review of recent research, International Journal of Refrigeration, 26 (2003) 373-392.
[50] A. Dalkilic, S. Wongwises, Intensive literature review of condensation inside smooth and enhanced tubes, Int. J. Heat Mass Transfer, 52 (2009) 3409-3426.
[51] M.M. Shah, General correlation for heat transfer during condensation in plain tubes: Further development and verification, in: ASHRAE Transactions, Vol. 119, 2013, pp. 3-11.
[52] A. Cavallini, D.D. Col, L. Doretti, M. Matkovic, L. Rossetto, C. Zilio, G. Censi, Condensation in horizontal smooth tubes: a new heat transfer model for heat exchanger design, Heat Transfer Engineering, 27 (2006) 31-38.
[53] M. Soliman, J. Schuster, P. Berenson, A general heat transfer correlation for annular flow condensation, J. Heat Transfer, 90 (1968) 267-274.
[54] H. Jaster, P. Kosky, Condensation heat transfer in a mixed flow regime, Int. J. Heat Mass Transfer, 19 (1976) 95-99.
[55] W.H. McAdams, Heat transmission, in, 1954.
[56] F. Dittus, L. Boelter, Heat Transfer in Automobile Radiators of the Tubular Type, University of California publications in Engineering, 2 (1930) 371.
[57] L. Boyko, G. Kruzhilin, Heat transfer and hydraulic resistance during condensation of steam in a horizontal tube and in a bundle of tubes, Int. J. Heat Mass Transfer, 10 (1967) 361-373.
[58] G.M. Hebbard, W.L. Badger, Steam–Film Heat Transfer Coefficients for Vertical Tubes, Industrial & Engineering Chemistry, 26 (1934) 420-424.
[59] G.P. Fieg, W. Roetzel, Calculation of laminar film condensation in/on inclined elliptical tubes, Int. J. Heat Mass Transfer, 37 (1994) 619-624.
[60] M. Wilson, T. Newell, J. Chato, C.I. Ferreira, Refrigerant charge, pressure drop, and condensation heat transfer in flattened tubes, International journal of refrigeration, 26 (2003) 442-451.

[61] N. Kim, E. Lee, H. Byun, Condensation heat transfer and pressure drop in flattened smooth tubes having different aspect ratios, Exp. Therm Fluid Sci., 46 (2013) 245-253.
[62] S. Lips, J.P. Meyer, Two-phase flow in inclined tubes with specific reference to condensation: a review, Int. J. Multiphase Flow, 37 (2011) 845-859.
[63] B.-X. Wang, X.-Z. Du, Study on laminar film-wise condensation for vapor flow in an inclined small/mini-diameter tube, Int. J. Heat Mass Transfer, 43 (2000) 1859-1868.
[64] D.R.E. Ewim, J.P. Meyer, S.M.A. Noori Rahim Abadi, Condensation heat transfer coefficients in an inclined smooth tube at low mass fluxes, Int. J. Heat Mass Transfer, 123 (2018) 455-467.
[65] Y. Lyulin, I. Marchuk, S. Chikov, O. Kabov, Experimental study of laminar convective condensation of pure vapor inside an inclined circular tube, Microgravity Science and Technology, 23 (2011) 439-445.
[66] R. Würfel, T. Kreutzer, W. Fratzscher, Turbulence transfer processes in adiabatic and condensing film flow in an inclined tube, Chem. Eng. Technol., 26 (2003) 439-448.
[67] M. Akhavan-Behabadi, R. Kumar, S. Mohseni, Condensation heat transfer of R-134a inside a microfin tube with different tube inclinations, Int. J. Heat Mass Transfer, 50 (2007) 4864-4871.
[68] D. Del Col, M. Bortolato, M. Azzolin, S. Bortolin, Effect of inclination during condensation inside a square cross section minichannel, Int. J. Heat Mass Transfer, 78 (2014) 760-777.
[69] D.G. Kröger, Air-cooled heat exchangers and cooling towers, PennWell Books, USA, 2004.
[70] M.M. Shah, Comprehensive correlations for heat transfer during condensation in conventional and mini/micro channels in all orientations, International journal of refrigeration, 67 (2016) 22-41.
[71] S. Lips, J.P. Meyer, Stratified flow model for convective condensation in an inclined tube, Int. J. Heat Fluid Flow, 36 (2012) 83-91.
[72] C.K. Chen, S.A. Yang, Laminar film condensation inside a horizontal elliptical tube with variable wall temperature, Int. J. Heat Fluid Flow, 15 (1994) 75-78.
[73] H. Brouwers, Film condensation on non-isothermal vertical plates, Int. J. Heat Mass Transfer, 32 (1989) 655-663.
[74] W.M. Kays, A.L. London, Compact heat exchangers, (1984).
[75] E. Sparrow, J. Gorman, J. Abraham, Quantitative assessment of the overall heat transfer coefficient U, J. Heat Transfer, 135 (2013) 061102-061101 - 061102-061107.
[76] A.P. Colburn, E.d.P. de, Mean temperature difference and heat transfer coefficient in liquid heat exchangers, Industrial & Engineering Chemistry, 25 (1933) 873-877.
[77] W. Roetzel, B. Spang, Design of heat exchangers, VDI-heat atlas. VDI-Verlag, Düsseldorf, pp Ca, (1993) 1-37.
[78] R. Shah, D. Sekulic, Nonuniform Overall Heat Transfer Coefficients in Conventional Heat Exchanger Design Theory—Revisited, J. Heat Transfer, 120 (1998) 520-525.
[79] J. Xiao, P. Hrnjak, Heat transfer and pressure drop of condensation from superheated vapor to subcooled liquid, Int. J. Heat Mass Transfer, 103 (2016) 1327-1334.
[80] W.A. Davies III, Y. Kang, P. Hrnjak, A.M. Jacobi, Heat transfer and flow regimes in large flattened-tube steam condensers, Appl. Therm. Eng., 148 (2019) 722-733.
[81] J.E. Park, F. Vakili-Farahani, L. Consolini, J.R. Thome, Experimental study on condensation heat transfer in vertical minichannels for new refrigerant R1234ze(E) versus R134a and R236fa, Exp. Therm Fluid Sci., 35 (2011) 442-454.
[82] T. Wu, K. Vierow, Local heat transfer measurements of steam/air mixtures in horizontal condenser tubes, Int. J. Heat Mass Transfer, 49 (2006) 2491-2501.

[83] M.M. Derby, H.J. Lee, R.C. Craft, G.J. Michna, Y. Peles, M.K. Jensen, Exploration of experimental techniques to determine the condensation heat flux in microchannels and minichannels, in: 2010 14th International Heat Transfer Conference, American Society of Mechanical Engineers, 2010, pp. 169-176.
[84] S.Z. Kuhn, V.E. Schrock, P.F. Peterson, An investigation of condensation from steam–gas mixtures flowing downward inside a vertical tube, Nucl. Eng. Des., 177 (1997) 53-69.
[85] S. Lips, J. Meyer, Experimental study of convective condensation in an inclined smooth tube. Part II: inclination effect on pressure drop and void fraction, Int. J. Heat Mass Transfer, 55 (2012) 405-412.
[86] A.O. Adelaja, J. Dirker, J.P. Meyer, Experimental study of the pressure drop during condensation in an inclined smooth tube at different saturation temperatures, Int. J. Heat Mass Transfer, 105 (2017) 237-251.
[87] J. Wen, X. Gu, S. Wang, Y. Li, J. Tu, Numerical investigation on condensation heat transfer and pressure drop characteristics of R134a in horizontal flattened tubes, International Journal of Refrigeration, 85 (2018) 441-461.
[88] W. Groenewald, D.G. Kröger, Effect of mass transfer on turbulent friction during condensation inside ducts, Int. J. Heat Mass Transfer, 38 (1995) 3385-3392.
[89] J. Li, P. Hrnjak, Separation in condensers as a way to improve efficiency, International Journal of Refrigeration, 79 (2017) 1-9.
[90] J. Chiou, The effect of the air flow nonuniformity on the thermal performance of automobile air conditioning condenser, SAE Transactions, 92 (1983) 587-600.
[91] R.J. Berryman, Airflow in air-cooled heat exchangers, Heat Transfer Engineering, 8 (1987) 40-44.
[92] M.G. Beiler, D.G. Kröger, Thermal Performance Reduction in Air-Cooled Heat Exchangers Due to Nonuniform Flow and Temperature Distributions, Heat Transfer Engineering, 17 (1996) 82-92.
[93] E.Y. Ng, P.W. Johnson, S. Watkins, An analytical study on heat transfer performance of radiators with non-uniform airflow distribution, Proceedings of the Institution of Mechanical Engineers, Part D: Journal of Automobile Engineering, 219 (2005) 1451-1467.
[94] T. Hallqvist, The Cooling Airflow of Heavy Trucks-a Parametric Study, SAE International Journal of commercial vehicles, 1 (2008) 119-133.
[95] J.N. Mao, H.X. Chen, H. Jia, Y.Z. Wang, H.M. Hu, Effect of air-side flow maldistribution on thermalehydraulic performance of the multi-louvered fin and tube heat exchanger, International Journal of Thermal Sciences, 73 (2013) 46-57.
[96] S. Lalot, P. Florent, S.K. Lang, A.E. Bergles, Flow maldistribution in heat exchangers, Appl. Therm. Eng., 19 (1999) 847-863.
[97] C.Y. Park, P. Hrnjak, Experimental and numerical study on microchannel and round-tube condensers in a R410A residential air-conditioning system, International journal of refrigeration, 31 (2008) 822-831.
[98] I.J. Kennedy, S.W. Spence, G.R. Spratt, J.M. Early, Investigation of heat exchanger inclination in forced-draught air-cooled heat exchangers, Appl. Therm. Eng., 54 (2013) 413-421.
[99] J. Wen, D. Tang, Z. Wang, J. Zhang, Y. Li, F. Sun, Numerical simulation of flow and heat transfer of a direct aircooled condenser cell in a power plant, in: ASME 2013 Heat Transfer Summer Conf. Collocated with the ASME 2013 7th Int. Conf. on Energy Sustainability and the ASME 2013 11th Int. Conf. on Fuel Cell Science, Engineering and Technology, HT 2013, Vol. 1, 2013.

[100] E. Walsh, R. Grimes, G. Griffin, Flow Distribution Measurements From an Air Cooled Condenser in a~ 400MW Power Plant, in: ASME 2011 International Mechanical Engineering Congress and Exposition, American Society of Mechanical Engineers, 2011, pp. 33-38.
[101] Z. Zhang, J. Yang, Y. Wang, A favorable face velocity distribution and a V-frame cell for power plant air-cooled condensers, Appl. Therm. Eng., 87 (2015) 1-9.
[102] Z.Y. Guo, W.Q. Tao, R.K. Shah, The field synergy (coordination) principle and its applications in enhancing single phase convective heat transfer, Int. J. Heat Mass Transfer, 48 (2005) 1797-1807.
[103] S.M.A.N.R. Abadi, W.A. Davies, P. Hrnjak, J.P. Meyer, Numerical study of steam condensation inside a long inclined flattened channel, Int. J. Heat Mass Transfer, 134 (2019) 450-467.
[104] A. Mills, Experimental investigation of turbulent heat transfer in the entrance region of a circular conduit, Journal of Mechanical Engineering Science, 4 (1962) 63-77.
[105] H. Yamashita, R. Izumi, S. Yamaguchi, Performance of the Cross-Flow Heat Exchanger With Variable Physical Properties: 1st Report, in Case Where the Overall Heat Transfer Coefficient Is Variable, Bulletin of JSME, 20 (1977) 1008-1015.
[106] H. Qiao, Correction of Log Mean Temperature Difference Method and Effectiveness-NTU Relations for Two-phase Heat Transfer with Pressure Drop and Temperature Glide, in: International Refrigeration and Air conditioning Conference, Purdue, 2018.
[107] H. Deng, J. Liu, Performance prediction of finned air-cooled condenser using a conjugate heat-transfer model, Appl. Therm. Eng., (2019) 386-397.
[108] W.A. Davies, Heat Transfer and Visualization in Large Flattened-Tube Condensers with Variable Inclination, Masters Thesis, University of Illinois at Urbana-Champaign, 2016.
[109] B. Cushman-Roisin, C. Gualtieri, D.T. Mihailovic, Environmental Fluid Mechanics: Current issues and future outlook, in: Fluid mechanics of environmental interfaces, Taylor & Francis, 2008, pp. 17-30.
[110] V.P. Carey, Liquid-vapor phase-change phenomena, (1992).
[111] Y.-G. Park, L. Liu, A.M. Jacobi, Rational approaches for combining redundant, independent measurements to minimize combined experimental uncertainty, Exp. Therm Fluid Sci., 34 (2010) 720-724.
[112] J.P. Abraham, E.M. Sparrow, Fluid flow and heat transfer in multiply-folded, continuous flow passages including conjugate thermal interaction between the fluid and bounding walls, Numerical Heat Transfer: Part A: Applications, 42 (2002) 327-344.
[113] Fluent, in, ANSYS, Canonsburg, PA, July 24, 2018.
[114] B.N. Taylor, C.E. Kuyatt, NIST technical note 1297: Guidelines for evaluating and expressing the uncertainty of NIST measurement results, in, National Institute of Standards and Technology, Gaithersburg, MD, 1994, pp. 24.
[115] S. Sugawara, I. Michiyoshi, Dropwise condensation, Mem. Fac. Eng., Kyoto Univ., Kyoto University, 18 (1956) 84-111.
[116] E. LeFevre, J. Rose, A theory of heat transfer by dropwise condensation, in: Chem. Eng. Prog., Vol. 62, AMER INST CHEMICAL ENGINEERS 345 E 47TH ST, NEW YORK, NY 10017, 1966, pp. 86-&.
[117] I. Tanasawa, Critical size of departing drops, in: Proceedings of 5th International Transfer Conference, Vol. 7, 1974, pp. 188.
[118] J. Rose, Dropwise condensation theory and experiment: a review, Proceedings of the Institution of Mechanical Engineers, Part A: Journal of Power and Energy, 216 (2002) 115-128.

[119] Y. Kang, W.A. Davies III, P. Hrnjak, A.M. Jacobi, Effect of inclination on pressure drop and flow regimes in large flattened-tube steam condensers, Appl. Therm. Eng., 123 (2017) 498-513.
[120] S. Zivi, Estimation of steady-state steam void-fraction by means of the principal of minimum entropy production, ASME reprint 63-HT-16, 6th Nat, in: Heat Transfer Conf., AIChE-ASME, Boston, Vol. 203, 1963.
[121] M.M. Shah, An improved and extended general correlation for heat transfer during condensation in plain tubes, Hvac&R Research, 15 (2009) 889-913.
[122] T.H. Chilton, A.P. Colburn, Mass transfer (absorption) coefficients prediction from data on heat transfer and fluid friction, Industrial & engineering chemistry, 26 (1934) 1183-1187.
[123] S.W. Churchill, Friction-factor equation spans all fluid-flow regimes, Chemical engineering, 84 (1977) 91-92.
[124] R.W. Hanks, H.C. Ruo, Laminar-Turbulent Transition in Ducts of Rectangular Cross Section, Industrial & Engineering Chemistry Fundamentals, 5 (1966) 558-561.
[125] C. Baroczy, Correlation of liquid fraction in two-phase flow with application to liquid metals, in, Atomics International. Div. of North American Aviation, Inc., Canoga Park, Calif., 1963.
[126] J. Thom, Prediction of pressure drop during forced circulation boiling of water, Int. J. Heat Mass Transfer, 7 (1964) 709-724.
[127] T.W. Sturm, Open channel hydraulics, McGraw-Hill New York, 2010.
[128] H. Einstein, R. Banks, Fluid resistance of composite roughness, Eos, Transactions American Geophysical Union, 31 (1950) 603-610.
[129] Y. Taitel, A. Dukler, A theoretical approach to the Lockhart-Martinelli correlation for stratified flow, Int. J. Multiphase Flow, 2 (1976) 591-595.
[130] R. Shah, Thermal entry length solutions for the circular tube and parallel plates, in: Third national heat mass transfer conference, Indian Institute of Technology, Bombay, India, Vol. 1, 1975, pp. 11-75.
[131] K. Terpilowski, D. Rymuszka, L. Holysz, E. Chibowski, Changes in wettability of polycarbonate and polypropylene pretreated with oxygen and argon plasma, in: Proceedings of the 8th International Conference MMT-20142, Ariel, Israel, Vol. 28, 2014, pp. 155-165.
[132] R. Rebba, S. Mahadevan, S. Huang, Validation and error estimation of computational models, Reliability Engineering and System Safety, 91 (2006) 1390-1397.
[133] J. Miropolski, Teplopreredacza pri kondensacji para vysokogo davlenija vnutri trub, Teploenergetika, 3 (1962) 79-86.
[134] A.F. Mills, A. Mills, Basic heat and mass transfer, Prentice hall Upper Saddle River, 1999.
[135] R. Shah, A. London, Lanimar flow forced convection in ducts: a source book for compact heat exchanger analytical data, Academic press, 1978.
[136] P. Sadasivan, J. Lienhard, Sensible heat correction in laminar film boiling and condensation, Journal of Heat Transfer (Transactions of the ASME (American Society of Mechanical Engineers), Series C);(United States), 109 (1987).
[137] J.W. Harris, H. Stöcker, Handbook of mathematics and computational science, Springer Science & Business Media, 1998.
[138] B. Ren, L. Zhang, J. Cao, H. Xu, Z. Tao, Experimental and theoretical investigation on condensation inside a horizontal tube with noncondensable gas, Int. J. Heat Mass Transfer, 82 (2015) 588-603.

APPENDIX A: Data

Visualization Data (L = 5.7 m)						
Tube Length [m]	**Date**	**Inc [º]**	**Z [m]**	**River depth [mm]**	**Flow Rate [g/s]**	**Regime and Comments**
	6/13/2018	5	0.00	0	13.10	Annular
			5.70	8		Stratified
	6/13/2018	30	0.00	0	13.00	Annular
			5.70	6		Stratified
	6/13/2018	49	0.00	0	13.40	Annular
			5.70	5		Stratified
	6/14/2018	7	0.00	0	13.30	Annular
			5.70	8		Stratified
	6/30/2018	6	0.00	0	12.30	Annular
			5.70	8		Stratified
	7/5/2018	4	0.00	0	13.00	Annular
			5.70	8		Stratified
5.7	7/5/2018	0.3	0.00	0	12.70	Annular
			5.70	11		Stratified
	7/5/2018	0	0.00	0	12.70	Annular
			5.70	11		Stratified
	7/6/2018	6	0.00	0	13.20	Annular
			5.70	6		Stratified
	7/18/2018	7	0.00	0	7.10	Annular
			5.70	5		Stratified
	7/23/2018	3	0.00	0	8.70	Annular
			5.70	5		Stratified
	8/6/2018	0	0.00	0	12.30	Annular
			5.70	12.5		Stratified
	8/6/2018	20	0.00	0	12.10	Annular
			5.70	5		Stratified

Visualization Data (L = 10.7 m)						
Tube Length [m]	**Date**	**Inc [º]**	**Z [m]**	**River depth [mm]**	**Flow Rate [g/s]**	**Regime and Comments**
10.7	4/6/2016	0.3	1.33	6.3	13.22	majority filmwise
			4.45	16.3		majority dropwise
			6.44	21.3		dropwise top and bottom, filmwise middle
			8.68	22.3		Majority dropwise
			10.61	14.3		majority filmwise
	4/6/2016	2.87	1.33	5.3	12.73	majority filmwise
			4.45	7.3		majority filmwise
			6.44	8.3		dropwise bottom, filmwise top and middle
			8.68	9.3		dropwise bottom, filmwise top and middle
			10.61	12.3		dropwise bottom, filmwise top and middle
	4/6/2016	6	1.33	4.3	13.08	Filmwise
			4.45	6.8		majority filmwise
			6.44	7.3		dropwise bottom, filmwise top and middle
			8.68	7.8		dropwise bottom, filmwise top and middle
			10.61	8.3		dropwise bottom, filmwise top and middle
	4/6/2016	8.7	1.33	5.3	13.20	Filmwise
			4.45	6.3		majority filmwise
			6.44	7.3		dropwise bottom, filmwise top and middle
			8.68	7.8		dropwise bottom, filmwise top and middle
			10.61	8.8		dropwise bottom, filmwise top and middle
	4/6/2016	11.7	1.33	3.8	13.26	Filmwise
			4.45	4.8		majority filmwise
			6.44	5.05		dropwise bottom, filmwise top and middle
			8.68	6.3		dropwise bottom, filmwise top and middle
			10.61	8.3		dropwise bottom, filmwise top and middle

Visualization Data (L = 10.7 m)						
Tube Length [m]	**Date**	**Inc [º]**	**Z [m]**	**River depth [mm]**	**Flow Rate [g/s]**	**Regime and Comments**
			1.33	3.8		Filmwise
			4.45	4.8		majority filmwise
			6.44	4.8		dropwise bottom, filmwise top and middle
	4/6/2016	13.2			12.96	
			8.68	6.3		dropwise bottom, filmwise top and middle
			10.61	8.8		dropwise bottom, filmwise top and middle
			1.33	6.5		Filmwise
			4.45	10.8		majority filmwise
			6.44	13.5		dropwise bottom, filmwise top and middle
	7/22/2016	0.3			12.66	
			8.68	16.5		dropwise bottom, filmwise top and middle
			10.61	16		dropwise bottom, filmwise top and middle
			1.33	5.5		majority filmwise
			4.45	9.5		majority filmwise
			6.44	9.5		dropwise bottom, filmwise top and middle
	7/22/2016	3			12.66	
			8.68	10		dropwise bottom, filmwise top and middle
			10.61	11		dropwise bottom, filmwise top and middle
			1.33	5.1		
			4.45	8		
	7/22/2016	6	6.44	8.5	12.71	
			8.68	8.5		
			10.61	10		
			1.33	4.7		
			4.45	6		
	8/3/2016	17	6.44	6.5	11.76	
			8.68	8.2		
			10.61	8.5		
			1.33	7.8		
			4.45	17.5		
	8/19/2016	0.3	6.44	22.5	12.23	
			8.68	22		
			10.61	17		

Visualization Data (L = 10.7 m)						
Tube Length [m]	**Date**	**Inc [º]**	**Z [m]**	**River depth [mm]**	**Flow Rate [g/s]**	**Regime and Comments**
			1.33	5.8		
			4.45	8.5		
	8/19/2016	3	6.44	9	12.66	
			8.68	10.7		
			10.61	12		
			1.33	5		
			4.45	7.5		
	8/19/2016	6	6.44	7.8	12.66	
			8.68	9.5		
			10.61	9.5		
			1.33	5		
			4.45	7		
	8/19/2016	9	6.44	7	11.85	
			8.68	8.5		
			10.61	9.8		
			1.33	8.5		
			4.45	24		
	9/17/2016	0.3	6.44	27	12.89	
			8.68	23		
			10.61	18		
			1.33	4.5		
			4.45	6		
	9/17/2016	30	6.44	5.5	11.62	
			8.68	7.2		
			10.61	8		
			1.33			
			4.45	4.5		
	9/18/2016	45	6.44	6	13.60	
			8.68	7		
			10.61	7.5		
			1.33			
			4.45	4		
	9/19/2016	60	6.44	5.5	12.31	
			8.68	6.3		
			10.61	6.7		

Visualization Data (L = 10.7 m)						
Tube Length [m]	**Date**	**Inc [º]**	**Z [m]**	**River depth [mm]**	**Flow Rate [g/s]**	**Regime and Comments**
			1.33			
			4.45	3.5		
	9/20/2016	70	6.44	5.5	12.13	
			8.68	7		Wavy- high uncertainty
			10.61	7		Wavy- high uncertainty
			1.33	8		
			4.45	16.5		
	10/19/2016	0.3	6.44	21.7	11.00	
			8.68	21		
			10.61	16		
			1.33	6.7		
			4.45	9		
	10/19/2016	1	6.44	10	11.08	
			8.68	11.9		
			10.61	16.7		
			1.33	5.3		
			4.45	9.5		
	10/19/2016	2	6.44	10	11.18	
			8.68	10.5		
			10.61	12.5		
			1.33	85		
			4.45	72		
	10/19/2016	-1	6.44	56	11.75	
			8.68	42		
			10.61	8		
			1.33	4.7		
			4.45	6		
	3/9/2017	17	6.44	6.5	12.34	
			8.68	8		
			10.61	8.5		
			1.33	8.5		
			4.45	13		
	3/9/2017	0.3	6.44	18	12.38	
			8.68	21.5		
			10.61	18.5		

Visualization Data (L = 10.7 m)						
Tube Length [m]	**Date**	**Inc [º]**	**Z [m]**	**River depth [mm]**	**Flow Rate [g/s]**	**Regime and Comments**
			1.33	9		
			4.45	28.5		
	4/4/2017	0	6.44	34	12.39	
			8.68	30		
			10.61	18		
			1.33	6		
			4.45	8.5		
	4/18/2017	3	6.44	8.5	12.51	
			8.68	10.6		
			10.61	11.8		
			1.33	5.1		
			4.45	8		
	4/18/2017	6	6.44	8.5	12.37	
			8.68	9		
			10.61	10.8		
			1.33	7.3		
			4.45	18		
	4/18/2017	0.3	6.44	26.5	11.87	
			8.68	26.5		
			10.61	18.5		
			1.33	19		
			4.45	42.6		
	4/18/2017	0	6.44	45	11.55	
			8.68	36		
			10.61	19		
			1.33	5.9		
			4.45	7.1		
	4/27/2017	6	6.44	8	12.24	
			8.68	8.7		
			10.61	10		
			1.33	5		
			4.45	7.5		
	4/27/2017	9	6.44	8	12.24	
			8.68	8.8		
			10.61	9		

Visualization Data (L = 10.7 m)						
Tube Length [m]	**Date**	**Inc [º]**	**Z [m]**	**River depth [mm]**	**Flow Rate [g/s]**	**Regime and Comments**
			1.33	3.9		
			4.45	6		
	4/27/2017	12	6.44	7	12.28	
			8.68	8.5		
			10.61	9		
			1.33	8.5		
			4.45	17		
	4/27/2017	0.3	6.44	26.5	11.88	
			8.68	26		
			10.61	18		
			1.33	26		
			4.45	46.8		
	4/27/2017	0	6.44	46.3	10.58	
			8.68	36.5		
			10.61	18.5		
			1.33	5		
			4.45	7.5		
	5/23/2017	6	6.44		12.25	
			8.68	8.5		
			10.61	10		
			1.33	5.5		
			4.45	7		
	5/23/2017	9	6.44		10.22	
			8.68	7		
			10.61	9.8		
			1.33	5.5		
			4.45			
	5/23/2017	12	6.44	6	11.78	
			8.68	7		
			10.61	7.5		
			1.33	6		
			4.45	7		
	5/23/2017	3	6.44	8	12.18	
			8.68	9		
			10.61	10		

Visualization Data (L = 10.7 m)						
Tube Length [m]	**Date**	**Inc [º]**	**Z [m]**	**River depth [mm]**	**Flow Rate [g/s]**	**Regime and Comments**
			1.33	8		
			4.45	15.5		
	5/23/2017	0.3	6.44	23	9.75	
			8.68	23.5		
			10.61	17		
			1.33	17		
			4.45	31		
	5/23/2017	0	6.44	42	10.28	
			8.68	42		
			10.61	18		
			1.33	6		
			4.45	7		
	6/1/2017	6	6.44		11.57	
			8.68	8.5		
			10.61	10		
			1.33	5.8		
			4.45	8		
	6/8/2017	3	6.44	8.5	10.66	
			8.68	9		
			10.61	11		
			1.33	6		-7 kPa
			4.45	8		
	7/8/2017	6	6.44	8.5	12.98	
			8.68	9.5		
			10.61	10		
			1.33	6		-7 kPa
			4.45			
	7/8/2017	9	6.44		11.14	
			8.68	8.5		
			10.61	9.8		
			1.33	5.8		-5 kPa
			4.45			
	7/8/2017	12	6.44	6.5	11.49	
			8.68	7.5		
			10.61	9		

Visualization Data (L = 10.7 m)						
Tube Length [m]	**Date**	**Inc [º]**	**Z [m]**	**River depth [mm]**	**Flow Rate [g/s]**	**Regime and Comments**
			1.33			-8 kPa
			4.45			
	7/8/2017	17	6.44	6.5	11.29	
			8.68	7		
			10.61	7		
			1.33	6.8		-9 kPa
			4.45	8.3		
	7/8/2017	3	6.44	8.8	11.08	
			8.68	10.5		
			10.61	11.3		
			1.33	7.5		-8 kPa
			4.45	12.5		
	7/8/2017	0.3	6.44	24.1	10.79	
			8.68	26.6		
			10.61	17.5		
			1.33	12		-8 kPa
			4.45	40.7		
	7/8/2017	0	6.44	44.5	10.73	
			8.68	34.5		
			10.61	18		
			1.33	10.5		-6 kPa
			4.45	27.5		
	8/9/2017	0	6.44	28	9.48	
			8.68	24.5		
			10.61	18		
			1.33	11.5		-4 kPa
			4.45	31.5		
	8/9/2017	0	6.44	32.2	10.14	
			8.68	30.5		
			10.61	19		
			1.33	5		
			4.45	6		
	8/21/2017	6	6.44	7	9.74	
			8.68	8		
			10.61	10		

Visualization Data (L = 10.7 m)

Tube Length [m]	Date	Inc [º]	Z [m]	River depth [mm]	Flow Rate [g/s]	Regime and Comments
			1.33	7.5		
			4.45	12		
	8/21/2017	0.3	6.44	17.5	9.40	
			8.68	17.5		
			10.61	15		
			1.33	13.5		
			4.45	28.5		
	8/21/2017	0	6.44	28.5	9.19	
			8.68	25.5		
			10.61	15.5		

Air-Cooled, L = 10.7 m

Inc	HTC	dP	Ps	Patm	Tatm	Cond. Flow Rate	Qa	Qs	Qbar	Tai	Tsat	dTin	Vair	Airflow Profile
[º]	[W m^{-2} K^{-1}]	[kPa]	[kPa]	[kPa]	[oC]	[g s^{-1}]	[kW]	[kW]	[kW]	[ºC]	[ºC]	[ºC]	[m s^{-1}]	
0		0.285	103.3	99.8	26	9.1	22.4	21.1	22.1	32.1	100.2	68.1	1.57	Inlet high
0		0.278	102.6	99.8	26	9.32	22.9	21.3	22.6	30.7	100	69.3	1.57	Inlet high
0		0.27	102.5	99.8	26	9.82	22.5	22.3	22.5	31.8	100.1	68.3	1.57	Inlet high
0		0.267	104.5	99.8	22	10.16	23.2	23.1	23.2	30.1	100.7	70.6	1.57	Inlet high
0		0.33	102.5	99.8	26	9.53	22.7	21.7	22.5	31.3	100	68.7	1.57	Inlet high
0		0.331	104.5	99.8	25	10.33	23	23.4	23.1	30.7	100.7	70	1.57	Inlet high
0		0.341	104.1	99.8	26	10.33	22.6	23.4	22.8	31.5	100.6	69.1	1.57	Inlet high
0		0.365	104.4	99.8	26	10.25	22.3	23.1	22.5	32.2	100.7	68.5	1.57	Inlet high
0		0.376	102	99.3	32.9	12.38	30	30.1	30	37.8	99.9	62.2	2.41	Down
3		0.363	102.1	99.3	33	12.34	29.9	29.9	29.9	37.9	99.9	62	2.41	Down
6		0.353	102.2	99.7	32	12.7	30.4	30.8	30.5	36.8	100	63.2	2.41	Down
9		0.38	102.4	99.7	33.4	12.43	29.7	30.1	29.8	38.6	99.9	61.3	2.41	Down
12		0.385	102.1	99.7	33.6	12.26	29.6	29.7	29.6	38.9	99.9	61.1	2.41	Down
17		0.294	102	99.3	33.8	12.34	29.6	29.9	29.7	38.4	100	61.6	2.41	Down
0.5		0.339	101.4	99.4	27	12.11	28.2	29.4	28.5	39.6	99.8	60.1	2.41	Down
3		0.392	103.4	99.4	26	12.15	28.5	29.5	28.7	39.5	100.3	60.8	2.41	Down
6		0.31	103.6	99.4	26	12.45	29.1	30.1	29.3	38.6	100.4	61.8	2.41	Down
9		0.417	102.5	99.6	21	12.76	30.7	30.9	30.7	36.1	100.1	64	2.41	Down
12		0.407	102.9	99.7	21	12.74	29.6	30.9	29.9	37.5	100.2	62.7	2.41	Down
17		0.348	103.4	99.7	22	12.51	29.3	30.3	29.5	38.1	100.3	62.2	2.41	Down
0		0.427	102.8	98.5	25	12.39	29.9	30.1	29.9	37.2	100.2	63	2.41	Down
1		0.413	101.8	98.5	24	12.72	30.8	30.8	30.8	36.3	100	63.6	2.41	Down

Air-Cooled, L = 10.7 m														
Inc	**HTC**	**dP**	**Ps**	**Patm**	**Tatm**	**Cond. Flow Rate**	**Qa**	**Qs**	**Qbar**	**Tai**	**Tsat**	**dTin**	**Vair**	**Airflow Profile**
[º]	[W m^{-2} K^{-1}]	[kPa]	[kPa]	[kPa]	[oC]	[g s^{-1}]	[kW]	[kW]	[kW]	[ºC]	[ºC]	[ºC]	[m s^{-1}]	
3		0.403	102.4	98.5	23	12.72	31.2	30.8	31.2	36.2	100.1	64	2.41	Down
6		0.41	101.7	98.5	21	12.66	30.7	30.7	30.7	36.7	99.9	63.3	2.41	Down
9		0.412	102.4	98.5	21	12.33	30.2	29.9	30.1	37.6	100.1	62.6	2.41	Down
12		0.383	102.3	98.5	22	12.46	29.9	30.2	30	38	100.1	62.1	2.41	Down
0		0.419	103.6	99.7	25	11.55	29.6	28.1	29.3	36.9	100.3	63.3	2.32	Down
0.3		0.333	102.8	99.7	25	11.87	30	28.9	29.8	37	100.1	63	2.32	Down
3		0.338	103.4	99.7	20	12.51	30.8	30.4	30.7	35.8	100.3	64.6	2.32	Down
6		0.351	102.4	99.7	24	12.37	30	30	30	36.5	100.1	63.6	2.32	Down
9		0.33	102.9	99.7	25	12	29.7	29.2	29.6	37.2	100.1	63	2.32	Down
12		0.299	103.9	99.7	25	11.98	29.2	29	29.2	38	100.4	62.5	2.32	Down
17		0.326	103.7	99.7	25	11.8	28.5	28.6	28.5	38.6	100.3	61.7	2.32	Down
0.3		0.366	100.7	98.3	23	11.88	29.7	28.8	29.5	36	99.7	63.7	2.32	Down
3		0.373	102.4	98.2	19	12.19	30.3	29.6	30.2	35.4	100.1	64.7	2.32	Down
6		0.358	101.8	98.3	21.2	12.24	29.8	29.7	29.8	36.1	99.9	63.8	2.32	Down
9		0.35	102	98.3	23	12.24	29.4	29.7	29.5	36.7	100	63.3	2.32	Down
12		0.341	101.8	98.3	23	12.28	29.2	29.8	29.3	37.2	99.9	62.7	2.32	Down
17		0.316	101.8	98.3	23	11.78	29.4	28.6	29.2	37.3	99.9	62.7	2.32	Down
0		0.412	104.4	98.4	26	10.28	24.7	25	24.8	38.3	100.6	62.3	1.95	Down
0.3		0.306	102.1	98.4	26	9.75	24.1	23.7	24	38.7	100	61.3	1.95	Down
3		0.293	101.5	98.4	25	12.18	24.2	29.6	25.4	38.6	99.8	61.2	1.95	Down
6		0.331	103.6	98.4	17.5	12.25	24.8	29.8	25.9	37.4	100.5	63.1	1.95	Down
9		0.313	103.4	98.4	20.5	10.22	24	24.8	24.2	38.4	100.4	62.1	1.95	Down
12		0.32	103.3	98.4	24	11.78	23.5	28.6	24.7	39.3	100.3	61	1.95	Down
17		0.35	104.5	98.4	25	10.68	23.7	25.9	24.2	39.8	100.7	60.9	1.95	Down
0.3		0.317	98.9	99.3	28	8.82	29.2	21.6	27.5	39	99	60	2.32	Down
0.3		0.298	98.4	99.3	28	9.99	27.1	25.3	26.7	37.9	98.9	60.9	2.32	Down
3		0.229	98.8	99.3	28	11.31	29	27.8	28.7	38.9	99	60.1	2.32	Down
3		0.233	99.1	99.3	28	11.51	29.3	28.3	29.1	38.7	99.1	60.5	2.32	Down
3		0.234	98.7	99.3	28	10.87	29.1	26.8	28.6	38.8	98.9	60.1	2.32	Down
6		0.226	99	99.3	21	11.7	31	29	30.5	35.6	99.2	63.5	2.32	Down
6		0.292	97.8	99.3	21	11.2	29.8	27.7	29.4	36.9	98.7	61.8	2.32	Down
6		0.239	99.3	99.3	21	11.57	29	28.2	28.9	38.9	99.2	60.3	2.32	Down
0.3		0.274	96.5	99.5	28	8.55	28.3	21	26.7	38.1	98.1	60.1	2.32	Down
3		0.293	96.4	99.5	27	10.66	28.3	26.2	27.9	37.8	98.1	60.3	2.32	Down
6		0.286	97.1	99.5	21	12.38	27.3	30.4	28	39.8	98.4	58.6	2.32	Down
9		0.298	97.5	99.5	28	11.13	28.5	27.2	28.2	38.7	98.5	59.8	2.32	Down
12		0.268	97.1	99.5	27	12.75	29.3	31.3	29.7	37.8	98.4	60.7	2.32	Down
17		0.278	97.3	99.5	27	10.85	28.6	26.5	28.1	38.5	98.4	60	2.32	Down

Air-Cooled, L = 10.7 m

Inc	HTC	dP	Ps	Patm	Tatm	Cond. Flow Rate	Qa	Qs	Qbar	Tai	Tsat	dTin	Vair	Airflow Profile
[°]	[W m^{-2} K^{-1}]	[kPa]	[kPa]	[kPa]	[oC]	[g s^{-1}]	[kW]	[kW]	[kW]	[°C]	[°C]	[°C]	[m s^{-1}]	
0		0.398	95.4	99.1	30	11.25	28	27.4	27.9	38.7	97.9	59.2	2.32	Down
0		0.405	90.9	99.1	30	10.73	27.4	26.3	27.1	38.3	96.5	58.2	2.32	Down
0.3		0.406	96.2	99.1	30	11.6	28.3	28.2	28.3	39.5	98.3	58.8	2.32	Down
0.3		0.328	90.6	99.1	30	10.79	27.8	26.5	27.5	38.3	96.5	58.2	2.32	Down
3		0.433	95.5	99.1	28.7	11.27	28.4	27.5	28.2	39.8	98.1	58.4	2.32	Down
3		0.388	90.1	99.1	28.7	11.08	27.8	27.3	27.7	38.9	96.4	57.5	2.32	Down
6		0.422	91.9	99	23	12.98	29	31.8	29.6	37.1	97.1	60	2.32	Down
6		0.433	88.7	99	23	11.15	28.2	27.3	28	37.5	96.1	58.6	2.32	Down
9		0.427	95.3	99.1	28	11.54	28.8	28.1	28.6	38.9	98.1	59.2	2.32	Down
9		0.422	90.1	99.1	28	11.14	27.9	27.3	27.8	38.5	96.5	58	2.32	Down
12		0.331	95.7	99.1	28	11.68	28.5	28.4	28.5	39.5	98.2	58.7	2.32	Down
12		0.379	93.7	99.1	28.4	11.49	28.2	28	28.1	39.4	97.6	58.2	2.32	Down
12		0.363	89.8	99.1	28.7	11.43	27.2	28.3	27.4	39.5	96.2	56.7	2.32	Down
17		0.342	95.4	99.1	28.7	11.34	27.4	27.6	27.4	40.6	98.1	57.6	2.32	Down
17		0.299	91.3	99.1	28.7	11.29	26.6	27.8	26.9	40.2	96.8	56.6	2.32	Down
0		0.411	89.7	99.1	26	10.99	29.5	27.2	28.9	34.9	96	61.1	2.32	Down
0.3		0.363	89.7	99.1	26	10.79	28.6	26.9	28.2	36.2	95.6	59.4	2.32	Down
3		0.371	89.5	99.1	25	10.96	29.2	27.3	28.8	35.5	95.7	60.2	2.32	Down
6		0.371	95.2	99.1	27.8	13.23	29.9	32.5	30.5	37.2	98	60.7	2.32	Down
17		0.418	90.4	99.1	22	10.67	28.4	26.5	28	36.3	96.2	59.9	2.32	Down
0.3	27509		104.1	99.1	24	13.23	29.6	30.4	29.8	27.5	99.8	72.3	1.98	Uniform
3.3	29445	0.314	103.5	99.1	25.3	12.67	29.1	29.1	29.1	28.3	99.6	71.3	1.98	Uniform
6	29928	0.307	102.9	99.1	25.4	12.31	28.5	28.3	28.5	29.3	99.5	70.2	1.98	Uniform
8.9	30174	0.356	103.4	99.1	26.7	12.82	28.3	29.5	28.5	29.9	99.6	69.7	1.98	Uniform
11.9	29677	0.334	103.1	99.1	26.7	13.05	27.8	30	28.3	30.6	99.5	68.9	1.98	Uniform
17	26556	0.319	102.7	99.1	26.1	12.76	27.9	29.4	28.2	30.3	99.4	69.1	1.98	Uniform
0.3	27920		100.8	99.2	29.1	12.23	26.6	28.1	27	32.5	99.6	67.1	1.98	Uniform
3	32033	0.412	102.4	98.9	30	12.66	26.6	28.8	27.1	33.1	100.0	66.9	1.98	Uniform
0.3	35222	0.378	102.7	99.2	27.5	12.07	27.1	27.6	27.2	31.9	100.1	68.3	1.98	Uniform
3	29873	0.386	102.5	99.2	30	12.17	26.3	27.6	26.5	33.8	100.1	66.3	1.98	Uniform
6	29627	0.421	103.1	99.2	30	13.6	26.1	30.8	27.1	34.3	100.2	65.9	1.98	Uniform
9	29568		104.2	99.2	30	12.14	26.3	27.7	26.6	34.2	100.5	66.4	1.98	Uniform
0	32595		103.4	99.3	24	12.59	29.8	29.3	29.7	27.2	100.3	73.0	1.98	Uniform
0	35341	0.376	104.4	98.9	25	12.89	29	29.5	29.1	29.0	100.6	71.6	1.98	Uniform
30	34987	0.322	104.5	98.9	28	11.62	28.5	26.4	28	30.7	100.6	69.9	1.98	Uniform
46	27612	0.332	102.3	99	21.3	13.6	30.9	30.9	30.9	24.5	100.1	75.6	1.98	Uniform
60	32032	0.306	104.7	99.3	24	12.31	30.5	28.2	30	27.3	100.6	73.3	1.98	Uniform
70	31278	0.294	105.4	99.5	27	12.13	28.5	27.6	28.3	31.1	100.8	69.7	1.98	Uniform

Air-Cooled, L = 10.7 m

Inc	HTC	dP	Ps	Patm	Tatm	Cond. Flow Rate	Qa	Qs	Qbar	Tai	Tsat	dTin	Vair	Airflow Profile
[°]	[W m^{-2} K^{-1}]	[kPa]	[kPa]	[kPa]	[oC]	[g s^{-1}]	[kW]	[kW]	[kW]	[°C]	[°C]	[°C]	[m s^{-1}]	
52	26172	0.331	101.4	99.4	24	13.05	29.1	29.8	29.3	28.5	99.7	71.2	1.98	Uniform
37	28129	0.321	101	99.4	25	12.97	29.3	29.6	29.4	27.9	99.6	71.7	1.98	Uniform
41	22204	0.311	101.9	99.3	25.1	13.19	28.9	30	29.1	28.9	99.9	71.0	1.98	Uniform
29	29604	0.327	102.4	99.3	23.5	13.55	29.5	30.8	29.8	27.1	100.1	73.0	1.98	Uniform
65	23120	0.309	102.2	99.4	23.6	12.55	29.4	28.5	29.2	27.2	99.9	72.7	1.98	Uniform
75	21915	0.291	101.1	99.4	20	14.53	31.1	33	31.5	23.8	99.6	75.8	1.98	Uniform
-1	7021	2.316	106	99.4	26	11.75	26.7	26.9	26.8	31.3	100.5	69.2	1.98	Uniform
1	27496	0.336	103.1	99.4	25.5	11.08	25.1	25.4	25.2	35.3	100.2	64.9	1.98	Uniform
2	28696	0.355	103.1	99.4	26	11.18	25.1	25.6	25.2	35.4	100.2	64.8	1.98	Uniform
0.4	28526	0.32	104.8	100.5	28.5	11.68	26.9	26.8	26.9	32.7	100.6	67.9	1.98	Uniform
17	31256		106.1	100.5	26.2	12.42	28.8	28.2	28.6	30.2	101.0	70.8	1.98	Uniform
3	26504		100.4	98.2	21.6	13.12	29.9	29.9	29.9	24.8	99.5	74.6	1.98	Uniform
9	26845		103.2	101.4	23	12.98	30.2	29.5	30.1	26.5	100.1	73.6	1.98	Uniform
0	20507	0.404	95.6	99.6	28.5	10.14	25.6	24.2	25.3	32.5	97.9	65.5	1.97	Uniform
0	19739	0.338	94	99.6	28.5	9.48	25.4	22.1	24.7	32.5	97.5	64.9	1.97	Uniform
0.3	23222	0.352	95.7	99.6	27.5	10.73	25.1	25	25.1	33.7	98	64.3	1.97	Uniform
0.3	24230	0.351	93.5	99.6	27.5	10.45	25	24.4	24.9	33.3	97.3	64	1.97	Uniform
3		0.394	94.9	99.6	27.5	12.18	25.1	28	25.8	33.4	97.8	64.4	1.97	Uniform
3		0.369	92.3	99.6	27.5	10.79	24.9	25.2	25	32.9	97	64.1	1.97	Uniform
6		0.371	95.3	99.6	21	12.47	26.2	28.8	26.8	31.1	98	66.9	1.97	Uniform
6		0.389	92.7	99.6	24	11.74	25.6	27.1	25.9	31.6	97.2	65.6	1.97	Uniform
6	21679	0.35	91.1	99.6	24	11.86	25.2	27.6	25.7	32	96.6	64.7	1.97	Uniform
9	22669	0.334	91.9	99.6	27.5	11.12	24.6	25.9	24.9	33.4	96.9	63.5	1.97	Uniform
9		0.306	95.5	99.6	27.5	11.33	25.3	26	25.4	33.2	98	64.9	1.97	Uniform
12		0.319	95.2	99.6	27.5	11.3	25.1	25.9	25.3	33.5	97.9	64.4	1.97	Uniform
12		0.302	91.9	99.6	27.5	10.29	24.8	24.1	24.6	33.1	96.9	63.8	1.97	Uniform
17	24307	0.343	95.5	99.6	27.5	13.1	25	30.1	26.2	34	98	64	1.97	Uniform
17		0.311	92.5	99.6	27.5	11.39	24.7	26.4	25.1	33.7	97.1	63.4	1.97	Uniform
0	18121	0.427	92.4	98.5	23	9.08	24.6	21.5	23.9	33.1	97	63.9	1.97	Uniform
0.3	23430	0.401	92.3	98.5	23	9.83	23.9	23.1	23.7	34.7	96.9	62.2	1.97	Uniform
3	24121	0.402	91.9	98.5	23	9.93	23.4	23.1	23.3	35.6	96.8	61.2	1.97	Uniform
17	24604		93.9	98.5	23	11.11	24.3	25.8	24.7	34.4	97.6	63.2	1.97	Uniform
0	31022	0.318	102.1	99.2	28	9.19	21.6	20.9	21.4	31.7	100.1	68.4	1.55	Uniform
0.3	35125	0.383	102.9	99.2	28	9.4	22.1	21.4	21.9	31.3	100.2	68.9	1.55	Uniform
3		0.357	102.5	99.2	27	9.53	22.2	21.6	22	30.9	100.1	69.2	1.55	Uniform
6		0.386	102.4	99.2	23	9.74	22.9	22.1	22.7	29	100.2	71.2	1.55	Uniform
6		0.325	101.8	99.2	28	9.68	21.1	21.9	21.3	33.3	99.9	66.6	1.55	Uniform
9		0.399	102	99.2	27	9.94	22.4	22.5	22.5	30	100	70	1.55	Uniform

Air-Cooled, L = 10.7 m														
Inc	**HTC**	**dP**	**Ps**	**Patm**	**Tatm**	**Cond. Flow Rate**	**Qa**	**Qs**	**Qbar**	**Tai**	**Tsat**	**dTin**	**Vair**	**Airflow Profile**
[º]	[W m^{-2} K^{-1}]	[kPa]	[kPa]	[kPa]	[oC]	[g s^{-1}]	[kW]	[kW]	[kW]	[ºC]	[ºC]	[ºC]	[m s^{-1}]	
12		0.329	102.1	99.2	27	9.8	21.9	22.2	21.9	31.4	100.1	68.7	1.55	Uniform
17	30741	0.337	102.8	99.2	27	10.01	21.5	22.7	21.8	32.4	100.2	67.9	1.55	Uniform

L = 5.7 m; Air and Water-Cooled

Cooling	Inc	HTC	Tri	Tro	dTr	Ts	dPg	Ps	Twall	G	x	m_dot_r	q"	Tw1	t_c
	[º]	[W m^{-2} K^{-1}]	[ºC]	[ºC]	[ºC]	[ºC]	[kPa]	[kPa]	[ºC]	[kg m^{-2} s^{-1}]		[g s^{-1}]	[W m^{-2}]	[ºC]	[m]
Water	1.5	5871	28.2	82.9	54.7	100.3	3.5	103.5	85.0	3.8	0.00	10.7	46.9	54.3	0.011
Water	0	6302	28.7	82.1	53.4	100.5	4.0	104.0	84.7	3.8	0.00	11.2	52.6	51.7	0.011
Water	26	4557	27.2	77.4	50.2	91.0	-25.8	74.0	78.4	2.7	0.00	7.8	29.3	56.3	0.007
Water	0.5	6201	27.7	77.8	50.0	90.6	-27.1	72.6	72.6	4.8	0.01	8.8	32.8	37.7	0.011
Water	0	4329	28.9	59.0	30.1	88.7	-31.2	67.3	67.1	2.8	0.00	16.8	37.5	32.5	0.011
Water	0.5	5902	25.4	76.0	50.6	88.9	-30.3	68.3	69.1	3.4	0.00	7.8	29.5	31.9	0.011
Water	0.5	4080	28.7	58.7	30.0	88.8	-31.1	67.5	66.0	3.4	0.01	16.8	37.4	32.1	0.011
Water	10	5156	32.2	62.1	30.0	95.1	-13.1	85.8	79.9	3.2	0.00	20.5	45.7	56.2	0.006
Water	10	6946	28.8	78.9	50.1	95.2	-13.2	85.8	81.6	3.4	0.00	11.5	43.0	57.8	0.011
Water	10	2790	27.6	78.9	51.4	92.7	-20.9	78.3	76.9	3.5	0.00	7.0	27.0	59.4	0.008
Water	0.5	6469	28.4	70.9	42.5	93.8	-17.8	80.7	78.1	3.9	0.01	14.7	46.6	52.8	0.006
Water	0.5	2396	29.2	60.6	31.4	93.7	-17.1	81.4	70.5	3.8	0.07	15.7	36.8	52.2	0.006
Water	0.5	7930	26.4	82.7	56.3	93.8	-17.8	80.7	79.0	3.8	0.01	8.2	34.8	49.2	0.007
Water	0.5	10751	53.6	85.6	32.1	95.4	-14.8	84.1	86.9	3.8	0.00	9.9	24.0	69.1	0.007
Water	0.5	8639	52.7	87.7	35.1	95.4	-13.8	85.1	87.3	3.8	0.00	7.9	20.9	69.8	0.007
Water	0.5	6768	28.2	88.2	60.0	101.4	7.7	107.1	85.7	1.1	0.35	9.4	42.3	57.0	0.006
Water	0.5	5586	36.2	66.8	30.6	100.5	5.1	104.5	81.7	2.1	0.51	24.1	54.9	54.3	0.006
Water	10	7474	29.6	89.6	60.0	100.9	6.5	105.9	86.5	2.7	0.26	8.9	40.0	61.6	0.006
Water	10	5834	31.5	81.5	50.0	100.4	5.3	104.6	84.4	2.7	0.27	12.0	44.9	59.6	0.006
Water	10	5426	33.1	73.1	40.0	100.0	3.2	102.6	82.8	2.9	0.28	16.8	50.1	58.3	0.006
Water	0.5	6445	31.4	81.4	50.1	101.0	6.9	106.3	84.1	2.8	0.19	12.9	48.3	54.5	0.006
Water	0.5	7286	29.0	89.0	60.0	101.1	7.2	106.5	85.4	1.7	0.35	9.3	41.8	55.3	0.006
Water	10	5516	36.1	67.1	31.0	100.4	4.4	103.8	82.3	2.7	0.31	23.6	54.4	57.6	0.006
Water	0.5	5941	33.8	73.9	40.0	100.9	6.5	105.9	83.0	2.4	0.21	17.5	52.3	54.2	0.006
Water	10	6203	31.0	81.0	50.0	101.2	7.7	106.0	85.4	2.7	0.41	13.0	48.7	59.8	0.006
Water	0.5	5546	32.0	74.1	42.0	100.9	7.6	106.0	83.3	2.8	0.34	16.7	52.3	55.3	0.006
Water	0.5	5640	31.1	81.2	50.0	101.0	7.6	106.0	84.0	2.4	0.40	13.0	48.8	55.7	0.006
Water	0.5	5160	36.0	66.2	30.2	101.0	7.5	105.8	81.8	2.4	0.42	25.3	56.7	54.5	0.006
Water	10	6950	29.6	89.6	60.0	101.6	7.7	106.0	87.0	2.6	0.39	9.8	44.2	61.2	0.006
Water	0.5	6815	29.2	89.2	60.0	101.3	7.7	106.0	85.9	2.5	0.34	9.5	42.8	57.0	0.006
Water	0.5	5217	30.0	80.1	50.0	101.3	7.7	106.7	84.1	1.7	0.60	13.1	48.8	55.2	0.006
Water	0.5	6130	28.0	88.0	60.1	101.6	7.7	106.8	85.8	1.4	0.67	9.8	44.2	56.0	0.006
Water	10	5500	30.9	80.9	50.0	101.6	7.7	106.8	84.7	1.1	0.82	12.9	48.0	57.3	0.006
Water	10	5402	33.4	73.4	40.0	101.4	7.7	106.8	83.9	1.3	0.70	17.5	52.1	57.9	0.006
Water	10	6275	29.4	89.4	60.0	101.9	7.7	106.8	86.6	1.2	0.79	9.5	42.9	59.8	0.006
Water	0.5	5077	32.9	72.9	40.0	101.0	6.8	105.9	83.0	1.5	0.69	17.4	51.7	54.5	0.006
Water	0.5	8252	70.9	93.9	23.0	103.6	7.7	107.2	94.7	1.1	0.68	18.4	32.0	81.9	0.006
Water	0.5	5162	32.7	62.0	29.3	94.3	-17.6	81.9	77.8	0.9	0.84	21.6	46.9	53.4	0.006
Water	0.5	5250	31.1	70.3	39.2	100.7	6.9	106.4	82.7	1.3	0.74	19.8	57.7	56.7	0.006

L = 5.7 m; Air and Water-Cooled

Cooling	Inc	HTC	Tri	Tro	dTr	Ts	dPg	Ps	Twall	G	x	m_dot_r	q"	Tw1	t_c
	[º]	[W m^{-2} K^{-1}]	[ºC]	[ºC]	[ºC]	[ºC]	[kPa]	[kPa]	[ºC]	[kg m^{-2} s^{-1}]		[g s^{-1}]	[W m^{-2}]	[ºC]	[m]
Water	1	5581	28.3	68.0	39.7	94.6	-14.9	84.6	77.9	1.3	0.77	16.8	49.5	50.4	0.006
Water	1	5911	25.8	85.9	60.1	102.0	7.7	107.2	84.9	1.6	0.78	11.3	50.8	54.6	0.006
Water	1	7223	24.1	84.1	60.0	95.1	-13.7	85.8	81.2	1.3	0.73	8.2	36.9	52.3	0.006
Water	1	5857	25.4	75.1	49.7	95.2	-13.2	86.3	79.1	2.1	0.47	12.4	45.9	50.2	0.006
Water	10	7939	26.7	87.1	60.4	95.4	-12.5	86.6	84.8	1.5	0.63	7.2	32.8	66.9	0.006
Water	10	5563	28.3	78.4	50.0	95.0	-14.1	85.0	82.4	2.2	0.45	10.5	39.4	65.1	0.006
Water	10	10153	48.8	89.8	41.0	96.2	-9.7	89.4	89.0	2.1	0.40	6.8	20.9	76.6	0.006
Water	10	5523	30.0	69.8	39.9	94.2	-16.0	83.1	80.7	2.1	0.46	15.2	45.2	63.1	0.006
Water	25	4919	26.9	76.9	50.0	95.6	-11.5	86.4	79.9	1.2	0.70	11.6	43.3	58.2	0.006
Water	25	18724	42.3	92.7	50.4	96.3	-8.9	89.1	88.7	1.2	0.60	4.2	16.0	71.8	0.006
Water	25	5285	30.9	81.0	50.1	102.7	7.7	105.6	84.1	1.2	0.83	15.9	59.6	60.6	0.006
Water	25	5056	32.0	61.9	29.9	94.9	-12.9	85.1	78.8	1.2	0.75	23.1	51.2	57.0	0.006
Water	25	4938	36.5	69.5	33.0	103.6	7.7	105.6	82.7	1.3	0.73	27.2	66.8	60.5	0.006
Water	25	5336	54.2	83.4	29.2	95.0	-14.0	84.7	86.4	1.2	0.67	10.7	23.6	76.4	0.006
Water	25	4636	29.2	79.3	50.1	94.4	-15.5	83.2	81.5	1.3	0.79	9.6	35.9	65.5	0.006
Water	25	7889	68.9	97.0	28.2	104.1	7.7	106.4	95.3	1.0	0.73	14.9	31.8	84.2	0.006
Water	1	4455	32.4	62.4	30.0	92.2	-21.9	78.0	76.4	1.2	0.49	19.2	42.7	53.2	0.006
Water	1	11135	45.4	89.0	43.6	94.3	-16.1	83.8	86.1	1.8	0.25	5.6	18.3	68.7	0.006
Water	1	6814	26.4	76.4	50.1	84.6	-42.1	57.7	74.8	0.9	0.42	7.1	26.6	57.3	0.006
Water	1	10722	38.7	80.4	41.6	86.0	-38.9	61.0	78.8	1.1	0.44	5.5	17.2	65.0	0.006
Water	10	9697	38.2	84.2	46.0	90.3	-28.5	71.4	81.6	1.7	0.12	6.5	22.4	66.4	0.006
Water	10	10688	59.2	97.8	38.6	103.5	7.7	107.5	94.7	1.7	0.54	10.6	31.0	79.4	0.006
Water	0.5	4813	34.7	65.0	30.3	94.8	-16.4	83.4	77.7	2.0	0.38	20.6	46.4	54.7	0.006
Water	0.5	5637	33.3	83.2	49.9	102.8	7.7	107.5	85.4	2.8	0.37	13.9	51.8	60.0	0.006
Water	0.5	6848	69.1	89.1	20.0	102.7	7.7	106.8	92.9	2.9	0.36	21.3	32.0	80.6	0.008
Water	0.5	5816	30.3	80.3	50.0	91.6	-24.7	74.4	79.1	1.0	0.29	8.3	31.2	57.7	0.006
Water	0.5	7851	53.5	93.9	40.4	101.3	7.7	106.9	91.5	3.8	0.09	8.6	26.2	74.7	0.006
Water	24.5	20404	38.7	89.0	50.3	93.4	-18.7	80.5	86.5	3.4	0.04	4.5	17.1	73.1	0.006
Water	0.5	5812	30.9	81.1	50.2	99.9	2.8	102.0	84.4	4.3	0.15	11.5	43.0	59.8	0.006
Water	0.5	5933	25.6	77.7	52.1	89.9	-28.0	71.2	77.4	4.4	0.25	8.9	34.8	55.4	0.006
Water	24.5	6711	28.1	79.6	51.5	90.7	-24.5	74.7	79.4	3.9	0.09	9.0	34.5	62.3	0.006
Water	0.5	6506	29.3	80.7	51.4	93.1	-17.1	80.9	81.0	4.0	0.14	9.4	36.3	59.5	0.006
Water	0.5	5467	30.7	60.6	29.9	91.1	-23.8	74.2	76.4	4.2	0.15	21.4	47.5	55.0	0.006
Water	0.5	3878	28.8	84.2	55.3	98.0	0.1	99.1	57.0	4.7	0.10	5.7	23.6	30.4	0.135
Water	0.5	2829	29.5	66.6	37.1	100.5	5.6	104.7	58.3	4.7	0.12	12.9	35.3	31.3	0.135
Water	0.5	4981	27.1	83.5	56.5	93.3	-18.8	80.3	68.6	4.4	0.11	6.2	26.2	34.2	0.068
Water	0.5	9965	27.2	86.8	59.6	94.2	-16.2	82.8	74.8	3.8	0.05	5.7	25.6	36.6	0.044
Water	0.5	4816	27.6	73.1	45.5	94.2	-16.2	82.8	70.9	4.7	0.06	11.8	39.9	34.2	0.044
Water	0.5	4208	27.9	72.0	44.1	94.5	-15.5	83.5	69.0	4.5	0.06	11.4	37.4	32.7	0.058

L = 5.7 m; Air and Water-Cooled

Cooling	Inc	HTC	Tri	Tro	dTr	Ts	dPg	Ps	Twall	G	x	m_dot_r	q"	Tw1	t_c
	[º]	[W m^{-2} K^{-1}]	[ºC]	[ºC]	[ºC]	[ºC]	[kPa]	[kPa]	[ºC]	[kg m^{-2} s^{-1}]		[g s^{-1}]	[W m^{-2}]	[ºC]	[m]
Water	0.5	7374	28.2	85.6	57.4	94.6	-14.9	84.1	72.2	4.9	0.04	5.8	25.1	34.8	0.058
Water	0.5	5378	27.9	75.1	47.2	95.2	-13.4	85.7	75.7	4.9	0.06	11.6	40.9	42.2	0.033
Water	0.5	4906	27.7	85.0	57.3	94.8	-14.0	85.0	66.4	4.4	0.11	5.8	24.8	33.0	0.110
Water	0.5	4049	27.1	82.8	55.7	93.2	-18.5	80.6	71.3	4.7	0.11	6.5	27.0	35.8	0.110
Water	0.5	4755	27.9	75.2	47.4	91.7	-25.0	75.6	72.2	1.1	0.44	9.8	34.6	44.6	0.016
Water	0.5	4730	27.5	74.9	47.4	92.1	-24.5	76.1	70.1	1.1	0.39	9.9	34.9	37.5	0.032
Water	0.5	4002	26.4	75.0	48.5	93.2	-21.9	78.7	69.1	1.1	0.37	9.9	36.0	35.3	0.052
Water	0.5	4523	27.2	74.4	47.2	92.1	-24.2	76.4	69.0	1.1	0.38	9.9	34.8	36.4	0.043
Water	0.5	4681	27.7	75.1	47.4	92.1	-24.8	75.8	71.5	1.1	0.38	9.7	34.4	40.4	0.024
Water	0.5	3953	24.7	71.9	47.2	92.2	-22.4	78.2	63.1	1.1	0.35	9.7	34.0	31.9	0.083
Water	3	6844	26.1	82.3	56.2	90.6	-29.4	71.3	76.9	1.9	0.15	6.5	27.4	53.9	0.012
Water	3	7140	24.4	75.0	50.6	85.0	-44.4	56.3	72.4	0.9	0.31	8.0	30.1	50.9	0.011
Water	0.5	4285	24.4	73.5	49.1	92.7	-21.3	79.3	65.6	1.1	0.36	9.5	34.9	33.4	0.069
Water	0.5	3823	28.0	73.5	45.5	91.8	-24.6	76.1	67.4	1.1	0.40	9.8	33.4	36.1	0.053
Water	0.5	4888	30.6	81.4	50.8	102.6	7.7	105.4	77.2	2.3	0.44	12.4	46.9	40.3	0.051
Water	0.5	5318	25.6	86.7	61.2	102.7	7.7	105.4	76.7	2.5	0.54	10.1	46.1	37.0	0.050
Water	0.5	4583	31.2	74.9	43.7	102.7	7.7	105.4	76.5	2.1	0.46	15.6	50.8	40.4	0.050
Water	0.5	5862	30.3	86.1	55.8	101.4	7.7	105.4	81.9	1.7	0.52	9.8	40.8	44.8	0.030
Water	38	7372	27.7	91.4	63.8	100.2	4.8	102.5	87.0	1.5	0.53	6.9	33.0	69.0	0.005
Water	38	18619	29.0	84.8	55.8	88.0	-32.4	65.3	80.4	1.6	0.42	3.3	13.8	64.4	0.006
Water	38	6546	52.0	89.2	37.2	100.3	5.3	103.0	89.9	1.6	0.51	9.7	27.1	77.9	0.006
Water	0.5	4851	31.0	82.4	51.4	102.9	7.7	105.4	77.3	2.1	0.51	12.0	46.2	41.1	0.050
Water	38	4458	29.3	80.1	50.8	99.9	3.7	101.4	83.3	1.5	0.53	11.6	43.9	66.0	0.005
Water	0.5	4682	32.1	79.5	47.3	103.1	7.7	105.8	74.9	3.9	0.27	13.0	45.7	41.6	0.072
Water	0.5	3685	32.0	78.8	46.8	103.2	7.7	105.8	72.5	3.9	0.27	12.9	45.0	40.6	0.087
Water	0.5	4168	37.8	68.6	30.8	103.5	7.7	105.8	76.0	3.9	0.28	23.2	53.0	44.9	0.060
Water	0.5	3757	36.7	71.6	35.0	103.9	7.7	105.8	74.1	3.9	0.27	19.1	49.5	44.1	0.075
Water	0.5	4105	35.5	75.1	39.7	103.8	7.7	105.8	76.2	3.9	0.28	17.0	50.1	44.2	0.068
Water	0.5	4776	32.5	81.0	48.5	103.0	7.7	105.8	77.1	3.9	0.27	12.9	46.7	42.6	0.058
Water	0.5	4143	39.4	67.7	28.3	103.6	7.7	105.8	76.2	3.9	0.28	25.7	53.8	45.9	0.062
Water	0.5	4609	33.6	83.9	50.3	103.8	7.7	105.8	79.8	3.9	0.27	12.9	48.4	45.1	0.042
Water	0.5	4391	38.2	69.7	31.5	103.5	7.7	105.8	77.1	3.9	0.28	22.9	53.5	45.8	0.053
Water	0.5	3998	35.5	81.6	46.1	104.0	7.7	105.8	75.6	3.9	0.26	12.9	44.3	44.6	0.076
Water	0.5	5370	33.9	88.3	54.4	103.8	7.7	105.8	83.6	3.9	0.27	11.7	47.8	49.7	0.025
Water	0.5	4159	35.4	74.2	38.8	103.5	7.7	105.8	76.2	3.9	0.27	17.2	49.5	44.0	0.062
Air	49	12283	37.7	87.8	50.1	100.0	2.6	101.3	98.5	4.0	1.00	106.2	11.8	99.1	0.001
Air	49	11770	34.1	90.7	56.6	100.0	2.6	101.3	98.4	4.0	0.86	115.1	14.5	99.1	0.002
Air	49	11337	32.7	86.5	53.8	100.0	2.6	101.3	97.7	4.0	0.68	120.9	14.6	95.8	0.003
Air	49	11776	33.0	89.7	56.7	100.0	2.6	101.3	97.9	4.0	0.50	110.7	14.1	93.8	0.004

L = 5.7 m; Air and Water-Cooled

Cooling	Inc	HTC	Tri	Tro	dTr	Ts	dPg	Ps	Twall	G	x	m_dot_r	q"	Tw1	t_c
	[º]	[W m^{-2} K^{-1}]	[ºC]	[ºC]	[ºC]	[ºC]	[kPa]	[kPa]	[ºC]	[kg m^{-2} s^{-1}]		[g s^{-1}]	[W m^{-2}]	[ºC]	[m]
Air	49	11084	33.5	91.1	57.7	100.0	2.6	101.3	98.2	4.0	0.33	120.4	15.5	96.6	0.005
Air	49	9810	32.3	85.9	53.6	100.0	2.6	101.3	97.8	4.0	0.14	96.4	16.6	95.5	0.006
Air	7	9261	34.3	86.5	52.2	99.7	0.9	100.4	92.2	3.9	1.00	106.2	12.5	92.2	0.001
Air	7	11494	34.2	90.5	56.3	99.7	0.9	100.4	92.2	3.9	0.83	115.1	14.6	92.2	0.003
Air	7	8744	33.8	86.3	52.5	99.7	0.9	100.4	92.2	3.9	0.63	120.9	14.3	92.2	0.004
Air	7	9035	34.5	89.3	54.7	99.7	0.9	100.4	92.2	3.9	0.44	110.7	13.6	92.2	0.006
Air	7	8625	34.3	89.3	55.0	99.7	0.9	100.4	92.2	3.9	0.27	120.4	14.9	92.2	0.007
Air	7	7288	31.4	71.5	40.2	99.7	0.9	100.4	85.8	3.9	0.09	96.4	12.5	53.4	0.008
Air	4	13983	34.6	87.2	52.6	100.9	5.6	104.6	99.5	3.9	1.00	103.1	12.1	98.7	0.001
Air	4	13583	34.5	88.3	53.9	100.9	5.6	104.6	99.5	3.9	0.84	109.5	13.2	96.7	0.002
Air	4	12756	34.1	86.8	52.7	100.9	5.6	104.6	98.8	3.9	0.67	120.3	14.2	96.4	0.004
Air	4	13588	35.2	91.3	56.1	100.9	5.6	104.6	98.9	3.9	0.49	112.2	14.0	94.5	0.005
Air	4	13133	36.5	92.9	56.5	100.9	5.6	104.6	99.5	3.9	0.31	114.1	14.3	97.4	0.006
Air	4	11909	34.9	87.6	52.7	100.9	5.6	104.6	99.3	3.9	0.13	83.1	14.0	97.0	0.007
Air	0	13673	33.5	87.6	54.1	100.6	4.0	103.5	98.4	3.8	1.00	103.0	12.6	98.7	0.002
Air	0	14627	33.9	91.4	57.5	100.6	4.0	103.5	98.3	3.8	0.84	107.6	13.9	95.9	0.004
Air	0	12974	33.1	90.4	57.3	100.6	4.0	103.5	97.9	3.8	0.66	108.7	14.1	95.7	0.006
Air	0	14225	33.9	92.0	58.1	100.6	4.0	103.5	97.8	3.8	0.48	104.8	13.7	93.0	0.008
Air	0	12854	35.1	92.8	57.7	100.6	4.0	103.5	98.5	3.8	0.30	108.9	14.1	95.9	0.009
Air	0	11343	33.1	84.9	51.8	100.6	4.0	103.5	98.4	3.8	0.12	81.9	13.7	95.6	0.011
Air	0.3	13760	34.6	88.4	53.7	101.2	6.2	105.8	99.8	3.7	1.00	103.0	12.4	99.7	0.002
Air	0.3	15177	34.7	92.1	57.4	101.2	6.2	105.8	99.6	3.7	0.84	107.6	13.9	99.7	0.004
Air	0.3	13039	34.1	91.1	57.0	101.2	6.2	105.8	99.0	3.7	0.66	108.7	13.9	96.8	0.006
Air	0.3	14710	35.0	92.7	57.8	101.2	6.2	105.8	98.9	3.7	0.48	104.8	13.6	95.0	0.008
Air	0.3	12915	36.0	93.5	57.5	101.2	6.2	105.8	99.4	3.7	0.30	108.9	14.0	99.7	0.009
Air	0.3	11402	34.1	85.5	51.4	101.2	6.2	105.8	99.2	3.7	0.12	81.9	13.5	97.1	0.011
Air	4	13978	34.9	88.9	54.1	101.3	6.9	106.4	99.7	3.8	1.00	103.0	12.5	95.0	0.001
Air	4	15170	35.1	92.3	57.2	101.3	6.9	106.4	99.7	3.8	0.84	107.6	13.8	92.6	0.002
Air	4	13227	34.3	91.2	56.9	101.3	6.9	106.4	99.5	3.8	0.66	108.7	13.9	92.8	0.004
Air	4	13922	35.3	92.9	57.6	101.3	6.9	106.4	99.5	3.8	0.48	104.8	13.5	90.5	0.005
Air	4	13316	36.4	93.7	57.4	101.3	6.9	106.4	99.7	3.8	0.30	108.9	14.0	94.1	0.006
Air	4	11903	34.4	85.2	50.8	101.3	6.9	106.4	99.7	3.8	0.12	81.9	13.4	94.4	0.007
Air	0.3	13798	33.1	86.8	53.7	100.4	3.0	103.0	98.9	3.9	1.00	103.0	12.6	97.8	0.001
Air	0.3	13514	32.9	90.4	57.5	100.4	3.0	103.0	98.7	3.9	0.84	107.6	14.1	96.1	0.003
Air	0.3	13065	32.6	89.4	56.8	100.4	3.0	103.0	98.1	3.9	0.66	108.7	14.0	95.9	0.004
Air	0.3	13712	33.7	91.9	58.1	100.4	3.0	103.0	97.9	3.9	0.48	104.8	13.8	93.9	0.006
Air	0.3	13127	35.0	92.7	57.6	100.4	3.0	103.0	98.4	3.9	0.31	108.9	14.2	96.6	0.007
Air	0.3	11687	33.2	88.1	54.9	100.4	3.0	103.0	98.2	3.9	0.13	81.9	14.6	96.0	0.008
Air	6	13937	33.1	86.7	53.6	100.3	2.5	102.5	98.8	3.9	1.00	103.0	12.5	97.6	0.001

L = 5.7 m; Air and Water-Cooled

Cooling	Inc	HTC	Tri	Tro	dTr	Ts	dPg	Ps	Twall	G	x	m_dot_r	q"	Tw1	t_c
	[º]	[W m^{-2} K^{-1}]	[ºC]	[ºC]	[ºC]	[ºC]	[kPa]	[kPa]	[ºC]	[kg m^{-2} s^{-1}]		[g s^{-1}]	[W m^{-2}]	[ºC]	[m]
Air	6	13672	33.2	90.4	57.3	100.3	2.5	102.5	98.9	3.9	0.84	107.6	14.0	95.0	0.002
Air	6	13032	32.5	89.4	56.9	100.3	2.5	102.5	98.3	3.9	0.66	108.7	14.0	94.8	0.003
Air	6	13783	33.7	91.8	58.1	100.3	2.5	102.5	98.3	3.9	0.48	104.8	13.8	91.6	0.004
Air	6	13256	35.0	92.6	57.6	100.3	2.5	102.5	98.9	3.9	0.31	108.9	14.2	94.4	0.005
Air	6	11909	33.0	87.9	54.9	100.3	2.5	102.5	98.6	3.9	0.13	81.9	14.6	94.0	0.006
Air	7	14335	33.6	87.9	54.2	101.1	6.6	105.5	99.7	3.8	1.00	89.7	10.9	98.9	0.001
Air	7	14633	34.0	92.8	58.8	101.1	6.6	105.5	99.8	3.8	0.86	92.3	12.2	97.1	0.002
Air	7	13711	32.7	91.2	58.5	101.1	6.6	105.5	99.4	3.8	0.70	96.2	12.6	97.0	0.003
Air	7	13269	33.1	91.5	58.4	101.1	6.6	105.5	99.1	3.8	0.54	115.7	15.2	94.6	0.004
Air	7	12768	33.8	92.2	58.4	101.1	6.6	105.5	99.4	3.8	0.34	119.0	15.6	96.9	0.005
Air	7	11444	32.3	87.4	55.1	101.1	6.6	105.5	99.2	3.8	0.14	91.4	16.2	96.7	0.006
Air	11	15611	34.0	88.0	54.0	100.9	6.1	104.8	99.7	3.8	1.00	74.1	8.9	98.9	0.001
Air	11	17372	34.5	93.1	58.6	100.9	6.1	104.8	99.8	3.8	0.89	83.8	11.0	97.3	0.002
Air	11	13559	33.0	91.2	58.2	100.9	6.1	104.8	99.6	3.8	0.74	102.0	13.3	97.3	0.003
Air	11	13229	32.9	90.7	57.8	100.9	6.1	104.8	99.0	3.8	0.57	124.2	16.1	94.6	0.003
Air	11	12533	33.7	91.4	57.7	100.9	6.1	104.8	99.3	3.8	0.37	137.7	17.8	96.7	0.004
Air	11	11443	32.3	86.5	54.2	100.9	6.1	104.8	99.0	3.8	0.14	93.4	16.2	96.5	0.005
Air	0	14915	31.3	88.1	56.8	100.4	3.2	102.7	98.7	3.7	1.00	74.1	9.6	98.1	0.002
Air	0	15024	33.3	92.1	58.8	100.4	3.2	102.7	98.6	3.7	0.88	83.8	11.1	96.0	0.003
Air	0	13268	31.5	90.4	58.8	100.4	3.2	102.7	98.1	3.7	0.74	102.0	13.6	95.9	0.005
Air	0	12853	31.5	89.7	58.3	100.4	3.2	102.7	97.3	3.7	0.57	124.2	16.4	92.7	0.006
Air	0	12167	32.0	90.3	58.2	100.4	3.2	102.7	98.0	3.7	0.37	137.7	18.2	94.8	0.007
Air	0	10943	30.9	86.0	55.1	100.4	3.2	102.7	97.9	3.7	0.14	93.4	16.7	94.3	0.009
Air	0.6	14915	30.1	88.2	58.1	100.7	4.5	104.1	99.1	3.9	1.00	74.1	9.8	97.2	0.001
Air	0.6	14900	32.1	92.2	60.2	100.7	4.5	104.1	99.2	3.9	0.88	83.8	11.4	94.5	0.003
Air	0.6	13260	30.8	90.7	59.8	100.7	4.5	104.1	98.9	3.9	0.74	102.0	13.9	94.0	0.004
Air	0.6	12871	30.8	89.9	59.1	100.7	4.5	104.1	98.1	3.9	0.57	124.2	16.7	90.4	0.006
Air	0.6	12243	31.8	90.5	58.7	100.7	4.5	104.1	98.6	3.9	0.36	137.7	18.3	93.1	0.007
Air	0.6	11033	30.7	85.4	54.7	100.7	4.5	104.1	98.2	3.9	0.14	93.4	16.6	93.9	0.008
Air	0	15103	34.7	88.7	54.0	100.2	3.0	102.1	98.3	3.6	1.00	74.1	9.0	96.0	0.002
Air	0	15274	36.4	92.7	56.3	100.2	3.0	102.1	98.4	3.6	0.88	83.8	10.5	94.0	0.004
Air	0	13388	35.3	90.9	55.6	100.2	3.0	102.1	98.0	3.6	0.74	102.0	12.7	93.5	0.007
Air	0	13947	35.6	90.3	54.8	100.2	3.0	102.1	97.2	3.6	0.57	124.2	15.2	90.1	0.009
Air	0	12157	36.2	90.8	54.6	100.2	3.0	102.1	97.6	3.6	0.37	137.7	16.7	91.9	0.010
Air	0	10878	35.1	86.7	51.6	100.2	3.0	102.1	97.4	3.6	0.14	93.4	15.4	92.4	0.013
Air	20	10691	35.6	88.2	52.6	99.8	1.7	100.8	98.5	3.6	1.00	74.1	8.7	97.6	0.001
Air	20	15566	37.1	92.4	55.4	99.8	1.7	100.8	98.7	3.6	0.88	83.8	10.3	96.2	0.002
Air	20	11586	35.6	90.7	55.1	99.8	1.7	100.8	98.4	3.6	0.74	102.0	12.5	96.2	0.003
Air	20	13682	35.6	90.2	54.7	99.8	1.7	100.8	97.9	3.6	0.57	124.2	15.1	94.0	0.003

L = 5.7 m; Air and Water-Cooled

Cooling	Inc	HTC	Tri	Tro	dTr	Ts	dPg	Ps	Twall	G	x	m_dot_r	q"	Tw1	t_c
	[º]	[W m^{-2} K^{-1}]	[ºC]	[ºC]	[ºC]	[ºC]	[kPa]	[kPa]	[ºC]	[kg m^{-2} s^{-1}]		[g s^{-1}]	[W m^{-2}]	[ºC]	[m]
Air	20	10559	36.3	90.7	54.3	99.8	1.7	100.8	98.4	3.6	0.37	137.7	16.7	96.0	0.004
Air	20	8038	35.3	85.2	49.8	99.8	1.7	100.8	97.8	3.6	0.14	93.4	14.8	95.5	0.005
Air	1	10002	31.2	82.4	51.2	94.2	-18.7	80.9	92.1	4.1	1.00	74.1	8.6	91.6	0.001
Air	1	10051	31.8	82.8	51.0	93.8	-17.3	82.2	91.6	2.9	1.00	83.8	8.6	92.1	0.003
Air	1	12830	33.1	86.4	53.4	94.2	-18.7	80.9	92.1	4.1	0.88	102.0	10.1	91.6	0.004
Air	1	12198	33.6	86.9	53.3	93.8	-17.3	82.2	91.6	2.9	0.88	124.2	10.1	92.1	0.006
Air	1	8938	31.8	84.5	52.7	94.2	-18.7	80.9	92.1	4.1	0.75	137.7	12.2	91.6	0.007
Air	1	8972	32.3	85.0	52.7	93.8	-17.3	82.2	91.6	2.9	0.74	93.4	12.2	89.4	0.008
Air	1	11295	31.9	84.0	52.1	94.2	-18.7	80.9	91.4	4.1	0.60	74.1	14.7	91.6	0.001
Air	1	10698	32.4	84.4	52.0	93.8	-17.3	82.2	91.6	2.9	0.56	83.8	14.6	86.9	0.003
Air	1	9613	32.6	84.3	51.8	94.2	-18.7	80.9	91.6	4.1	0.43	102.0	16.1	91.6	0.004
Air	1	8272	33.1	84.7	51.6	93.8	-17.3	82.2	91.6	2.9	0.36	124.2	16.0	87.8	0.006
Air	1	7481	32.0	80.0	48.0	94.2	-18.7	80.9	90.9	4.1	0.25	137.7	14.5	84.9	0.007
Air	1	7354	32.7	79.1	46.4	93.8	-17.3	82.2	90.8	2.9	0.13	93.4	14.0	85.4	0.008
Air	20	12340	33.4	82.9	49.5	94.0	-17.5	81.7	90.5	3.2	1.00	103.0	11.4	90.3	0.001
Air	20	17648	33.8	86.3	52.5	94.0	-17.5	81.7	90.5	3.2	0.83	107.6	12.7	90.3	0.002
Air	20	11942	32.8	85.0	52.2	94.0	-17.5	81.7	90.5	3.2	0.65	108.7	12.8	90.3	0.003
Air	20	12634	34.1	86.3	52.2	94.0	-17.5	81.7	90.5	3.2	0.47	104.8	12.3	90.3	0.003
Air	20	8817	35.0	86.5	51.5	94.0	-17.5	81.7	90.5	3.2	0.29	108.9	12.6	90.3	0.004
Air	20	7783	33.7	78.8	45.1	94.0	-17.5	81.7	90.5	3.2	0.11	81.9	11.8	82.3	0.005
Air	0	9089	34.5	82.8	48.3	93.6	-18.5	80.4	89.6	3.1	1.00	103.0	11.1	89.9	0.002
Air	0	13295	35.8	86.0	50.2	93.6	-18.5	80.4	89.6	3.1	0.83	107.6	12.0	89.9	0.004
Air	0	8786	35.2	84.9	49.7	93.6	-18.5	80.4	89.6	3.1	0.65	108.7	12.0	89.9	0.007
Air	0	11746	36.5	86.1	49.5	93.6	-18.5	80.4	89.6	3.1	0.46	104.8	11.5	89.9	0.009
Air	0	8709	37.2	86.2	49.0	93.6	-18.5	80.4	89.6	3.1	0.29	108.9	11.8	89.9	0.010
Air	0	7534	36.4	78.8	42.4	93.6	-18.5	80.4	88.8	3.1	0.11	81.9	11.0	84.0	0.013
Air	0.5	9185	34.6	82.7	48.1	93.4	-19.1	79.9	89.8	3.1	1.00	103.0	11.1	89.3	0.002
Air	0.5	13473	35.7	85.9	50.1	93.4	-19.1	79.9	89.8	3.1	0.83	107.6	12.0	89.3	0.004
Air	0.5	8855	35.1	84.8	49.6	93.4	-19.1	79.9	89.8	3.1	0.65	108.7	12.0	89.3	0.006
Air	0.5	11135	36.3	85.9	49.6	93.4	-19.1	79.9	89.8	3.1	0.46	104.8	11.5	89.3	0.008
Air	0.5	8841	37.2	86.1	48.9	93.4	-19.1	79.9	89.8	3.1	0.29	108.9	11.8	89.3	0.009
Air	0.5	7625	36.6	78.7	42.1	93.4	-19.1	79.9	88.9	3.1	0.11	81.9	10.9	89.3	0.011
Air	20	9499	35.4	83.2	47.7	93.8	-18.0	80.9	89.3	3.2	1.00	103.0	11.0	89.8	0.001
Air	20	14453	35.8	86.2	50.4	93.8	-18.0	80.9	89.3	3.2	0.83	107.6	12.1	89.8	0.002
Air	20	8864	35.0	85.1	50.1	93.8	-18.0	80.9	89.3	3.2	0.65	108.7	12.1	89.8	0.003
Air	20	10060	36.4	86.3	49.9	93.8	-18.0	80.9	89.3	3.2	0.46	104.8	11.6	89.8	0.004
Air	20	8909	37.1	86.3	49.2	93.8	-18.0	80.9	89.3	3.2	0.29	108.9	11.9	89.8	0.005
Air	20	7821	36.1	77.6	41.5	93.8	-18.0	80.9	89.3	3.2	0.11	81.9	10.8	81.3	0.006
Air	0.8	14516	35.3	89.6	54.3	101.3	6.9	106.3	99.7	3.2	1.00	87.5	10.7	94.4	0.001

L = 5.7 m; Air and Water-Cooled															
Cooling	**Inc**	**HTC**	**Tri**	**Tro**	**dTr**	**Ts**	**dPg**	**Ps**	**Twall**	**G**	**x**	**m_dot_r**	**q"**	**Tw1**	**t_c**
	[º]	**[W m^{-2} K^{-1}]**	**[ºC]**	**[ºC]**	**[ºC]**	**[ºC]**	**[kPa]**	**[kPa]**	**[ºC]**	**[kg m^{-2} s^{-1}]**		**[g s^{-1}]**	**[W m^{-2}]**	**[ºC]**	**[m]**
Air	0.8	14853	35.7	93.5	57.9	101.3	6.9	106.3	99.8	3.2	0.83	89.0	11.5	93.0	0.002
Air	0.8	14486	34.5	92.8	58.3	101.3	6.9	106.3	99.5	3.2	0.64	81.3	10.7	93.2	0.004
Air	0.8	15399	35.7	93.4	57.7	101.3	6.9	106.3	99.0	3.2	0.47	77.6	10.0	90.6	0.005
Air	0.8	14168	36.5	94.3	57.8	101.3	6.9	106.3	99.4	3.2	0.30	85.2	11.0	93.2	0.006
Air	0.8	13094	35.4	88.5	53.1	101.3	6.9	106.3	98.7	3.2	0.12	65.3	11.1	92.6	0.007
Air	3	14694	35.9	89.5	53.7	101.2	6.6	106.0	99.7	3.2	1.00	87.5	10.5	98.7	0.001
Air	3	15112	36.6	93.5	56.9	101.2	6.6	106.0	99.8	3.2	0.83	89.0	11.3	97.2	0.002
Air	3	14543	35.5	92.8	57.2	101.2	6.6	106.0	99.5	3.2	0.64	81.3	10.4	97.3	0.003
Air	3	15533	36.8	93.5	56.7	101.2	6.6	106.0	99.1	3.2	0.46	77.6	9.8	95.3	0.004
Air	3	14480	37.5	94.3	56.8	101.2	6.6	106.0	99.6	3.2	0.30	85.2	10.8	97.0	0.005
Air	3	13290	36.2	88.4	52.2	101.2	6.6	106.0	99.0	3.2	0.12	65.3	10.9	96.2	0.006
Air	20	14588	37.5	89.3	51.8	101.0	5.8	105.1	99.6	3.1	1.00	87.5	10.1	98.5	0.001
Air	20	15070	37.5	93.2	55.7	101.0	5.8	105.1	99.7	3.1	0.83	89.0	11.0	96.6	0.002
Air	20	14477	36.1	92.5	56.5	101.0	5.8	105.1	99.5	3.1	0.64	81.3	10.3	96.4	0.003
Air	20	15386	37.0	93.3	56.2	101.0	5.8	105.1	99.1	3.1	0.47	77.6	9.7	93.8	0.003
Air	20	14267	37.8	94.1	56.4	101.0	5.8	105.1	99.6	3.1	0.31	85.2	10.7	95.5	0.004
Air	20	13158	36.2	88.6	52.4	101.0	5.8	105.1	99.0	3.1	0.13	65.3	10.9	94.1	0.005
Air	20	10680	37.9	83.0	45.1	93.5	-18.7	80.2	92.1	2.7	1.00	87.5	8.7	92.1	0.002
Air	20	18909	38.2	86.6	48.4	93.5	-18.7	80.2	92.1	2.7	0.83	89.0	9.5	92.1	0.004
Air	20	11019	37.0	85.6	48.6	93.5	-18.7	80.2	92.1	2.7	0.64	81.3	8.8	92.1	0.005
Air	20	15325	37.6	86.9	49.3	93.5	-18.7	80.2	92.0	2.7	0.47	77.6	8.5	88.6	0.007
Air	20	12032	38.3	87.6	49.3	93.5	-18.7	80.2	92.1	2.7	0.31	85.2	9.3	92.1	0.008
Air	20	8208	36.9	82.4	45.5	93.5	-18.7	80.2	91.8	2.7	0.13	65.3	9.4	88.5	0.010

HTC at Tube Bottom (in Condensate River); L = 5.7 m; Water Cooled						
River Depth	**HTC**	**Ts**	**G**	**Subcooling**	**Tw1**	**Hydraulic Depth of River**
[mm]	[W m^{-2} k^{-1}]	[^oC]	[kg m^{-2} s^{-1}]	[^oC]	[^oC]	[mm]
135	130	98.0	4.6	54.6	30.4	132
135	164	100.5	4.6	53.4	31.3	132
14.5	2206	92.3	4.6	0.0	57.7	11
68	266	93.3	4.6	25.3	34.2	65
44	272	94.2	4.6	11.7	36.6	41
44	385	94.2	4.6	12.2	34.2	41
58	351	94.5	4.6	18.0	32.7	55
58	227	94.6	4.6	17.8	34.8	55
46	208	95.0	4.6	10.8	39.7	43
31	757	95.5	4.6	6.6	49.8	28
33	447	95.2	4.6	6.9	42.2	30
110	215	94.8	4.6	27.7	33	107
110	280	93.2	4.6	15.8	35.8	107
16	730	91.7	1.2	11.7	44.6	13
32	497	92.1	1.2	15.1	37.5	29
43	432	92.1	1.2	19.2	36.4	40
10	1802	82.4	1.2	0.2	51	7
24	666	92.1	1.2	12.6	40.4	21
83	366	92.2	1.2	33.0	31.9	80
12	1115	90.6	1.2	2.3	53.9	9
11	1282	85.0	1.2	0.1	50.9	8
69	379	92.7	1.2	26.2	33.4	66
53	402	91.8	1.2	23.3	36.1	50
32	505	101.6	1.7	12.6	44.4	29
52	511	102.6	1.0	21.2	40.3	49
52	680	102.7	2.3	20.9	37	49
52	549	102.7	2.5	19.0	40.4	49
32	519	101.9	2.1	11.7	43.6	29
32	577	101.4	1.9	12.2	44.8	29
52	535	102.9	2.0	23.9	41.1	49
52	675	102.3	1.7	22.1	35.6	49
74.25	438	103.2	3.92	22.3	41.6	71
62	454	103.5	3.92	16.3	44.9	59
77	444	103.9	3.92	22.4	44.1	74
69.5	495	103.8	3.92	19.8	44.2	66
59.5	478	103.0	3.92	19.3	42.6	56
63.5	393	103.6	3.92	20.3	45.9	60
43.5	501	103.8	3.92	10.3	45.1	40

HTC at Tube Bottom (in Condensate River); L = 5.7 m; Water Cooled						
River Depth	**HTC**	**Ts**	**G**	**Subcooling**	**Tw1**	**Hydraulic Depth of River**
[mm]	[W m^{-2} k^{-1}]	[^oC]	[kg m^{-2} s^{-1}]	[^oC]	[^oC]	[mm]
55	460	103.5	3.92	13.0	45.8	52
78.25	454	104.0	3.92	23.1	44.6	75
27	1044	103.8	3.92	7.1	49.7	24
64	447	103.5	3.92	18.7	44	61
116	215	99.4	5.5	50.2	32.2	113
80	310	99.0	5.5	33.7	36.5	77
70	504	100.0	5.5	30.4	36.9	67
45	624	99.8	5.5	13.2	39.8	42
37	616	99.2	5.5	8.8	42.3	34

Pressure Drop; L = 5.7 m; Air-Cooled

Inc	Re_vi	mdot	v_si	Tai	Ts	Ps	Qa	dP	dP_m	dP_g	dP_f	Tatm	f
[o]		[g s^{-1}]	[m s^{-1}]	[^{o}C]	[^{o}C]	[kPa]	[kW m^{-2}]	[Pa]	[Pa]	[Pa]	[Pa]	[^{o}C]	
0.5	12616	9.4	10.8	29.6	91.9	77.0	34.1	42.2	-9.7	-0.2	52.1	22	0.028
10	10436	7.1	8.2	29.1	94.8	85.3	28.2	110.6	-5.4	-4.9	121.0	20	0.118
0.5	9853	6.7	11.0	29.1	90.4	72.6	26.4	77.7	-8.3	-0.2	86.2	20	0.055
30	9823	6.9	6.6	33.8	98.8	102.6	37.5	27.0	-13.6	-16.8	57.3	30	0.104
24.5	9788	6.8	9.0	31.9	90.9	73.8	24.8	11.8	-5.5	-10.3	27.6	23	0.025
0.5	9761	6.7	9.1	28.4	89.5	70.2	26.0	28.0	-5.3	-0.2	33.4	23	0.032
0.5	9750	6.7	8.7	27.0	91.2	74.2	27.1	21.0	-5.2	-0.2	26.4	22	0.026
0.5	9690	6.6	6.5	30.1	99.6	102.0	29.5	76.1	-4.0	-0.3	80.4	23	0.104
0.5	9532	7.0	7.8	29.1	93.3	81.4	27.4	104.1	-5.2	-0.2	109.5	20	0.111
24.5	9522	6.6	8.4	31.6	91.2	74.7	25.1	2.3	-5.1	-10.4	17.8	23	0.018
0.3	9501	6.5	6.4	33.4	98.5	103.0	35.5	38.3	-4.0	-0.2	42.5	28.5	0.056
0.5	9246	6.4	5.9	31.6	101.0	106.9	29.4	65.0	-3.4	-0.3	68.7	23	0.106
0.5	9167	6.3	7.6	30.8	93.5	80.9	26.2	25.4	-4.3	-0.2	30.0	22	0.036
0.3	9101	6.2	5.9	34.2	99.4	101.9	27.9	105.7	-3.3	-0.2	109.2	20	0.175
24.5	9060	6.2	7.1	31.8	93.0	80.2	25.8	4.5	-3.8	-11.1	19.5	23	0.026
3	9023	6.8	5.9	29.5	100.6	105.5	38.8	56.4	-4.2	-1.8	62.5	22	0.078
0.5	8737	6.0	7.8	26.8	91.3	75.3	28.0	66.7	-4.3	-0.2	71.2	20	0.088
0.5	8650	5.9	7.4	28.2	92.3	78.0	27.8	90.3	-4.0	-0.2	94.5	20	0.126
0.5	8647	5.9	7.2	28.7	92.8	79.9	27.6	54.3	-3.9	-0.2	58.4	21	0.080
0.5	8568	5.8	8.3	26.9	88.6	67.5	26.4	64.5	-4.3	-0.2	69.0	20	0.084
0.5	8559	5.8	8.2	26.6	88.9	68.3	26.7	65.1	-4.3	-0.2	69.5	20	0.086
0.5	8531	5.7	8.1	26.7	88.8	68.1	26.6	63.5	-4.2	-0.2	67.8	20	0.086
10	8509	6.0	7.4	29.8	92.0	78.3	26.8	58.8	-4.1	-4.6	67.5	19	0.087
10	8461	5.7	7.2	29.7	91.3	75.8	26.4	74.4	-3.7	-4.4	82.5	19	0.118
10	8345	5.9	7.3	29.7	91.6	76.6	26.5	67.4	-3.9	-4.5	75.8	19	0.102
1	8204	6.2	5.9	32.7	87.4	82.2	32.1	37.3	-3.2	-0.5	41.0	25	0.068
10	8034	5.6	6.6	29.2	94.9	85.8	28.2	75.6	-3.5	-5.0	84.1	20	0.127
20	7956	5.7	6.5	28.6	91.6	76.8	27.1	34.2	-3.0	-8.8	46.0	19	0.080
0.5	7810	5.6	5.6	29.1	93.2	80.7	27.3	69.5	-2.4	-0.2	72.1	20	0.158
20	7705	5.3	6.6	28.7	91.6	76.9	27.1	2.7	-3.2	-8.8	14.7	19	0.024
0	7419	5.0	7.1	26.0	88.6	67.4	26.8	69.9	-3.2	0.0	73.1	20	0.119
1.5	7278	5.0	5.8	35.2	82.7	71.7	22.9	14.8	-2.2	-0.6	17.7	30	0.042
0	7244	5.1	7.0	27.0	88.7	67.8	26.4	70.7	-3.1	0.0	73.8	20	0.126
1	7219	5.5	7.0	32.1	90.1	80.9	32.4	8.3	-3.4	-0.5	12.1	24	0.019
0	7217	4.9	7.0	26.9	88.5	67.3	26.3	63.6	-3.1	0.0	66.6	20	0.115
1.8	6986	4.8	6.0	33.6	91.6	77.6	24.9	25.8	-2.6	-0.8	29.2	26	0.059
10	6731	5.7	4.0	44.3	99.7	102.6	18.3	45.1	-2.2	-5.9	53.1	21	0.119
10	6396	5.4	3.0	46.5	100.9	106.0	16.2	8.6	-1.1	-6.1	15.8	21	0.060

Pressure Drop; L = 5.7 m; Air-Cooled

Inc	Re_vi	mdot	v_si	Tai	Ts	Ps	Qa	dP	dP_m	dP_g	dP_f	Tatm	f
[o]		[g s^{-1}]	[m s^{-1}]	[^{o}C]	[^{o}C]	[kPa]	[kW m^{-2}]	[Pa]	[Pa]	[Pa]	[Pa]	[^{o}C]	
3	6235	3.2	4.0	38.1	101.9	108.2	17.0	44.1	-1.0	-1.9	47.0	22	0.236
0.5	5887	5.3	3.9	43.8	100.5	105.9	18.2	49.9	-2.3	-0.3	52.6	21	0.113
0.5	5773	4.8	1.6	55.3	101.0	106.7	9.2	4.2	-0.2	-0.3	4.7	20	0.089
10	5395	4.8	4.3	51.9	94.7	85.0	9.8	51.6	-1.8	-4.9	58.4	20	0.133
10	5385	5.2	4.4	51.1	93.7	81.9	9.7	42.5	-2.0	-4.8	49.3	20	0.099
1	5354	5.3	4.2	50.7	95.1	86.3	9.5	57.4	-2.0	-0.5	59.9	18	0.121
10	5301	5.1	4.3	52.0	94.1	83.1	9.6	40.8	-2.0	-4.8	47.6	20	0.099
10	5208	4.3	3.9	52.7	96.0	89.4	9.8	39.9	-1.5	-5.2	46.6	20	0.135
0.5	5109	5.1	3.4	57.0	100.5	105.1	8.9	46.5	-1.6	-0.3	48.3	20	0.124
1	4967	4.7	4.1	46.7	93.3	81.5	11.4	40.6	-2.1	-0.5	43.1	22	0.100
25	4625	3.3	3.8	55.7	93.3	80.2	8.2	20.7	-1.0	-11.3	33.0	24	0.132
1	4391	4.1	3.6	47.9	94.2	83.8	10.9	48.0	-1.6	-0.5	50.1	22	0.153
1	4345	4.1	3.5	48.7	93.9	83.2	10.6	53.5	-1.6	-0.5	55.6	22	0.171
10	4180	3.6	3.8	45.5	89.9	71.4	11.3	49.0	-1.5	-4.2	54.7	22	0.189
0.5	3383	2.3	2.8	28.9	93.2	80.7	27.5	57.4	-0.6	-0.2	58.2	20	0.512
25	3073	2.2	2.3	54.0	96.1	89.1	9.3	9.7	-0.4	-12.5	22.6	18	0.197
25	3070	2.2	2.4	53.2	94.8	85.1	9.2	6.4	-0.3	-12.0	18.6	18	0.153
25	3065	2.2	2.4	53.2	95.2	86.4	9.3	-3.3	-0.3	-12.2	9.2	18	0.077
0.5	2810	2.5	2.5	46.1	91.2	74.4	12.7	33.0	-0.7	-0.2	33.9	21	0.240
0.5	2344	2.1	2.1	46.2	91.2	74.4	12.7	38.5	-0.5	-0.2	39.2	21	0.406
1	2299	1.9	1.8	46.8	93.7	82.6	11.4	4.4	-0.3	-0.5	5.2	22	0.076
1	2298	1.9	2.0	48.2	92.2	78.0	10.3	42.0	-0.3	-0.5	42.8	22	0.544
0.5	2283	2.0	2.1	45.4	89.6	72.0	12.6	33.4	-0.5	-0.2	34.1	21	0.368
1	2109	1.7	2.0	43.4	84.4	57.7	10.3	33.3	-0.3	-0.3	33.9	22	0.558
1	2108	1.7	1.9	44.3	86.4	62.7	10.4	5.8	-0.2	-0.4	6.3	22	0.111
10	2098	1.7	1.6	45.6	90.4	72.6	11.4	8.6	-0.1	-4.2	13.0	22	0.274
10	1992	1.7	1.6	51.9	95.1	86.6	9.9	27.5	-0.2	-5.0	32.6	20	0.617
1	1836	1.5	1.9	43.9	85.7	61.0	10.3	19.2	-0.3	-0.4	19.8	22	0.336
25	1365	1.8	1.1	54.5	94.9	84.7	8.9	1.2	-0.2	-11.9	13.3	24	0.223
25	1330	1.7	1.1	54.5	94.4	83.2	8.5	-3.0	-0.1	-11.7	8.8	24	0.193
49	9776	13.4	6.8	33.9	98.2	101.3	37.0	17.0	-13.6	-25.3	55.9	28.5	